# Transported Probability Density Function for the Numerical Simulation of Flames characteristic of Fire

Daria Burot

▶ **To cite this version:**

Daria Burot. Transported Probability Density Function for the Numerical Simulation of Flames characteristic of Fire . Reactive fluid environment. Université d'Aix Marseille, 2017. English. ⟨NNT : ⟩. ⟨tel-01475592v2⟩

**HAL Id: tel-01475592**

**https://hal.science/tel-01475592v2**

Submitted on 12 Mar 2017

**HAL** is a multi-disciplinary open access archive for the deposit and dissemination of scientific research documents, whether they are published or not. The documents may come from teaching and research institutions in France or abroad, or from public or private research centers.

L'archive ouverte pluridisciplinaire **HAL**, est destinée au dépôt et à la diffusion de documents scientifiques de niveau recherche, publiés ou non, émanant des établissements d'enseignement et de recherche français ou étrangers, des laboratoires publics ou privés.

HAL Authorization

ED 353 – Sciences pour l'ingénieur : Mécanique, Physique, Micro et Nanoélectronique
Institut Universitaire des Systèmes Thermiques Industriels – UMR CNRS 7343

Thèse présentée pour obtenir le grade universitaire de docteur
Discipline : Energétique

Daria BUROT

# TRANSPORTED PROBABILITY DENSITY FUNCTION FOR THE NUMERICAL SIMULATIONS OF FLAMES CHARACTERISTIC OF FIRE

Soutenue le 27 Janvier 2017

Devant le Jury composé de :

**Mouna EL AFI**, Ecole des Mines d'Albi Carmaux, **Rapporteur**
**Epaminondas MASTORAKOS**, University of Cambridge, **Rapporteur**
**Denis VEYNANTE**, Ecole Centrale Paris, **Président du jury**
**Lounes TADRIST**, Aix-Marseille Université, **Examinateur**
**Fatiha NMIRA**, Direction R&D, EDF-Chatou, **Responsable industiel**
**Jean-Louis CONSALVI**, Aix-Marseille Université, **Directeur de thèse**

# Remerciements

Ces trois années passées en thèse au sein d'EDF ont été excellentes et ceci n'aurait pas été le cas sans la présence et le soutien de nombreuses personnes, et en tout premier lieu bien sûr Jean-Louis Consalvi et Fatiha Nmira, que je remercie chaleureusement pour leur fabuleux encadrement tout au long de ces trois ans. Merci de m'avoir offert cette formidable opportunité qui m'a permis de grandir non seulement professionnellement, mais aussi humainement. Merci de m'avoir poussée à avancer et remise sur la bonne route quand j'en avais besoin.

Merci à Mouna El Afi et Epaminondas Mastorakos d'avoir accepté de rapporter ma thèse, ainsi qu'à Denis Veynante et Lounes Tadrist d'avoir accepté de participer au jury.

Cette thèse s'est déroulée au sein du département MFEE d'EDF, en collaboration avec l'IUSTI d'Aix-Marseille Université. Je tiens, à ce titre, à remercier chaleureusement Cécile Clarenc-Macé, Isabelle Flour et Frédéric Baron pour leur accueil à MFEE. Merci également au pilote stratégique Céline Cheviet d'avoir accordé le financement de la thèse. Je remercie Lounes Tadrist de m'avoir accueillie dans le laboratoire IUSTI.

Merci également aux membres du projet incendie, au groupe I8D et précédemment I81 pour leur accueil chaleureux et la bonne humeur dans les couloirs, et en particulier aux doctorants : ma chère ancienne collègue de bureau Solène, ma chère nouvelle collègue de bureau Sarah, William, Sophie et Antoine.

Evidemment, je remercie très fort également ma famille : papa, maman, Chloé, Martin, qui ont toujours été là pour me soutenir et m'encourager dans ce que je souhaite faire même s'ils ne le comprenaient pas forcément. De même à mes plus vieux amis, comme aux plus récents, que je ne citerai pas tous mais en vrac : Popiette, Auré, Claire, Agnès, Edith, Quentin, Aymeric, Maud, Camille (les 2), Pauline (les 2), Clément, Corentin, Léa… Toujours disponibles pour aller prendre un verre quand ça va ou pas.

# Résumé de la thèse en français

Electricité De France, en tant qu'exploitant, est responsable de la sûreté des centrales nucléaires et définit les moyens et l'organisation mis en place, conformément aux textes réglementaires, pour s'assurer que ses installations ne présentent pas de risques ou d'inconvénients pour le public et l'environnement. Ces règles sont soumises à l'ASN (Autorité de Sûreté Nucléaire) qui contrôle les activités de l'exploitant en vérifiant la mise en application de la réglementation, notamment lors d'inspections in situ.

L'incendie dans une centrale nucléaire est le risque potentiel d'agression interne le plus élevé. Outre la sécurité de son personnel et le bon fonctionnement de ses installations, EDF possède un intérêt économique (lié à la perte de matériels et à l'immobilisation du moyen de production) à diminuer le risque incendie en assurant un niveau de sûreté élevé sans recourir à des moyens de défense contre l'incendie surdimensionnés, parfois imposés par des règles prescriptives censées couvrir le maximum de situations. La démonstration de l'efficacité de la sûreté incendie à l'aide d'outils numériques, rendue possible par l'amélioration des connaissances, des capacités de calcul et l'évolution réglementaire, est en croissance puisqu'elle permet de défendre certaines dispositions plus adaptées aux situations de terrain.

Les outils de simulation numérique développés par la direction Recherche et Développement d'EDF (EDF R&D) participent depuis plusieurs années aux réponses apportées par EDF. Aujourd'hui, le code de référence incendie à EDF est le code MAGIC, code bi-zones reposant sur l'hypothèse de stratification des gaz chauds au-dessus d'une couche de gaz frais. Ce type de modélisation présente l'avantage d'un coût de calcul faible et répond à la majorité des besoins industriels. Cependant, dans le cas de grands volumes, de géométries complexes ou étirées (tunnels, galeries, etc.), l'hypothèse de stratification est critiquable, d'où la nécessité d'une modélisation plus détaillée. Pour ce faire, EDF R&D s'est appuyé sur *Code_Saturne*, code de mécanique des fluides développé par le

département Mécanique des Fluides, Energies et Environnement (MFEE). Les codes à champs, en résolvant les bilans de masse, de quantité de mouvement et d'énergie à l'échelle de la maille, permettent une modélisation plus fine de la physique. Par ailleurs, de nombreux paramètres doivent être pris en compte afin de représenter correctement l'ensemble des processus physiques qui ont cours dans un feu et une bonne estimation des risques liés à l'incendie.

La dynamique des feux est au croisement de nombreux processus physiques variés dont la modélisation numérique implique différentes stratégies [1]. Ceci inclue la dynamique des fluides, les transferts radiatifs, les écoulements multiphasiques, la combustion gazeuse, la production de suie, la dégradation thermique des matériaux, et la turbulence. De plus, tous ces processus sont couplés les uns aux autres, en particulier à travers la turbulence qui introduit des problèmes de fermeture, notamment pour les termes de production/destruction des espèces gazeuses et des particules de suie, et pour les termes d'absorption et d'émission du rayonnement.

Les flammes caractéristiques des incendies sont généralement des flammes de diffusion turbulentes contrôlées par les forces de flottabilité et chargées en suies. Le rayonnement échangé entre ces flammes, du fait des gaz chauds de combustion et de la suie, et le combustible solide et/ou liquide environnant contribue à vaporiser et enflammer ce dernier et ainsi à entretenir le développement de l'incendie. La modélisation de ces échanges de chaleur est complexe car elle nécessite de décrire proprement la combustion, la production de particules de suie et les transferts radiatifs ainsi que leur couplage avec la turbulence. Les forts degrés de confinement rencontrés dans certains feux de compartiment ajoutent à la complexité dans la mesure où la combustion s'effectue dans des conditions sous-ventilées conduisant à des extinctions partielles ou totales des flammes. Les combustibles imbrûlés peuvent alors se mélanger à l'oxydant et se ré-enflammer. Dans cette configuration notamment, l'hypothèse simplificatrice de chimie rapide n'est plus valable. Une des principales difficultés consiste à modéliser les interactions suie/turbulence, rayonnement/turbulence et chimie/turbulence dans les flammes de diffusion chargées en suies. Cet aspect est généralement ignoré ou traité de manière simplifié dans les modèles actuels de feux [1,2].

L'objectif de cette thèse est de mettre en place un modèle permettant de prendre en compte ces interactions turbulentes de façon précise, en conjonction avec des modèles validés pour la combustion, la production de suie et les transferts radiatifs.

La turbulence est modélisée dans un cadre RANS par le modèle $k_T - \varepsilon$, où $k_T$ représente l'énergie cinétique turbulente et $\varepsilon$ son taux de dissipation. La combustion est modélisée par un modèle de flammelettes laminaires stationnaires non-adiabatiques (modèle EDFM pour *Enthalpy Defect laminar Flamelet Model*) [3,4]. Le concept repose sur le fait que les échelles de temps de la convection et la diffusion sont du même ordre de grandeur tandis que les échelles de temps des réactions chimiques (combustion) sont beaucoup plus petites. On peut donc supposer que le mécanisme de réaction chimique atteint toujours un état stationnaire avant que les changements de l'écoulement se produisent ; la structure de la flamme locale s'adapte instantanément aux variations locales de l'écoulement. Par conséquent, la cinétique chimique et la dynamique de l'écoulement peuvent être traitées séparément. En ce sens, la structure de la flamme (i.e. les fractions de massiques des espèces, la température, la densité) peut s'exprimer en fonction de la fraction de mélange $\zeta$, du taux de dissipation scalaire $\chi$ et du paramètre de non-adiabaticité $X_R$. Une flamme de diffusion turbulente peut être assimilée à un ensemble de flammelettes locales dont la description instantanée est pré-tabulée. L'interaction turbulence-chimie est alors assurée par la connaissance de la distribution statistique de ces paramètres.

Par ailleurs, la production des particules de suie est prise en compte à l'aide du modèle semi-empirique de Lindstedt [5,6] basé sur l'acétylène et le benzène comme précurseur de la suie. Ce modèle introduit deux paramètres supplémentaires, le nombre densité de particules de suie, $N_s$, et la fraction massique de suie, $Y_s$. Les termes sources pour $N_s$ et $Y_s$ sont stockés dans la base de flammette en utilisant la méthode proposée par Carbonell *et al.* [7]. Les transferts radiatifs sont quant à eux modélisés par un modèle à large-bandes k-corrélé [8] (WBCK pour *Wide-Band Correlated-k*) pour les propriétés radiatives des gaz, le modèle de Rayleigh couplé à la corrélation de Chang et Charalampopoulos [9] pour les propriétés radiatives des particules de suie, l'approximation des fluctuations optiquement minces (OTFA pour *Optically Thin Fluctuations Approximation*) pour traiter les interactions rayonnement-turbulence

d'absorption [10], et une méthode des Volumes Finis [11] pour résoudre l'équation de transferts radiatif (RTE pour *Radiative Transfer Equation*). Les grandeurs thermodynamiques moyennes sont alors calculées par une approche statistique :

$$\tilde{Q}(\boldsymbol{x},t) = \int Q(\zeta,\chi,X_R,N_s,Y_s)\,\widetilde{f_{\phi,\chi}}(\zeta,\chi,X_R,N_s,Y_s;\boldsymbol{x},t)d\zeta d\chi dX_R dN_s dY_s \tag{1}$$

où $\widetilde{f_\phi}(\zeta,\chi,X_R,N_s,Y_s;\boldsymbol{x},t)$ est la fonction densité de probabilité à masse volumique variable (PDF pour *Probability Density Function*). Le taux de dissipation scalaire $\chi$ est supposé statistiquement indépendant des autres scalaires et sa PDF est supposée être un Dirac autour de sa valeur moyenne [12–15]. Le vecteur composition considéré ici est donc $\boldsymbol{\psi} = (\zeta, X_R, N_s, Y_s)$ et la PDF de composition est notée $\widetilde{f_\phi}(\boldsymbol{\psi};\boldsymbol{x},t)$.

Le problème revient donc à déterminer $\widetilde{f_\phi}(\boldsymbol{\psi};\boldsymbol{x},t)$. Les méthodes classiques se basent sur une forme présumée de cette fonction, ce qui généralement contraint à supposer que les scalaires sont statistiquement indépendants. Ceci revient à négliger toutes les interactions turbulentes entre eux. Par ailleurs, la PDF est ensuite modélisée à partir de la moyenne et de la variance de la fraction de mélange, ce qui introduit une approximation dans la mesure où tous les moments devraient être considérés. Une méthode alternative est de ne pas faire d'hypothèses sur l'indépendance des variables ou la forme de la PDF mais de l'obtenir en résolvant son équation de transport [12,13].

Les méthodes de transport de PDF ont fait l'objet de nombreux développements et d'études dans les trente dernières années [12,13]. L'équation de transport de la PDF est obtenue à partir des équations de conservation des différents scalaires du vecteur composition. Dans notre cas, cette équation s'écrit :

$$\begin{aligned}\frac{\partial\langle\rho\rangle\widetilde{f_\phi}}{\partial t} + \frac{\partial\langle\rho\rangle\widetilde{f_\phi}\widetilde{u_\iota}}{\partial x_i} - \frac{\partial}{\partial x_i}\left[\Gamma_T\frac{\partial\widetilde{f_\phi}}{\partial x_i}\right] \\ = \frac{\partial}{\partial\psi_\alpha}\left[\frac{1}{2}C_{\phi,\alpha}\frac{\varepsilon}{k_T}\left(\tilde{\phi}_\alpha - \psi_\alpha\right)\right] + \frac{\partial}{\partial\psi_\alpha}\left[\langle\rho\rangle\widetilde{f_\phi}\frac{\Theta_\alpha(\boldsymbol{\psi})}{\rho(\boldsymbol{\psi})}\right]\end{aligned} \tag{2}$$

où $\rho$ est la densité, $u_i$ la vitesse locale de l'écoulement, $\Gamma_T$ le coefficient de diffusion turbulente lié au modèle de turbulence. $\phi_\alpha$ et $\psi_\alpha$ représentent respectivement les scalaires du vecteur composition $\boldsymbol{\phi} = (\zeta, X_R, N_s, Y_s)$ et l'ensemble des réalisations correspondantes. $C_{\phi,\alpha}$ est le coefficient de micro-mélange (généralement constant), et $\Theta_\alpha$

représente le terme source du scalaire $\phi_\alpha$. La PDF est donc transportée à la fois dans l'espace physique (termes du membre de gauche dans l'équation (2)) par convection par l'écoulement moyen (1er et 2ième termes) et par diffusion turbulente (3ième terme) et dans l'espace de composition par micro-mélange (1er terme du membre de droite de l'équation (2)) et par les termes sources (2ième terme).

La PDF faisant intervenir de nombreuses variables (les scalaires du vecteur composition, les variables d'espace, et le temps), la résolution de cette équation ne peut pas se faire avec les méthodes classiques de type volumes finis. Plusieurs méthodes alternatives ont été proposées [12–14]. La méthode choisie pour le présent travail est la méthode des « Stochastic Eulerian Fields (SEF) » proposée pour un scalaire par Valiño [16] et étendue au cas multi-scalaires par Hauke et Valiño [17]. Dans cette méthode, la PDF est représentée par un ensemble de $N_F$ champs stochastiques $\boldsymbol{\phi_n} = \left(\phi_{\alpha,n}\right)_{\alpha=1,N_\alpha}$, qui contiennent chacun les valeurs des scalaires dans tout le domaine de calcul. Ces champs doivent être deux fois continument dérivables et la PDF s'exprime :

$$\widetilde{f_\phi}(\boldsymbol{\psi};\boldsymbol{x},t) = \frac{1}{N_F}\sum_{n=1}^{N_F}\prod_{\alpha=1}^{N_\alpha}\delta\left(\psi_\alpha - \phi_{\alpha,n}(\boldsymbol{x},t)\right) \tag{3}$$

Les champs sont gouvernés par des équations aux dérivées partielles stochastiques qui sont obtenues à partir de l'équation de transport de la PDF (Eq. (2)) :

$$\begin{aligned} d\phi_{\alpha,n} = &-\tilde{u}_j\frac{\partial\phi_{\alpha,n}}{\partial x_j}dt + \frac{1}{\langle\rho\rangle}\frac{\partial}{\partial x_j}\left[\frac{\mu_T}{\sigma_T}\frac{\partial\phi_{\alpha,n}}{\partial x_j}\right]dt + \left[\frac{\Theta_\alpha(\boldsymbol{\phi_n})}{\rho}\right]dt \\ &-\frac{1}{2}C_\phi\frac{\varepsilon}{k_T}\left(\phi_{\alpha,n}-\tilde{\phi}_\alpha\right)dt + \left(\frac{2}{\langle\rho\rangle}\frac{\mu_T}{\sigma_T}\right)^{\frac{1}{2}}\frac{\partial\phi_{\alpha,n}}{\partial x_j}dW_{j,n}\,, \\ &n = 1,\dots N_F \text{ and } \alpha = 1,\dots N_\alpha \end{aligned} \tag{4}$$

La moyenne de Favre d'une quantité $Q$ dépendant uniquement du vecteur composition, $Q(\zeta, X_R, N_s, Y_s, \chi) = Q(\boldsymbol{\psi},\chi)$ s'obtient alors par la moyenne d'ensemble sur les champs :

$$\tilde{Q} = \iint Q(\boldsymbol{\psi},\chi)\widetilde{f_\phi}(\boldsymbol{\psi};\boldsymbol{x},t)\delta[\chi-\tilde{\chi}(\boldsymbol{x},t)]d\boldsymbol{\psi}d\chi = \frac{1}{N_F}\sum_{n=1}^{N_F}Q(\boldsymbol{\phi_n},\tilde{\chi}) \tag{5}$$

avec $\tilde{\chi}$ la valeur moyenne du taux de dissipation scalaire [12–15]. D'une manière générale, n'importe quel moment $M_r$ d'ordre *r* de la grandeur $Q(\boldsymbol{\psi}, \chi)$ s'obtient par :

$$M_r(Q)(\boldsymbol{x}, t) = \frac{1}{N_F} \sum_{n=1}^{N_F} [Q(\boldsymbol{\phi_n}(\boldsymbol{x}, t), \tilde{\chi})]^r \tag{6}$$

La méthode complète a été implémentée et validée en simulant douze flammes de diffusion turbulentes de type jet faisant intervenir une large gamme de nombre de Reynolds et de combustibles, dans des configurations expérimentales variées afin d'évaluer la robustesse de la méthode. Une comparaison systématique des données expérimentales et des résultats de la simulation, incluant les températures et les fractions volumiques de suie ainsi que leurs fluctuations, la fraction massique de certaines espèces, et les flux radiatifs pariétaux a montré des écarts inférieurs à 20% dans l'ensemble (dans un facteur 2 pour la fraction volumique de suie), et une nette amélioration des résultats par rapport à ce qui était obtenu avec la méthode de PDF présumée. La Figure 1 illustre cette amélioration très significative sur les profils axiaux de fraction volumique de suie et de température obtenus avec les deux méthodes (PDF présumée de type Beta et PDF transportée), ainsi que les données expérimentales, sur une flamme d'éthylène étudiée expérimentalement par Kent et Honnery [18]: le combustible est injecté dans l'air ambiant à travers un brûleur de diamètre intérieur de 3 mm à une vitesse de 52.90 m/s, avec un nombre de Reynolds à l'injection d'environ 15,000.

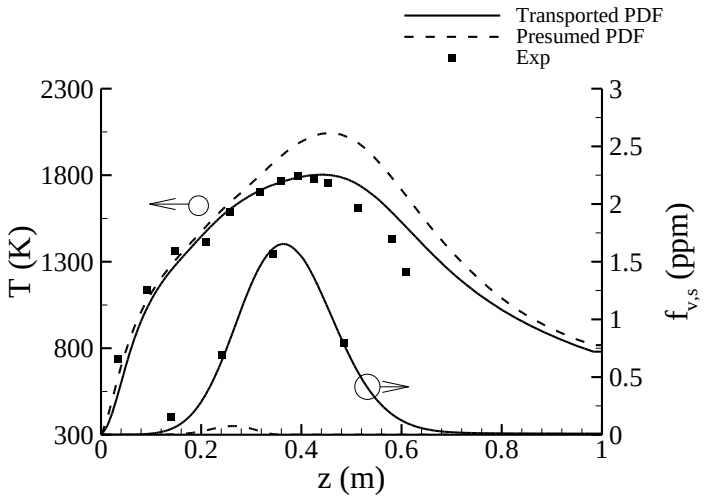


**Figure 1. Evolution axiale de température et de fraction volumique de suie pour une flamme d'éthylène-air.**

La méthode mise en place permet également d'évaluer la performance de modèles approchés pour le rayonnement, tels que le modèle de flamme optiquement mince (OTA pour *Optically Thin Approximation*), qui néglige l'auto-absorption dans la flamme et permet de ne pas avoir à résoudre la RTE, et un modèle gris pour les propriétés radiatives des gaz et des suies (i.e. pas de dépendance spectrale du coefficient d'absorption). Cette étude a permis de montrer que ces modèles approchés introduisent des erreurs non négligeables, malgré le gain important en termes de temps de calcul. Les flux radiatifs obtenus, qui sont l'un des paramètres qui nous intéressent particulièrement pour la simulation incendie, sont impactés d'au moins 20% avec le modèle OTA et 10% avec le modèle gris.

Par ailleurs, une étude a été réalisée sur la forme de la PDF du taux de dissipation scalaire (SDR pour *Scalar Dissipation Rate*), supposé statistiquement indépendant des autres variables. Le SDR a un impact important pour les problèmes liés à l'extinction locale. Il représente un temps de relaxation de la flamme au sein de l'écoulement. Si ce terme est trop élevé, la flamme n'a pas le temps de s'adapter aux conditions de l'écoulement et se retrouve trop étirée ce qui conduit à son extinction. Dans la méthode utilisée ici, la PDF du SDR est modélisée par une fonction de Dirac autour de la valeur moyenne du SDR, elle-même calculée à partir de la variance de la fraction de mélange :

$$\tilde{\chi} = C_\chi \widetilde{\zeta''^2} \frac{\varepsilon}{k_T} \tag{7}$$

Toutefois, une autre approche consiste à modéliser cette PDF par une fonction log-normale dont les paramètres sont liés à $\tilde{\chi}$ et $\widetilde{\chi''^2}$ [19]. Cette seconde modélisation a été mise en place afin d'évaluer l'impact de la forme de la PDF sur les résultats, et une étude paramétrique a été réalisée sur les paramètres de la fonction log-normale. Dans tous les cas, les écarts constatés sur les profils de fraction volumique de suie, température et espèces, entre les résultats de simulations obtenus avec une PDF en Dirac et ceux avec une log-normale n'excèdent 7.5%, ce qui implique que la PDF en Dirac est suffisamment précise pour modéliser le type de flammes turbulentes considérées dans cette étude.

Dans un second temps, les travaux réalisés au cours de cette thèse se sont focalisés sur les interactions turbulentes habituellement négligées dans les méthodes de PDF présumée. Deux interactions en particulier ont été étudiées en détails : les interactions

rayonnement/turbulence (TRI pour *Turbulence-Radiation Interactions*) et les interactions rayonnement/combustion.

Les problèmes liés à l'existence de la TRI sont connus et étudiés depuis longtemps, en particulier dans le cadre de la modélisation des écoulements réactifs. Numériquement la TRI apparait lorsque l'on prend la moyenne temporelle de la RTE :

$$\frac{d\langle I_\eta \rangle}{ds} + \langle \kappa_\eta I_\eta \rangle = \langle \kappa_\eta I_{b\eta} \rangle \tag{8}$$

Le second terme dans le membre de gauche de l'équation (8) représente la TRI d'absorption et est modélisé ici par l'OTFA, valide dans le cas des flammes modérément suitantes à l'échelle du laboratoire [20] :

$$\langle \kappa_\eta I_\eta \rangle = \langle \kappa_\eta \rangle \langle I_\eta \rangle + \langle \kappa_\eta' I_\eta' \rangle \approx \langle \kappa_\eta \rangle \langle I_\eta \rangle \tag{9}$$

Le terme dans le membre de droite de l'équation (8) représente la TRI d'émission et est modélisé de manière exacte par l'approche PDF :

$$\langle \kappa_\eta I_{b\eta} \rangle = \int_{\boldsymbol{\phi}} \kappa_\eta(\boldsymbol{\psi}) I_{b\eta}(\boldsymbol{\psi}) f_{\boldsymbol{\phi}}(\boldsymbol{\psi}) d\boldsymbol{\psi} \tag{10}$$

C'est sur ce second terme que l'étude présentée ici se concentre. L'effet de la TRI sur l'émission radiative des gaz a été étudiée en détails et il a été montré que la TRI avait pour effet d'augmenter les pertes radiatives dans les flammes [10]. Par contre ses effets sur l'émission radiative de la suie sont mal connus. La méthode de PDF transportée mise en place ici permet d'analyser, d'une part, les propriétés radiatives des flammes turbulentes de diffusion, et d'autre part l'importance des effets de la TRI sur l'émission radiative des particules de suie. Cinq flammes ont été modélisées pour répondre à ces questions : trois flammes d'éthylène-air avec un nombre de Reynolds de 8,000, 12,000 et 22,000, une flamme de propane-air et une flamme de méthane-air, toutes deux avec un Reynolds de 12,000. Ces cinq cas permettent d'étudier l'influence de l'intensité turbulente et celle de la propension du combustible à former de la suie. Cette étude a permis de caractériser les paramètres déterminant les effets de la TRI.

Tout d'abord, l'émission totale de la suie diminue si le nombre de Reynolds augmente ou si la propension du combustible à former de la suie diminue. La même

tendance peut être observée pour la proportion de rayonnement émis par les particules de suie par rapport à l'émission des gaz. Par ailleurs, cette proportion de rayonnement émis par les suies ne peut pas être négligée localement, même dans le cas de flammes peu suitantes. Les effets de la TRI ont été observés en calculant le terme d'émission des suies avec la TRI et sans : comme pour les gaz, la TRI tend à augmenter l'émission radiative des suies. Par contre, cette augmentation est d'autant plus faible que le nombre de Reynolds est élevé. Pour comprendre ce phénomène, le terme d'émission a été calculé avec plusieurs fermetures, permettant d'évaluer les différentes contributions à la TRI :

$$\langle E_s \rangle_{NoTRI} \approx 4\pi\kappa_{s,P}\big(\langle f_{v,s}\rangle, \langle T\rangle\big) I_b(\langle T\rangle) = 4\pi\kappa_{s,P}\big(\langle f_{v,s}\rangle, \langle T\rangle\big)\frac{\sigma\langle T\rangle^4}{\pi} \tag{10}$$

$$\begin{aligned}\langle E_s\rangle &= 4\pi\big(\langle\kappa_{s,P}\rangle\langle I_b\rangle + \langle\kappa_{s,P}{}' I_b{}'\rangle\big)\\ &= \underbrace{\underbrace{4\pi\langle\kappa_{s,P}\rangle\frac{\sigma\langle T\rangle^4}{\pi}}_{\mathrm{TRI}_1} + \underbrace{4\pi\langle\kappa_{s,P}\rangle\left[\frac{6\sigma\langle T\rangle^2\langle T'^2\rangle}{\pi} + \frac{4\sigma\langle T\rangle^2\langle T'^3\rangle}{\pi} + \frac{\sigma\langle T'^4\rangle}{\pi}\right]}_{\mathrm{TRI}_2} + 4\pi\langle\kappa_{s,P}{}' I_b{}'\rangle}_{\text{Full TRI}}\end{aligned} \tag{11}$$

Les quatre fermetures NoTRI, $TRI_1$, $TRI_2$ et Full TRI illustrent ces différentes contributions :

- L'expression $TRI_1$ permet d'étendre le cas NoTRI en prenant en compte les fluctuations de la moyenne de Planck du coefficient d'absorption des suies. Ce dernier a le même comportement que la corrélation entre la fraction volumique de suie et la température. Cette corrélation est négative dans les régions dominées par la présence de la suie. Ce terme tend donc à faire diminuer l'émission radiative de la suie, et ce d'autant plus que le nombre de Reynolds est élevé.
- La fermeture $TRI_2$ ajoute à $TRI_1$ l'effet des fluctuations de la température. Ce terme est toujours positif et est la raison pour laquelle la TRI augmente l'émission radiative de la suie.
- Enfin, Full TRI inclut le dernier terme contribuant à la TRI qui est la corrélation entre le coefficient d'absorption des suies et la fonction de Planck. Il a la même

évolution que la corrélation entre la fraction volumique de suie et la température et tend donc également à faire diminuer l'effet de la TRI.

Toutefois, ces considérations globales cachent les effets locaux de la TRI dans les flammes suitantes. En effet, là où la suie est fortement présente, le caractère négatif de la corrélation peut l'emporter sur les fluctuations de température. Par conséquent, la TRI peut donc localement diminuer l'émission radiative de la suie.

Nous avons étudié également la corrélation entre la fraction de mélange et le paramètre de non-adiabaticité en simulant une flamme turbulente d'éthylène-air [21]. La fraction de mélange et le paramètre de non-adiabaticité sont fortement corrélés sur une large partie de la flamme, positivement en amont et négativement en aval de la stœchiométrie. L'impact de cette corrélation sur la structure de flamme et les pertes radiatives est évalué en comparant deux simulations, l'une prenant en compte cette corrélation et l'autre les négligeant en considérant le paramètre de non-adiabaticité statistiquement indépendant des autres scalaires. L'effet de cette corrélation est plus significatif dans la partie aval de la flamme où les transferts radiatifs sont les plus importants. Les fluctuations de température sont les plus impactées, augmentant de façon importante lorsque la corrélation est négligée. Les pertes radiatives globales de la flamme sont elles aussi surestimées d'environ 20%.

Les travaux réalisés au cours de cette thèse ont donc permis de développer et d'implémenter une méthode de transport de la PDF de composition. Les résultats de simulations mettent en évidence un accord raisonnable avec les expériences sur des flammes de diffusion turbulentes de type jet. La méthode mise en place a permis d'étudier en détails des corrélations turbulentes habituellement négligées et de montrer l'importance de les prendre en compte de façon précise. L'application de la méthode à des flammes turbulentes pilotées par les forces de flottabilités nécessite de modifier le régime d'écoulement et les études de la littérature montrent que l'approche Large Eddy Simulation (LES) est souvent nécessaire dans ce cas.

L'un des plus importants problèmes pour la simulation des incendies est celui du panache de feu piloté uniquement par les forces de flottabilité. L'utilisation de modèles RANS pour modéliser ce phénomène amène à des écarts significatifs entre les prédictions de simulation et les données expérimentales, ainsi qu'une dépendance importante aux

conditions limites en amont [22–24]. Les modèles RANS sont en général moins adaptés à la simulation des flammes de flottabilité qu'à celle des flammes jet. Ceci est dû à la difficulté de modéliser la turbulence générée par les forces de flottabilité et les importantes fluctuations de structure de flamme qui en résultent, ainsi qu'à la nécessité de modéliser toutes les échelles de la turbulence. De nombreuses études numériques récentes [25–31] sur les panaches ont été réalisées avec une modélisation aux grandes échelles (LES pour *Large Eddy Simulation*), ce qui limite les difficultés intrinsèques des méthodes RANS en résolvant les grandes échelles de la turbulence. Les méthodes de transport de la PDF peuvent alors être utilisées comme modèles de sous-maille (méthodes à fonction de densité filtrée).

Par ailleurs, le modèle EDFM ne permet pas de prendre en compte les phénomènes d'extinction locale. Ces processus sont nécessaires pour la simulation des feux confinés. Le confinement crée un manque d'oxygène au sein de l'enceinte qui peut causer une extinction partielle du feu et l'émission de combustible imbrûlés et chauds, pouvant être évacués de la pièce et risquant de se ré-enflammer en rencontrant de l'air frais. La mise en place d'une cinétique chimique détaillée et finie à la place du modèle de flammelettes est une voie de développement.

Les interactions turbulence/absorption du rayonnement ne sont pas encore bien comprises. Elles représentent le couplage non linéaire entre le rayonnement incident et le coefficient d'absorption local. Elles sont la conséquence des fluctuations des propriétés radiatives dans tout le domaine et leur modélisation nécessite de connaitre de manière détaillée les champs instantanés de température et les concentrations des espèces radiatives. Modest, Haworth et leurs collaborateurs tirent avantage du fait que la méthode de PDF transportée basée sur la méthode de particules Lagrangiennes fourni des réalisations de l'écoulement, ce qui permet de modéliser ces interactions de manière exactes en introduisant une méthode de Monte-Carlo à photons couplée au transport de la PDF [20,32,33]. Ils ont ainsi montré que la TRI d'absorption peut être négligée dans le cas de flammes lumineuses ou non-lumineuses à l'échelle du laboratoire, mais qu'elle doit être prise en compte pour des flammes plus grandes. Toutefois, la limite de validité de cette approximation n'a pas été clairement établie. C'est un problème important car le

coût de calcul de la méthode de Monte-Carlo à photon est très élevé. Des approches simplifiées devront être développées pour prendre en compte la TRI d'absorption.

Enfin, la modélisation de la production de suie peut être améliorée de deux façons. La première est liée à la cinétique de la production de la suie en considérant un modèle basé sur les HAP (Hydrocarbure aromatique polycyclique). L'une des difficultés associées à ce type des modèles est liée au traitement des HAP, qui sont régis par une chimie relativement lente et ne peuvent donc a priori pas être intégrés directement à la librairie de flammelettes. Un autre point d'amélioration est lié à une meilleure description de la morphologie des particules de suie. Il est possible de considérer une PDF du volume et de la surface des agrégats. Une méthode doit être développée pour résoudre l'équation de conservation de la population correspondante. La méthode des moments semble être appropriée pour ce problème [34–42].

# Contents



# Nomenclature

# Roman letters

| | |
|---|---|
| $A_S$ | Surface area of soot per unit volume |
| $C_\mu, C_{\varepsilon 1} C_{\epsilon 2}$ | $k_T - \varepsilon$ model constants |
| $C_{min}$ | Minimum number of carbon atoms in a soot particle |
| $C_a$ | Agglomeration constant |
| $C_s$ | Soot absorption coefficient constant |
| $C_{s,P}$ | Soot Planck absorption coefficient constant |
| $C_\eta$ | Soot absorption coefficient factor |
| $C_\alpha, C_{\phi,\alpha}$ | Mixing coefficient |
| $C_{P,k}$ | Species heat capacity at constant pressure |
| $C(f_{v,s}, T)$ | Correlation coefficient |
| $C_\chi$ | Scalar dissipation rate constant |
| $D_k$ | Species diffusion coefficient |
| $D_{th}$ | Thermal diffusivity |
| $d_n$ | Injection diameter |
| $E_{g\eta}, E_g$ | Gaseous species radiative emission term |
| $E(\kappa_T)$ | Turbulent kinetic energy spectrum |
| $E_{s\eta}, E_s$ | Soot radiative emission term |
| $\left(F_j\right)_{j=1,3}$ | Volume forces |
| $f_\phi$ | Conventional composition PDF |
| $\widetilde{f_\phi}$ | Density-weighted composition PDF |
| $F_\phi$ | Mass density function |
| $f_{v,s}$ | Soot volume fraction |
| $f(\boldsymbol{\phi}, k)$ | Distribution function |
| $g$ | Gravitational acceleration |
| $g(\boldsymbol{\phi}, k)$ | Cumulative of the distribution function |
| $g_i^{WB}$ | Cumulative function for the i$^{th}$ wide band |
| $g_k$ | Interpolation point for the cumulative function |
| $g_j^{NB}$ | Cumulative function for the j$^{th}$ narrow band |
| $\mathcal{G}_\eta$ | Local radiative intensity integrated over all possible directions |
| $h$ | Total enthalpy |
| $\Delta h_{f,k}^0$ | Formation enthalpy of species $k$ at $T_0$ |
| $\Delta h_c$ | Heat of combustion |
| $J_{Y_s}$ and $J_{N_s}$ | Soot diffusive fluxes |
| $I_{gk}^i$ | Radiative intensity at the i$^{th}$ WB and for the k$^{th}$ quadrature point |
| $I_{b\eta}$ $(I_{b\eta,i})$ | Planck function (at the i$^{th}$ WB) |
| $I_\eta$ | Radiative intensity |
| $I_T$ | Turbulent intensity |
| $k_s, n_s$ | Refractive and absorptive index of soot |
| $k_T$ | Turbulent kinetic energy |
| $k_k^i$ | Interpolation point for the cumulative function |
| $k_{n,C_2H_2}, k_{n,C_6H_6}, k_{sg}$ | Soot chemical reaction kinetic constants |
| $L$ | Characteristic length |
| $\mathcal{L}, l_\mathcal{P}, l_D$ | Integral length scale, production range lower limit, dissipation range higher limit |

| | |
|---|---|
| $L_{sp}$ | Laminar smoke point |
| $L_v$ | Latent heat of vaporization |
| $m, n, s$ | Number of: carbon atoms, hydrogen atoms, carbon atoms as a gaseous product in the combustion of a typical hydrocarbon species |
| $M_c$ | Soot molecular mass |
| $M_r(\boldsymbol{Q})$ | Moment of order r of Q |
| $m_\lambda = n_\lambda - ik_\lambda$ | Complex index of refraction of soot |
| $\dot{m}''_{pyr}$ | Pyrolysis mass flow rate |
| $N_s$ | Soot number density |
| $N_k$ | Number of species |
| $\boldsymbol{n_k}$ | Outward normal vector of surface $A_k$ |
| $N_\alpha$ | Number of scalar in the composition vector |
| $n$ | Medium refractive index |
| $N_{WB}$ | Number of wide band |
| $N_F$ | Number of stochastic Eulerian fields |
| $N_g$ | Number of quadrature points |
| $p$ | Pressure |
| $\mathcal{P}_k$ | Turbulent kinetic energy production term |
| $(q_i)_{i=1,3}$ | Heat flux |
| $\boldsymbol{q_R}$ | Radiative flux |
| $q_{fl,rad}$, $q_{fl,conv}$, $q_{rr}$ and $q_{cond}$ | Heat flux from the flame (radiative, convective), radiative heat flux from the fuel surface, and heat flux transferred in the material by conduction |
| $\boldsymbol{q_\eta}$ | Spectral radiative flux |
| $\dot{Q}_{rad}, \dot{Q}_{R,abs}, \dot{Q}_{R,emi}$ | Radiative, absorbed and emitted radiative source term |
| $Q$ | Typical physical quantity |
| $\dot{Q}_C$ | Chemical heat release |
| $R_f$ | Flame radius |
| $\boldsymbol{s}$ | Radiation optical path |
| $S_{n,N}, S_c, S_{n,Y}, S_{sg}, S_o$ | Soot processes source terms |
| $S_{N_s}$ | Soot number density source term |
| $S_{Y_s}$ | Soot mass fraction source term |
| $S_{burn}$ | Pyrolysing surface |
| $t$ | Time |
| $T$ | Temperature |
| $t_{res}$ | Residence time |
| $u_i, u_{inj}, U$ (or $u$) | Flow velocity: local, injection and characteristic |
| $V_i$ | Thermophoretic velocity of soot particles |
| $w_k$ | Quadrature weights |
| $dW_{j,n}$ | Wiener process |
| $X_R$ | Enthalpy defect parameter |
| $x_i$ | Cartesian coordinates |
| $Y_k$ | Species mass fraction |
| $Y_s$ | Soot mass fraction |

# Greek letters

| | |
|---|---|
| $\Gamma$ | Control volume surface |
| $\Gamma_T$ | Turbulent diffusion coefficient |

| | |
|---|---|
| $\varepsilon$ | Turbulent dissipation rate |
| $\zeta$ | Mixture fraction |
| $\eta_K$ | Kolmogorov scale |
| $\eta$ | Radiation wavenumber |
| $\Theta_\alpha, \Theta_{\alpha,mix}, \Theta_{\alpha,prod}$ | Governing equations source terms, mixing part and production part |
| $\kappa_T$ | Turbulent wave number |
| $\kappa_\eta$ | Medium spectral absorption coefficient |
| $\lambda$ | Heat conductivity or radiation wavelength |
| $\mu$ | Dynamic viscosity |
| $\mu_\chi$ | Mean value of $\ln(\chi_{st})$ |
| $\nu$ | Kinematic viscosity or radiation frequency |
| $\sigma_k, \sigma_\varepsilon$ | $k_T - \varepsilon$ model constants |
| $\sigma_\chi$ | Variance of $\ln(\chi_{st})$ |
| $\sigma_{s\eta}$ | Directional diffusion coefficient |
| $\rho$ | Local density |
| $\tau$ | Characteristic time-scale |
| $(\tau_{ij})_{i,j=1,3}$ | Viscous tensor |
| $\tau_{\mathrm{R}_f}$ | Flame optical thickness |
| $\tau_{\mathrm{R}_s}$ | Soot optical thickness |
| $\tau_{\Delta\eta}$ | Transmittance of a narrow band |
| $\boldsymbol{\phi}$ | Composition vector |
| $\phi$ | Scalar dissipation rate variable density effect factor |
| $\phi_\eta$ | Scattering phase function |
| $\phi_{\alpha,n}$ | Stochastic fields |
| $\chi$ | Scalar dissipation rate |
| $\chi_s$ | Size parameter |
| $\boldsymbol{\psi}$ | Sample-space variables corresponding to $\boldsymbol{\phi}$ |
| $(\dot{\omega}_k)_{k=1,N_k}$ | Species reaction rate |
| $\dot{\omega}_T$ | Total combustion heat release |

# Subscripts

| | |
|---|---|
| ad | Adiabatic |
| ext | Extinction limit |
| eq | Equivalent |
| inj | Injection |
| $i, j$ | Cartesian coordinates |
| $k$ | Species |
| LFA | Laminar flamelet approximation |
| K | Kolmogorov scale |
| $q$ | Quenching |
| rms | Root mean square |
| $st$ | Stoichiometric |
| $T$ | Turbulent |
| u | Unburnt |
| $\infty$ | Quantities at the oxidizer side |

# Adimensioned numbers

| | | |
|---|---|---|
| $Da$ | Damköhler number | $Da = \tau_f/\tau_c$ |
| $Fr$ | Froude number | $Fr = u_{inj}^2/gL$ |
| $Le$ | Lewis number | $Le = \lambda/\rho D C_p$ where D is the diffusion coefficient |
| $Re$ | Reynolds number | $Re = UL/\nu$ |
| $Sc$ | Schmidt number | $Sc = \mu/\rho D$ |

# Symbols

| | |
|---|---|
| $\langle \cdot \rangle$ | Reynolds average |
| $\cdot'$ | Reynolds fluctuation |
| $\tilde{\cdot}$ | Favre average |
| $\cdot''$ | Favre fluctuation |
| $\langle \cdot \vert \boldsymbol{\psi} \rangle$ | Conventional average conditioned on the value of $\boldsymbol{\psi}$ |

# Constants

| | | |
|---|---|---|
| $c_0$ | Speed of light in a vacuum | $c_0 = 2.99792458\times10^8\ m/s$ |
| $h_P$ | Planck constant | $h_P = 6.626070040\times10^{-34} J.s$ |
| $k_B$ | Boltzmann constant | $k_B = 1.38064852\times10^{-23} J.K^{-1}$ |
| $\mathcal{N}_A$ | Avogadro number | $\mathcal{N}_A = 6.0221409\times10^{23}\ mol^{-1}$ |
| $\sigma$ | Stefan-Boltzmann constant | $\sigma = 5.670373\times10^{-8} W.m^{-2}.K^{-4}$ |

# List of figures

# List of tables

# Chapter I Introduction

## I.1 Context

Electricité de France (EDF), as an operator, is responsible for the safety of the nuclear plants and defines, in agreement with the regulation, the means and the organization implemented to ensure that its facilities do not present risks for the public and the environment.

Unwanted fires in nuclear plants is the most important risk for internal damage. Besides the safety of its staff and the operation of its facilities, EDF has an economical interest, related to the loss of material and immobilization, to reduce the fire risk by ensuring a high level of safety without using oversized firefighting means. The demonstration of the efficiency of fire safety with numerical models, due the improvement of knowledge and of computational resources, is increasing. The modeling tools developed by EDF R&D have been used for several years to answer questions relative to fire safety. Today, the two-zone code MAGIC is used as reference. It is based on the assumption of a stratification of the hot gases above the fresh gases and can provide rapid answers due to its low computational cost. Although this approach is efficient, it is not able to capture all the processes of the fire phenomena. In addition, it becomes less relevant in absence of stratification.

In order to circumvent these drawbacks, a CFD model of fire spread in nuclear plants is under development [43]. The present work is related to these developments. In particular, they will focus on soot production and radiative heat transfer and their coupling with turbulence.

Mass burning, flame spread and fire growth on hazardous scales are mainly driven by the radiative flux emitted by the gas combustion products, including soot, toward the environment and the condensed fuel surface, soot radiation being dominant in most

applications [44]. These fluxes provide the energy required to preheat the condensed fuel up to a sufficiently high temperature to vaporize it and, then, to release the gaseous fuel. This gaseous fuel is mixed with air and is ignited by the hot gas, ensuring the self-sustaining combustion process and/or the flame spread. Once the ignition phase processes are completed, these radiative fluxes provide the energy required to sustain the vaporization of the condensed phase on which the flame is established in order to supply it with gaseous fuel. In addition, because of the high levels of confinement encountered in building fires, the combustion takes place in relatively low-oxygenated conditions leading to partial or complete extinction of the flames. An accurate description of the evolution of fire in a confined environment requires, therefore, to correctly predict the concentrations of soot, the radiation of soot and combustion products, and to have a sufficiently detailed turbulent combustion model to describe local extinction/re-ignition processes.

# I.2 Motivations

Fire dynamics are at the crossroads of several physical processes for which numerical modeling involve different strategies. As discussed previously, this includes fluid dynamics, heat and mass transfer including radiative transfer, combustion, soot production, thermal degradation of solid/liquid materials, multi-phase flow, and turbulence. In addition, most of these processes are strongly coupled mainly because of the turbulent nature of the flow [1,45]. This introduces closure problems for, on the one hand, the chemical reaction rates for both gaseous species and soot, and, on another hand, for the absorption and emission radiative terms [13]. These closure problems result from the non-linear nature of these terms. In the following, the closure problems due to the strong nonlinearity of the gaseous and soot production chemical source term will be denoted as Turbulence-Chemistry Interactions (TCI) and Turbulence Soot Production Interactions (TSI), respectively, and those due to the non-linearity of both absorption and emission radiative terms will be denoted as Turbulence-Radiation Interactions (TRI). TCI, TSI and Emission TRI depend on the turbulent fluctuations of local properties only (temperature, species concentrations) and can be evaluated by using a one-point one-time joint PDF of these quantities [19,46,47]. The simplest method, used commonly in fire simulation [1,48–51], is based on the conserved scalar approach and uses the uncorrelated approach to express the joint probability density function (PDF) of the

mixture fraction, scalar dissipation rate to measure the degree of departure from the equilibrium state, enthalpy defect to include radiative loss, and soot quantities [52]. The scalars involved in the PDF are assumed to be statically independent. The PDF of mixture fraction is often modelled as a clipped Gaussian or a $\beta$-PDF [19] whereas for the others scalars, including soot quantities, the corresponding PDF are modeled as Dirac delta functions centered on the mean value of the property [52]. This simplified approach is convenient on a numerical point of view but neglects the correlations between these quantities. The effects of these approximations are illustrated in Fig. I-1, which represents the axial profiles of temperature and soot volume fraction obtained by using the presumed PDF approach in a turbulent ethylene-air jet flame with a Reynolds of about 15,000 [18]. This figure shows clearly that the soot volume fraction is underestimated by more than one order of magnitude and, as a result, the temperature is overestimated. The sources of these discrepancies were explained by Moss and co-workers [52,53] and by Consalvi et al. [54]. They are due to the fact that the correlation between the mixture fraction and soot quantities, neglected in the present simulations, significantly affects the soot oxidation rate.

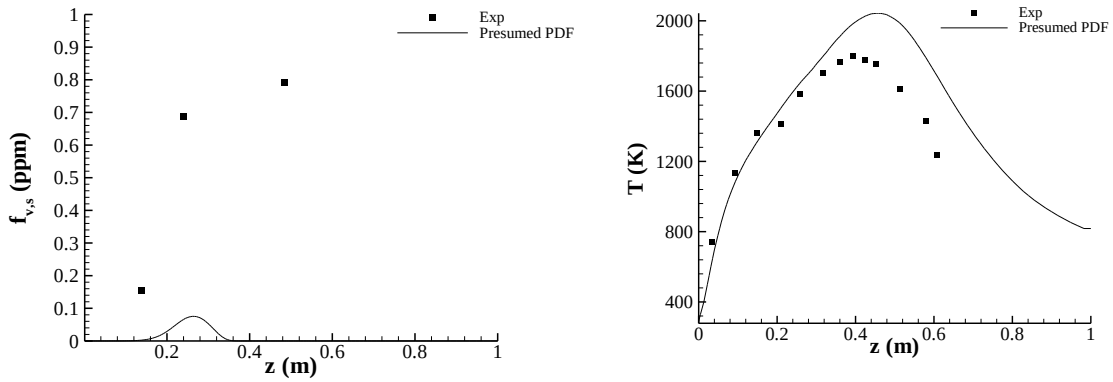


**Figure I-1. Predicted and measured Left) soot volume fraction and Right) temperature in a turbulent ethylene-air jet flame by using a presumed PDF method.**

The same issue arises for the interactions between turbulence and soot emission radiative term which is a non-linear function of the soot volume fraction and temperature. The correlation between the soot volume fraction and the temperature, which is not taken

into account in the presumed-PDF approach, was found to be highly negative [55,56], which can have a significant effect on soot emission [48].

An alternative to the presumed-PDF approach is the transported PDF methods. They provide an elegant and effective resolution to the closure problems described previously. PDF methods are discussed in details in the books by Pope [57] and Fox [14]. A comprehensive review can be found in [13], and a perspective on recent advances and trends can be found in [47]. In addition, the modeling of extinction/re-ignition processes encountered in under-ventilated fires require to use a direct coupling between the chemical kinetic and the flow, and TCI are handled in an exact manner by transported PDF methods [12,13].

# I.3 Objectives of the thesis

The main objective of the present thesis is to develop, implement and validate a transported PDF method, in conjunction with well-established sub-models for turbulent combustion, soot production and radiative transfer. The developments are performed in a RANS framework and by using a flamelet combustion model. These latter choices are not limitations of the model since transported PDF methods can be also used as sub-filter-scale models for large-eddy simulation (filtered density function methods) and are designed to model exactly chemical source terms. A semi-empirical acetylene-benzene-based two equations model for soot production [6], and a Wide-Band Correlated-k (WBCK) model for the gas radiative properties [8] will be considered.

The second objective of the thesis to provide a better understanding of soot emission TRI which can be modeled exactly using the transported PDF method. The effects of the correlation between the mixture fraction and enthalpy defect, which are usually disregarded when presumed PDF methods are used, will also be investigated.

# I.4 Bibliographic survey

## I.4.1 Physical processes governing fire dynamics

This section will describe the main processes involved in the development of fires. First, the combustion and heat transfer regimes encountered will be discussed as well as

the main steps observed in the development of a fire in a compartment. Finally, the specificity of under-ventilated fires will be discussed.

### I.4.1.1 Flow, combustion and heat transfer regimes of fires

Combustion studies are usually divided into three categories [19]: premixed flames for which the reactants are mixed before ignition, diffusion flames for which the reactants are brought separately to the reaction zone, and partially premixed flames for which a fraction of injected reactants mixes before reaching the reaction zone. Flames encountered in well-ventilated fires usually burn in the diffusion flame regime.

In diffusion flames, the reactants are injected separately and diffuse to the reaction zone. The schematic structure of a diffusion flame is given in Fig. I-2. A key characteristic of diffusion flames is the fact that they do not propagate, the mixture being either too rich (on the fuel side) or too lean (on the oxidizer side) for the combustion zone to spread. Diffusion flames are therefore safer to operate in industrial processes than premixed flames. Mixing is the key issue in diffusion flames dynamics. The chemical reaction will only take place in a limited region where the reactants are mixed close to the stoichiometric proportions. The lack of propagation also makes diffusion flames more sensitive to velocity fluctuations and, therefore, to turbulence.

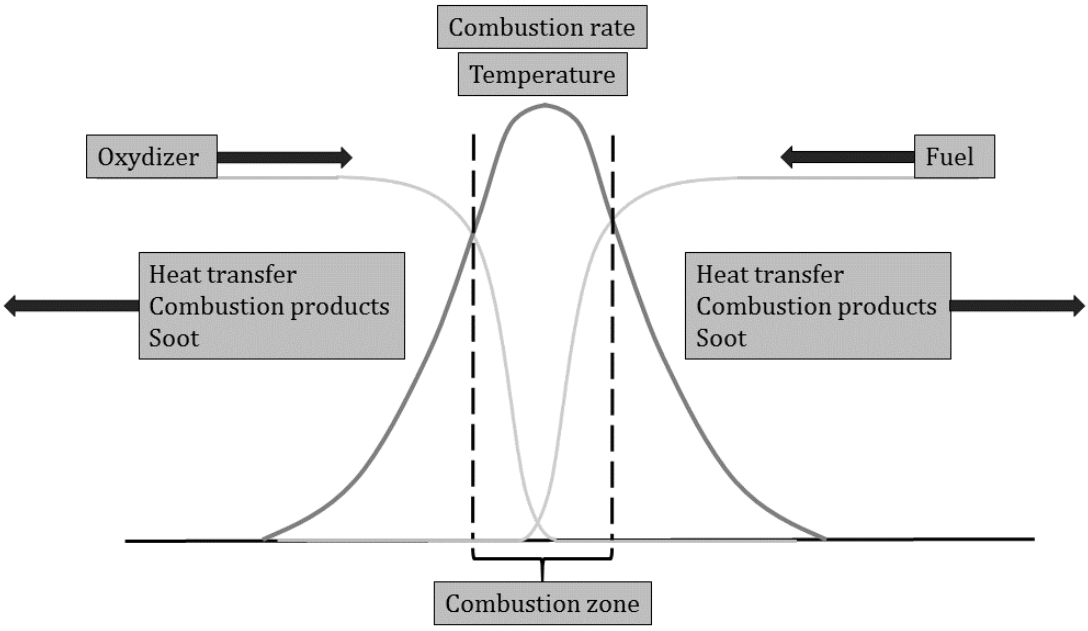


**Figure I-2. Diffusion flame structure.**

One of the most common kind of diffusion flame is the jet flame, for which an instantaneous picture is given in Fig. I-3a. Gaseous fuel is injected with a high velocity in an oxidizer co-flow or in atmospheric air, and ignited. Jet flames are often used as validation cases for turbulent combustion model. The high injection velocity implies that the production of turbulence due to buoyancy can usually be neglected in the case of laboratory-scale turbulent jet flames.

a) 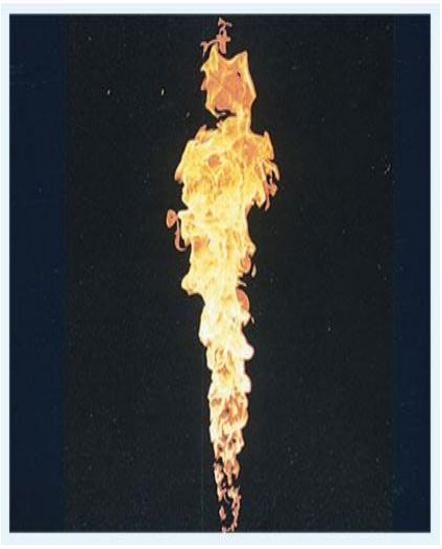

b) 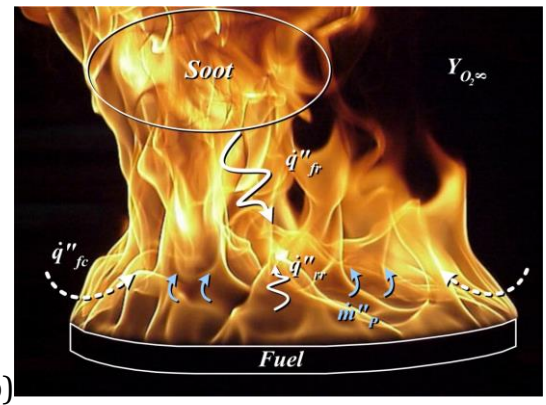


**Figure I-3. Diffusion flames structure: a) Jet diffusion flame, and b) Pool fire.**

Unwanted fires mostly evolve in the buoyancy-driven regime (see Fig. I-3b). The Froude number, $Fr = u_{inj}^2/gL$, is typically in the range $10^{-6}$-$10^{-2}$. In the previous expression $u_{inj}$ is a typical fuel injection velocity, $g$ is the gravitational acceleration and $L$ is a characteristic length, typically the flame length or the diameter of the burner in the present example. The pool fire scenario, described in Fig. I-3b, represents a simplified version of fires that occur in practice. In this case, the condensed phase (liquid or solid) is transformed into gaseous volatiles either by pyrolysis (degradation of solid or heavy liquid by convective or radiative heat transfer) or by vaporization (for light liquids). The gasification processes occur due to the influence of the convective and radiative fluxes transferred by the flame. Gaseous fuel is then transported by convection/diffusion to the reaction zone where they mix with the oxygen of air to react, which makes this process

self-sustained. For well-ventilated medium, the chemistry can generally be assumed to be fast as compared to the mixing which allows simplifying the description of the gas phase combustion.

The dominant mode of heat transfer between the flame and the condensed material depends on the size of the pool: at small-scale the heat transfer is dominated by convection whereas for pool fires with diameters greater than a meter thermal radiation prevails. Let us consider the energy balance at the surface of a liquid fuel:

$$\dot{m}''_{pyr} L_v = q_{fl,rad} + q_{fl,conv} - q_{rr} - q_{cond} \quad \text{(I-1)}$$

where $\dot{m}''_{pyr}$ is the pyrolysis mass flow rate. $q_{fl,rad}$, $q_{fl,conv}$, $q_{rr}$ and $q_{cond}$ represent the heat flux transferred by the flame by radiation and convection, the heat flux emitted by the fuel surface and the heat flux transferred in the material by conduction. $L_v$ is the latent heat of vaporization. This expression can be simplified for large-scale fires on the basis of the analysis carried out previously:

$$\dot{m}''_{pyr} L_v \cong q_{fl,rad} \quad \text{(I-2)}$$

On the other hand, the heat release rate can be written as:

$$\dot{Q} = \dot{m}''_{pyr} S_{burn} \Delta h_c \quad \text{(I-3)}$$

where $S_{burn}$ represents the pyrolysing surface and $\Delta h_c$ is the heat of combustion. As a consequence, it appears that for large-scale fires, the radiative flux transferred from the flame toward the condensed material plays a crucial role in the determination of the heat release rate. Gaseous combustion products ($CO_2$, $H_2O$, CO, and some hydrocarbons) and soot are responsible for the radiative heat flux from the flame. Gaseous species emit radiation on some discrete bands, whereas the radiation from soot is continuous, covering the entire thermal spectrum. The contribution of soot depends widely on the combustible. Nevertheless, in “real” fires, their contribution usually prevails [44].

In addition, flames encountered in fires are turbulent. The influence of turbulent motions on diffusion flames is important on several levels. First, for any combustion problem, turbulent-related phenomena include flame-generated vorticity, viscous effects, and stretching [19]. Second, diffusion flames do not propagate and have little impact on

flow dynamics. Therefore, they are much more sensitive to turbulent motions than premixed flames (especially regarding stretching and quenching). Furthermore, buoyancy, natural convection and entrainment effects, as well as molecular diffusion can all be affected by turbulence [19].

## I.4.1.2 Development of a confined fire

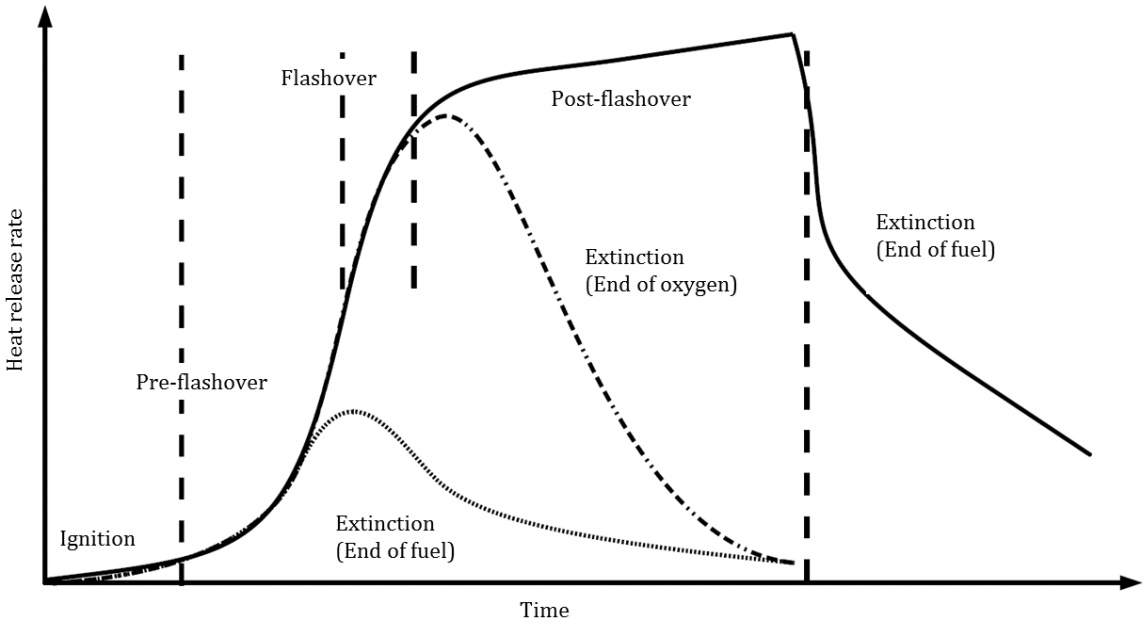


**Figure I-4. Heat release rate during the evolution of a fire.**

The development of a confined fire can be divided into the following five major stages [58,59], illustrated on Fig. I-4:

**Ignition:** Ignition can be considered as a process that produces an exothermic reaction characterized by an increase in temperature greatly above the ambient. It can occur either by piloted ignition (by flaming match, spark, or other pilot source) or by spontaneous ignition (through accumulation of heat in the fuel). The accompanying combustion process can be either flaming combustion or smoldering combustion.

**Growth:** Following ignition, the fire may grow at a slow or a fast rate, depending on the type of combustion, the type of fuel, interaction with the surroundings, and access to oxygen. The fire can be described in terms of the rate of energy released and the production of combustion gases. A smoldering fire can produce hazardous amounts of

toxic gases while the energy release rate may be relatively low. The growth period of such a fire may be very long, and it may die out before subsequent stages are reached. The growth stage can also occur very rapidly, especially with flaming combustion, where the fuel is flammable enough to allow rapid flame spread over its surface, where heat flux from the first burning fuel package is sufficient to ignite adjacent fuel packages, and where sufficient oxygen and fuel are available for rapid fire growth. Fires with sufficient oxygen available for combustion are said to be fuel-controlled.

**Flashover:** Flashover is the transition from the growth period to the fully developed stage in fire development. In fire safety engineering, the word is used as the demarcation point between two stages of a compartment fire, i.e., pre-flashover and post-flashover. Flashover is not a precise term: several variations in definition can be found in the literature. The criteria given usually demand that the temperature in the compartment has reached 500–600°C, or that the radiation to the floor of the compartment is 15 to 20 $kW/m^2$, or that flames appear from the enclosure openings. These occurrences may all be due to different mechanisms resulting from the fuel properties, fuel orientation, fuel position, enclosure geometry, and conditions in the upper layer. Flashover cannot be said to be a mechanism, but rather a phenomenon associated with a thermal instability.

**Fully developed fire:** At this stage the energy released in the enclosure is at its greatest and is very often limited by the availability of oxygen. This is called ventilation-controlled burning (as opposed to fuel-controlled burning), since the oxygen needed for the combustion is assumed to enter through the openings. In ventilation-controlled fires, unburnt gases can collect at the ceiling level, and as these gases leave through the openings they burn, causing flames to stick out through the openings. The average gas temperature in the enclosure during this stage is often very high, in the range of 700 to 1200°C.

**Decay:** As the fuel becomes consumed, the energy release rate diminishes and thus the average gas temperature in the compartment declines. At this point, the fire may go from ventilation-controlled to fuel controlled.

As can be seen from the steps outlined above, fire dynamics are at the crossroads of several different physical processes. It involves fluid dynamics, combustion, hydrocarbon

chemistry, radiative transfer, thermal degradation of solid and liquid fuels, multi-phase flow, production of soot, and all these phenomena are coupled (see Fig. I-5).

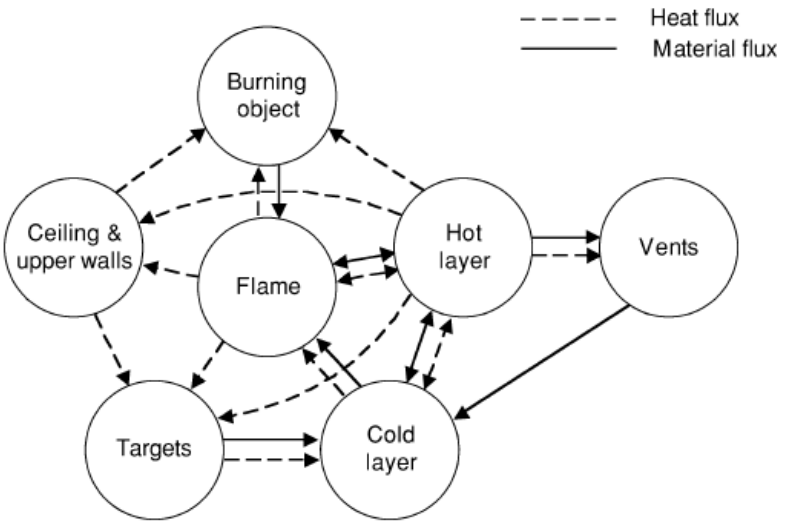


**Figure I-5. Schematic of the processes involved in a compartment fire [58]**

## I.4.1.3 Fire in confined compartments

The specificity of fires in nuclear plants is that they occur with a high level of confinement, leading to conditions for combustion generally different from those encountered in well-ventilated fires. Air feeding the flame becomes rapidly vitiated, which leads to incomplete combustion. Gaseous combustibles, soot, carbon monoxide and other pollutants then escape from the fire and are released in the surroundings. This can lead to extremely dangerous hazards, especially if the gaseous combustible mixes with air and encounter points with a sufficiently high temperature to ignite this mixture.

The vitiation of air should lead to a reduction in flame temperature, implying a decrease in the radiative heat transfers and then pyrolysis mass flow rates. These trends appear clearly in the evolution of the pyrolysis mass flow rate measured during the PRISME experiments performed at the IRSN for different levels of vitiation [60]. On the other hand, the high temperature of the enclosure walls surrounding the fire should produce a supplementary source of heating for the pyrolysis and growth processes. The

soot production should be also considerably affected [61]: on one hand the decrease in flame temperature should reduce the soot formation rates, leading to lower soot concentrations. On the other hand, decreasing the oxidation process, should lead to higher soot concentration. As a consequence, it is difficult to determine a priori how the total amount of soot will evolve when the oxygen concentration will decrease.

## I.4.2 Soot production

Soot is a mass of impure carbon particles resulting from the incomplete combustion of hydrocarbons. Soot is not a uniquely defined chemical substance in that it contains mostly carbon, with up to 10% (mol) of hydrogen. The atomic C/H ratio is about 8 to 1. The mass density of soot is about 2 g/cm$^3$. Electron microscopy studies show that a soot particle often consists of chain-like aggregates of nearly spherical particles. These spherical particles, called the primary particles, may contain between $10^5$ to $10^6$ carbon atoms, and usually have diameters between 20 to 50 nm [62].

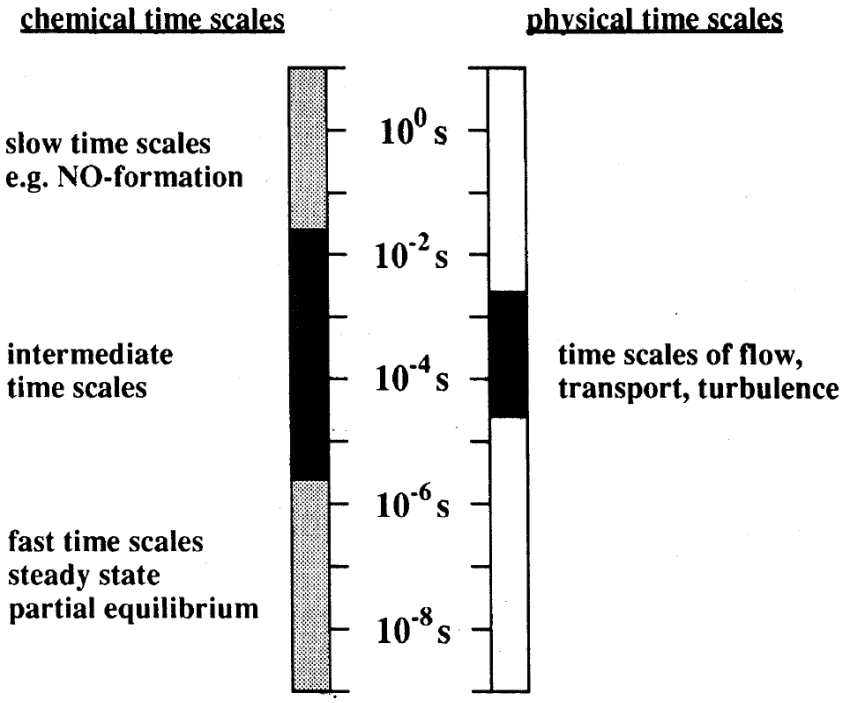


**Figure I-6. Characteristic time scales for the chemical and physical processes (From Mass and Pope [63])**

The modeling of soot production introduces two difficulties as compared to the modeling of gaseous reactants:

- The first difficulty can be analyzed from Fig. I-6 which shows the characteristic time scales for the different physical and chemical processes. When the chemistry is sufficiently fast, i.e. characteristic times for chemical processes are much lower than those of the flow, the chemical reactions attain a quasi-steady state and adjust with short relation times to local flow conditions. Consequently, the chemistry and the mixing processes can be decoupled. This is the basis concept of the flamelet [3]. State relationships for the different reactive scalars can then be generated, such as the temperature or the species mass fraction, as a function of a reduced number of parameters describing the local flow conditions (mixture fraction, scalar dissipation rate, radiative loss). Figure I-6 shows that the chemistry associated to soot, and more generally to pollutants, is slow. As a consequence, the simplifications described previously cannot be rigorously applied.

- The second difficulty comes from the fact that, contrary to NO and other pollutants, soot acts on the flow through the radiative losses that it produces. As a consequence, the formation of soot cannot be considered at posteriori, i.e. once the flow-field has been predicted. This implies that radiative heat transfer must be taken into account in an accurate manner, soot formation/oxidation processes being sensitive to temperature. The effects of the coupling between soot formation and radiative heat transfer are significant in both laminar and turbulent coflow diffusion flames [64–67].

## I.4.2.1 Physical mechanisms

Soot formation and dynamics in combustion systems are usually decomposed into four different processes: nucleation, surface reaction growth, oxidation and coagulation. Nucleation and coagulation control the number of primary particles, whereas surface reactions (surface growth and oxidation) control the carbon mass accumulated in soot.

### I.4.2.1.1 Nucleation

The first step of soot formation is the nucleation. The first soot particles appear from PAH (Polycyclic Aromatic Hydrocarbons), which are formed from species like acetylene and benzene, produced by the degradation of hydrocarbon. Nucleation can itself be divided into 3 sub-processes [68]: initial PAH formation (formation of the first aromatic

ring), planar PAH growth (replicating-like growth) and particle nucleation (coalescence of the planar PAH into a 3D particle).

*PAH formation - The first aromatic ring*

Several hypothesis regarding the first aromatic ring formation from hydrocarbon pyrolysis products have been proposed. The relative importance of those products, such as acetylene $C_2H_2$ and propargyl $C_3H_3$, has been studied extensively by Frenklach and Wang [68], and Frenklach [69]; the first aromatic ring itself is assumed to be benzene $C_6H_6$ or phenyl (benzene with an active site). From this first ring, PAH and soot formation processes can be assumed to be independent of the fuel. Another possible precursor for the formation of the initial aromatic ring is cyclopentadienyl radical ($c$–$C_5H_5$). Initial rings will then combine with one another until the resulting molecules reach a certain number of rings $i_0$. At this size, aromatic growth is dominated by addition of other species (see below).

*PAH planar growth*

Aromatics growth (or PAH planar growth) is the step between the apparition of the first aromatic ring and actual soot particle inception. It is therefore a key process in order to study soot formation. Several mechanisms can be considered in order to model this process; most often, the so-called HACA mechanism (for *H-abstraction-$C_2H_2$-addition*) is assumed [68]. Here, $A_i$ is an aromatic molecule with $i$ rings and $A_i^\bullet$ is its radical, for $i \geq i_0$. The HACA mechanism consists in a repetitive sequence of three steps (simplified from a more complex mechanism [68]):

$$A_i + H \rightleftharpoons A_i^\bullet + H_2 \tag{I-4}$$

$$A_i^\bullet + C_2H_2 \rightleftharpoons A_iC_2H_2^\bullet \tag{I-5}$$

$$A_iC_2H_2^\bullet + C_2H_2 \rightarrow A_{i+1} + H \tag{I-6}$$

The first step, Eq. (I-4), activates a molecule by converting it to a radical. This conversion can be done by other species than H, but it has been established as the predominant one in typical flame experiments [69]. The second and third steps, Eqs. (I-5) and (I-6), add acetylene to the molecule. Different HACA kinetic regimes depending on local flow characteristics can be identified [69], due to the reversibility of Eqs. (I-4) and

(I-5). Actual PAH growth takes place on the third irreversible step, which initiates a new cycle, and occurs until the resulting molecules reach a size of about 1 nm.

*Oxidation of aromatics*

Aromatics oxidation is mostly due to $O_2$ [69], which explains why soot inception happens at the vicinity of the main combustion zone (rich in H to account for the HACA mechanism, poor in $O_2$ to account for low oxidation). Oxidation by OH is usually unimportant [69].

*Coalescence of the planar PAH*

This step represents the transition between PAH (which are gaseous macro-molecules) and soot particles (which are usually considered as solid particles). This is the least understood part of the soot formation process [69]; it is due both to chemical growth and PAH growth by collisions. The resulting solid particles are called NOC for *Nanoparticles of Organic Carbon* and are the smallest soot particles considered, usually with a size between 1 and 10 nm. More details can be found in [70–72]. Those nanoparticles interact both with the surrounding gaseous species (see Section I.4.2.1.2) and with each other (see Section I.4.2.1.3).

## I.4.2.1.2 Surface reactions

*Surface growth*

Soot particles growth by surface reactions involves mostly acetylene in a mechanism similar to the HACA reactions (Eqs. (I-4) to (I-6)) where aromatics molecules $A_i$ are replaced by soot particles $C_s$ [73]:

$$C_s + H \rightleftharpoons C_s^\bullet + H_2 \quad \text{(I-7)}$$

$$C_s^\bullet + H \rightarrow C_s \quad \text{(I-8)}$$

$$C_s^\bullet + C_2H_2 \rightarrow C_s + H \quad \text{(I-9)}$$

Equation (I-7) is similar to the first step of the HACA mechanism Eq. (I-4). Equation (I-8) corresponds to the deactivation of soot particle surface, and Eq. (I-9) corresponds to actual soot particle growth. This last equation has to be completed by a fourth step where the active site on the soot particle surface is conserved [74]:

$$C_s^\bullet + C_2H_2 \rightarrow C_s^\bullet + H_2 \quad \text{(I-10)}$$

Both Eqs. (I-9) and (I-10) take place at the same time, their relative predominance depending on temperature. This has been shown experimentally and computationally by Wang *et al.* [74]. Another mechanism for surface growth of soot particles is PAH condensation [73,75–78]. Both mechanisms take place simultaneously, HACA being dominant in hot, rich zones of the flame while PAH condensation takes place in colder zones. Both should be considered for accurate diffusion flames modeling.

Surface growth is limited by particle aging, which has been revealed experimentally. Soot particles are less susceptible to grow by surface reactions if they have been present in the reaction zone for a long time. This can be explained by a depletion of H atoms in the zone, or by a decrease in particle surface active sites [69].

*Oxidation*

Similar to aromatic molecules, carbon mass in soot particles can be decreased by oxidation from gaseous species, such as OH and $O_2$. Other species such as O, $CO_2$ or $H_2O$ can be involved but to a lesser degree. OH is responsible for most of soot particle oxidation [79]. Soot oxidation is also responsible for another less known phenomenon called particle fragmentation, shown experimentally by Echavarria *et al.* [80]: oxidant molecules are small enough to get inside a soot aggregate and oxidize carbon there, leading to the fragmentation of the particle and resulting in a higher number of smaller soot particles.

### I.4.2.1.3 Coagulation

Coagulation comprises all the interactions resulting in a size growth between soot particles. When two soot particles collide, two possible outcomes can be observed:

- the two particles will merge, forming a new, bigger, spherical particle; this process is called coalescence;
- the two particles will stick together while keeping their own form; this is agglomeration.

In both those processes, soot mass is conserved but the number density will decrease. Two points of view can be adopted to understand those processes better [81,82]: the mechanical behavior of soot particles is analogue to viscous particles, or

surface reactivity characterizes the form of the resulting particles (high reactivity will smooth the particle after collision, while low reactivity will leave the particle as an agglomerate). For usual laboratory scale flames at atmospheric pressure, most soot particles keep their spherical form [66].

## I.4.2.2 Numerical models

Modeling the processes described in Section I.4.2.1 is usually done by considering two separate levels: soot formation kinetic on one side, which deals with chemical mechanisms such as soot nucleation and surface reactions, and particles dynamics on the other, which deal with coagulation processes.

### I.4.2.2.1 Soot kinetic models

Several tricky issues have to be taken into account when designing a soot formation model. First, the number of initial and intermediate species involved in soot formation processes (see Section I.4.2.1), as well as intermediate reactions, is huge; they cannot all be considered in a model and even a reduced number of species and reactions can be computationally prohibitive. Second, time-scales for those reactions is much higher than usual chemical time-scales. Finally, several formation regimes can be identified depending on temperature and mixture composition, and the significant contribution of soot adds to the difficulty.

Three levels of description can be considered for soot kinetics [83]:

1. Empirical models are based entirely on correlations with experimental results; soot volume fraction is computed as function of fuel mass fraction or mixture fraction. No details of nucleation and surface growth mechanisms is necessary, and soot precursors (acetylene, benzene) mass fractions are not needed. Therefore, those models can be used with a global chemistry. However, they do not compute localized processes such as the temperature dependence of the HACA mechanism, which can regulate soot formation globally. Empirical models are also extremely case-dependent and must usually be tuned to achieve agreement with experimental data.

2. Semi-empirical models are also based on experimental correlations, but for these models soot volume fraction is related to soot precursors (most often acetylene $C_2H_2$). They can therefore better depict soot chemical processes and resulting soot levels, and

are not fuel dependent. However, this implies that the concentrations of soot precursors are determined by the chemistry, which means using a sufficiently detailed chemical mechanism that can be computationally expensive. The flamelet model used here for combustion computations is a solution to this drawback. However, Kennedy [83] argues that even for semi-empirical models, one or two reaction rates must be adjusted from one case to another in order to be accurate.

3. Detailed models use no empirical correlations but are based on the complete detailed mechanisms described in Section 2.1: PAH formation, PAH growth, inception of soot from PAH, HACA and PAH condensation for surface growth, and oxidation of soot particles [68,84].

#### I.4.2.2.2 Particles dynamics

The most advanced models for the dynamic of soot particles (interactions between soot particles) include a description of the fractal nature of the soot particles as well as the coagulation and agglomeration processes. Soot particles are assumed to be aggregates of primary particles and the Number Density Function (NDF) of surface and volume of aggregates is used to characterize the local distribution in surface and volume. Its evolution is governed by the population balance equation [35]. This population balance equation can be solved by different methods:

- Stochastic methods [36]. This kind of calculations are extremely consuming in computational resources and are devoted to simple configurations and to validate simplified numerical approaches.

- Moment methods where the moments of the size distribution of soot particles are solved [34,35,37–42]. Among these methods, the Direct Quadrature Method of Moments (DQMOM) [34,35,40,41], the Method of Moments with Interpolative Closure (MOMIC), and a Hybrid Method of Moments (HMOM) [42], which combines the advantages of the two former, have been developed.

- Sectional methods where the size distribution of soot particles is divided into discrete sections [84,85].

The two-equation acetylene/benzene based soot production model proposed by Lindstedt will be described in details in Chapter II, section II.2 [6]. This model belongs to

the category of the semi-empirical models although it involves a PAH-based description of the nucleation process and a description of the surface growth of soot particles based on acetylene (as in the HACA mechanism). The oxidation model was initially based on $O_2$ but subsequent studies have improved it by adding oxidation based on OH [64,65]. The model does not consider the agglomeration process and, as consequence, soot particles are assumed spherical. Two moment of the particle size distribution, namely the soot number density and the soot volume fraction, are used to describe the particle geometry.

## I.4.3 Radiative heat transfer

An accurate prediction of radiative heat transfer in turbulent flames is a difficult task since it requires a precise solution of the Radiative Transfer Equation (RTE), a proper modelling of the spectral dependence of radiating species (radiatively participating gases and soot particles) and a proper evaluation of the Turbulence-Radiation Interactions (TRI). Here a brief description of the works of the literature concerning the radiative property models for soot and gaseous radiatively participating species and for turbulence-radiation interactions is provided.

### I.4.3.1 Radiative property models

The determination of accurate solutions for radiative heat transfer in media involving combustion products is difficult due to the strong dependence of the absorption coefficient of gases on the wavenumber. For example, the line-by-line method (LBL) requires about $10^6$ resolutions of the RTE to consider this effect [86], involving computation requirements which are too large for practical applications. Various alternative gas property models have been developed or extended in recent decades to overcome this difficulty.

Narrow Band (NB) models, such as the Statistical Narrow Band (SNB) and the Correlated k-distribution (CK), have retained attention [86–90]. In particular, studies were conducted to establish new databases for these methods [89,90]. The accuracy of the SNB model, which gives the spectral transmissivity over a NB, is well recognized. However, this method suffers from two drawbacks. First, it cannot be easily coupled with differential solution methods of the RTE, such as the Discrete Ordinates Method (DOM) [91], the Finite Volume Method (FVM) [92] or the P1 [93], without the introduction of

approximations leading to a loss in accuracy [94,95]. In order to keep its accuracy, the SNB model is generally coupled with the Ray Tracing (RT) method. As the RT method is time consuming, the SNB model is often limited to determining radiative intensity along a line of sight [96–98] or to providing benchmark solutions when LBL solutions are not available [99–101]. Secondly it is not a feasible way to account for scattering unless the Monte Carlo method is used, which increases even more the computational time. The CK method, on the other hand, gives the absorption coefficient, so it can be coupled with arbitrary RTE solvers and can account for scattering. This method consists in reordering the absorption coefficient in a NB into a smooth, monotonically increasing function called the k-distribution. Integration over numerous wavenumbers can then be replaced by a simple quadrature scheme with few points. The CK method is accurate but very demanding computationally, especially when dealing with a gas mixture due to overlapping bands [100]. Several ways have been found to reduce its computational cost [102–106].

Global models are generally limited to problems with grey walls and/or particles. The Weighted-Sum-of-Grey-Gases (WSGG) model, initially developed by Hottel and Sarofim [107], can be applied to any method for solving the RTE [108]. It consists in replacing the non-grey gas by a number of grey gases, for which the radiative rates are computed independently. The Spectral-Line-Based Weighted-Sum-of-Grey-Gases (SLW) [109,110] and the Full-Spectrum k-distribution model (FSK) [111] can be viewed as improvements of the WSGG. The basic idea of these methods consists in reordering the absorption coefficient over the entire spectrum into a smooth, monotonically increasing function called the full-spectrum (FS) k-distribution. The integration over about $10^6$ lines is then reduced to the integration of a single smooth function. As shown by Modest [86], the SLW and FSK models differ in the methodology employed to perform this integration. The SLW uses a simple trapezoidal scheme, defining $N_G$ grey gases, whereas the FSK uses a quadrature scheme. Solovjov and Webb [106,112] and Modest and Riazzi [105] developed models to generate a single FS k-distribution for a mixture of gases and soot.

The accuracy and the computational efficiency of some of these models were assessed by considering 1D [113–115], 2D [100] and 2D axisymmetric [116–118] configurations. These comparisons showed that models of the “correlated-k distribution”

family are the most accurate and FSCK (Full-Spectrum k-distribution) and WBCK (Wide-Band correlated-k) are the most suitable in terms of accuracy and computational efficiency.

### I.4.3.2 Turbulence radiation interactions

TRI are an important issue in problems involving turbulent flames, their modelling being fundamental if accurate predictions of temperature, radiative fluxes [10] and production of pollutants such as NO [119] or soot [20] are desired.

The treatment of turbulence radiation interactions (TRI) within a turbulent reactive flow is made difficult by the highly nonlinear dependence to the radiative intensity with regards to the flow state (and in particular to the temperature T) [86]:

$$\langle I_{b\eta}(T)\rangle \neq I_{b\eta}(\langle T\rangle) \tag{I-11}$$

$$\langle \kappa_\eta(\boldsymbol{\phi})\rangle \neq \kappa_\eta(\langle \boldsymbol{\phi}\rangle) \tag{I-12}$$

Taking the Reynolds average of the RTE introduces the two parts of TRI:

$$\frac{d\langle I_\eta\rangle}{ds} + \underbrace{\langle \kappa_\eta I_\eta\rangle}_{\text{Absorption TRI}} = \underbrace{\langle \kappa_\eta I_{b\eta}\rangle}_{\text{Emission TRI}} \tag{I-13}$$

Taking TRI into account requires then the modelling of two terms in Eq. (I-13). The first term, known as “absorption TRI”, represents the nonlinear coupling between incident radiation and the local absorption coefficient. It is the consequence of property fluctuations across the domain and its modelling requires having a detailed knowledge of the instantaneous fields of temperature and species. Absorption TRI is generally neglected by considering the Optically Thin Fluctuation Approximation (OTFA), i.e. assuming that the local intensity is weakly correlated with the local absorption coefficient. This approximation was found to be valid over a wide range of conditions [10], with the exception of large-scale sooting flames [82]. The second term, referred to as “emission TRI”, is determined on the basis of local properties only and can be evaluated by using either presumed Probability Density Function (PDF) approaches [119–121] or PDF composition methods [20,66,82,122–124]. Li and Modest [122,123], Habibi et al. [119] and Consalvi [121] isolate and quantify different levels of closure for emission TRI in turbulent non-luminous jet flames and buoyant diffusion flames. They showed that the

complete absorption coefficient-Planck function correlation must be considered to obtain a reliable evaluation.

A significant amount of studies considered decoupled fluid flow/radiative transfer calculations by specifying both the temperature and the species concentrations as input data [96,97,125]. The methodology initiated by Faeth and co-workers consisted in solving the instantaneous RTE along a line of sight by using stochastic methods to prescribe the instantaneous scalar data. This model was systematically applied to a vast quantity of fuels burning in still air, considering both non-luminous and luminous flames. The authors established that radiative emission from a flame may be as much as 50 to 300% higher than would be expected based on mean values of temperature and absorption coefficient. Coupled fluid flow/radiative transfer calculations were also carried out. Modest and co-workers [20,66,82,124] proposed a comprehensive formulation, combining a photon Monte Carlo method with a composition PDF method, which allows an accurate description of both absorption and emission TRI. This model was applied to investigate the influence of TRI in non-sooting and sooting jet flames. They showed that the absorption TRI is negligible in lab-scale flames as long as soot levels are of the order of few ppm. Supplementary calculations [82] showed that this conclusion does not hold in large-scale flames where absorption TRI can always be neglected in the gas-phase radiation but is of the order of 10% in soot radiation. In addition, the emission TRI in soot radiation was found to be reduced as compared to lab-scale flames, this being the possible consequence of negative temperature-soot volume fraction correlations. The highly negative behavior of the correlation between temperature and soot volume fraction was also evidenced experimentally by Sivathanu et al. [126,127] and by Murphy et al. [128] and numerically by Kollmann et al. [56]. The effects of this correlation on soot emission were assessed by Consalvi et al. [48] by using a simplified approach.

## I.4.4 Transported PDF methods

Several approaches have been developed for modeling turbulent reacting flows [47]. As example, the unsteady flamelet [129], the Conditional Moment Closure (CMC) method [130] and the transported PDF methods [20,53,56,66,131] do not suffer from the drawback of the uncorrelated approach when modeling TSI. The first takes into account the correlation between mixture fraction and soot quantities by solving the transport

equation for soot quantities in the mixture fraction space [129], and the second by considering the means of soot quantities conditioned by the mixture fraction [130] and the third gives direct access to the joint PDF and provides an exact closure of the soot formation and oxidation terms [20,53,56,66,131]. Very encouraging soot predictions in laboratory-scale turbulent diffusion flames have been reported by using these three methods [20,53,56,66,129–134]. Among these methods, the transported probability density function (PDF) methods have proved to be particularly powerful in capturing TCI, TSI and TRI [13] (see also the previous section for the studies related to TRI). For clarity and concreteness, only composition PDF methods are considered in the present study, velocity–composition PDF methods being disregarded.

In a composition PDF method, a modeled transport equation is solved for the one-point, one-time joint PDF of a set of variables (the composition variables) that is sufficient to specify the local thermochemical state of the reacting system [12–14]. The main advantage of PDF methods is that the chemical source term, and terms that correspond to other one-point processes (e.g., radiative emission), appear in closed form. Any chemical mechanism (detailed, skeletal and/or reduced) can be used directly in simulations of turbulent flames with minimal further modeling required to account for the effects of turbulent fluctuations [12–14].

In most of the studies reported in the literature, the PDF transport equation was solved by using a hybrid Lagrangian particle/Eulerian mesh (LPEM) method [20,53,66,131]. However, the implementation of the LPEM method in CFD code is not straightforward and requires careful attention to issues of consistency and statistical control error [12–15]. In addition a large number of particles are required and particle-based PDF methods are computationally expensive [13,15,131]. Eulerian Fields methods have emerged in the last decade as alternatives for solving the PDF transport equation and are more compatible with conventional CFD codes than LPEM methods [13,15]. Both stochastic [16,135] and deterministic Eulerian field [14] methods have been developed. Jaishree and Haworth assessed the ability of the LPEM method, the Valiño Stochastic Eulerian Field (SEF) method and the deterministic Eulerian Field method with a direct quadrature-of-moments (DQMOM) closure [14] to simulate Sandia flames D, E and F. This comparative study revealed that the LPEM and SEF methods have similar accuracy and

computational efficiency. The DQMOM was found to be the most efficient computationally but provided a lower level of agreement with the experimental data.

# I.5 Organisation of the manuscript

The present manuscript is organized as follow. The combustion model, the soot production model, the radiative property model used in the present study are described in details in the Chapter II. Chapter III focuses on transported PDF methods, the numerical method used to solve the transported PDF approach and the validation of the model. The method is validated by simulating twelve turbulent diffusion jet flames. In addition, a specific study regarding the statistics of the SDR is presented. Furthermore, the validity of common approximate radiation models is also evaluated.

The second part of this manuscript is related to the effects of turbulent interactions that are usually neglected in presumed-pdf approaches, by taking advantage of the transported PDF method. Chapter IV concerns soot emission TRI. To the author' best knowledge such a detailed analysis of soot emission TRI has not been reported in the literature. Chapter V deals with the correlation between mixture fraction and the enthalpy defect that is also generally disregarded in presumed PDF approaches. The impact of neglecting this correlation on flame structure and radiative quantities is evaluated.

Finally, conclusions drawn from the present study are presented and perspectives for future works and developments are outlined.

# Chapter II Physical models and solution methods

In this chapter, the flow-field model, the combustion model, the two-equation acetylene/benzene-based soot production model, and the radiative model used in the present study are described.

## II.1 Turbulent combustion

### II.1.1 Turbulent flows

The existence of turbulence is due to the highly non-linear nature of the Navier-Stokes conservation equations. These non-linear terms prevail over the diffusion terms in turbulent flows, characterized by a high Reynolds number $Re = UL/\nu$, where $U$ is a typical velocity and $\nu$ is the fluid kinematic viscosity. A large range of time and space scales can be found in these flows, which are described by the *Kolmogorov theory of turbulence*, briefly summarized here. More details can be found in Ref. [57].

Any perturbation in initial or boundary conditions or in material properties may lead to entirely different flow realizations for the same experimental setting. This is why physical quantities are considered as *random variables*. Turbulent motions are characterized by a range of length scales which can take values between $\eta_K$ (Kolmogorov scale, the smallest) and $\mathcal{L}$ (the *integral* length, i.e. a characteristic length of the flow, the largest). Turbulent kinetic energy is produced at the largest scale, between $\mathcal{L}$ and a certain lower scale $l_{\mathcal{P}}$ ($\eta_K \ll l_{\mathcal{P}} < \mathcal{L}$), and transferred to the smallest scales to be dissipated by viscous forces between $\eta_K$ and a certain $l_D$ ($\eta_K < l_D \ll l_{\mathcal{P}}$). The *energy cascade* is the process describing this energy transfer from large scales to small scales, and takes place in the *inertial range* (between $l_D$ and $l_{\mathcal{P}}$) (see Fig. II-1).

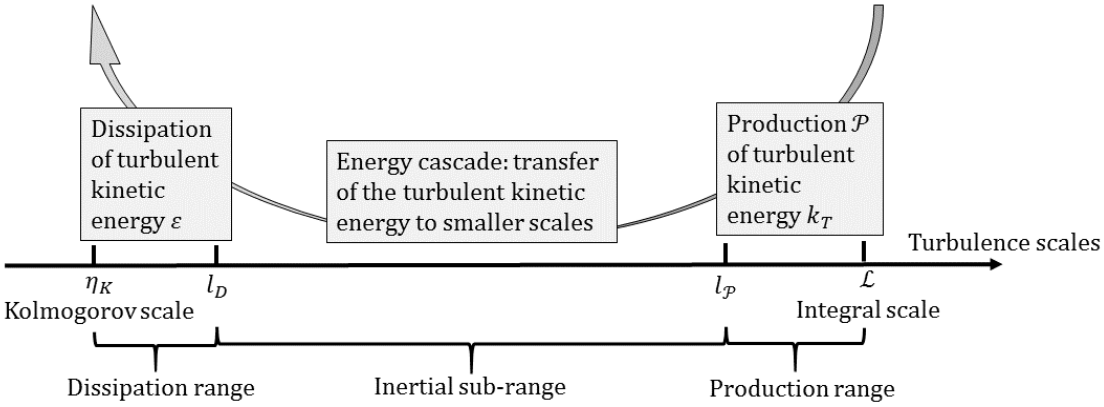


**Figure II-1. Turbulent energy cascade**

Three hypothesis were introduced by Kolmogorov to formulate his theory: *local isotropy* (for sufficiently high Reynolds number flows, the small-scale (between $\eta_K$ and $l_D$) turbulent motions are isotropic), *similarity of the smallest scales* (the statistics at the smallest scales $\ll l_{\mathcal{P}}$ have a universal form that is uniquely determined by the turbulent dissipation rate $\varepsilon$ and the kinematic viscosity $\nu$), and *similarity of the intermediate scale* (the statistics in the inertial range (between $l_D$and $l_{\mathcal{P}}$) have a universal form that is uniquely determined by $\varepsilon$ and independent of $\nu$).

Turbulent kinetic energy $k_T$ is related to the large turbulent motions and is defined by the root mean square (rms) velocity of the largest eddies:

$$k_T = \frac{1}{2}u_i'^2 \tag{II-1}$$

where $u_i$ is comparable to the characteristic flow velocity and $u_i'$ its fluctuation. The turbulent dissipation rate $\varepsilon$ is related to the smallest eddies, i.e. to the Kolmogorov scale $\eta_K$. Ratio between the integral scale and Kolmogorov scale are related to the flow Reynolds number by:

$$\frac{\eta_K}{\mathcal{L}} \sim Re^{-3/4}; \qquad \frac{u_{\eta_K}}{u_{\mathcal{L}}} \sim Re^{-1/4}; \qquad \frac{\tau_{\eta_K}}{\tau_{\mathcal{L}}} \sim Re^{-1/2} \tag{II-2}$$

where $Re = UL/\nu$. All these notions can be expressed in term of the *energy spectrum* $E(\kappa_T)$. The turbulent kinetic energy $k_{T,[a,b]}$ contained in the motion range $[l_b, l_a]$ is given by:

$$k_{T,[a,b]} = \int_{\kappa_{T,a}}^{\kappa_{T,b}} E(\kappa_T) d\kappa_T \tag{II-3}$$

while the contribution to the dissipation rate $\varepsilon_{a,b}$ from the same motion range is given by:

$$\varepsilon_{[a,b]} = \int_{\kappa_{T,a}}^{\kappa_{T,b}} 2\nu\kappa_T^2 E(\kappa_T) d\kappa_T \tag{II-4}$$

where $\kappa_T = 2\pi/l$ is the wave number associated to the length scale $l$ and $E(\kappa_T)$ is the energy spectrum function. Figure II-2 illustrates the three characteristic scales of turbulence on the energy spectrum.

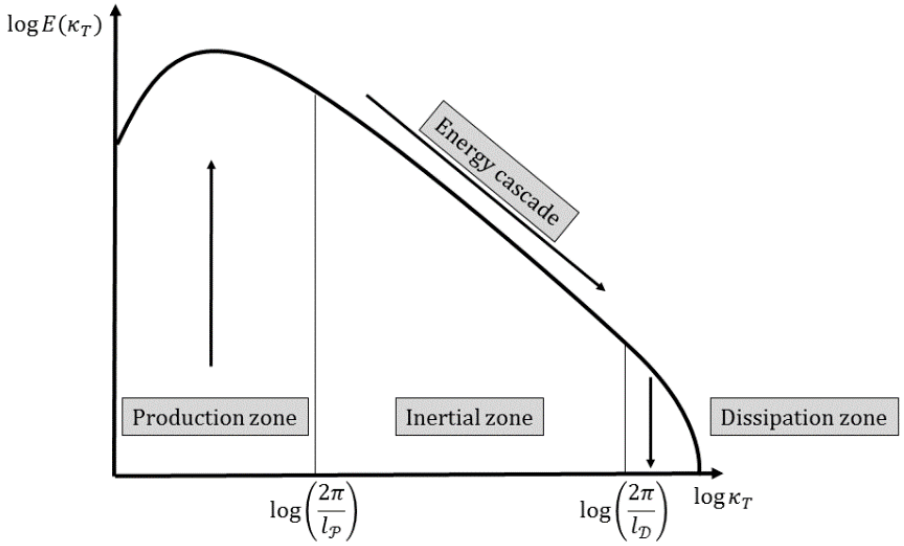


**Figure II-2. Turbulent energy spectrum**

Numerical modeling of turbulent flows needs to deal with the large range of scales introduced above. Three numerical approaches (illustrated in Fig. II-3) can be considered, taking into account different turbulent scales:

1. Direct Numerical Simulation, or DNS, is the highest level of turbulent flow computation; it solves every space and time scales of turbulence (from the Kolmogorov scale to the integral scale). This method is therefore extremely computationally expensive: in order to solve the smallest scales, the mesh cell size must be comparable to the Kolmogorov scale. Furthermore, the higher the flow Reynolds number is, the smaller the Kolmogorov scale is (see Eq. (II-2)); DNS is therefore only used with very simple

academic configurations and low Reynolds number flows for research purposes and to provide reference solutions.

2. Large Eddy Simulation, or LES, solves only the largest scales of turbulence and models the smallest. This decomposition is justified by the fact that the largest scales are mostly dependent on the case geometry and configuration, while the smallest scales have a more universal behavior. LES is more cost-efficient than DNS and is therefore a very promising method for industrial applications, even though it is highly more expensive than typical RANS methods (see next point).

3. Reynolds Averaged Navier-Stokes, or RANS methods are the most common numerical approaches because they are the most cost-efficient methods. Here, only the mean flow characteristics are computed and all turbulent scales are modeled. The immediate advantage comes from the fact that meshes can be much coarser than in DNS or LES, which makes RANS methods easy to implement for complex industrial configurations. However, all information regarding fluctuations are modeled, contrary to LES or DNS, and a special care should be taken in order to ensure that these models are accurate.

The present work will be limited to a RANS description of the turbulent flow. The main features of this numerical approach are presented in the next section.

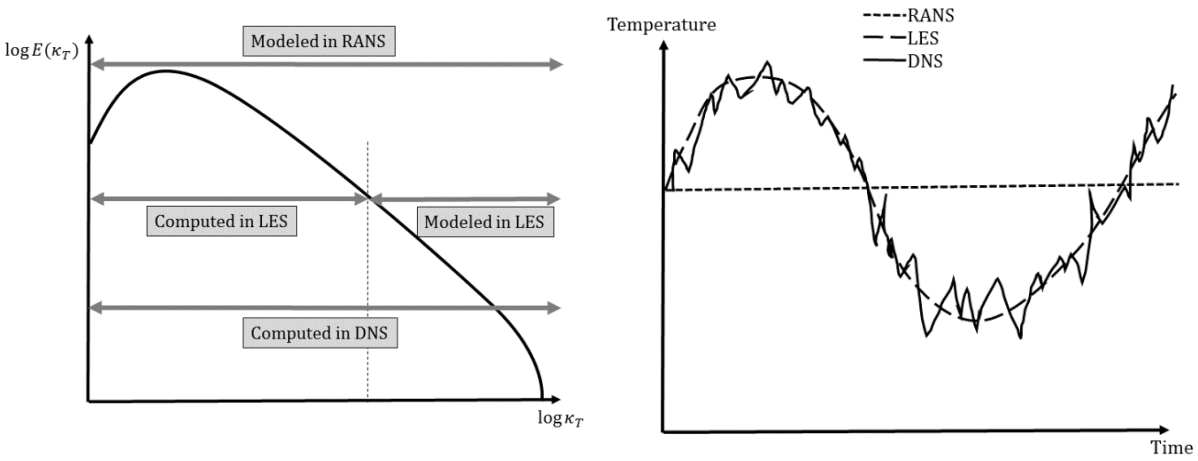


**Figure II-3. Numerical approaches for turbulent flows simulations: Left) modeled vs. solved ranges on the energy spectrum, and Right) schematic example of the time evolution of temperature at one point in the computational domain**

# II.1.2 RANS modeling

## II.1.2.1 Time-averaging

For RANS models, it is assumed that the mean flow time-scale $t_1$ and the fluctuations time-scale $t_2$ are un-correlated, so that any quantity $Q$ can be split in two parts, its mean value $\langle Q \rangle$ and its fluctuation $Q'$: $Q = \langle Q \rangle + Q'$. For a variable $Q(t)$, assuming a short-time averaging over $\Delta t$ ($t_1 < \Delta t < t_2$), the time-averaged mean $\langle Q \rangle$ is defined as:

$$\begin{aligned} \langle Q \rangle &= \frac{1}{\Delta t}\int_t^{t+\Delta t} Q(t')dt' \\ \langle Q' \rangle &= 0 \end{aligned} \tag{II-5}$$

For combustion processes, large density variations are frequent and induce the introduction of density-weighted averages (Favre averages):

$$\tilde{Q} = \frac{\langle \rho Q \rangle}{\langle \rho \rangle} \tag{II-6}$$

which leads to the splitting in Favre mean $\tilde{Q}$ and Favre fluctuations $Q''$: $Q = \tilde{Q} + Q''$. This allows for a more compact formulation of the governing equations (see next section) and fewer unknown correlations to model.

## II.1.2.2 Favre averaged governing transport equations

For diffusion flames studied in the present work, it can be assumed the species diffusion and heat conduction follow the Fick law and the Fourier law, respectively. In this case, the Favre-averaged transport equations governing a turbulent reactive flow are [19]:

1. Mass conservation

$$\frac{\partial \langle \rho \rangle}{\partial t} + \frac{\partial \langle \rho \rangle \widetilde{u_i}}{\partial x_i} = 0 \tag{II-7}$$

where $\rho$ is the local density and $(u_i)_{i=1,3}$ is the flow velocity;

2. Momentum conservation

$$\frac{\partial \langle \rho \rangle \widetilde{u_i}}{\partial t} + \frac{\partial \langle \rho \rangle \widetilde{u_i}\widetilde{u_j}}{\partial x_j} + \frac{\partial \langle p \rangle}{\partial x_i} = \frac{\partial}{\partial x_i}\left(\widetilde{\tau_{ij}} - \overline{\rho}\widetilde{u_i''u_j''}\right) + \langle F_i \rangle \tag{II-8}$$

where $p$ is the pressure, $(\tau_{ij})_{i,j=1,3}$ is the viscous tensor defined as $\tau_{ij} = -\frac{2}{3}\mu\frac{\partial u_k}{\partial x_k}\delta_{ij} + \mu\left(\frac{\partial u_i}{\partial x_j} + \frac{\partial u_j}{\partial x_i}\right)$ with $\mu = \rho\nu$ the dynamic viscosity and $(F_i)_{j=1,3}$ are the volume forces;

3. Species mass conservation

$$\frac{\partial\langle\rho\rangle\widetilde{Y_k}}{\partial t} + \frac{\partial\langle\rho\rangle\widetilde{u_i}\widetilde{Y_k}}{\partial x_i} = -\frac{\partial}{\partial x_i}\left(D_k\frac{\partial\langle Y_k\rangle}{\partial x_i} + \langle\rho\rangle\widetilde{u_i''Y_k''}\right) + \langle\dot{\omega}_k\rangle, \text{for } k = 1, N_k \tag{II-9}$$

where $(Y_k)_{k=1,N_k}$ are the species mass fractions, $(D_k)_{k=1,N_k}$ are the species diffusion coefficients, $N_k$ is the number of species and $(\dot{\omega}_k)_{k=1,N_k}$ are the species reaction rates, which verify $\sum_{k=1}^{N_k}\dot{\omega}_k = 0$;

4. Energy conservation

$$\frac{\partial\langle\rho\rangle\tilde{h}}{\partial t} + \frac{\partial\langle\rho\rangle\widetilde{u_i}\tilde{h}}{\partial x_i} = -\frac{\partial\langle q_i\rangle}{\partial x_i} - \frac{\partial\langle\rho\rangle\widetilde{u_i''h''}}{\partial x_i} - \langle\dot{Q}_{rad}\rangle \tag{II-10}$$

where $h$ is the total enthalpy defined as:

$$h = \sum_{k=1}^{N_k} Y_k\left(\Delta h_{f,k}^0 + \int_{T_0}^{T} C_{pk}(T')dT'\right) \tag{II-11}$$

with $\Delta h_{f,k}^0$ is the formation enthalpy at $T_0$ and $C_{pk}$ is the heat capacity at constant pressure of species $k$, $(q_i)_{i=1,3}$ is the heat flux modeled by Fourier law:

$$q_i = -\lambda\frac{\partial T}{\partial x_i} \tag{II-12}$$

with $\lambda$ is the heat conductivity, and finally $\dot{Q}_{rad}$ is the volumetric heat source term corresponding to the radiative source term in the present work (see section II.3).

Several unclosed quantities appear in Eqs. (II-7) to (II-10): the Reynolds stresses $\widetilde{u_i''u_j''}$, the species, $\widetilde{u_i''Y_k''}$, and enthalpy, $\widetilde{u_i''h''}$, turbulent fluxes, and the species mean chemical rate $\langle\dot{\omega}_k\rangle$. The next sections present the usual models used to close these quantities.

### II.1.2.3 Models for unclosed quantities

In order to close the Reynolds stresses term, Boussinesq introduced the turbulent viscosity $\mu_T$ [19]:

$$\langle\rho\rangle\widetilde{u_i''u_j''} = -\mu_T\left(\frac{\partial\widetilde{u_i}}{\partial x_j}+\frac{\partial\widetilde{u_j}}{\partial x_i}-\frac{2}{3}\delta_{ij}\frac{\partial\widetilde{u_k}}{\partial x_k}\right)+\frac{2}{3}\langle\rho\rangle k_T \tag{II-13}$$

where $k_T$ is the turbulent kinetic energy introduced in section II.1.1 (Eq. (II-1)). The closure problem is therefore shifted from Reynolds stresses to the turbulent viscosity, for which a model is needed. Several approaches have been proposed and a non-exhaustive list can be found for example in Ref. [19]. In the current work a two equations $k_T-\varepsilon$ model is used, in which the evolution equation of turbulent kinetic energy and its dissipation rate are described as:

$$\frac{\partial\langle\rho\rangle k_T}{\partial t}+\frac{\partial\langle\rho\rangle\widetilde{u_i}k_T}{\partial x_i}=\frac{\partial}{\partial x_i}\left[\left(\mu+\frac{\mu_T}{\sigma_k}\right)\frac{\partial k_T}{\partial x_i}\right]+\mathcal{P}_k+G-\langle\rho\rangle\varepsilon \tag{II-14}$$

$$\frac{\partial\langle\rho\rangle\varepsilon}{\partial t}+\frac{\partial\langle\rho\rangle\widetilde{u_i}\varepsilon}{\partial x_i}=\frac{\partial}{\partial x_i}\left[\left(\mu+\frac{\mu_T}{\sigma_\varepsilon}\right)\frac{\partial\varepsilon}{\partial x_i}\right]+C_{\varepsilon1}\frac{\varepsilon}{k_T}\mathcal{P}_k+C_{\varepsilon3}\frac{\varepsilon}{k_T}G-C_{\varepsilon2}\langle\rho\rangle\frac{\varepsilon^2}{k_T} \tag{II-15}$$

where the turbulent viscosity $\mu_T$ is estimated as [19]:

$$\mu_T=\langle\rho\rangle C_\mu\frac{k_T^2}{\varepsilon} \tag{II-16}$$

the production term $\mathcal{P}_k$ is given by:

$$\mathcal{P}_k=-\langle\rho\rangle\widetilde{u_i''u_j''}\frac{\partial\widetilde{u_i}}{\partial x_j} \tag{II-17}$$

and the buoyancy production term $G$ is given by:

$$G=-\frac{\mu_T}{\sigma_T}\frac{1}{\langle\rho\rangle^2}\frac{\partial\langle\rho\rangle}{\partial x_j}\frac{\partial\langle p\rangle}{\partial x_j} \tag{II-18}$$

Usual values for the model constants are $C_\mu=0.09$, $C_{\varepsilon1}=1.44$, $C_{\varepsilon2}$=1.92, $C_{\varepsilon3}=1.44$, $\sigma_k=1$ and $\sigma_\varepsilon=1.3$.

Turbulent fluxes of species and enthalpy are usually closed using a gradient diffusion hypothesis:

$$\langle\rho\rangle\widetilde{u_i''Y_k''} = -\frac{\mu_T}{Sc_{kT}}\frac{\partial\widetilde{Y}_k}{\partial x_i} \quad \text{(II-19)}$$

$$\langle\rho\rangle\widetilde{u_i''h''} = -\frac{\mu_T}{Sc_{hT}}\frac{\partial\tilde{h}}{\partial x_i} \quad \text{(II-20)}$$

where $Sc_{kT}$ and $Sc_{hT}$ are turbulent Schmidt numbers.

Finally, closing the mean species chemical term is the key issue of turbulent combustion modeling. In the present work, the flamelet concept is applied and presented next section.

## II.1.3 Enthalpy defect Laminar Flamelet model

The large number of chemical species and chemical reactions involved in the soot formation and oxidation processes is prohibitive when performing numerical simulation of soot formation within CFD codes. Under the assumption of widely separated time scales for chemical reactions and transport processes, the combustion chemistry attains a quasi-steady state and immediately adjusts to local flow field conditions. By this, the chemical kinetics can be decoupled from the mixing process. This idea is realized in the flamelet concept [3].

Assuming a one-dimensional behaviour of the flame, "flamelet equations" governing the thermodynamic properties in the direction normal to the flame front can be derived from energy and species transport equations and applying a coordinate transformation. In these equations, temperature and species mass fractions are functions of the conserved scalar $\zeta$ (mixture fraction). In addition, the parameter which takes into account the flow field into the flamelet structure is the scalar dissipation rate. This parameter measures the degree of departure from the equilibrium state, taking the value $\chi_{st}$ at the flame surface. It can be interpreted as the inverse of a characteristic diffusion time or as a diffusivity in the mixture fraction space. In order to incorporate heat losses in the flamelet description, an enthalpy defect parameter is introduced by using the methodology described by Carbonell *et al.* [4]. This parameter is defined as:

$$X_R = \frac{h - h_{ad}}{h_u - h_{ad}} \quad \text{(II-21)}$$

where $h_{ad}$ and $h_u$ are the adiabatic and the unburned enthalpies respectively. The flamelet library is generated by solving the governing equations of counterflow diffusion flames (physical space) at a series of specified stretch rates. The link between the physical space and the mixture fraction coordinate is given by a properly defined mixture fraction. Once the solutions of these counterflow diffusion flames are obtained in the physical space, via the OPPDIF code [136], the mixture fraction distributions are obtained by solving transport equations for the mixture fraction, as suggested by Pitsch and Peters [137]. The procedure for the generation of the flamelet library can be described as follows. First, temperature and species equations were solved in adiabatic conditions for a series of stretch rates ranging from $0.2s^{-1}$ to extinction. Secondly, for each stretch rate, the flamelet temperature and species equations were solved for several different values of the volumetric radiative source term in the flamelet energy equation and the maximum value of these imposed radiative losses was adjusted to be near quenching conditions. The full chemical kinetic scheme developed by Qin et al. [138] was used. Figure II-4 illustrates flamelet profiles for the temperature for different enthalpy defects and two dissipation rates for a propane/60% $N_2$-40% $O_2$ diffusion flame.

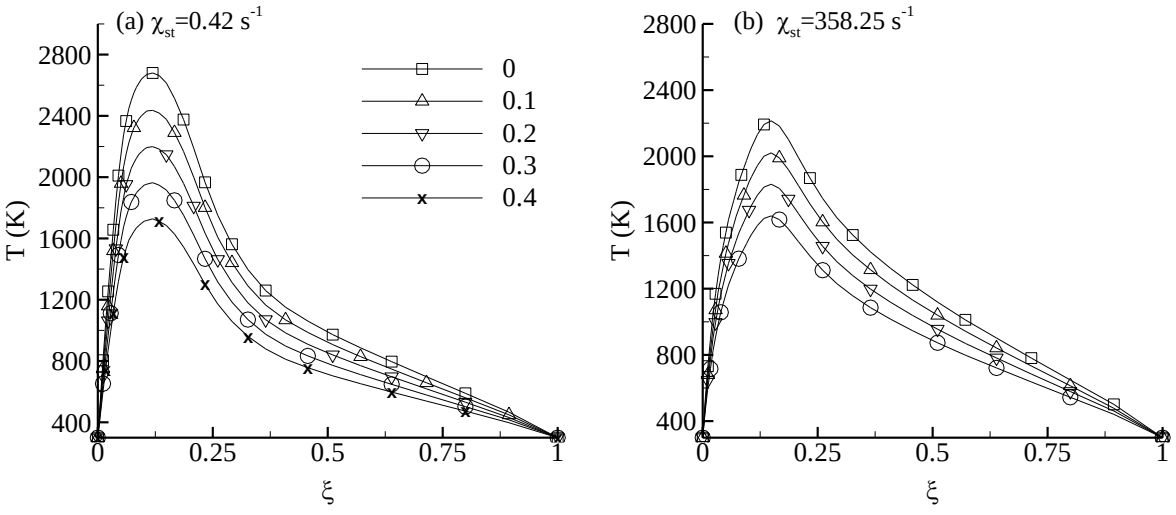


**Figure II-4. Temperature profiles as a function of the mixture fraction for different enthalpy defects and two scalar dissipation rates of a) 0.42 $s^{-1}$ and b) 358.25 $s^{-1}$.**

# II.2 Soot production model

Leung and Lindstedt [5] proposed a semi-empirical model based originally on acetylene. Later, Lindstedt completed the nucleation step by taking into account the benzene contribution [6]. This model has initially been applied to counter-flow non-premixed flames, before being used to model soot production in laminar coflow diffusion flames and turbulent diffusion flames [67,131,133,134,139–142]. This soot model has been intensively validated by simulating about thirty $C_1$-$C_3$ axisymmetric laminar normal and inverse diffusion flames and was found to provide peaks of soot volume fractions and integrated soot volume fractions for these flames within a factor of 2 of measurements [140]. It will be used to model soot production in the present study.

Soot particle dynamics are described by two moments of the Particle Size Distribution function: the soot number density, $N_s$, (defined as the number of particles per unit mass of mixture) and soot mass fraction, $Y_s$. The transport equations for these two quantities are:

$$\frac{\partial \rho Y_s}{\partial t} + \frac{\partial \rho u_i Y_s}{\partial x_i} = -\frac{\partial \rho Y_s V_i}{\partial x_i} + S_{Y_s} \tag{II-22}$$

$$\frac{\partial \rho N_s}{\partial t} + \frac{\partial \rho u_i N_s}{\partial x_i} = -\frac{\partial \rho N_s V_i}{\partial x_i} + S_{N_s} \tag{II-23}$$

where the thermophoretic velocity $\boldsymbol{V} = (V_i)_{i=1,3}$ is given by [143]:

$$V_i = -0.55 \frac{\mu}{\rho T} \frac{\partial T}{\partial x_i} \tag{II-24}$$

Source term $S_{Y_s}$ (in kg/m$^3$/s) for soot mass fraction accounts for the contribution of nucleation ($S_{n,Y}$), surface growth ($S_{sg}$) and oxidation by $O_2$ and OH ($S_o$), while the source term for soot number density $S_{N_s}$ (in particles/m$^3$/s) accounts for the contribution of nucleation ($S_{n,N}$) and coagulation ($S_c$):

$$S_{Y_s} = S_{n,Y} + S_{sg} - S_o \tag{II-25}$$

$$S_{N_s} = S_{n,N} - S_c \tag{II-26}$$

They are expressed from kinetic models described in the rest of this section.

Benzene and acetylene are assumed to be responsible for the soot nucleation:

$$C_2H_2 \rightarrow 2C_s + H_2 \tag{II-27}$$

$$C_6H_6 \rightarrow 6C_s + 3H_2 \tag{II-28}$$

for which the reaction rates are given by:

$$R_{n,C_2H_2} = k_{n,C_2H_2}(T)[C_2H_2] \quad \text{with} \quad k_{n,C_2H_2}(T) = 0.63\times10^4 \exp(-21{,}000/T) \tag{II-29}$$

$$R_{n,C_6H_6} = k_{n,C_6H_6}(T)[C_6H_6] \quad \text{with} \quad k_{n,C_6H_6}(T) = 0.75\times10^5 \exp(-21{,}100/T) \tag{II-30}$$

The total reaction rate for nucleation is then given by:

$$R_n = 2R_{n,C_2H_2} + 6R_{n,C_6H_6} \tag{II-31}$$

and $S_{n,Y}$, $S_{n,N}$ are obtained by

$$S_{n,Y} = M_c R_n \tag{II-32}$$

$$S_{n,N} = \frac{\mathcal{N}_A}{C_{min}} R_n \tag{II-33}$$

where $M_c = 12.011\ kg/kmol$ is the soot molecular weight, $\mathcal{N}_A$ is the Avogadro number and $C_{min}$ is the minimum number of carbon atoms in a soot particle, usually assumed as $C_{min} = 60$. This nucleation steps ignore the fact that soot is not exclusively composed of carbon, but it is a reasonable assumption since the mass of the hydrogen atoms present in the soot particle can be neglected as compared to that of the carbon atoms [83].

Acetylene is assumed to control the surface growth:

$$C_2H_2 + nC_s \rightarrow (n+2)C_s + H_2 \tag{II-34}$$

with a reaction rate given by:

$$R_{sg} = k_{sg}(T) f(A_s)[C_2H_2] \quad \text{with} \quad k_{sg}(T) = 0.4\times10^3 \exp(-12{,}100/T) \tag{II-35}$$

where $A_s$ is the surface area of soot per unit volume of mixture and is given by:

$$A_s = \rho(N_s\pi)^{1/3}\left(\frac{6Y_s}{\rho_s}\right)^{2/3} \tag{II-36}$$

which assumes spherical soot particles. $\rho_s$ the soot density and $f(A_s)$ is expressed as $f(A_s) = A_s$ . Surface growth source term is then expressed as:

$$S_{sg} = M_c R_{sg} \tag{II-37}$$

The rate of oxidation by $O_2$ was computed with the Nagle and Strickland-Constable (NSC) model [144], while oxidation rates for OH and O was based on the Fenimore and Jones model [145], with a collision efficiency factors of $\varphi_{OH} = 0.06 \;\; and \; \varphi_O = 0.2$. It should be pointed out that the collision factor for OH is lower than those of 0.13 and 0.14 recommended by Neoh *et al.* [146] and Xu *et al*. [147], respectively, but is consistent with the value proposed by Guo *et al.* [139] in the case of the simulation of axisymmetric laminar ethylene diffusion flames.

Finally, the coagulation is given by:

$$R_c = 2C_a\rho^2 \left(\frac{6}{\pi\rho_s}\right)^{1/6} \left(\frac{6k_B T}{M_c}\right)^{1/2} {Y_s}^{1/6} {N_s}^{11/6} \tag{II-38}$$

where $C_a$ is the agglomeration rate constant, chosen as $C_a = 9$. The coagulation source term is then obtained by:

$$S_c = -R_c \tag{II-39}$$

In the present study soot formation and oxidation rates were stored in a flamelet library in the same manner as described by Carbonell et al. [7]: the gas phase-related part of formation/oxidation terms are stored in the library as a function of $\zeta$, $\chi$ and $X_R$. During the sequence of calculations, the local values of these gas phase-related terms are extracted interactively from the flamelet library based on the local values of $\zeta$, $\chi$ and $X_R$ and, if necessary, are multiplied by the local values of the soot-related part to obtain the complete terms. Figure II-5 illustrates flamelet profiles for the nucleation rate for different enthalpy defects and two scalar dissipation for a propane/60% $N_2$-40% $O_2$ diffusion flame [148].

When using this model, it should be kept in mind that soot formation process and gaseous species reactions are uncoupled, in the sense that is the soot precursors/oxidizers are not consumed by soot formation and oxidation.

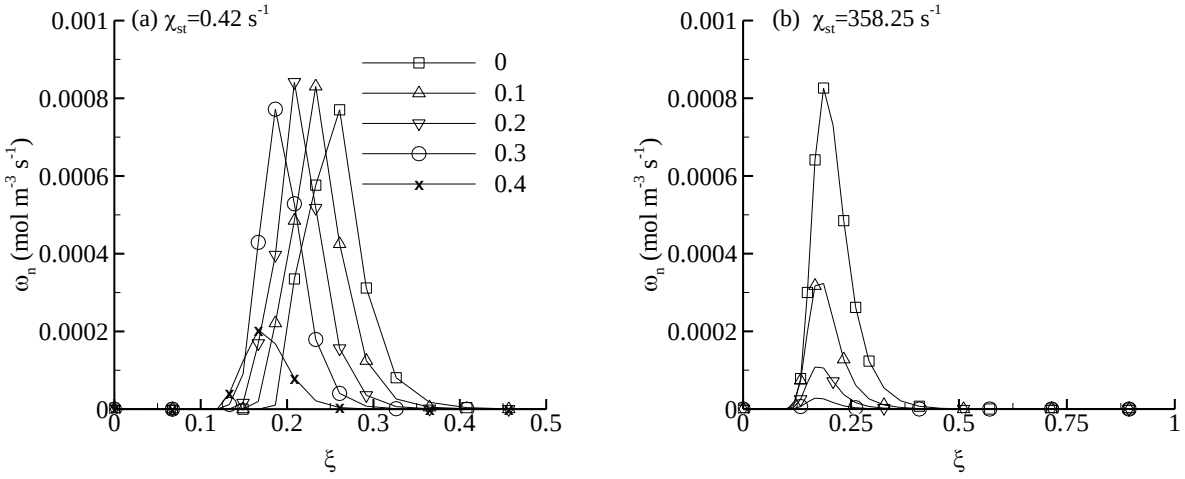


**Figure II-5. Profiles of soot nucleation rates as a function of the mixture fraction for different enthalpy defect and two scalar dissipation rate of a) 0.42 $s^{-1}$ and b) 358.25 $s^{-1}$.**

# II.3 Radiative heat transfer

The spectral coverage range considered in the present study is 200-9200 $cm^{-1}$. The radiatively participating species considered are $CO_2$, $H_2O$, and soot.

## II.3.1 Soot radiative properties

Soot particles are assumed to be spherical and small as compared with the wavelength, Rayleigh's theory then being applied to obtain the soot absorption coefficient:

$$\kappa_{s\eta} = C_\eta f_{v,s} \eta \quad \text{with} \quad C_\eta = \frac{36\pi n_s k_s}{(n_s^2 - k_s^2 + 2)^2 + 4n_s^2 k_s^2} \tag{II-40}$$

where $f_{v,s}$ is the soot volume fraction and $\eta$ the wavenumber. Values for $n_s$ and $k_s$ are obtained by using the correlations of Chang and Charalampopoulos [9]:

$$n_s = 1.877 + 0.1263\times \ln(1/\eta) + 0.0270 \times(\ln(1/\eta))^2 + 0.0417\times(\ln(1/\eta))^3 \tag{II-41}$$

$$k_s = 0.5821 + 0.1213\times \ln(1/\eta) + 0.2309 \times(\ln(1/\eta))^2 + 0.0100\times(\ln(1/\eta))^3 \tag{II-42}$$

## II.3.2 Gas radiative properties

The WBCK is used in the present study. In this section, the NBCK is also presented since the WBCK is derived from it.

### II.3.2.1 The Narrow Band Correlated-k model

A narrow-band, $\Delta\eta$, is a band narrow enough to assume that the Planck function and the radiative properties of particles are constant on its interval but broad enough to contain a large number of spectral lines. In the case of combustion modeling, the width of a NB is typically $\Delta\eta \approx 25\ cm^{-1}$ [86]. The Narrow Band Correlated-k model (NBCK) introduces two new variables, namely the distribution function $f(\boldsymbol{\phi}, k)$ and its cumulative function $g(\boldsymbol{\phi}, k)$:

$$f(\boldsymbol{\phi}, k) = \frac{1}{\Delta\eta}\int_{\Delta\eta} \delta\big(k - \kappa_\eta(\boldsymbol{\phi})\big)d\eta \tag{II-43}$$

$$g(\boldsymbol{\phi}, k) = \int_0^k f(\boldsymbol{\phi}, k')dk' \tag{II-44}$$

Each NB has its own distribution. For a given NB, all the radiative properties of the gas phase (here the mean transmittance is considered for example) can be written as:

$$\langle\tau_{\Delta\eta}\rangle = \int_0^{+\infty} \exp(-kL) f(\boldsymbol{\phi}, k)dk = \int_0^1 \exp(-k(g)L)\, dg \tag{II-45}$$

Since the g-function is monotically increasing, it can be modeled by a simple quadrature scheme; this gives an ensemble of $(g_i)_{i=1,N_g}$ values associated to the quadrature weights $w_i$. The last step consists in an inversion in order to express $k_i = k_i(g_i)$. The mean transmittance is then given by:

$$\langle\tau_{\Delta\eta}\rangle = \sum_{i=1}^{N_g} \exp(-k_i L) w_i \tag{II-46}$$

The modeling is therefore reported on a correct estimation for the g-function. Two procedures can be developed to do this task: Line by line (LBL) calculations from the definition of $f$ and $g$ (Eqs. (II-43)and (II-44)) or modeling from SNB calculations, which is presented succinctly here.

Equation (II-45) shows that $\langle\tau_{\Delta\eta}\rangle$ is the Laplace transform of the function $f(\boldsymbol{\phi},k)$ (with a fixed value for $\boldsymbol{\phi}$). Therefore, $f(\boldsymbol{\phi},k)=\mathcal{L}^{-1}\left[\langle\tau_{\Delta\eta}\rangle\right]$. Having an analytical expression for $\langle\tau_{\Delta\eta}\rangle$ from Statistical Narrow Band (SNB) models, an expression for $f(\boldsymbol{\phi},k)$ can be computed and integrated, leading to an expression for $g(\boldsymbol{\phi},k)$, depending on SNB parameters.

In order to take into account a non-homogeneous, non-isothermal medium, a special treatment must be done. In the following, $\boldsymbol{\phi}=\left(x_i,p,T,f_{v,s}\right)$ is a vector representation of the medium state and $\boldsymbol{\phi_0}$ a reference state. Two assumptions can be made in order to express radiative properties of a gas mixture on a narrow-band:

1. Correlated treatment: for every wavenumber where $\kappa_\eta(\boldsymbol{\phi}_0)=k_\eta$, then $\kappa_\eta(\boldsymbol{\phi})=k_\eta^*$ depends on both $\boldsymbol{\phi}$ and $k_\eta$: $\kappa_\eta(\boldsymbol{\phi})=k_\eta^*(\boldsymbol{\phi},k_\eta)$;

2. Scaled treatment: in addition to the correlated hypothesis, the ratio between $k_\eta$ and $k_\eta^*$ is assumed to be a constant depending only on the reference and the current mixture state:

$$\frac{k_\eta^*(\boldsymbol{\phi},k_\eta)}{k_\eta}=u(\boldsymbol{\phi},\boldsymbol{\phi}_0) \tag{II-47}$$

In this correlated/scaled case, the definition of the distribution function (Eq. (II-43)) leads to:

$$f(k)dk=f(k^*)dk^* \tag{II-48}$$

and it follows that $g(k)=g(k^*)$ and $g$ is unique for all medium state. Applying the scaled approximation, the transmittance can therefore be expressed as:

$$\langle\tau_{\Delta\eta}\rangle=\int_0^1\exp\left(-k(g)\int_0^s u(\boldsymbol{\phi}(s'),\boldsymbol{\phi}_0)ds'\right)dg \tag{II-49}$$

This expression shows that the transmittance has the same expression as in the homogeneous case (Eq. (II-45)) but with an equivalent optical length $\int_0^s u(\boldsymbol{\phi}(s'),\boldsymbol{\phi}_0)ds'$ instead of $L$. The correlated/scaled approximation is valid for soot but shows some discrepancies for gas mixture, especially for strong spatial inhomogeneities in the composition of species mixtures and/or temperature.

Treatment of gas mixture is done following the method proposed by Modest and Riazzi [105]. The cumulative function of a mixture of two gases (gas 1 and gas 2, which in the present work refer to $CO_2$ and $H_2O$) is computed on each NB by:

$$g_{mix}(k_{mix}) = \int_{g_1=0}^{1} g_2(k_{mix} - k_1) dg_1 \tag{II-50}$$

Finally, the RTE on a narrow-band can be re-written as [48]:

$$\frac{dI_g}{ds} + k^*(\boldsymbol{\phi}, g) I_g = k^*(\boldsymbol{\phi}, g) I_{b\eta}(T) \tag{II-51}$$

The number of RTE to be solved is therefore drastically reduced compared to a Line-by-line method. Total intensity is finally obtained as:

$$\langle I \rangle = \sum_{NB} \langle I_{\Delta\eta} \rangle \Delta\eta \quad \text{with} \quad \langle I_{\Delta\eta} \rangle = \int_0^1 I_g dg \tag{II-52}$$

However, while the NBCK model is a clear improvement in term of computational time compared to Line-by-Line calculations, the reordering of the gas absorption coefficient can be done over wider bands (Wide-Band Correlated-k (WBCK) model) or even over the full spectrum (Full Spectrum Correlated-k (FSCK) model). In these cases, the computational efficiency is improved without a significant loss in accuracy. The WBCK has been chosen for the present work and is detailed next section.

### II.3.2.2 Wide-Band Correlated-k model

The spectrum was divided into $N_{WB}$=14 WBs as follows: 10 WB of 500 $cm^{-1}$ between 200 and 5200 $cm^{-1}$ and 4 WB of 1000 $cm^{-1}$ between 5200 and 9200 $cm^{-1}$. On each wide band WB k-distributions were assembled from a narrow band (NB) database (see the previous paragraph), generated form high-temperature spectroscopic databases (CDSD-1000 for $CO_2$ [149] and HITEMP 2010 for $H_2O$ [150]), by using a lumping strategy [103]:

$$g_i^{WB}(k, \boldsymbol{\phi}) = \sum_{j=1}^{NB_i} \frac{\Delta\eta_{NB,j}}{\Delta\eta_{WB}} g_j^{NB}(k, \boldsymbol{\phi}) \tag{II-53}$$

where $\boldsymbol{\phi}$ is an array of state variables that affects the absorption coefficient of the gas phase, $k$ is the absorption coefficient variable at state $\boldsymbol{\phi}$, $NB_i$ is the number of NBs that

composed the i$^{th}$ WB (typically 10 with $\Delta\eta_{NB}$ of the order of 50 cm$^{-1}$). $g_i^{WB}$ and $g_j^{NB}$ are the cumulative k-distributions over the i$^{th}$ WB and the j$^{th}$ NB, respectively. Gas mixture is treated at the NB level by using the mixing scheme developed by Modest and Riazzi [105] (see Eq. (II-50)). Since the cumulative k-distribution is smooth and increases monotonically, integration over the g-space can be performed by using a Gauss quadrature scheme with few points. In the present study, the number of quadrature points, $N_G$, is taken equal to 4 [117]. The RTE, for the i$^{th}$ WB and for the k$^{th}$ quadrature point, and the total intensity are then expressed as:

$$\frac{dI_{gk}^i}{ds} + \left[k_k^i(g_k, \boldsymbol{\phi}) + \kappa_{s\eta,i}\right] I_{gk}^i = \left[k_k^i(g_k, \boldsymbol{\phi}) + \kappa_{s\eta,i}\right] I_{b\eta,i}(T) \tag{II-54}$$

$$I = \int I_\eta d\eta = \sum_{i=1}^{N_{WB}} \sum_{k=1}^{N_G} I_{gk}^i w_k \Delta\eta_{WB} \tag{II-55}$$

$I_{b\eta}$ and $\kappa_{s\eta}$ are evaluated at the center of the WB. The WB model was found to provide spectrally-integrated quantities in very good accordance with those obtained with both NB and line-by-line models [151].

## II.3.3 Turbulence-radiation interactions

Taking the Reynolds average of the RTE introduces the two parts of TRI:

$$\frac{d\langle I_\eta\rangle}{ds} + \underbrace{\langle\kappa_\eta I_\eta\rangle}_{\text{Absorption TRI}} = \underbrace{\langle\kappa_\eta I_{b\eta}\rangle}_{\text{Emission TRI}} \tag{II-56}$$

Emission TRI depends only on local conditions $\boldsymbol{\phi}$ and can therefore be modeled in an exact manner by the PDF approach:

$$\langle\kappa_\eta I_{b\eta}\rangle = \int \kappa_\eta(\boldsymbol{\psi}) I_{b\eta}(\boldsymbol{\psi}) f_\phi(\boldsymbol{\psi}) d\boldsymbol{\psi} \tag{II-57}$$

The effect of TRI on the soot emission term will be studied in details in Chapter III. Absorption TRI involves non local quantities (namely the knowledge of the instantaneous incident emission $I_\eta$ over the entire computational domain). For this term, the usual strategy is to introduce the OTFA approximation, which assumes that the local intensity

is only slightly correlated with the local absorption coefficient [49]. The absorption TRI term can therefore be written:

$$\langle \kappa_\eta I_{b\eta} \rangle = \langle \kappa_\eta \rangle \langle I_{b\eta} \rangle + \langle \kappa_\eta{}' I_{b\eta}{}' \rangle \approx \langle \kappa_\eta \rangle \langle I_{b\eta} \rangle \quad \text{(II-58)}$$

The OTFA is valid for a wide range of conditions except for large-scale sooting flames [20] and has been adopted in the present work.

# II.4 Transported composition PDF method

## II.4.1 Definition of the composition PDF

The local thermochemical properties of the reactive flows are determined by a set of scalar variables, namely the mixture fraction, $\zeta$, the enthalpy defect, $X_R = h - h_{ad}$, the scalar dissipation rate, $\chi$, the soot mass fraction, $Y_s$, and the soot number density, $N_s$. This set of composition variables is denoted by $\boldsymbol{\phi}$, a vector with a dimension of $N_\alpha$, and the corresponding one-point one-time composition joint PDF is denoted by $f_\phi = f_\phi(\boldsymbol{\psi}; \boldsymbol{x}, t)$. The scalar dissipation rate is assumed to be statistically independent of the other scalars and its PDF is modeled by a Dirac function [12–15]. Our default set of composition variables, therefore, is $\boldsymbol{\phi} = (\zeta, X_R, Y_s, N_s)$.

In a composition PDF method, all the scalars are treated as random variables. The composition PDF quantifies the probability for any scalar to reach a certain value. Therefore, the composition PDF is a function of scalars $\boldsymbol{\psi}$, spatial location $\boldsymbol{x}$ and time $t$:

$$f_\phi(\boldsymbol{\psi}; \boldsymbol{x}, t) d\boldsymbol{\psi} = Proba\{\boldsymbol{\psi} < \boldsymbol{\phi}(\boldsymbol{x}, t) < \boldsymbol{\psi} + d\boldsymbol{\psi}\} \quad \text{(II-59)}$$

The notation $(\boldsymbol{\psi}; \boldsymbol{x}, t)$ has been chosen to highlight the fact that the PDF is defined at *one-point, one-time*. Therefore, no two-point correlations can be represented by this PDF; for example, no information can be extracted for spatial or temporal derivative of the variable $\boldsymbol{\phi}$. This implies that any term involving spatial gradients needs to be modeled. One of the most important characteristic of the PDF for a composition vector $\boldsymbol{\phi}$ is the fact that the ensemble average (i.e. conventional average) of any $\boldsymbol{\phi}$-dependent physical property $Q(\boldsymbol{\phi})$ of the flow can be expressed from the PDF as [12–14]:

$$\langle Q \rangle(\boldsymbol{x}, t) = \int Q(\boldsymbol{\psi})\, f_\phi(\boldsymbol{\psi}; \boldsymbol{x}, t) d\boldsymbol{\psi} \quad \text{(II-60)}$$

Furthermore, for variable-density flows, it is interesting to use the density-weighted PDF $\widetilde{f_\phi}$, related to the mass density function $F_\phi$ and to the conventional PDF $f_\phi$ by [12,13]:

$$\widetilde{f_\phi} = \frac{\rho f_\phi}{\langle\rho\rangle} = \frac{F_\phi}{\langle\rho\rangle} \tag{II-61}$$

## II.4.2 Composition PDF transport equation

The derivation of the composition PDF transport equation can be obtained from the conservation equation of each scalar:

$$\rho \frac{D\phi_\alpha}{Dt} = \frac{\partial \rho \phi_\alpha}{\partial t} + \frac{\partial \rho u_i \phi_\alpha}{\partial x_i} = \Theta_\alpha \tag{II-62}$$

where $\phi_\alpha$ is one of the variables of $\boldsymbol{\phi}$, $\rho$ is the mixture density, $u_i$ is the flow velocity, and $\Theta_\alpha$ is the source term. The density-weighted joint composition PDF transport equation can be then written as follows [13-16] (the details of the derivation are provided in Appendix A):

$$\frac{\partial \langle\rho\rangle \widetilde{f_\phi}}{\partial t} + \frac{\partial \langle\rho\rangle \widetilde{f_\phi} \widetilde{u_\iota}}{\partial x_i} + \frac{\partial}{\partial x_i}\left[\langle\rho\rangle \widetilde{f_\phi} \langle u_i'' | \boldsymbol{\psi}\rangle\right] = \sum_\alpha \frac{\partial}{\partial \psi_\alpha}\left[\langle\rho\rangle \widetilde{f_\phi} \left\langle \frac{\Theta_\alpha}{\rho} \middle| \boldsymbol{\psi} \right\rangle\right] \tag{II-63}$$

where $\widetilde{f_\phi}$ is the density-weighted composition PDF. $\langle Q|\boldsymbol{\psi}\rangle$ is the conventional mean of $Q$, conditioned on the value of the scalar vector $\boldsymbol{\psi}$. This equation shows the dual transport of the PDF, in the physical space on the left-hand side, and in the composition space on the right-hand side.

## II.4.3 Unclosed terms treatment

### II.4.3.1 PDF transport in the physical space

Transport of the PDF in the physical space is therefore due to transport by the mean flow and turbulent diffusivity [14]. The term involving the conditional mean of the velocity fluctuation $u_i''$ represents the mesomixing term and is dealt with a gradient-diffusion model [14]:

$$\langle\rho\rangle \widetilde{f_\phi} \langle u_i'' | \boldsymbol{\psi}\rangle = -\Gamma_T \frac{\partial \widetilde{f_\phi}}{\partial x_i} \tag{II-64}$$

where $\Gamma_T = \mu_T/\sigma_T$ is a turbulent diffusion coefficient which depends on local values of the turbulent kinetic energy $k_T$ and its dissipation rate $\varepsilon$. $\sigma_T = 0.7$ is an apparent Schmidt number. Equation (II-63) then becomes:

$$\frac{\partial\langle\rho\rangle\widetilde{f_\phi}}{\partial t} + \frac{\partial\langle\rho\rangle\widetilde{f_\phi}\widetilde{u_\iota}}{\partial x_i} - \frac{\partial}{\partial x_i}\left[\Gamma_T\frac{\partial\widetilde{f_\phi}}{\partial x_i}\right] = \sum_\alpha \frac{\partial}{\partial\psi_\alpha}\left[\langle\rho\rangle\widetilde{f_\phi}\left\langle\frac{\Theta_\alpha}{\rho}\middle|\boldsymbol{\psi}\right\rangle\right] \tag{II-65}$$

## II.4.3.2 PDF transport in the scalar space

In our case, the source term $\Theta_\alpha$ for each variable is given by:

$$\Theta_\zeta = \frac{\partial}{\partial x_i}\left[\rho D_{th}\frac{\partial\zeta}{\partial x_i}\right] \tag{II-66}$$

$$\Theta_{X_R} = \frac{\partial}{\partial x_i}\left[\frac{\lambda}{C_P}\frac{\partial X_R}{\partial x_i}\right] - \dot{Q}_{rad} \tag{II-67}$$

$$\Theta_{Y_s} = -\frac{\partial}{\partial x_i}\left[\rho V_{T,i}\frac{\partial Y_s}{\partial x_i}\right] + S_{Y_s} \tag{II-68}$$

$$\Theta_{N_s} = -\frac{\partial}{\partial x_i}\left[\rho V_{T,i}\frac{\partial N_s}{\partial x_i}\right] + S_{N_s} \tag{II-69}$$

where $D_{th}$ is the thermal diffusivity, $\lambda$ is the mixture thermal conductivity, $C_p$ is the species heat capacity at constant pressure, $\dot{Q}_{rad}$ is the radiation heat source term, $\boldsymbol{V_T}$ is the thermophoretic velocity of soot particles (see Chapter I, section I.5.2.2), $\mu$ is the mixture dynamic viscosity, $T$ is the local temperature and $S_{Y_s}$ and $S_{N_s}$ are the soot transport equation source terms (see Section II.2 of Chapter II).

The development of the conditional means of the scalar source terms is given in this section. As can be seen in Eqs. (II-66) to (II-69), all source terms can be expressed as the sum of two parts:

$$\Theta_\alpha = \Theta_{\alpha,mix} + \Theta_{\alpha,prod} \tag{II-70}$$

where the mixing term $\Theta_{\alpha,mix}$ is given by:

$$\Theta_{\alpha,mix} = \frac{\partial}{\partial x_i}\left[C_\alpha\frac{\partial\phi_\alpha}{\partial x_i}\right] \tag{II-71}$$

and the production term, $\Theta_{\alpha,prod}$, corresponds to the source term. Modeling the transport of the PDF by the mixing (or *micro-mixing*) term is a difficult challenge in transported PDF method [12–14]. Several mixing models have been developed depending on their

application [12–14,152]. Here, the model chosen is the Interaction by Exchange with the Mean (IEM) model, which has been largely used in the literature because of its simple form. The effective Schmidt number for soot is very high and soot is not effectively transported by molecular species. As a consequence, the soot scalars are not mixed. All other conditional means of mixing terms are written:

$$\left\langle \frac{1}{\rho}\frac{\partial}{\partial x_i}\left[C_\alpha \frac{\partial \phi_\alpha}{\partial x_i}\right] \middle| \boldsymbol{\psi} \right\rangle = \frac{1}{2} C_\phi \frac{\varepsilon}{k_T}\left(\tilde{\phi}_\alpha - \phi_\alpha\right) \tag{II-72}$$

where $C_\phi$ is a constant taken equal to 2 [14].

The production term $\Theta_{\alpha,prod}$ is zero for the mixture fraction. For the soot terms, PDF transport by the production term is straightforward since $S_{Y_s}$ and $S_{N_s}$ depend only on the composition vector:

$$\begin{aligned} \frac{\partial}{\partial Y_s}\left[\langle\rho\rangle\widetilde{f_\phi}\left\langle \frac{S_{Y_s}}{\rho} \middle| \boldsymbol{\psi} \right\rangle\right] &= \frac{\partial}{\partial Y_s}\left[\langle\rho\rangle\widetilde{f_\phi}\frac{S_{Y_s}(\boldsymbol{\psi})}{\rho(\boldsymbol{\psi})}\right] \\ \frac{\partial}{\partial N_s}\left[\langle\rho\rangle\widetilde{f_\phi}\left\langle \frac{S_{N_s}}{\rho} \middle| \boldsymbol{\psi} \right\rangle\right] &= \frac{\partial}{\partial N_s}\left[\langle\rho\rangle\widetilde{f_\phi}\frac{S_{N_s}(\boldsymbol{\psi})}{\rho(\boldsymbol{\psi})}\right] \end{aligned} \tag{II-73}$$

As a consequence, the production/destruction rates of soot mass fraction and soot number density are closed in an exact manner.

Regarding the radiation term, its source term corresponds to the radiative loss in the flame, obtained by solving the RTE. It can be written as follow:

$$\left\langle \frac{\dot{Q}_{rad}}{\rho} \middle| \boldsymbol{\psi} \right\rangle = \left\langle \frac{1}{\rho(\boldsymbol{\psi})}\int \kappa_\eta(\boldsymbol{\psi})\mathcal{G}_\eta d\eta \middle| \boldsymbol{\psi} \right\rangle - \left\langle \frac{1}{\rho(\boldsymbol{\psi})}\int 4\pi\kappa_\eta(\boldsymbol{\psi})I_{b\eta}(\boldsymbol{\psi})d\eta \middle| \boldsymbol{\psi} \right\rangle \tag{II-74}$$

where $\mathcal{G}_\eta = \int_{4\pi} I_\eta(\vec{s})d\Omega$, the spectral incident radiation, is obtained from the solution of the RTE. Using the OTFA, the correlation between local absorption coefficient and incident radiation is neglected. Therefore, Eq. (II-74) can be written:

$$\left\langle \frac{\dot{Q}_{rad}}{\rho} \middle| \boldsymbol{\psi} \right\rangle = \frac{1}{\rho(\boldsymbol{\psi})}\int \kappa_\eta(\boldsymbol{\psi})\langle\mathcal{G}_\eta\rangle d\eta - \frac{1}{\rho(\boldsymbol{\psi})}\int 4\pi\kappa_\eta(\boldsymbol{\psi})I_{b\eta}(\boldsymbol{\psi})\, d\eta = \frac{\dot{Q}_{Rad}(\boldsymbol{\psi})}{\rho(\boldsymbol{\psi})} \tag{II-75}$$

so that:

$$\frac{\partial}{\partial X_R}\left[\langle\rho\rangle\widetilde{f_\phi}\left\langle\frac{\Theta_{X_R,prod}}{\rho}\middle|\boldsymbol{\psi}\right\rangle\right] = -\frac{\partial}{\partial X_R}\left[\langle\rho\rangle\widetilde{f_\phi}\,\frac{\dot{Q}_{Rad}(\boldsymbol{\psi})}{\rho(\boldsymbol{\psi})}\right] \tag{II-76}$$

The closed PDF transport equation is finally written:

$$\begin{aligned}\frac{\partial\langle\rho\rangle\widetilde{f_\phi}}{\partial t} + \frac{\partial\langle\rho\rangle\widetilde{f_\phi}\widetilde{u_\iota}}{\partial x_i} - \frac{\partial}{\partial x_i}\left[\Gamma_T\frac{\partial\widetilde{f_\phi}}{\partial x_i}\right] \\ = \frac{\partial}{\partial\psi_\alpha}\left[\frac{1}{2}C_{\phi,\alpha}\frac{\varepsilon}{k_T}\left(\tilde{\phi}_\alpha - \psi_\alpha\right)\right] + \frac{\partial}{\partial\psi_\alpha}\left[\langle\rho\rangle\widetilde{f_\phi}\,\frac{\Theta_\alpha(\boldsymbol{\psi})}{\rho(\boldsymbol{\psi})}\right]\end{aligned} \tag{II-77}$$

# II.5 Resolution methods

## II.5.1 Introduction

The high number of variables of the composition PDF makes usual finite volume (FV) or finite difference (FD) methods impracticable to solve the transport equation. Several methods have been proposed, including the Lagrangian Particles Monte-Carlo (LPMC) [14,153], the Direct Quadrature Method of Moments (DQMOM) [14,152,153] and the Stochastic Eulerian Fields method (SEF) [16,152–154]. A detailed comparison between these three methods was performed by Jaishree and Haworth [152], which guided the choice of the SEF in the present work. This comparison was made by considering the SANDIA flames D, E, and F. Table III-1 summarizes the strengths and the weakness of the three methods.

Table III-1 shows that the DQMOM presents the advantage to be both fast and deterministic, so that there is no statistical error to deal with. Furthermore, it is by far the computationally fastest method [153]. However, it is limited to 3 environments due to numerical instabilities [47] and exhibits the lowest accuracy of the three methods [152].

The comparative study performed in [153] revealed that the LPEM and SEF methods have similar accuracy and computational efficiency (see also Table III-1). The SEF method was mainly chosen due to its direct compatibility with Eulerian code and is presented in details in the next section. However, its most important drawbacks should be kept in mind: 1) the fact that all fields must be twice continuously differentiable; in particular, this condition limits the choice of micro-mixing models to the IEM model (see section II.4.3.2). 2) scalar boundedness is not ensured [154].

| LPMC | |
|---|---|
| Strengths | Weaknesses |
| - No limitations on mixing model<br>- Readily extended to velocity composition or velocity composition-turbulent frequency PDF<br>- Realizable compositions | - Specialized numerical algorithms and consistency considerations required<br>- Large number of particles per cell required of the order of 20 to 50; computationally expensive<br>- Spatial fields of mean quantities are not smooth |
| DQMOM | |
| Strengths | Weaknesses |
| - Compatible with Eulerian CFD codes<br>- Deterministic equations<br>- Computationally efficient | - Numerically ill-conditioned source terms<br>- Violates realizability for multi-component systems<br>- Results do not improve with increasing the number of environments<br>- Lowest accuracy of 3 methods |
| Stochastic Eulerian Fields (SEF) | |
| Strengths | Weaknesses |
| - Compatible with Eulerian CFD<br>- Numerically robust random source<br>- Spatially smooth fields of mean quantities | - Large equation set for typical values of the Number of fields; computationally expensive<br>- Random term does not guarantee scalar boundedness<br>- Limitations on mixing model |

**Table II-1. Relative strengths and weaknesses of three PDF methods (from [153])**

## II.5.2 The Stochastic Eulerian Field method

The joint composition PDF transport equation is solved using the Stochastic Eulerian Field (SEF) method based on Ito calculus, first developed by Valiño [16] for single scalar and extended to the mutli-scalar case by Hauke and Valiño [17]. In this method, PDF transport is represented by an ensemble of $N_F$ stochastic fields where each field contains values for each scalar at points throughout the whole spatial domain of the flow. All fields are required to be twice differentiable in space [16]:

$$\widetilde{f_\phi}(\boldsymbol{\psi};\boldsymbol{x},t)=\frac{1}{N_F}\sum_{n=1}^{N_F}\prod_{\alpha=1}^{N_\alpha}\delta\left(\psi_\alpha-\phi_{\alpha,n}(\boldsymbol{x},t)\right) \tag{II-78}$$

Each of these fields evolves according to a stochastic partial differential equation (SPDE) which has been derived (see Appendix B), in the Ito sense, from the joint composition PDF transport equation (Eq. (II-77)):

$$\begin{aligned} d\phi_{\alpha,n}=&-\tilde{u}_j\frac{\partial\phi_{\alpha,n}}{\partial x_j}dt+\frac{1}{\langle\rho\rangle}\frac{\partial}{\partial x_j}\left[\frac{\mu_T}{\sigma_T}\frac{\partial\phi_{\alpha,n}}{\partial x_j}\right]dt+\left[\frac{\Theta_\alpha(\boldsymbol{\phi_n})}{\rho}\right]dt\\ &-\frac{1}{2}C_\phi\frac{\varepsilon}{k_T}\left(\phi_{\alpha,n}-\tilde{\phi}_\alpha\right)dt+\left(\frac{2}{\langle\rho\rangle}\frac{\mu_T}{\sigma_T}\right)^{\frac{1}{2}}\frac{\partial\phi_{\alpha,n}}{\partial x_j}dW_{j,n}\,,\\ &n=1,\dots N_F \text{ and } \alpha=1,\dots N_\alpha \end{aligned} \tag{II-79}$$

The first three terms on the right-hand side of Eq. (II-79) correspond, respectively, to advection by the mean flow, to the effect of turbulent diffusion, and to source terms. The fourth term represents the effect of micro-mixing which causes scalar fluctuations to decay. The final term is the Wiener process that varies in time, but is independent of spatial location. Within a field the same values of $dW_{j,n}$ are used for all scalars. As Eq. (II-79) is derived to be used in the Ito sense the integrand of the Wiener term must be independent of $dW_{j,n}$.

Favre averaged values for a quantity of interest, $Q(\zeta,X_R,N_s,Y_s,\chi)=Q(\boldsymbol{\psi},\chi)$, are obtained by ensemble averaging over the fields:

$$\tilde{Q}=\iint Q(\boldsymbol{\psi},\chi)\widetilde{f_\phi}(\boldsymbol{\psi};\boldsymbol{x},t)\delta[\chi-\tilde{\chi}(\boldsymbol{x},t)]d\boldsymbol{\psi}d\chi=\frac{1}{N_F}\sum_{n=1}^{N_F}Q(\boldsymbol{\phi_n},\tilde{\chi}) \tag{II-80}$$

where $\tilde{\chi}$ is the local mean value of the scalar dissipation rate [12–15]. In general, any moment $M_r$ of order $r$ of $Q(\boldsymbol{\psi},\chi)$ is given by:

$$M_r(Q)(\boldsymbol{x},\boldsymbol{t})=\frac{1}{\boldsymbol{N}_F}\sum_{n=1}^{N_F}[Q(\boldsymbol{\phi_n}(\boldsymbol{x},t),\tilde{\chi})]^r \tag{II-81}$$

## II.5.3 Numerical procedure

A time marching technique is used until a statistically stationary state is reached. The conservation equations for momentum, turbulent kinetic energy and dissipation rate

of turbulent kinetic energy are solved in cylindrical coordinates using a finite volume method on a staggered grid. For the convective terms, the ULTRASHARP approach is applied [155], combining the third order upwind scheme QUICK with a flux limiter strategy. A second-order central difference scheme is used for diffusion terms. The pressure-velocity coupling is solved using the Iterative PISO algorithm [156]. The Ito SPDE (Eq.(II-79)) is solved using an operator splitting technique [154]:

$$d\phi_{\alpha,n} = -\tilde{u}_j \frac{\partial \phi_{\alpha,n}}{\partial x_j} dt + \frac{1}{\langle\rho\rangle} \frac{\partial}{\partial x_j} \left[ \frac{\mu_T}{\sigma_T} \frac{\partial \phi_{\alpha,n}}{\partial x_j} \right] dt + \left[ \frac{\Theta_\alpha(\boldsymbol{\phi_n})}{\rho} \right] dt \tag{II-82}$$

$$d\phi_{\alpha,n} = \left( \frac{2}{\langle\rho\rangle} \frac{\mu_T}{\sigma_T} \right)^{\frac{1}{2}} \frac{\partial \phi_{\alpha,n}}{\partial x_j} dW_{j,n} \tag{II-83}$$

$$d\phi_{\alpha,n} = -\frac{1}{2} C_\phi \frac{\varepsilon}{k_T} \left( \phi_{\alpha,n} - \tilde{\phi}_\alpha \right) dt \tag{II-84}$$

Equation (II-82) can be recast in a deterministic transport equation and is solved by using the finite volume method with the same numerical scheme as described above. The outcome from first step, $\phi_{\alpha,n}(t^*)$ is updated for the random forcing term, which constitutes the second step in the fractional step procedure. This step is solved following Garmory [154], using the Euler-Maruyama approximation:

$$\phi_{\alpha,n}(t^{**}) = \phi_{\alpha,n}(t^*) + \left( \frac{2}{\langle\rho\rangle} \frac{\mu_T}{\sigma_T} \right)^{1/2} \frac{\partial \phi_{\alpha,n}}{\partial x_j} \Delta W_{j,n} \tag{II-85}$$

where $\Delta W_{j,n} = \sqrt{\Delta t}\, \eta_{j,n}$ with $\eta_{j,n}$ a {-1,+1} dichotomic vector, independent for each spatial dimension and field. Equation (II-85) is solved for each scalar $\alpha$ and for every field $n$ at every point in space. The random jump at each time step introduced by the Wiener process can lead to unphysical field compositions (e.g., mixture fraction or soot mass fraction are not bounded between zero and one). The procedure proposed by Garmory [154] has been implemented to avoid these unphysical solutions: rather than bound the scalar after the Wiener step (which would induce bias toward values away from the limit), the maximum size of the 'jump' provided by the Wiener term is limited to the difference between the current scalar value and its upper or lower physical limit (see Fig. III-1).

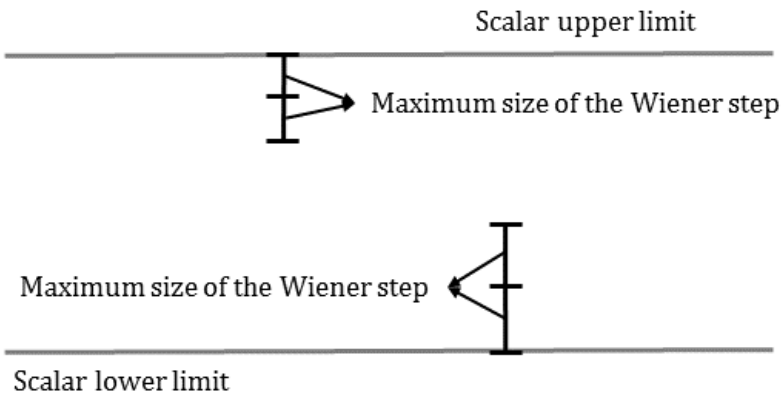


**Figure II-1. Determination of the maximum size of the Wiener step (from [154]).**

The final fractional step concerns the micro-mixing (Eq. (II-84)), and is solved analytically [154]:

$$\phi_{\alpha,n}(t^{***}) = \widetilde{\phi_\alpha} + \left(\phi_{\alpha,n}(t^{**}) - \widetilde{\phi_\alpha}\right)\exp\left(-\frac{\Delta t}{2}\frac{\varepsilon}{k_T}C_\phi\right) \qquad \text{(II-86)}$$

where $\widetilde{\phi_\alpha}$ is the local mean value of scalar $\phi_\alpha$. In any stochastic method, a key numerical parameter is the number of samples required to ensure that the results are acceptably converged (independent of the number of samples). In a preliminary study, $N_F$ has been varied to establish the number of samples that is required, showing that $N_F = 60$ is suitable. It should be pointed out that this value is consistent with that of $N_F = 40$ used by Jaishree and Haworth [152] to model Sandia flames D, E and F.

Finally, the radiative transfer equation is solved by the Finite Volume Method (FVM) using the mapping developed by Chui et al. [157] for axisymmetric configurations. In this method the dependence of radiative intensity on two space coordinates and two angles is transformed into three space coordinates and one angle. Computations are carried out using the first-order UPWIND spatial discretization scheme and an angular mesh with 12×16 control angles.

# II.6 Summary

The Favre-Averaged Navier-Stokes equations in a low Mach-number formulation are solved in axisymmetric cylindrical coordinates. The turbulence closure is modeled by

means of the $k_T - \varepsilon$ model with $C_\mu = 0.09$, $C_{\varepsilon 1} = 1.44$, $C_{\varepsilon 2}$=1.92, $C_{\varepsilon 3} = 1.44$, $\sigma_k = 1$ and $\sigma_\varepsilon = 1.3$. The EDFM model is used to obtain state relationships for density, species, and temperature as unique functions of $\zeta$, $\chi$, and $X_R$. The flamelet library is generated using a full chemical kinetic scheme developed by Qin *et al.* [138]. It consists of 70 species and 463 reactions and is optimized for the oxidation of $C_3$ hydrocarbon species. Enthalpy defect parameterization is introduced by using the methodology described by Carbonell *et al.* [4]. Soot production is modeled by the two equations semi-empirical Lindstedt model. The gas-phase related part of the source terms of the transport equations for $Y_s$ and $N_s$ are stored in the flamelet library as unique functions of $\zeta$, $\chi$ and $X_R$, following the procedure described by Carbonell *et al.* [7].

Regarding radiative transfer, the WBCK model is used for gas radiative properties whereas the Rayleigh theory is applied for soot particles. The OTFA approximation is used to treat absorption TRI whereas emission TRI, which depends only on local quantities, is treated in an exact manner with the composition PDF. The composition PDF is obtained by solving its transport equation using the Stochastic Eulerian Field method. The validation of the overall numerical model is presented next chapter.

# Chapter III Turbulent jet diffusion flames simulations

## III.1 Method validation

### III.1.1 Introduction

The models and methods presented in the previous chapter have been used to simulate twelve laboratory-scale $C_1$-$C_3$ hydrocarbon turbulent jet flames in order to validate the global method. These flames covered a wide range of Reynolds number and fuel sooting propensity. The predictions are found to be in a reasonable agreement with experimental data in terms of flame structure, soot quantities and radiative loss.

### III.1.2 Experimental data

The twelve laboratory-scale $C_1$–$C_3$ hydrocarbon turbulent jet flames simulated in this study were investigated experimentally in Refs. [18,158–164]. The main burning and radiation characteristics of each flame are provided in Table III-1. The methane-air flames [158] were studied at 1 atm and 3 atm. The ethylene-air flames were investigated by Kent and Honnery [18], Coppalle and Joyeux [159], Young [160] and Lee *et al.* [161]. The Adelaide Jet Flame 1, with a volumetric composition of 40% $C_2H_4$, 40% $H_2$, and 20% $N_2$ was investigated by Mahmoud *et al*. [162]. The propane-air flame of Nashida and Mukohara [163] was studied with air preheated to a temperature of 323 K. Four flames investigated in Ref. [164] are also considered. They involve pure propane and a methane/ethylene mixture (90/10% by volume) with an oxygen index (OI), define as the fraction of oxygen in the oxidizer, of 21% (air) and 30%. The BM-3atm, $W_{C3H8}$-OI30, and $W_{blend}$-OI30 flames allow the evaluation of the capability of the model to capture the influence of moderate increases in pressure and in oxygen index.

Table III-1 shows that a wide range of jet Reynolds numbers and sooting characteristics is covered. The fuel sooting propensity is known to be inversely proportional to the laminar smoke point height, $L_{sp}$, i.e. the height of an over-ventilated laminar flame at which soot just begins to be released from the flame tip [165] (see the ninth column of Table III-1). The tenth column of Table III-1 reports residence times, which cover a wide range. Flame and soot optical thicknesses are reported in the two last columns of Table III-1. They have a substantial impact on radiative transfer and are defined here on the basis of the flame radius, $R_f$, and the Planck mean absorption coefficient of the participating species, i.e. $H_2O$, $CO_2$ and soot:

$$\tau_{R_f} = \max_z \left[ \int_0^{R_f} \left( \kappa_{p,H_2O} + \kappa_{p,CO_2} + \kappa_{p,s} \right) dr \right] \quad \text{and} \quad \tau_{R_s} = \max_z \left[ \int_0^{R_f} \kappa_{p,s} dr \right] \qquad \text{(III-1)}$$

Table III-1 shows that gas radiation prevails in the BM-1atm, BM-3atm, AJF1, NM, $W_{C3H8}$-OI21 and $W_{blend}$ flames whereas the contribution of soot becomes significant for the other flames.

In the experiments of Brookes and Moss [158] and of Young [160] (BM-1atm, BM-3atm, and YM flames), radial temperature and soot volume fraction profiles were measured by using thermocouples and a laser extinction technique at 632 nm coupled with either an onion Peeling or a Fourier convolution procedure. Kent and Honnery [18] (KH flame) carried out extinction measurements at 632 nm and radial soot volume fractions were estimated using an Abel inversion technique. Temperature was measured by means of thermocouples. Coppalle and Joyeux [159] (CJ flame) used extinction measurements at 632 nm to determine the soot volume fraction and a two-color pyrometry technique at 632 nm and 900 nm to obtain temperature. Lee *et al.* [161] (LTS flame) used laser induced incandescence (LII) techniques and coherent anti-Stokes Raman spectroscopy (CARS) to measure soot volume fraction and temperature, respectively. Mahmaoud *et al.* [162] (Adelaide Jet Flame 1, AJF1) used also LII techniques to measure soot volume fraction. Mean and root mean square (rms) conditional temperatures based on conditional averaging of T > 800 K only were measured by using the nonlinear excitation regime two lines atomic fluorescence (NTLAF) technique. In addition, the vertical distribution of the incident heat flux at a distance of 28 cm from the flame axis was measured by using a wide-angle heat flux gauge. Nishida and Mukohara

[163] (NM flame) measured temperature with a thermocouple. The soot volume fraction and molar concentration of gaseous species were obtained by means of a sampling technique. Wang *et al.* [164] (W flames) performed laser extinction at 632 nm and computed an 'equivalent' soot volume fraction:

$$f_{v,s,eq}(z) = \frac{1}{d_n}\int_{-\infty}^{+\infty} f_{v,s}(r,z)dr = \frac{\lambda}{6\pi Im\left(\frac{m_s^2-1}{m_s^2+2}\right)}\ln\frac{I}{I_0} \qquad \text{(III-2)}$$

where $\lambda$ is the wavelength of the laser and $I/I_0$ is the measured attenuation of intensity as the beam passes through the flame. In addition, radiative heat fluxes were measured along the wall of the combustion chamber by using a wide-band radiometer. This review of the experimental techniques shows that most soot measurements were performed using laser light extinction. Even though this optical technique is not intrusive and causes no disturbance to the flame, certain assumptions must be introduced in order to retrieve the soot volume fraction from measured transmissivity, and this gives rise to significant uncertainties. According to Brookes and Moss [158], the uncertainties associated with these measurements have four principal sources, namely the measurement of the mean extinction profile, the value of the refractive index chosen, the application of the Rayleigh limit, and the assumption that the particles are spherical. They estimated that the uncertainties resulting from these four contributions are expected to be ±50%, mainly due to the uncertainties concerning the optical properties of the soot. On the other hand, the uncertainty in soot concentration measurements related to LII techniques is estimated to be about 20%, mostly due to uncertainties in the extinction and calibration process [161,162].

Most of the flames considered in the present study were used to validate soot and radiation models. Table III-2 summarizes the combustion, soot and radiation models used in these numerical works. This literature survey is limited to modelling approaches based on a Reynolds averaged Navier–Stokes (RANS) description of turbulence.

| Fuel | Name | Oxidizer | p (atm) | $d_n$ (mm) | Re (-) | $u_{fuel}$ $(m/s)$ | $T_{fuel}$ $(K)$ | $L_{sp}$ $(cm)$ | $t_{res}$ $(ms)$ | $\tau_{R_f}$ | $\tau_{R_s}$ |
|---|---|---|---|---|---|---|---|---|---|---|---|
| **$CH_4$** | BM-1atm [158] | Air | 1 | 4.07 | 5000 | 20.30 | 290 | 29.00[a] | 68 | 0.087 | 0.005 |
| | BM-3atm [158] | Air | 3 | 4.07 | 5000 | 6.77 | 290 | 9.66[b] | 78 | 0.270 | 0.052 |
| **$C_2H_4$** | KH [18] | Air | 1 | 3.00 | 14660 | 52.90 | 322 | 10.60[a] | 46 | 0.132 | 0.073 |
| | CJ [159] | Air | 1 | 4.00 | 11800 | 29.50 | 322 | 10.60[a] | 67 | 0.163 | 0.100 |
| | YM [168] | Air | 1 | 3.10 | 8600 | 24.50 | 300 | 10.60[a] | 59 | 0.122 | 0.072 |
| | LTS [161] | Air | 1 | 2.18 | 12000 | 48.70 | 295 | 10.60[a] | 42 | 0.098 | 0.052 |
| **$C_2H_4/H_2/N_2$ 40%/40%/20%** | AJF1 [162] | Air | 1 | 4.40 | 15000 | 57.00 | 294 | 16.80 | 32 | 0.085 | 0.017 |
| **$C_3H_8$** | NM [163] | Air | 1 | 2.00 | 13000 | 30.00 | 298 | 16.20[a] | 66 | 0.079 | 0.009 |
| | $W_{C3H8}$-OI21 [164] | Air | 1 | 3.00 | 14810 | 21.80 | 300 | 16.20[a] | 84 | 0.090 | 0.014 |
| | $W_{C3H8}$-OI30 [164] | 30% $O_2$ | 1 | 3.00 | 14810 | 21.80 | 300 | -[c] | 65 | 0.107 | 0.047 |
| **Blend $C_2H_4/CH_4$ 10%/90%** | $W_{blend}$-OI21[164] | Air | 1 | 3.00 | 6697 | 35.40 | 300 | 22.5[d] | 47 | 0.080 | 0.006 |
| | $W_{blend}$-OI30 [164] | 30% $O_2$ | 1 | 3.00 | 6697 | 35.40 | 300 | -[c] | 41 | 0.082 | 0.015 |

[a] taken from Ref. [166]
[b] computed by assuming that $L_{sp}$ varies inversely with pressure [165]
[c] not available
[d] computed by using $L_{sp} = 1/\left[\sum_i Y_i/L_{sp,i}\right]$ where the summation is over all the fuel species [167]

**Table III-1. Characteristics of the flames investigated. The characteristic residence time is defined as the time required to convect along the flame axis from the burner exit to the stoichiometric flame height.**

## III.1.3 Numerical setup

In the present simulations the computational domain extends to 1m the axial direction. The radial dimension was either adjusted to match the dimension of the experimental combustion chamber when necessary or extended to 25 times the diameter of the inner burner for the cases in which no confinement was experimentally applied. The maximum radial dimension was of 0.1m. In this case a non-uniform mesh of 54 (r) × 80 (z) was found to be sufficient to achieve an independent grid solution. For the AJF1 case, radiative fluxes were measured at 28 cm from the flame axis. As a consequence, the radial dimension was extended to 28 cm and a mesh with 84 (r) × 80 (z) was used. The highest grid resolution was concentrated close to the inflow boundary and in the mixing zone. The boundary conditions are summarized in Table III-3. Plug profiles have been used for velocity, turbulent kinetic energy, and dissipation of turbulent kinetic energy at the fuel stream. The estimation for $k_{T,inj}$ and $\varepsilon_{inj}$ was based on a turbulent intensity of 5% and the nozzle diameter, with the exception of the AJF1 case where injection velocity and turbulent intensity profiles were taken from the measurements.

| Reference | Flames | Combustion | Soot | Radiation Model |
|---|---|---|---|---|
| Fairweather *et al.* [141] | NM | Steady flamelet | Two-equation; N: $C_2H_2$; SG: $C_2H_2$;Ox: $O_2$ | -- |
| Bai *et al.* [38] | YM | Steady flamelet | Method of moments; N: PAH; SG: HACA; Ox: OH and $O_2$ | OTA |
| Brooke and Moss [158] | BM-1atm; BM-3atm | Steady flamelet | Two-equation; N: $C_2H_2$; SG: $C_2H_2$;Ox: $O_2$ and OH | OTA |
| Pitsch *et al.* [129] | KH | Unsteady flamelet | Method of moments; N: pyrene; SG: HACA; Ox: $O_2$ and OH | OTA |
| Kronenburg *et al.* [130] | BM-1atm; BM-3atm | CMC | Two-equation; N: $C_2H_2$; SG: $C_2H_2$;Ox: $O_2$ and OH | OTA |
| Ma *et al.* [169] | KH and YM | Steady flamelet | Two-equation; N: napthtalene; SG: $C_2H_2$;Ox: $O_2$ and OH | OTA |
| Lindstedt and Louloudi [131] | KH and CJ | Composition transported PDF | Method of moments; N: $C_2H_2$; SG: naphthalene; Ox: $O_2$, OH and O | OTA |
| Mauss *et al.* [132] | YM | Unsteady flamelet | Method of moments; N: PAH; SG: HACA; Ox: $O_2$ and OH | OTA |
| Aksit and Moss[53] | BM-1atm; BM-3atm | Transported PDF of $\zeta$, $X_R$, $Y_S$ and $N_S$ | Two-equation; N: $C_2H_2$; SG: $C_2H_2$;Ox: $O_2$ and OH | OTA |
| Yunardi *et al.* [133]; Woolley *et al.*[134] | BM-1atm, BM-3atm, KH, CJ, YM, NM | CMC | Two-equation; N: $C_2H_2/C_6H_6$; SG: $C_2H_2$;Ox: $O_2$ and OH | OTA |
| Metha *et al.* [20,66] | KH, CJ, $W_{blend}$-OI21, $W_{blend}$-OI30 | Composition PDF method | Method of moments; N: $C_2H_2$; SG: HACA; Ox: $O_2$ and OH | - PMC method coupled to the PDF<br>- Line by Line |

**Table III-2. Main numerical works concerning the flames investigated in the present study. N, SG and Ox denote nucleation, surface growth and oxidation, respectively.**

A typical simulation time is about three days on a 64-bit Intel® quad core processor (2.9 GHz, 16 Go RAM). For the CJ flame (typical of the simulations reported here), less than 1% of the CPU time is devoted to the calculation of the flow (velocity components, pressure/velocity coupling, turbulent kinetic energy, dissipation of the turbulent kinetic energy); 32% of the CPU time was spent in the resolution of the Ito SPDE for each field and each scalar ($\zeta, X_R, Y_s, N_s$), 48% was for the radiation model and 17% was relative to

the determination of the scalar dissipation rate, the interpolation in the flamelet library and the determination of the averaged values for the quantities of interest.

| | |
|---|---|
| **Solid wall** | $u_r = u_z = k_T = 0;\ \frac{\partial p}{\partial n} = 0;\ \frac{\partial \phi_{\alpha,n}}{\partial n} = 0;\quad \varepsilon_p = \frac{C_\mu^{0.75} k_{T,p}}{\kappa \Delta p}$, where $p$ is the index of the first calculation point at a distance $\Delta p$ normal to the wall and $\kappa$ is the von Karman constant |
| **Symmetry plane** | $u_z = 0;\ \frac{\partial u_r}{\partial r} = \frac{\partial p}{\partial r} = \frac{\partial k_T}{\partial r} = \frac{\partial \varepsilon}{\partial r} = \frac{\partial \phi_{\alpha,n}}{\partial r} = 0$ |
| **Free inflow ($u_n < 0$[a])** | $u_t = 0;\ \frac{\partial u_n}{\partial n} = 0;\quad P = P_\infty;\ k_T = \varepsilon = 10^{-6};\quad \phi_{\alpha,n} = \phi_\infty$ |
| **Free outflow ($u_n > 0$[a])** | $P = P_\infty;\quad \frac{\partial u_n}{\partial n} = \frac{\partial u_t}{\partial n} = \frac{\partial k_T}{\partial n} = \frac{\partial \varepsilon}{\partial n} = \frac{\partial \phi_{\alpha,n}}{\partial n} = 0$ |
| **Fuel or oxidizer stream** | $\frac{\partial P}{\partial z} = 0;\ u_r = 0;\quad u_z = 0;\quad k_T = k_{T,inj};\quad \varepsilon = \varepsilon_{inj};\quad \phi_{\alpha,n} = \phi_{inj}$ |

[a] $\boldsymbol{u_n} = \vec{\boldsymbol{u}} \cdot \vec{\boldsymbol{n}}$ where $\vec{\boldsymbol{n}}$ is the normal (pointing away from surface into the medium)

**Table III-3. Boundary conditions for the turbulent jet flames simulations**

# III.1.4 Comparisons with experimental data

In this section, a systematic comparison between simulation results and available experimental data is presented for the twelve turbulent jet diffusion flames. Numerical simulations have been also performed by using a presumed $\beta$-shape PDF for mixture fraction and Dirac function for other variables and axial profiles of soot volume fractions are shown in Figs. III-3a (BM1), III-5a (KH) and III-6b (CJ). The results are referred to as presumed PDF. The results show clearly that using transported PDF that allows taking into account the correlation between mixture fraction and soot improve considerably the predictions obtained by presumed PDF.

## III.1.4.1 Methane flames

Figure III-2 displays axial and radial distributions of the mixture fraction and temperature for the BM-1atm flame. Both predicted axial and radial mixture fraction profiles are in good agreement with the experiments. Figure III-2a shows that the increase in temperature along the centerline is generally captured quite well. The flame length is slightly over-predicted and the temperature at the furthest downstream locations is somewhat too low.

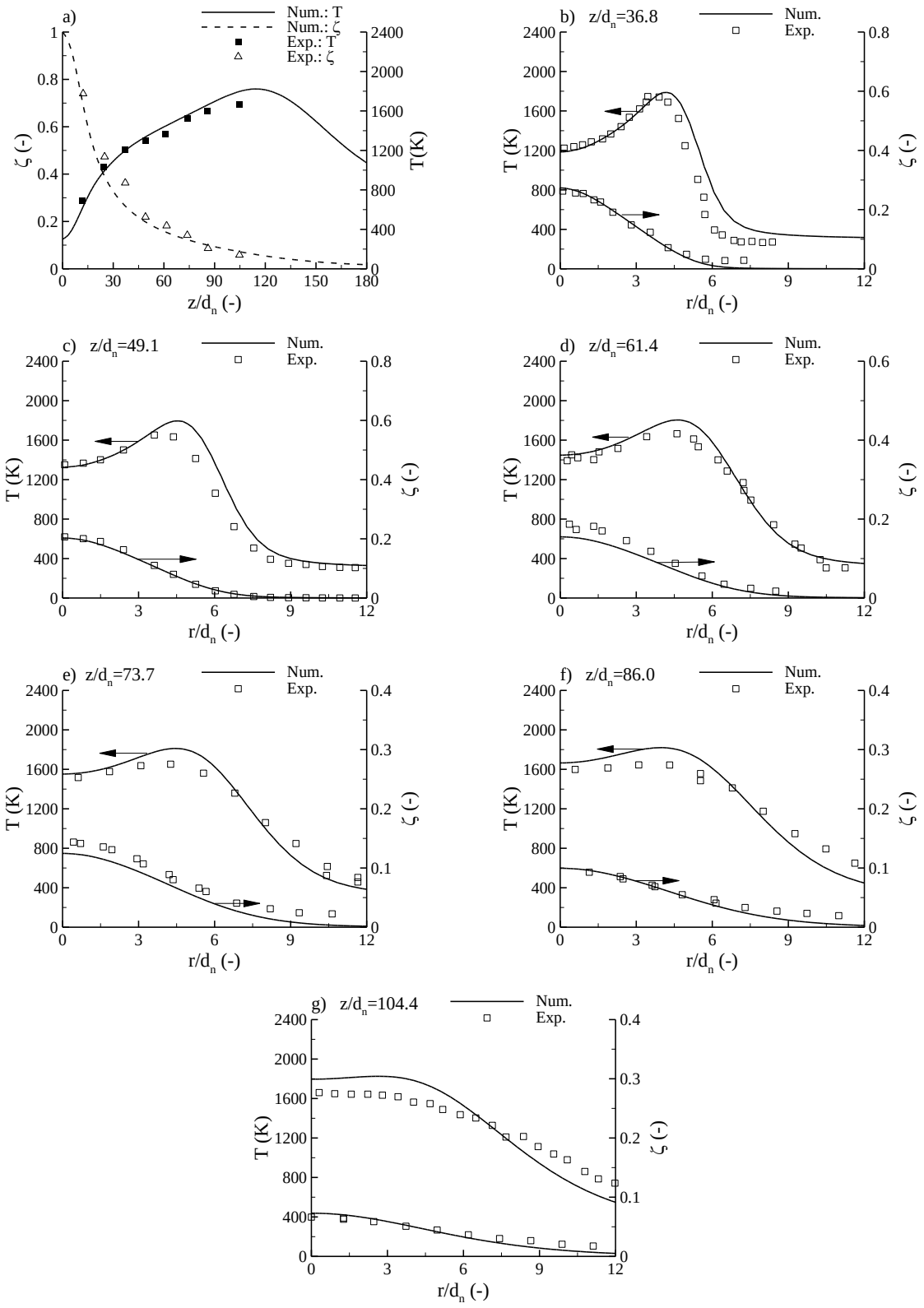


**Figure III-1. BM-1atm flame. Temperature and mixture fraction distributions: a) axial distribution, b) to g) radial distributions at different heights.**

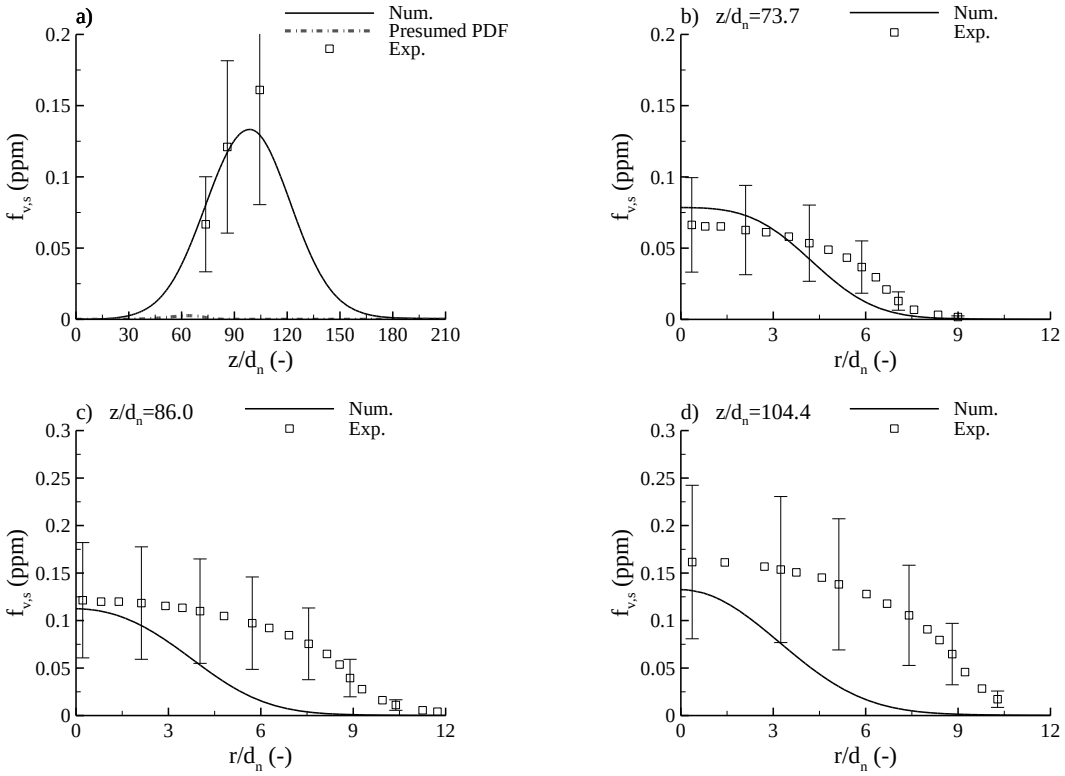


**Figure III-2. BM-1atm flame. Soot volume fraction distributions: a) axial distribution, b) to d) radial distributions at different heights.**

Radial temperatures are also on the whole well represented by the model (Figs. III-2b–g). The temperature in the fuel-rich region as well as the location of temperature peaks are well reproduced by the numerical model. Nevertheless, the magnitude of temperature peaks is over-predicted between $z/d_n = 49.1$ and $z/d_n = 73.7$ . At $z/d_n = 86$ the experimental profile is rather flat in the fuel-rich region, whereas the model exhibits a slightly more pronounced M-shaped profile. This confirms that the model over-predicts flame height. On the other hand, an examination of the temperature profiles in the fuel-lean region shows that the spreading of the flame is captured correctly by the model. Figure III-3a presents the axial profile of the soot volume fraction. Soot measurements were performed only in the soot formation region at $z/d_n = 73.7,\ 86$ and 104.4 and soot volume fraction data are not available in the oxidation region. The model predicts the axial soot volume fraction reasonably well. Experimental observations suggested that the soot was fully oxidized at $z/d_n = 147.4$ [158]. On the contrary, soot is still present at this height in the numerical simulation, suggesting that the rate of

oxidation is slightly underestimated. Radial profiles of soot volume fractions at $z/d_n = 73.7$, $z/d_n = 86$ and $z/d_n = 104.4$ are plotted in Figs. III-3b, c and d respectively. A satisfactory accordance between prediction and measurement is observed at $z/d_n = 73.7$. At higher locations the experimental profiles are significantly larger than those computed. In addition, the radial growth of the sooting region with downstream distance is not reproduced by the model. It should be mentioned that similar discrepancies were observed in previous numerical simulations of this flame [53,130,134].

An increase in pressure is known to enhance substantially both soot production, due to physical and chemical effects, and radiative heat transfer. The enhancement of radiative heat transfer results, on the one hand, from an increase in the absorption coefficient of the gaseous radiatively participating species and, on the other hand, from an increase in the soot volume fraction. Consequently, the BM-3atm flame is a suitable benchmark for assessing the ability of the numerical model to capture the influence of a moderate increase in pressure on both soot production and radiative loss. The comparison of computed and measured radial profiles of temperature at different heights along the flame, displayed in Figs. III-4a to d, reveals similar trends to those observed for the BM-1atm flame: the overall agreement is satisfactory although temperature peaks at $z/d_n = 36.8$ and $z/d_n = 49.1$ are overestimated and the computed temperature at the highest location exhibits an M-shaped profile, whereas a bell-shaped profile is observed for the measurements. Figure III-4e shows the axial evolution of the soot volume fraction. A reasonable agreement between the model and the experimental data is observed. However, the peak of the soot volume fraction is predicted slightly downstream as compared to the experiments. Consequently, the soot volume fraction is overestimated in the oxidation zone, although the soot oxidation rate seems to be consistent with the experimental data. Figures III-4f-h shows the radial distributions of the soot volume fraction at different heights. Predictions are in reasonable agreement with measurements, although the radial expansion of the soot profile is underestimated.

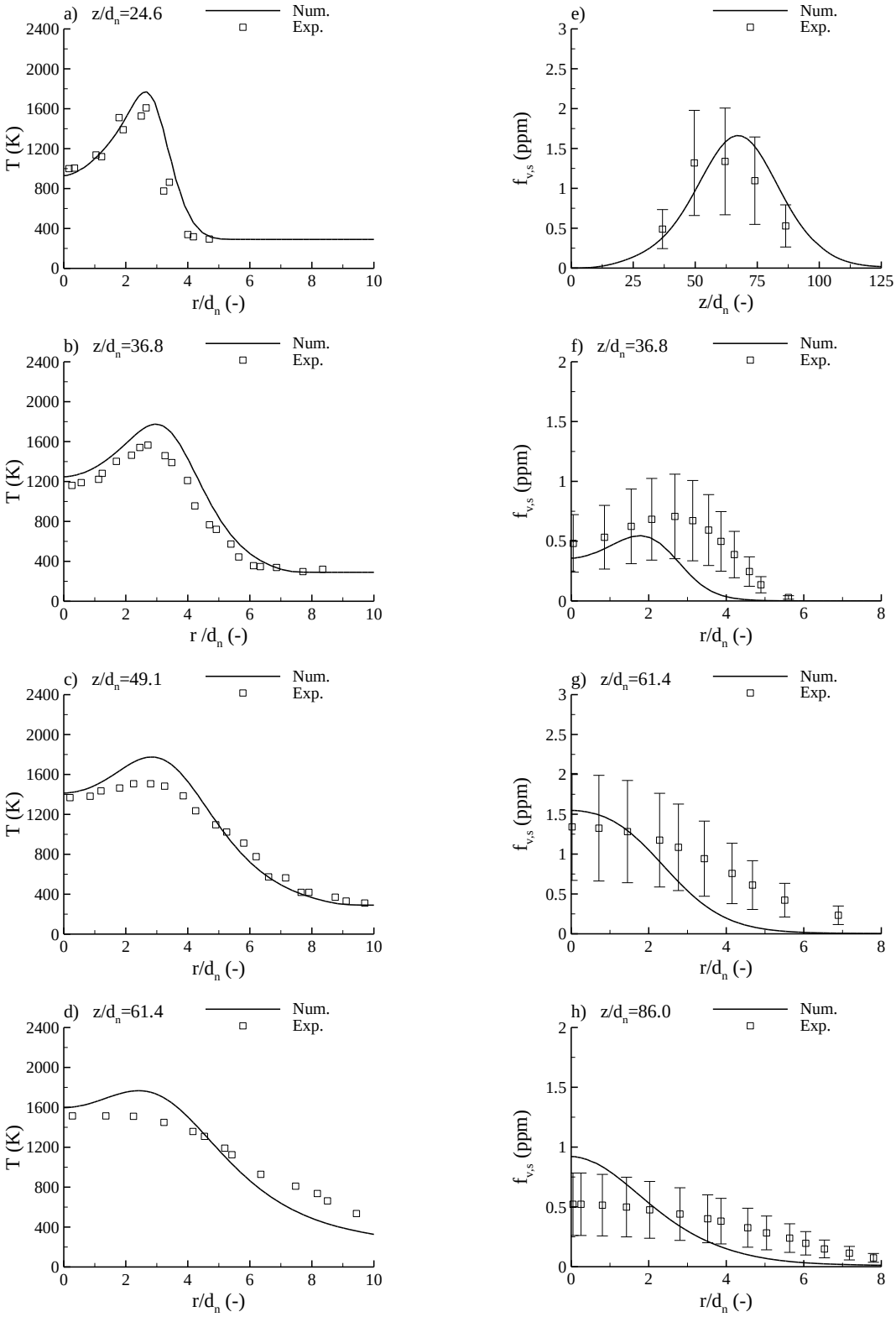


**Figure III-3. BM-3atm flame. a) to d) radial distributions of temperature at different heights, e) axial distribution of soot volume fraction, f) to h) radial distributions of soot volume fraction at different heights.**

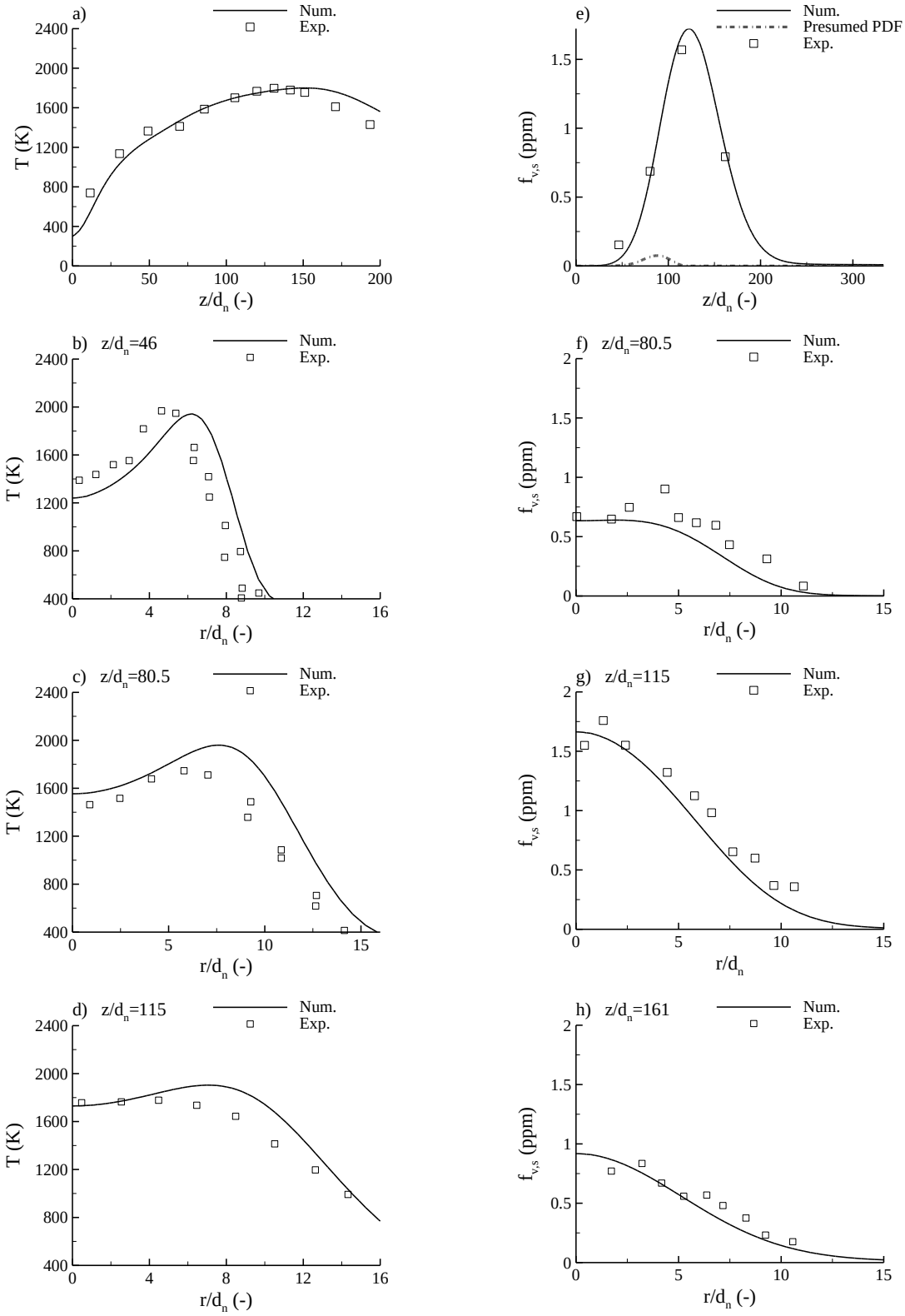


**Figure III-4. KH flame. a) axial distribution of temperature distributions, b) to d) radial distributions of temperature at different heights, e) axial distribution of soot volume fraction, f) to h) radial distributions of soot volume fraction at different heights.**

### III.1.4.2 Ethylene flames

Let us first consider the KH flame. The computed mean temperature centerline is compared with the experiments in Fig III-5a. Computed temperatures are in line with measurements up to $z/d_n = 150$ despite the fact that the temperature peak is shifted slightly downstream as compared to the experiments. The predicted peak value is 1799 K, which is in close agreement with the measured temperature peak of 1778 K. Beyond this height, however, temperature is over-predicted by up to 200 K in the furthest downstream positions. Similar discrepancies were also observed in the calculations of Ma *et al.* [169], Yunardi *et al.* [133], and Lindstedt and Louloudi [131]. Computed radial distributions of temperature at different heights are also consistent with the available experimental data (Figures III-5b to d). The discrepancies between predictions and measurements are the same as those observed for methane flames, i.e. the temperature peak at $z/d_n = 80.5$ is overestimated and the bell-shaped profile observed experimentally at $z/d_n = 115$ is not reproduced well by the model. Figures III-5e to h shows the model provides a satisfactory agreement with the experimental data in terms of both axial and radial profiles of the soot volume fraction.

Figure III-6a shows the axial evolution of mean temperature and rms values of temperature fluctuations for the CJ flame. As observed for the KH flame, simulated mean temperature is in good agreement with experiments up to the peak and is overestimated downstream. Predicted temperature fluctuation is also in line with measurements in the region located between $z/d_n = 50$ and $z/d_n = 125$. In the lower and upper parts of the flame, the measured rms values of temperature fluctuations are substantially higher than in the core of the flame. This behavior is not reproduced by the numerical model. Figure III-6b compares the axial profile of the mean soot volume fraction and rms values of soot volume fraction fluctuations to measured data. The computed mean soot volume fraction is in good agreement with the experimental data up to $z/d_n = 75$. Beyond this position soot growth is overestimated, which leads to an over-prediction of the soot peak by 60% and, in turn, to an overestimation of the soot volume fraction in the oxidation region. Fluctuations of the soot volume fraction along the axis are in satisfactory accordance with the experiments although they are underestimated up to $z/d_n = 84.5$. Figures III-6c and d shows that predicted radial profiles of the mean soot volume fraction and rms values of

soot volume fraction fluctuations compare favorably with measurements. It should be pointed out that the discrepancies observed for the CJ flame are similar to those reported by Lindstedt and Louloudi [131].

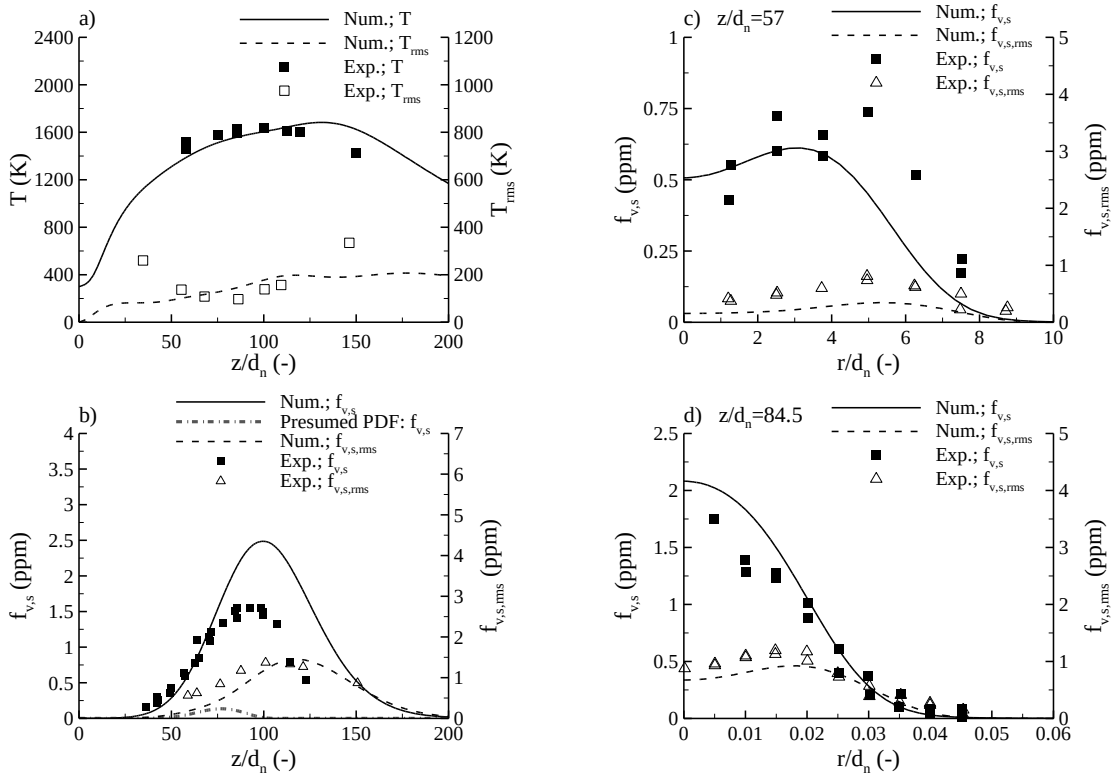


**Figure III-5. CJ flame. a) Axial distributions of mean and r.m.s values of temperature, b) axial distributions of mean and r.m.s. values of soot volume fraction, c) and d) radial distribution of mean and r.m.s. values of soot volume fraction at $z/d_n$ = 57 and $z/d_n$ = 84.5, respectively.**

Figure III-7 depicts axial and radial distributions of the mixture fraction and temperature for the YM flame. It is clear from Fig. III-7a that although the calculated centerline mean mixture fraction is in very good agreement with measurements, the predicted axial temperature is less in accordance. In particular, in the region located between 0.15m and 0.30m the temperature is over-predicted by about 200 K. Outside this range a much better agreement is found. Similar discrepancies were observed by Bai *et al.* [38], Ma *et al.* [169], Mauss *et al.* [132], and Yunardi *et al.* [133]. As mentioned by these authors, the observed discrepancies could arise from the experimental data and, more specifically, from the inherent difficulty of measuring temperature with thermocouples in the core of sooting flames. Figures III-7b to e shows accurate predictions for the radial

profiles of both the mixture fraction and temperature at different heights. The use of thermocouples could also account for the over-predictions observed in the core of the flame at $z/d_n = 51.6$ and $z/d_n = 64.5$. Figure III-8 concerns axial and radial profiles of the soot volume fraction. Along the centerline soot growth is reproduced well whereas soot oxidation is overestimated, which leads to an under-prediction of the soot volume fraction at $z/d_n = 145.1$. On the whole radial profiles are in good agreement with experimental data. However, the width the radial profiles is underestimated at $z/d_n = 112.9$. In addition, consistent with the axial prediction, the calculated soot volume fraction at $z/d_n = 145.1$ is significantly lower than in the experiments.

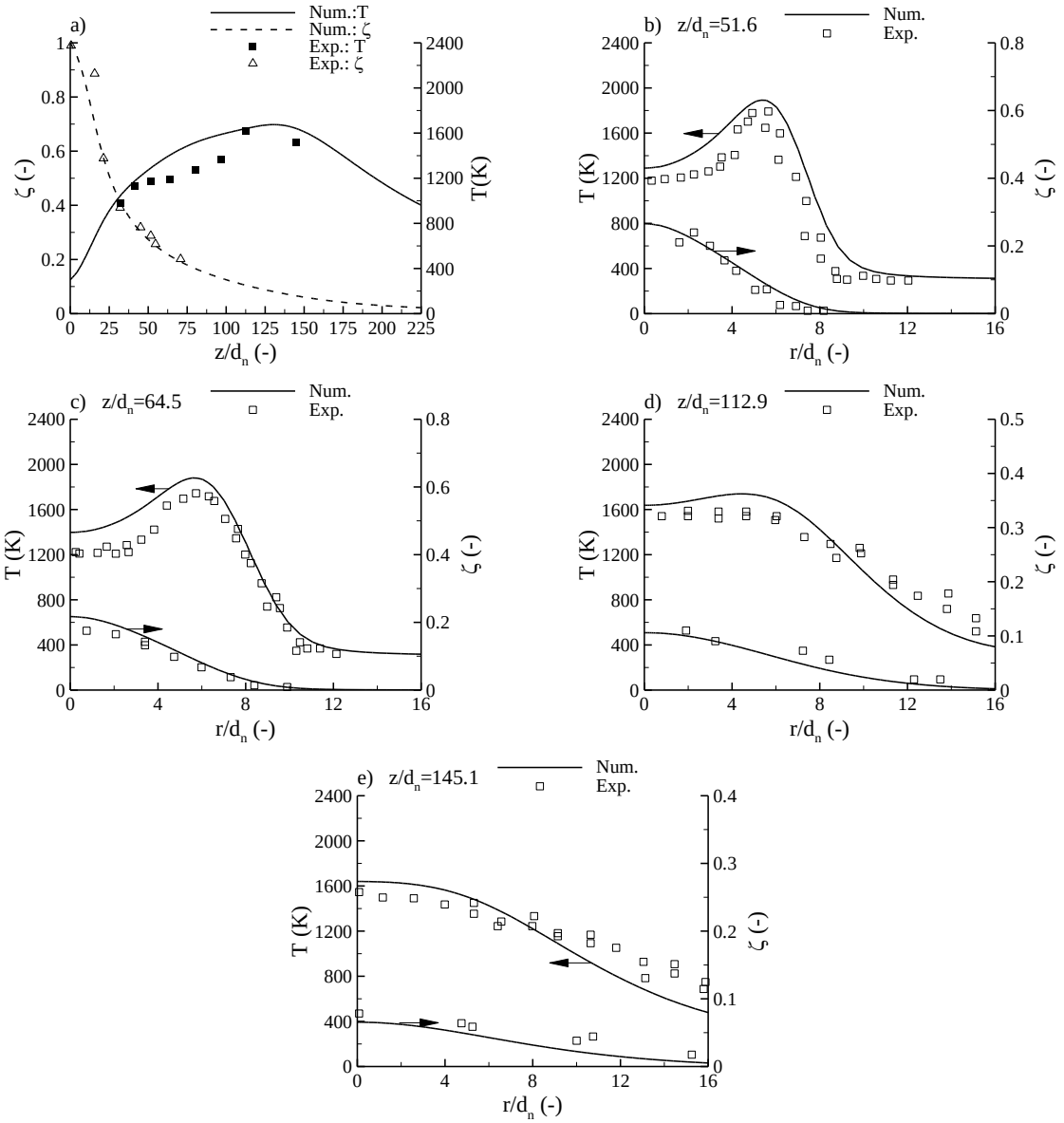


**Figure III-6. YM flame. Temperature and mixture fraction distributions: a) axial distributions, b) to e) radial distributions at different heights.**

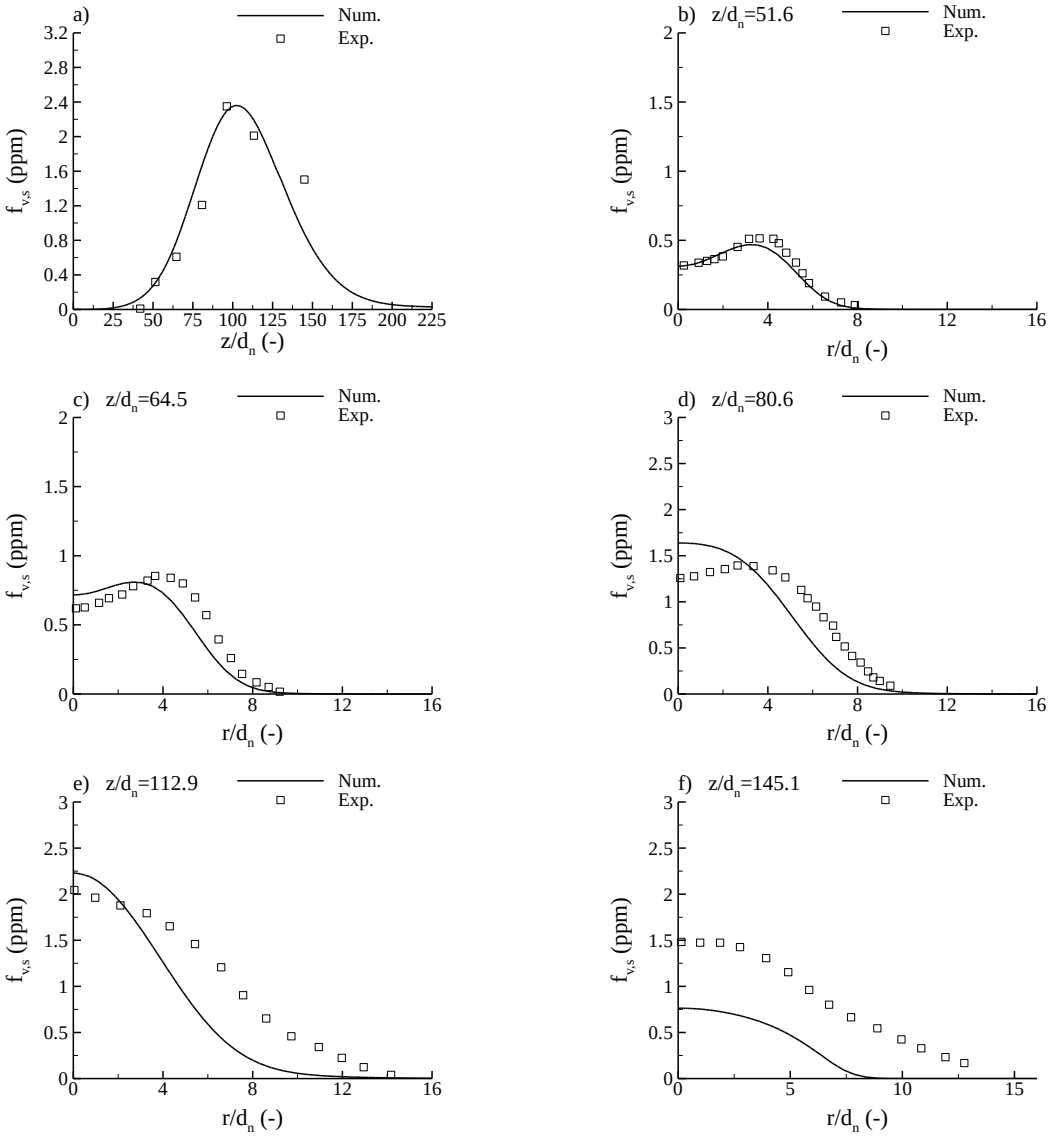


**Figure III-7. YM flame. Soot volume fraction in the YM flame: a) axial distribution, b) to f) radial distributions at different heights.**

Figure III-9 displays the radial distributions of mean temperature and rms values of temperature fluctuations at different heights for the LTS flame. Predicted mean values are in reasonable agreement with the experimental data. The mean temperature at the vicinity of the axis is underestimated. However, this underestimation tends to be reduced as the distance above the burner increases. Figures III-9a and b show also that the location of the peak of mean temperature at $z/d_n = 60$ and $z/d_n = 90$ is shifted away from the axis as compared to the experiments. Computed temperature fluctuations are also consistent with the experiments although they are on the whole underestimated and the location of the peak is also shifted away as compared to the experiments. The axial

evolutions of the mean soot volume fraction and the rms values of soot volume fraction fluctuations are shown in Fig III-10a. The overall agreement between model results and experimental data is satisfactory. The computed peak of mean soot volume fraction is within 20% of the measurements and its location is predicted slightly upstream as compared to the experiments. On the other hand, the peak of soot volume fraction fluctuations is underestimated by 25% approximately. The computed radial profiles of the mean soot volume fraction at different heights, plotted in Figs. III-10b to f, are also in line with the measurements.

Predicted peaks of the soot volume fraction in the pure ethylene flames studied here are 1.68 ppm for the LTS flame, 1.72 ppm for the KH flame, 2.35 ppm for the YM flame, and 2.48 ppm for the CJ flame. As expected, these peak values are found to increase with the residence time (see Table III-1).

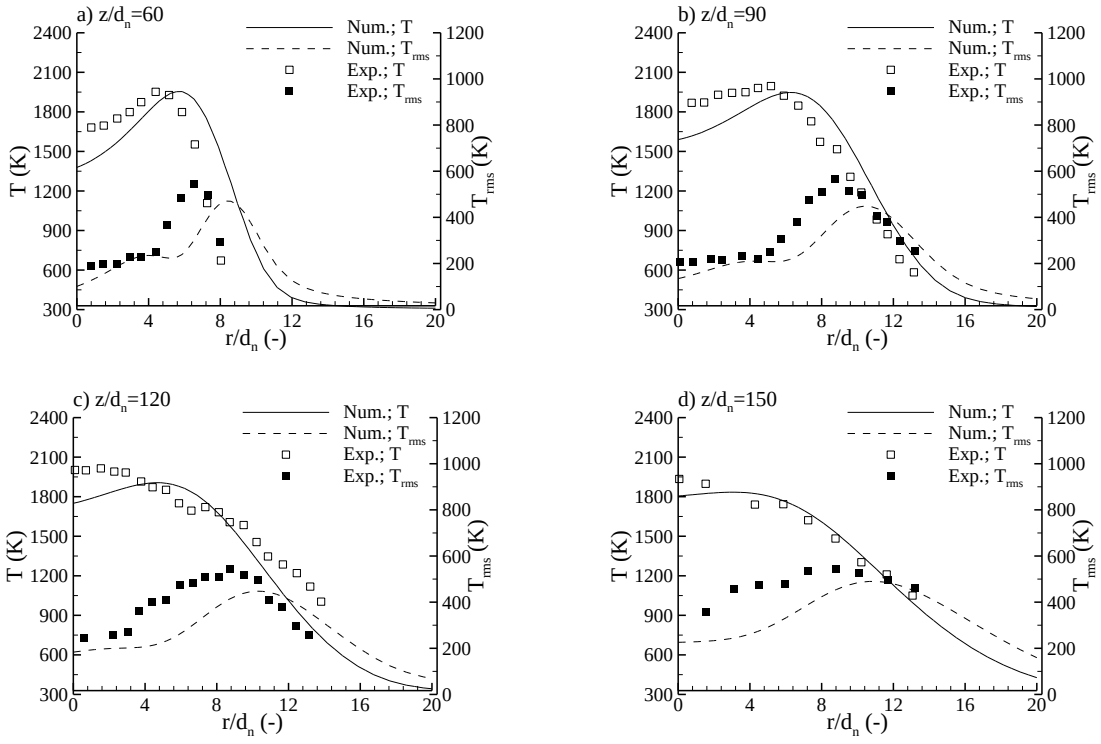


**Figure III-8. LTS flame. Radial distribution of mean and r.m.s values of temperature at different heights.**

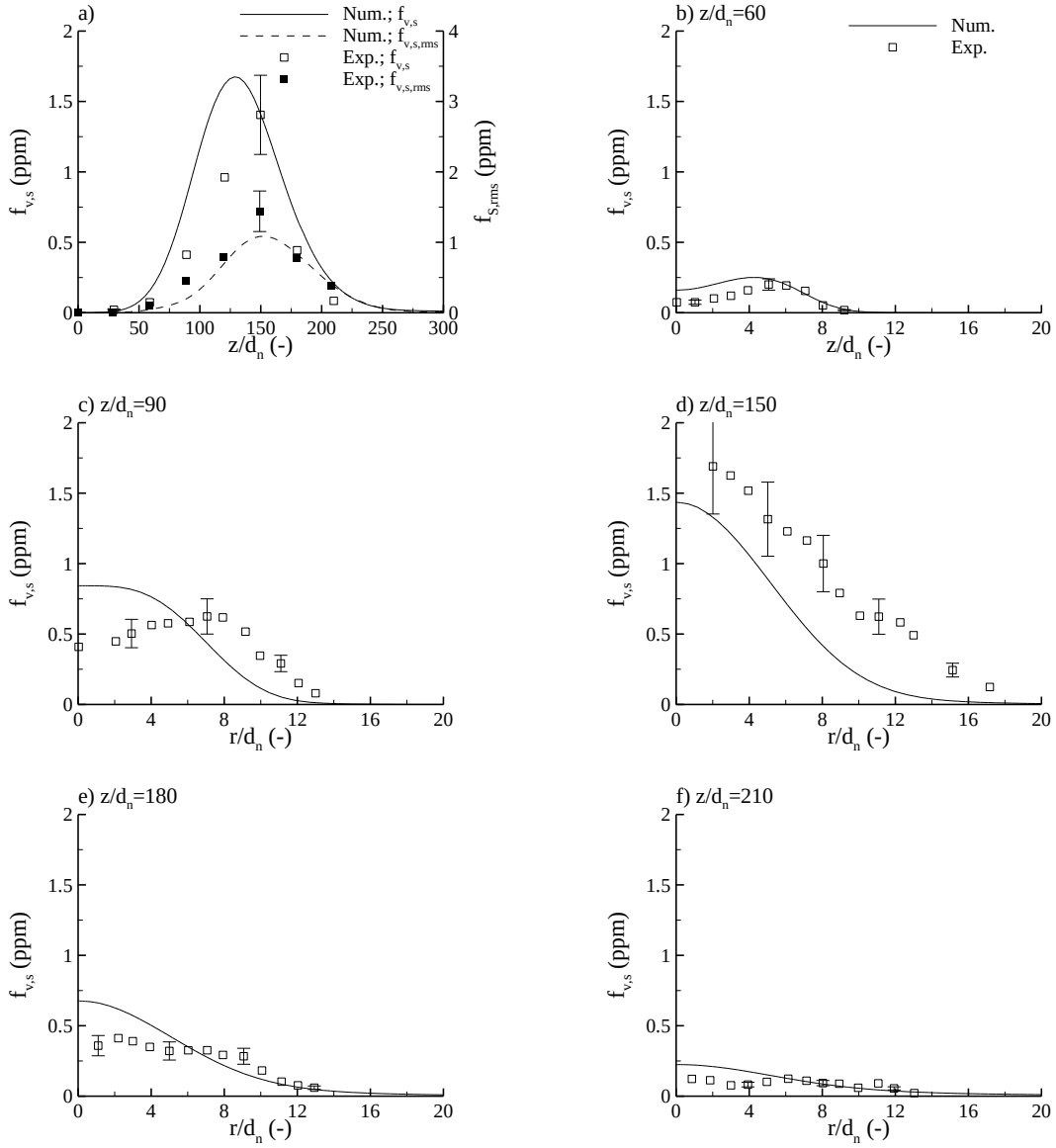


**Figure III-9. LTS flame. a) Axial evolution of mean and rms values of soot volume fraction, b) to f) radial distribution of mean soot volume fraction at different heights.**

## III.1.4.3 Ethylene/hydrogen/nitrogen flame

Computed and experimental data for the AJF1 are compared in Fig. III-11. Figures III-11a, b and c concern the radial distribution of mean and rms conditional temperatures based on conditional averaging of T > 800 K only. The uncertainty in measurements is estimated to be approximately 180 K [162]. The overall agreement between computed and measured conditional data is reasonable. Conditional mean and rms temperatures

tend to be over and underestimated, respectively and Figs. III-11a, b and c suggest that these discrepancies increase with the height above the burner. The axial evolutions of mean soot volume fraction and rms values of soot volume fraction fluctuations are plotted in Fig. III-11d. The addition of hydrogen and nitrogen to ethylene contributes to reduce the soot production. Nitrogen acts through dilution effects only whereas the addition of hydrogen is expected to reduce the soot formation through both dilution and chemical effects. In particular, Guo *et al.* [139] showed that the addition of hydrogen in ethylene tends to decrease the soot surface growth rate resulting from the HACA process (H-abstraction $C_2H_2$ addition, see chapter I, section I.4.2.1). The semi-empirical soot surface growth model considered in the present study does not take explicitly these effects into account which may explain that the rate of growth of the mean soot volume fraction is over-predicted between $z/d_n = 40$ and $z/d_n = 80$. Moreover, the location of the peak is predicted at $z/d_n = 85$ instead of $z/d_n = 103$ in the experiments. Beyond the peak the rate of decrease of the mean soot volume fraction is in line with the experiments. The axial evolution of the rms values of soot volume fraction fluctuations is in reasonable agreement with the experimental data. However, some discrepancies can be observed: the model over-predicts the experiments between $z/d_n = 40$ and $z/d_n = 100$, the peak location is predicted upstream as compared to the experiments and the peak value is over-estimated by a factor of 1.36. Figures III-11e and f show that the computed radial profiles of mean and rms soot volume fraction at $z/d_n = 100$ and $z/d_n = 135$ are consistent with the experimental data. The first height corresponds approximately to the location of the peak of mean soot volume fraction whereas the second is located in the region where soot oxidation prevails.

Figure III-11g shows the incident radiative flux as a function of the height above the burner at a distance of 28 cm from the flame axis. A satisfactory agreement is observed between numerical predictions and experimental data. The peak value is predicted within 20% of the experiments. In addition, the contribution of the soot to the radiative loss was estimated from a frozen analysis (i.e. based on the notional Eulerian fields in a statistically steady state) by computing the radiant fractions with and without taking soot radiation into account. Soot radiation was found to contribute for 17% only of the total radiative loss.

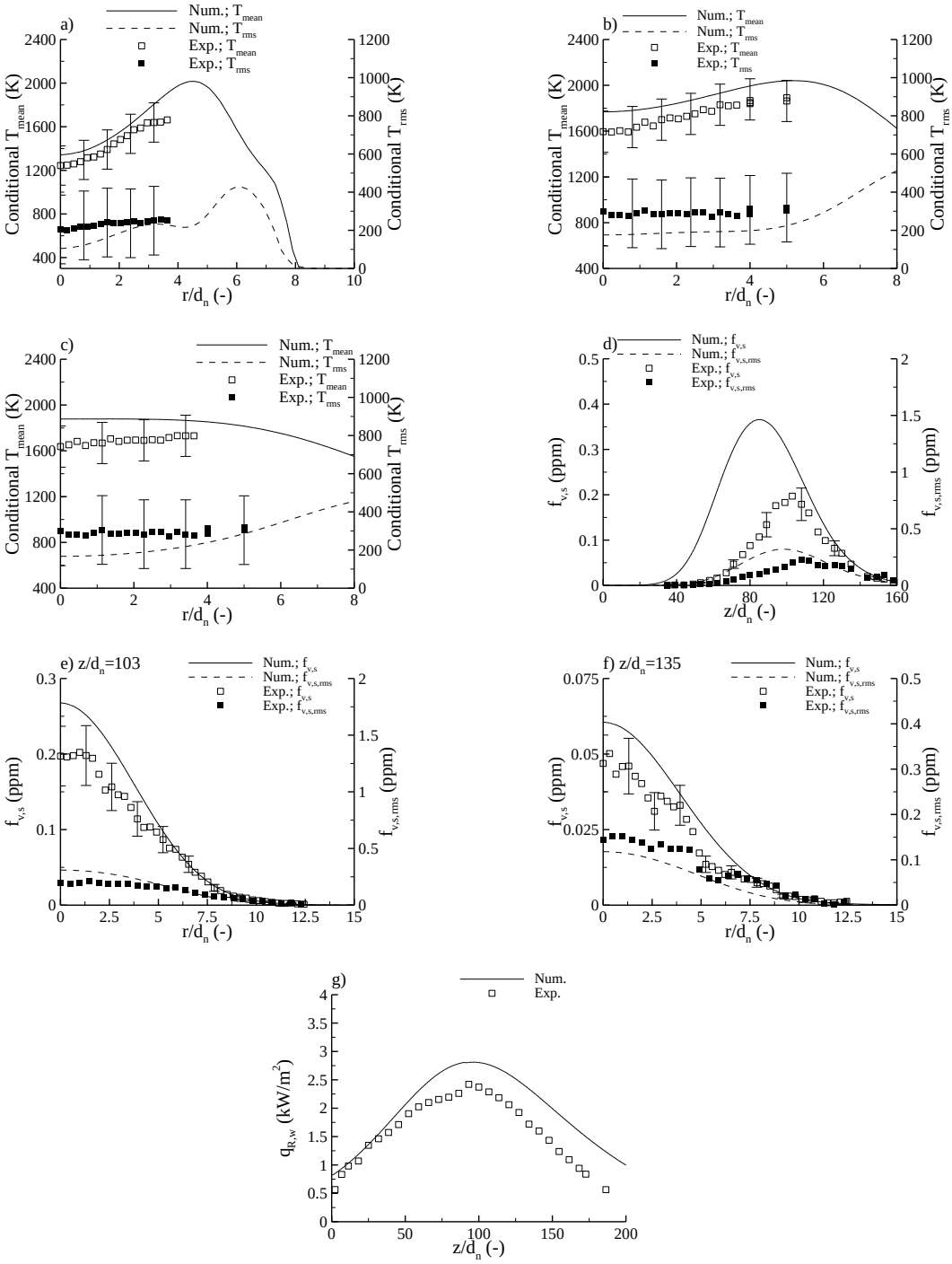


**Figure III-10. AJF1 Flame. a) to c) Radial distribution of mean and rms conditional temperatures at $z/d_n$ = 35, $z/d_n$ = 70 and $z/d_n$ = 100, respectively, d) axial evolutions of mean soot volume fraction and r.m.s. values of soot volume fraction fluctuations, e) and f) radial distribution of mean soot volume fraction and r.m.s. values of soot volume fraction fluctuations at $z/d_n$ =105 and $z/d_n$ =135, respectively, g) radiative flux at a distance of 280 mm from the flame axis as a function of the height above the burner.**

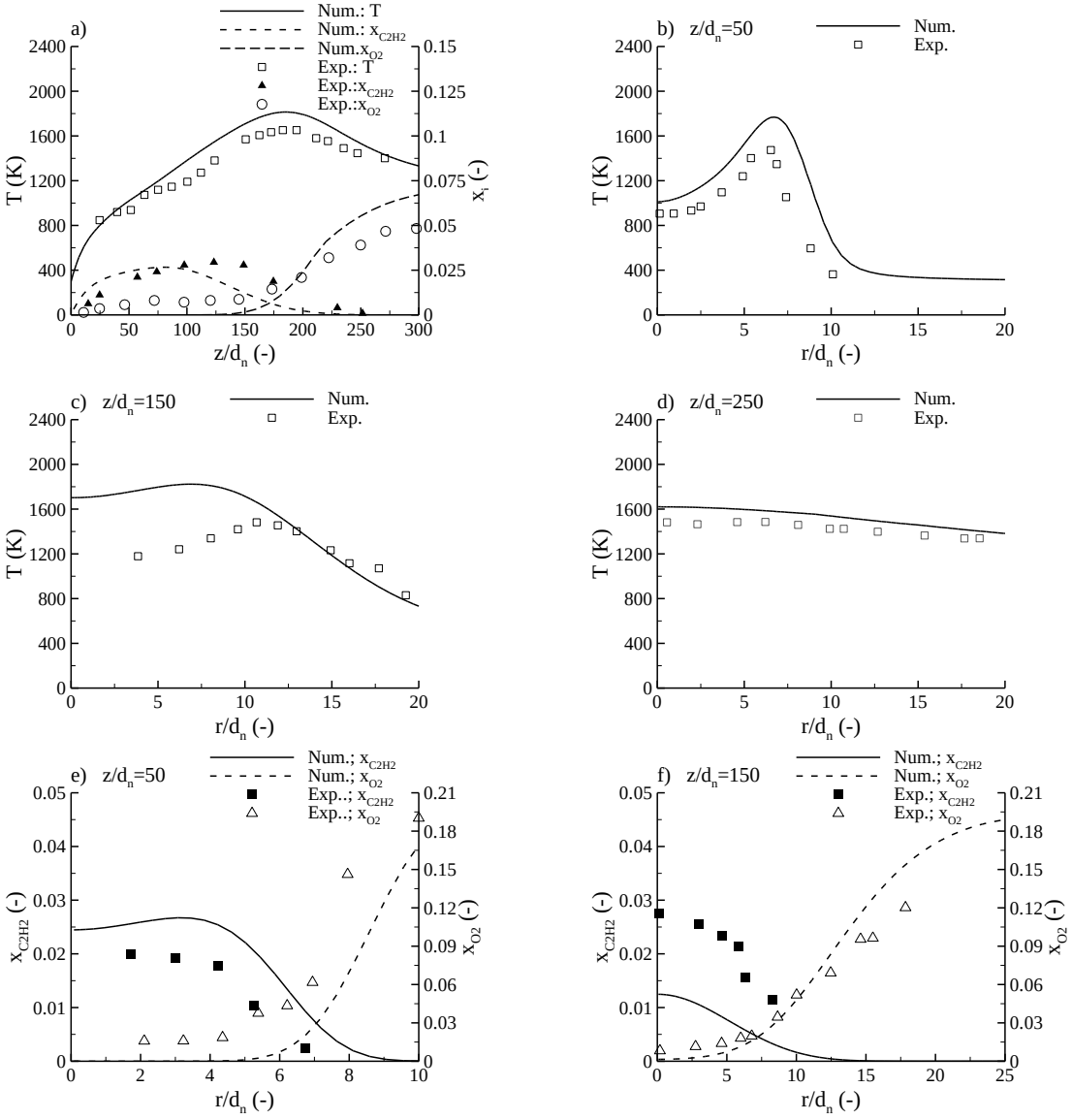


**Figure III-11. NM flame. a) axial distributions of temperature and mole fraction of C2H2 and O2, b) to d) radial distributions of temperature at different heights, and e) and f) radial distributions of mole fraction of C2H2 and O2 at $z/d_n$ = 50 and $z/d_n$ = 150, respectively.**

# III.1.4.4 Propane flames

Figures III-12a to d compare computed and measured axial and radial temperatures in the NM flame. Axial temperatures are reproduced well in the lower ($z/d_n < 50$) and upper ($z/d_n > 250$) parts of the flame. Between these two limits predictions are higher than measurements by more than 150 K. As discussed previously, the presence of soot may have affected the measurements performed with thermocouples and at least partially

account for these discrepancies. The same reason can be invoked to explain the overestimation observed in the fuel-rich region at $z/d_n = 150$ (see Figure 14c). On the other hand, radial profiles at $z/d_n = 50$ and $z/d_n = 250$ are found to be in line with measurements and the spreading of the flame is correctly captured by the model. Similar predictions were found by Fairweather *et al.* [141]. Figures III-12a, e and f show the axial and radial distributions of the mole fraction of acetylene and oxygen, these two species playing a significant role respectively in the growth and oxidation of soot. The centerline levels of acetylene are reproduced well up to $z/d_n = 125$ but are under-predicted beyond this location. The model tends to under-predict the oxygen concentration in the fuel-rich region (see Fig. III-12a) and to be in reasonable agreement with the experiments as the oxygen concentration becomes more significant. This level of agreement obtained for the computed molar concentration is comparable to that reported by Fairweather *et al.* [141]. Axial and radial distributions of the soot mass fraction are plotted in Fig. III-13. They are given per unit volume at normal temperature and pressure (NTP) in line with the experimental data. The axial evolution of the soot mass fraction is captured well by the model up to $z/d_n = 125$. Between $z/d_n = 125$ and $z/d_n = 165$, both acetylene and oxygen mole fractions are underestimated (Fig. III-12a) which is expected to lead to an under-prediction of both soot formation and soot oxidation rates. Figure III-13a shows that soot growth is higher than in the experiments in this region, leading to an over-prediction of the peak by 54%. This suggests that the discrepancies on the soot oxidation process have a greater impact than those on the soot formation process. Figure III-13a also shows that soot oxidation is significantly overestimated, with soot burn-out being predicted at $z/d_n = 275$ instead of $z/d_n = 375$ in the experiments. These discrepancies can be explained by the over-prediction of the oxygen mole fraction for a height greater than $z/d_n = 200$ (see Fig. III-12a). The radial soot volume fraction is on the whole in line with the experimental data up to $z/d_n = 150$. The width of the soot region is underestimated at $z/d_n = 200$ and, as expected from the centerline observation, the soot mass fraction is significantly under-predicted at $z/d_n = 250$ (see Figs. III-13a and b).

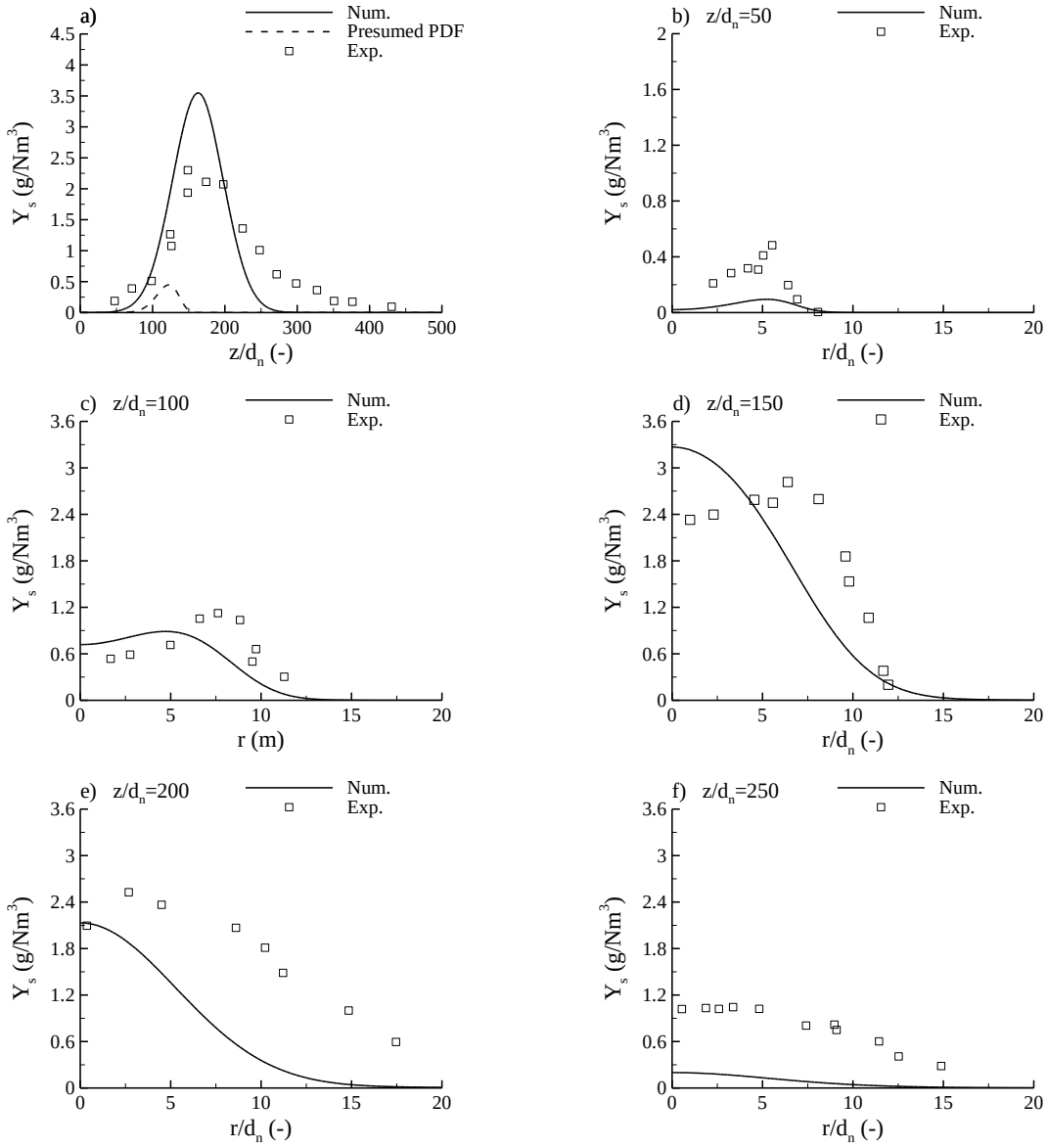


**Figure III-12. NM flame. Soot mass concentration fraction: a) axial distribution, b) to f) radial distributions at different heights.**

An increase in the OI is expected to affect soot production due to the competition between several mechanisms. On the one hand, the resulting increase in flame temperature is expected to lead to higher rates of soot nucleation and growth mechanisms, and thus to higher soot concentrations [170,171]. On the other hand, the increased presence of oxygen promotes oxidative mechanisms and reduces the flame length, which leads to a reduction in flame residence time. This tends to decrease soot concentrations [61]. Figure III-14a shows the evolution along the axis of the equivalent soot volume fraction (see Eq. (III-2)) for the propane flames investigated in [164] with an

OI of 21% and 30%. Figure III-14a a shows that as the OI increases, the location of the peak of the equivalent soot volume fraction moves toward the jet nozzle and the flame height diminishes. The magnitude of the peak increased by more than one order of magnitude. The model reproduced these trends but to a lesser degree. For the flame burning in air (OI 21), the predicted equivalent soot volume fraction is higher than the measurements. For the oxygen-enriched flame (OI 30), the soot formation is delayed as compared to the experiments. However, the soot formation rate is consistent with the experiments. The peak is predicted upstream and its magnitude is underestimated by about 30%. The equivalent soot volume fraction is under-predicted in the oxidation zone and soot burn-out occurs earlier as compared to the experiments. A careful examination of Fig. III-14a shows that the rate of decrease of the equivalent soot volume fraction in the oxidation zone is in good agreement with the experimental data. Figure III-14b displays the incident radiative fluxes along the enclosure wall. The calculation presents a rather good agreement with the experimental data. In both cases the peak location is predicted upstream as compared to the experiments. The peak value is in good accordance with the experimental data for the OI-21 flame and is underestimated by 14% in the OI-30 flame.

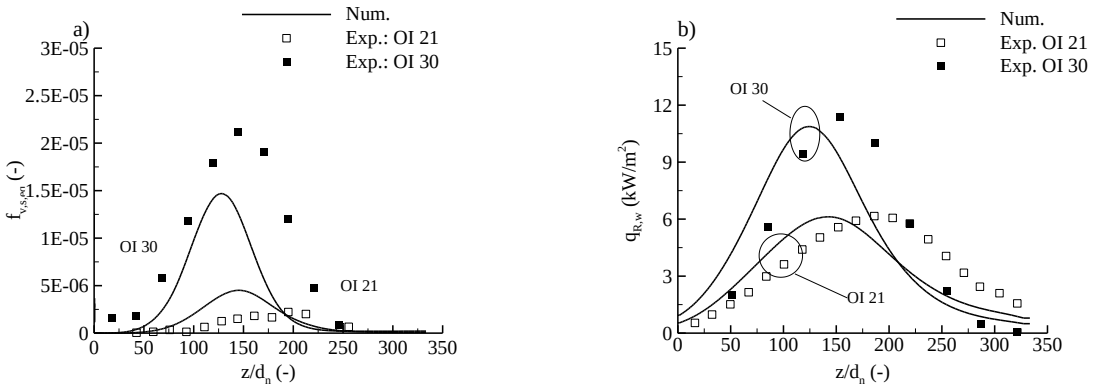


**Figure III-13. $W_{C3H8}$-OI21 and $W_{C3H8}$-OI30 flames. a) Axial evolution of the equivalent soot volume fraction and b) radiative wall heat flux.**

## III.1.4.5 Methane/ethylene blend flames

Figure III-15a displays the axial evolution of the equivalent soot volume fraction for the $W_{blend}$ flames. For these flames, Wang and co-workers reported a random-error element in the equivalent soot volume fraction of approximately $\pm 5\times10^{-7}$, and hence for small volume fractions as encountered in OI 21, the signal-to-noise ratio is too low for

reliable measurements [164]. Computed equivalent soot volume fractions exhibit the same tends as those observed for the $W_{C3H8}$ flames. The peak of the equivalent soot volume fraction is significantly raised as the oxygen index is increased from 21% to 30%. For the OI-30 flame the agreement between computed and measured equivalent soot volume fraction is satisfactory. For both OIs, Fig. III-15b shows that the location of the peaks of wall radiative flux is well predicted. Calculated peak values are higher than experimental values by 23.1% and 11.9% for the OI-21 and OI-30 flames, respectively.

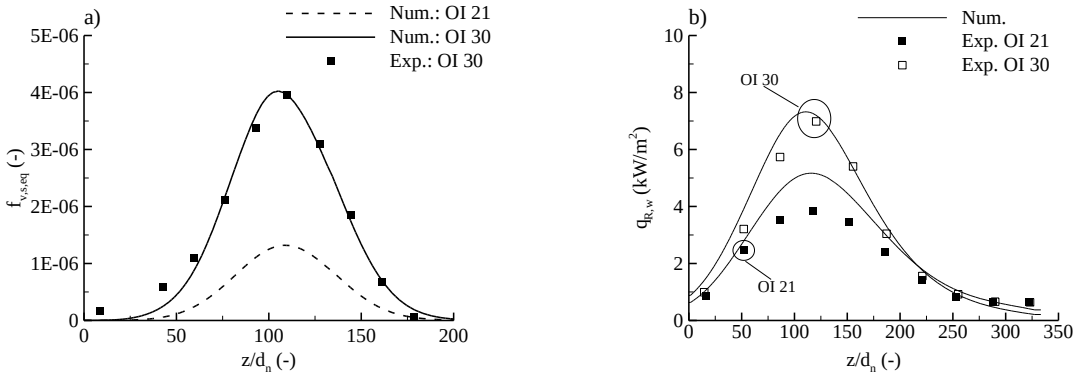


**Figure III-14. $W_{blend}$-OI21 and $W_{blend}$-OI30 flames. a) Axial evolution of the equivalent soot volume fraction and b) radiative wall heat flux.**

# III.1.5 Summary and conclusions

The peaks of the soot volume fraction, $f_{v,s,max}$ and of the wall radiative heat flux, $q_{R,w,max}$, and the radiant fraction, $\chi_R$, defined as the fraction of the heat release rate radiating away from the flame, were selected to provide an overall evaluation of the model. Computed values and the ratio of computed to experimental values are reported in Table III-4. The ideal model would have values close to unity for all 12 flames. To facilitate interpretation of Table III-4, ratios outside the range from 0.5 to 1.5 for $f_{v,s,max}$ and from 0.8 to 1.2 for $\dot{q}_{R,w,max}$ and $\chi_R$ have been shaded. The limits for $f_{v,s,max}$ are expected to correspond to the experimental uncertainties encountered in laser light extinction techniques (see section III.1.2). Most of the predicted peaks of soot volume fractions are either within or close to these limits. More generally, predicted soot volume fractions are on the whole within a factor of 2 of the measurements. This factor is in line with the accuracy of the present soot model established over a significant amount of laminar and turbulent flames burning in air or in under- or over-oxygenated conditions with an OI ranging between 17% and 35% [6,130,131,133,134,142]. Results summarized

in Table III-4 show that the peaks of the radiative wall flux and the radiant fractions are on the whole within a factor 1.2 of the measurements. In particular, the enhancement of the radiative wall flux and radiative loss with moderate increases in pressure and the OI is reproduced well by the numerical model.

Finally, the following conclusions can be drawn:

1. A reasonable agreement between predictions and experimental measurements was obtained in terms of the means and fluctuations of temperature and the soot volume fraction, radiant fractions and wall radiative fluxes. In particular, the soot volume fraction and radiative outputs were, on the whole, predicted respectively within a factor of two and within 20% of the experiments. This is a clear improvement compared to what was obtained with a presumed PDF method using the same flamelet, soot production and radiation models.

2. The model captures rather well the effects of a moderate increase in pressure or in the oxygen index on both soot production and radiative heat transfer. Further studies are required to assess its applicability in cases involving higher pressure and oxygen indexes.

| Flame | $f_{v,s,max}$ (ppm) | $R_{f_{v,s,max}}$ | $\chi_R$ (-) | $R_{\chi_R}$ | $R_{q_{R,w,max}}$ |
|---|---|---|---|---|---|
| **BM-1atm** | 0.133 | 0.82 | 0.196 | 0.98 | -[d] |
| **BM-3atm** | 1.66 | 1.05 | 0.355 | 0.89 | -[d] |
| **KH** | 1.72 | 1.10 | -[d] | -[d] | -[d] |
| **CJ** | 2.48 | 1.60 | -[d] | -[d] | -[d] |
| **YM** | 2.35 | 1.00 | -[d] | -[d] | -[d] |
| **LTS** | 1.68 | 1.16 | -[d] | -[d] | -[d] |
| **AJF1** | 0.36 | 1.78 | 0.125 | 1.19 | 1.16 |
| **NM** | 3.55[a] | 1.55[b] | -[d] | -[d] | -[d] |
| **$W_{C3H8}$-OI21** | 4.51[c] | 2.03 | 0.154 | 0.96 | 0.99 |
| **$W_{C3H8}$-OI30** | 14.68[c] | 0.70 | 0.223 | 1.08 | 0.86 |
| **$W_{blend}$-OI21** | 1.31[c] | -[d] | 0.171 | 0.77 | 1.23 |
| **$W_{blend}$-OI30** | 4.02[c] | 1.02 | 0.229 | 1.16 | 1.09 |

[a] $Y_{s,max}$ in g/Nm$^3$
[b] $R_{Y_s,\max}$
[c] peak of equivalent soot volume fraction
[d] experimental data not available.

**Table III-4. Comparison between predicted and measured values of $f_{v,s,max}$, $q_{R,w,max}$ and $\chi_R$. $R_{fv,s,max}$, $R_{qR,w,max}$ and $R_{\chi R}$ represents the ratio of computed to measured values.**

# III.2 Effect of approximate radiation models

## III.2.1 Introduction

The resolution of the spectral RTE is computationally expensive and, in our case, is the most expensive part of the numerical simulations (48% of the total CPU time). Therefore, simpler models such as the OTA and grey radiative properties are often used in order to reduce computational time (see Table III-2). In order to evaluate the ensuing errors, calculations were made using these two approximate radiative models for each flame presented in section III.1. The first model disregards reabsorption (OTA) whereas the second assumes that the radiatively participating species (combustion gases and soot) behave as a grey medium (grey). Grey absorption coefficients are then estimated using a Planck mean absorption coefficient. Since these models treat the reabsorption term in a simplified manner, their influence on the solution is expected to be directly related to the optical thickness. Most of the flames considered in the present study have an optical thickness between 0.08 and 0.11 (see Table III-1). The BM-3atm flame exhibits the highest optical thickness (0.277) since the absorption coefficient of the gaseous radiatively participating species depends linearly on pressure. In the case of flames burning at atmospheric pressure, Table III-1 shows that the highest optical thickness is of 0.163 and is encountered for the CJ flame which exhibits the highest soot production (see Table III-4). The influence of the OTA and the grey approximation on soot production, flame structure and radiative outputs will be investigated in details for these two flames. A third flame, namely the $W_{C3H8}$-OI30, will be also studied in order to consider a flame with an optical thickness ranging between 0.08 and 0.11.

## III.2.2 Results and discussion

Figures III-16, III-17 and III-18 illustrate the influence of the OTA and the grey approximation for the BM-3atm, CJ and $W_{C3H8}$-OI30 flame, respectively. The contributions of soot to the total radiative loss were found to be 17%, 52% and 33%, respectively. The two approximate models tend to minimize reabsorption, which is expected to produce an increase in radiative loss. Table III-5 shows the radiant fractions are overestimated by about 79%, 30%, and 22% for the BM-3atm, CJ and $W_{C3H8}$-OI30 flames when the OTA is applied and by 41%, 25% and 18% when the grey approximation is considered. These

results show that the discrepancies induced by these approximations increase with the optical thickness. This enhancement in radiative loss produces a reduction in temperature which is illustrated in Figs. III-16a, III-17a and III-18a. The decrease in temperature peaks in the OTA and the grey approximation is approximately 42 K and 24 K for the BM-3atm flame, 73 K and 37 K for the CJ flame and 53K and 41 K for the $W_{C3H8}$-OI30 flame. This in turn leads to a decrease in soot growth and oxidation rates, affecting local soot production rates and, thus, the soot volume fraction (Figs. IIII-16a, III-17a and III-18a). As the OTA and the grey approximation are applied, the peak of the soot growth rate is decreased by 32% and 24% for the BM-3atm flame, 21% and 12% for the CJ flame and 14% and 8% for the $W_{C3H8}$-OI30 flame. The corresponding reductions in the soot oxidation rate are 27% and 21% for the BM-3atm flame, 27% and 14% for the CJ flame and 13% and 8% for the $W_{C3H8}$-OI30 flame. Figures III-16b, III-17b and III-18b show that these changes in soot growth and oxidation rates induce a decrease in soot production, the peak of the soot volume fraction being reduced when the OTA and grey approximation is used by 28% and 18% for the BM-3atm flame, 15% and 8% for the CJ flame and 14% and 7% for the $W_{C3H8}$-OI30 flame. Figures III-16c, III-17c and III-18c show that considering the OTA and the grey approximation tends also to reduce temperature and soot volume fraction fluctuations. In particular, the peak of rms values of soot volume fraction fluctuations is reduced when the OTA and the grey approximation are considered by about 35% and 24% for the BM-3atm flame, 21% and 10% for the CJ flame and 17% and 10% $W_{C3H8}$-OI30 flame. Figures III-16d, III-17dand III-18d display the incident heat flux as a function of the height above the burner at a given distance from the flame axis. These figures shows that, in line with the results reported for the radiant fraction in Table III-5, the radiative fluxes are enhanced as the approximate radiative models are considered. When the OTA is considered, the peak of radiative flux is overestimated as compared to the reference solution by 31% for the BM-3atm flame, 18% for the CJ flame and 16% for the$W_{C3H8}$-OI30 flame. When the grey approximation is used, these peaks are higher than the reference solution by 27% for the BM-3atm flame, 14% for the CJ flame and 15% for the$W_{C3H8}$-OI30 flame. In the case of the BM-3atm flame, the discrepancies are found to increase significantly downstream the peak of radiative flux when the approximate models are considered (see Fig. III-16d).

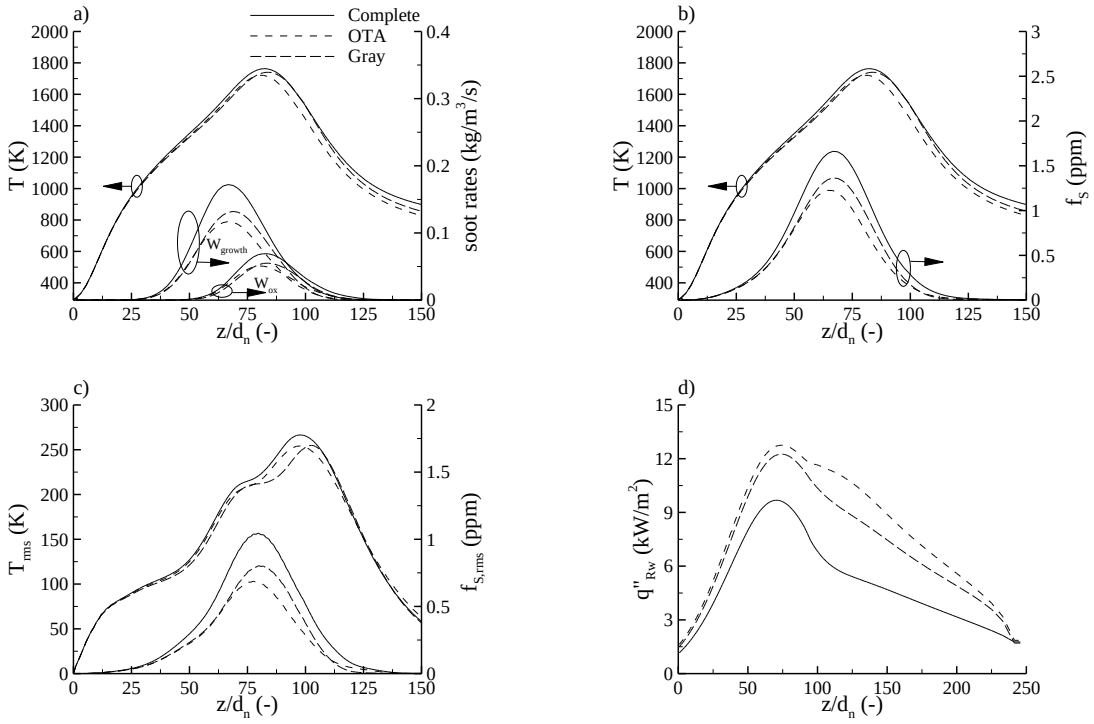


**Figure III-15. Influence of approximate radiative models in the BM-3atm flame on: a) axial temperature and soot mass growth and oxidation rates, b) axial soot volume fraction, c) axial root mean square of temperature and soot volume fractions, and d) wall heat flux as a function of $z/d_n$ at $z/d_n$ = 25.**

The previous analysis and the results summarized in Table III-5 show that the use of the OTA and the grey approximation affects significantly the radiative outputs although the grey approximation leads to improvements as compared to the OTA. As a consequence, these approximations are not recommended if accurate predictions of radiative flux are of interest. At atmospheric pressure the errors produced by using the OTA and the grey model on the peaks of temperature and soot volume fraction range between 12% and 24% and between 8% and 23%, respectively, and are within both experimental and model uncertainties. However, the study of the BM-3atm flame showed that these errors increase with pressure, suggesting that an accurate description of the self-absorption should be considered at higher pressure.

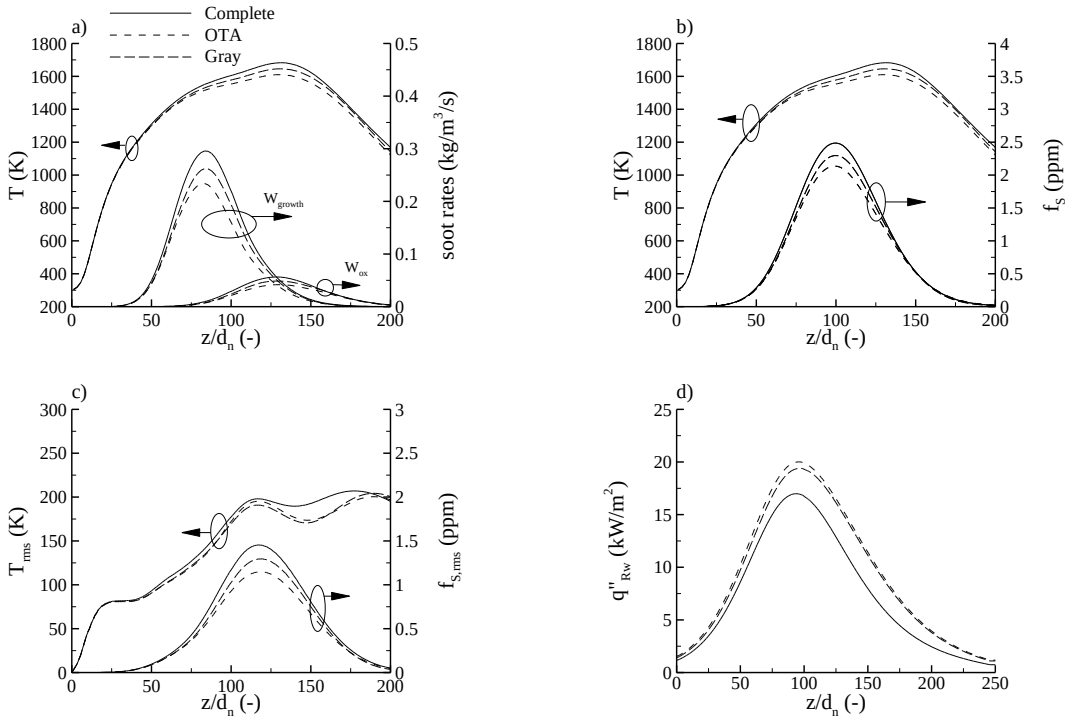


**Figure III-16. Influence of approximate radiative models in the CJ flame on: a) axial temperature and soot mass growth and oxidation rates, b) axial soot volume fraction, c) axial root mean square of temperature and soot volume fractions, and d) wall heat flux as a function of $z/d_n$ at $z/d_n$ = 18.4.**

# III.2.3 Conclusions

The influence of the OTA and the grey approximation on soot production was quantified, showing that these two approximations lead to significant discrepancies with regard to radiative loss even for flames fueled by low sooting hydrocarbons. As a consequence, these approximate treatments of the absorption term should be avoided if accurate predictions of the radiative flux are desired. At atmospheric pressure, the relative errors on the peaks of temperature and soot volume fraction are within both experimental and model uncertainty. However, the effects of these approximations on flame structure and soot production are found to increase with pressure, suggesting that they should not be applied at higher pressure.

| Flame | $\tau_{R_f}$ | OTA | | | Gray | | |
|---|---|---|---|---|---|---|---|
| | | $R_{\chi_R}$ | $\Delta T_{peak}$ (K) | $R_{f_{v,s,max}}$ | $R_{\chi_R}$ | $\Delta T_{peak}$ (K) | $R_{f_{v,s,max}}$ |
| **BM-1atm** | 0.087 | 1.44 | 41 | 0.88 | 1.17 | 58 | 0.83 |
| **BM-3atm** | 0.270 | 1.79 | 42 | 0.72 | 1.41 | 24 | 0.82 |
| **KH** | 0.132 | 1.23 | 47 | 0.88 | 1.07 | -4 | 0.77 |
| **CJ** | 0.163 | 1.30 | 73 | 0.85 | 1.25 | 37 | 0.92 |
| **YM** | 0.122 | 1.13 | 35 | 0.87 | 1.11 | 24 | 0.85 |
| **LTS** | 0.098 | 1.25 | 53 | 0.89 | 1.16 | 38 | 0.91 |
| **AJF1** | 0.085 | 1.35 | 57 | 0.82 | 1.14 | 33 | 0.83 |
| **NM** | 0.079 | 1.14 | 31 | 0.82 | 1.11 | 23 | 0.84 |
| **$W_{C3H8}$-OI21** | 0.090 | 1.21 | 37 | 0.76 | 1.14 | 32 | 0.80 |
| **$W_{C3H8}$-OI30** | 0.107 | 1.22 | 53 | 0.86 | 1.18 | 41 | 0.93 |
| **$W_{blend}$-OI21** | 0.080 | 1.19 | 18 | 0.82 | 1.12 | -3 | 0.89 |
| **$W_{blend}$-OI30** | 0.082 | 1.22 | 42 | 0.92 | 1.27 | 39 | 0.94 |

**Table III-5. Influence of approximate radiative models on the peaks of temperature and soot volume fraction along the centerline. The error on the peak of temperature is calculated as $\Delta T_{peak}=T_{peak,ref}-T_{peak,approx}$ and the relative error on the peak of soot volume fraction and on the radiant fraction is computed as $R_\phi=\phi_{approx}/\phi_{ref}$. The complete radiative model is used as reference.**

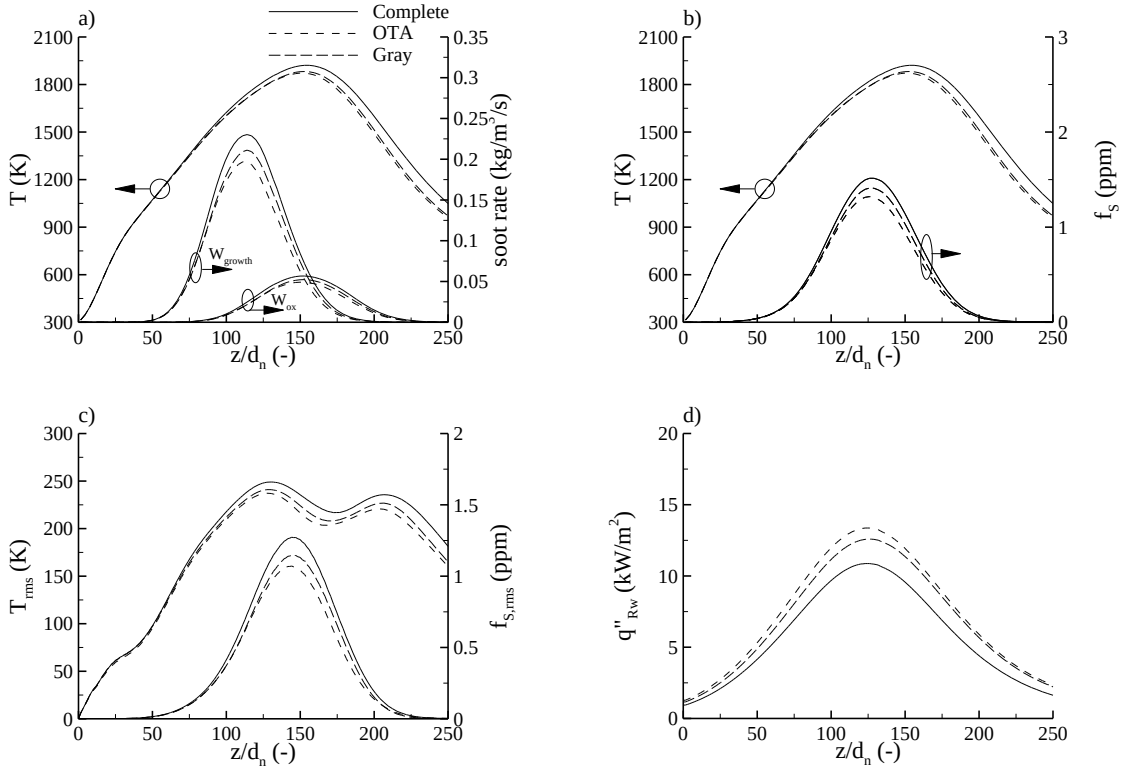


**Figure III-17. Influence of approximate radiative models in the $W_{C3H8}$-OI30 flame on: a) axial temperature and soot mass growth and oxidation rates, b) axial soot volume fraction, c) axial root mean square of temperature and soot volume fractions, and d) wall heat flux as a function of $z/d_n$ at $z/d_n$ = 25.**

# III.3 Effect of the scalar dissipation rate PDF

In the simulations presented previously, it was assumed that the scalar dissipation rate (SDR) was statistically independent of the other scalars, and that its PDF could be modeled by a Dirac function. However, another approach is to consider a log-normal distribution, for which the parameters are related to the local mean value of $\tilde{\chi}$ and its variance $\widetilde{\chi''^2}$ [19]. In this section, the physical meaning of the SDR and its statistics is reviewed and the necessity to consider a more precise statistical modeling for this parameter is analyzed.

## III.3.1 Problem presentation

The derivation of the Steady Laminar Flamelet equations, which express the one-dimensional dependence of the temperature and other gas related quantities to the mixture fraction, introduces the scalar dissipation rate (SDR) of the mixture fraction, defined as:

$$\chi = 2D\left(\frac{\partial \zeta}{\partial x_i}\right)^2 \tag{III-3}$$

where $\zeta$ is the mixture fraction and $D$ the diffusion coefficient.

This parameter has the dimension of the inverse of a time and can be interpreted as the inverse of a characteristic diffusion time of the flame [3]. It quantifies the rate to which scalar fluctuations are destroyed, i.e. the stretch of the flamelet under the influence of the turbulent flow-field, between full equilibrium ($\chi = 0$, no stretch) and quenching ($\chi > \chi_q$, where the stretching is too high for chemical reactions to be sustainable).

The SDR and its fluctuations have important effects in turbulent reacting flows. Heyl and Bockhorn [172] showed that taking into account low values of SDR in the generation of the flamelet library has an important impact on NOx formation, because reactions of NOx formation are generally much slower than fuel combustion reactions. A low SDR is equivalent to a high residence time which tends to favor these reactions. Furthermore, the process of auto-ignition tends to occur at lower values of $\chi$, while local flame extinction occurs at higher values [173]. In the flamelet model used here, local extinction (quenching) cannot be taken into account; all flamelets in the library are in quasi-steady

state. However, several more advanced models, such as unsteady flamelets [174], have been proposed in order to include $\chi > \chi_q$ values for the SDR, so that local extinction can be taken into account.

Therefore, a detailed knowledge of the SDR statistical properties is necessary to model turbulent reacting flows. Statistics of the SDR and of the conditional SDR (conditioned on mixture fraction) have been studied both experimentally and numerically [173,175] and have shown that the PDF of unconditional and conditional SDR present a lognormal behavior, except for very low or very high values of the SDR, where small but consistent deviations can be observed. These deviations are beyond the scope of the present study due to the lack of information. However, the log-normal behavior can be proposed and analyzed for the simulation of laboratory-scale turbulent diffusion jet flames, which is the subject of this section.

In the transported PDF method used in the present work, the scalar vector is composed of the mixture fraction $\zeta$, the scalar dissipation rate $\chi$, the enthalpy defect parameter $X_R$, soot number density $N_S$ and soot mass fraction $Y_s$. Furthermore, the scalar dissipation rate is assumed to be statistically independent of the other scalars [172]:

$$\tilde{f}_{\zeta,\chi,X_R,N_S,Y_S}(\zeta,\chi,X_R,N_S,Y_s) = \widetilde{f_\phi}(\boldsymbol{\psi};\boldsymbol{x},t)\widetilde{f_\chi}(\chi) \tag{III-4}$$

where $\boldsymbol{\psi} = (\zeta, X_R, N_S, Y_s)$. This assumption is justified by Poinsot and Veynante [19] by invoking the fact that mixture fraction is mostly controlled by large flow scale motions whereas $\chi$ is related to the local flame structure and is therefore governed by small scale features. In this work, the PDF $\widetilde{f_\phi}$ is obtained by the Stochastic Eulerian Fields method while a presumed shape is assumed for $\widetilde{f_\chi}$. In previous sections the SDR PDF was assumed to be a Dirac function at the local mean value $\tilde{\chi}$:

$$\widetilde{f_\chi}(\chi) = \delta(\chi - \tilde{\chi}) \tag{III-5}$$

This local mean value can be expressed as a function of the mixture fraction variance [12–15]:

$$\tilde{\chi} = C_\chi \widetilde{\zeta''^2} \frac{\varepsilon}{k_T} \tag{III-6}$$

However, it has been argued in several experimental and numerical studies that the SDR PDF is better represented by a log-normal distribution [3,19,172,173,176]:

$$\widetilde{f}_{\chi}(\chi) = \frac{1}{\sigma_{\chi}\chi\sqrt{2\pi}} \exp\left(-\frac{\left(\ln(\chi) - \mu_{\chi}\right)^2}{2{\sigma_{\chi}}^2}\right) \tag{III-7}$$

where the parameters $\mu_{\chi}$ and $\sigma_{\chi}$ are related to the mean scalar dissipation rate and its variance:

$$\mu_{\chi} = \ln(\tilde{\chi}) - \frac{{\sigma_{\chi}}^2}{2} \quad \text{and} \quad {\sigma_{\chi}}^2 = \ln\left(\frac{\widetilde{\chi''^2}}{\tilde{\chi}^2} + 1\right) \tag{III-8}$$

Usually, the term $\sigma_{\chi}$ is assumed to be a constant of order 1. A recent experimental and DNS study [173] shows that the ratio $\widetilde{\chi''^2}/\tilde{\chi}^2$ is globally constant away from the scalar source, i.e. from the injection zone, so that $\sigma_{\chi} = 1.36$. Effelsberg and Peters [177] experimentally estimated the value $\sigma_{\chi} = 1$. Heyl and Bockhorn [172] used a value of $\sqrt{2}$ and argued that the value of $\sigma_{\chi}$ should not affect results. Liew *et al.* [178] used an empirical expression linking $\sigma_{\chi}$ to the Reynolds number of the flow: ${\sigma_{\chi}}^2 = 0.5\ln(0.1Re^{1/2})$. Finally, Haworth *et al.* [176,179] use a non-constant value, related to the intermittency function $\tilde{\gamma}(\boldsymbol{x})$ which represents the probability that the flow is turbulent at location $\boldsymbol{x}$: ${\sigma_{\chi}}^2(\boldsymbol{x}) = 1.0\tilde{\gamma}(\boldsymbol{x})$. The choice of a value for $\sigma_{\chi}$ will be analyzed and discussed in the next sections.

The implementation of log-normal presumed form for the SDR PDF is done following the proposition of Haworth *et al.* [176,179]. In their studies, the PDF considered is the joint velocity-composition PDF, for which the transport equation is solved by a Lagrangian Monte Carlo method. Each Lagrangian particle is characterized by its position and velocity in the computational domain as well as its mixture fraction and scalar dissipation rate. The scalar dissipation rate of each particle is chosen by random selection from a log-normal distribution whose parameters are determined from the local one-point flow statistics (Eq. (III-8)). This method has also been used in Ref. [180], again in the Lagrangian particles framework.

Here, the same implementation is adapted for the Stochastic Eulerian Fields model: for each stochastic field, a random selection is performed following the log-normal

distribution in Eq. (III-7). The parameter $\mu_\chi$ is computed following Eq. (III-8), based on the mean value modeled by Eq. (III-6). Finally, following Refs. [172,177,178], the parameter $\sigma_\chi$ is assumed to be a constant. Its specific value is discussed in the next sections. To the best of the author's knowledge, this implementation has never been used with the Stochastic Eulerian Field method.

## III.3.2 Effect of using a log-normal PDF for the SDR

The modeled flame is an ethylene-air flame at atmospheric pressure investigated experimentally by Kent and Honnery [18]. The fuel is injected at 52.9 m/s by a 3 mm internal diameter (i.d.) injector (Re=15,000). This flame belongs to the set of flames used to validate the model [67].

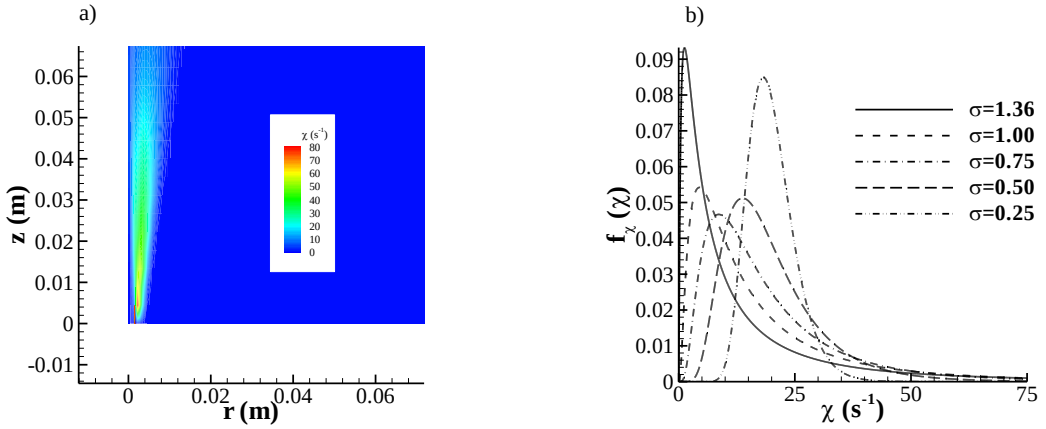


**Figure III-18. a) Mean scalar dissipation rate field close to injection and b) shapes of PDF of the SDR for different values of $\sigma_\chi$ for a mean $\chi$ at 20 $s^{-1}$**

As explained in details in Ref. [173], the ratio $\widetilde{\chi''^2}/\tilde{\chi}^2$ tends to be mostly independent of the value of $\chi$, and increases from zero at the scalar source to a constant value away from the scalar source, i.e. in our case away from the fuel injection. This has a significant influence on the local value of $\sigma_\chi$ (see Eq. (III-8)). Furthermore, away from the injection, the mean SDR is very low (close to zero, see Fig. III-19a). In this case, the shape of the PDF $\widetilde{f_\chi}(\chi)$ tends to a Dirac function around $\tilde{\chi}$. Therefore, the value of $\sigma_\chi$ is unimportant. On the other hand, the value of $\sigma_\chi$ becomes important for the shape of the PDF when $\tilde{\chi}$ reaches significant values, as it is the case close to fuel injection (see Fig. III-19b), particularly when $\sigma_\chi < 1$. Therefore, in this region, SDR statistics could have an important impact on flame structure, and this influence can be evaluated by choosing a constant value for $\sigma_\chi (< 1)$ since it only has an impact where $\tilde{\chi}$ are significant.

In order to evaluate the effect of the value of $\sigma_\chi$, four computations using different values for $\sigma_\chi$ are run. Selected values are $\sigma_\chi = 1.36$ (chosen from results obtained in Ref. [173]), $\sigma_\chi = 1.00$ (from Ref. [177]), $\sigma_\chi = 0.25$ and $\sigma_\chi = 0.5$. The results obtained are compared to the computation using a Dirac shaped-PDF (Eq. (III-5)).

Figure III-20 shows the axial profile of mean and rms temperature (Figs. III-20a and b), mean and rms soot volume fraction (Figs. III-20c and d), divergence of net heat flux (Fig. III-20e), and the radiative wall flux (Fig. III-20f). Very little differences can be noticed between the different models. The mean temperature is higher by about 50K in the downstream region of the flame for the $\sigma_\chi = 1.36$ case, while the other cases show no discrepancies. Rms values are at the most 10K higher for the $\sigma_\chi = 1.00$ run. Peak values for mean and rms soot volume fraction are at the most 6-7% lower than the Dirac run for $\sigma_\chi = 0.25, \sigma_\chi = 0.50$ and $\sigma_\chi = 1.00$ and only slightly higher than the Dirac case for $\sigma_\chi = 1.36$. This explains the slight decrease in radiative quantities (-5% for both the radiative source term and the wall radiative flux) for $\sigma_\chi = 0.25, \sigma_\chi = 0.50$ and $\sigma_\chi = 1.00$ and the small increase for the radiative wall flux for $\sigma_\chi = 1.36$. However, radiant fractions only increase by 2% ($\sigma_\chi = 1.00$ and $\sigma_\chi = 0.50$), 4% ($\sigma_\chi = 1.36$) and 5% ($\sigma_\chi = 0.25$) compared to the computations performed with the Dirac-shaped PDF. The impact of using a log-normal shape for the PDF of the scalar dissipation rate seems therefore negligible in the flames studies here, which is consistent with previous studies on the subject [172].

## III.3.3 Conclusions

In this section, the influence of the shape of the scalar dissipation rate PDF has been investigated by comparing results obtained in section III.1 with those obtained by considering a log-normal PDF based on local values of mean SDR and its variance. The interest of using realistic statistics for this parameter in the framework of steady laminar flamelet models has been outlined; the SDR has a significant impact on local extinction, auto-ignition and pollutant emission in turbulent reactive flows. The log-normal distribution has been implemented using the local value of mean SDR to obtain $\mu_\chi$ and a constant value for $\sigma_\chi$. The value of $\sigma_\chi$ is closely dependent on the SDR variance. However, very little experimental data are available concerning this quantity. Several values for $\sigma_\chi$ have therefore been tested here. For all computations, the maximum discrepancies from

the computation using a Dirac function PDF of flame structure and radiative characteristics of the flame are lower than 7.5%. These results confirm previous studies; for laboratory-scale turbulent diffusion jet flames, the shape of the SDR PDF can be assumed to be a Dirac function, even close to injection where SDR statistics are poorly known.

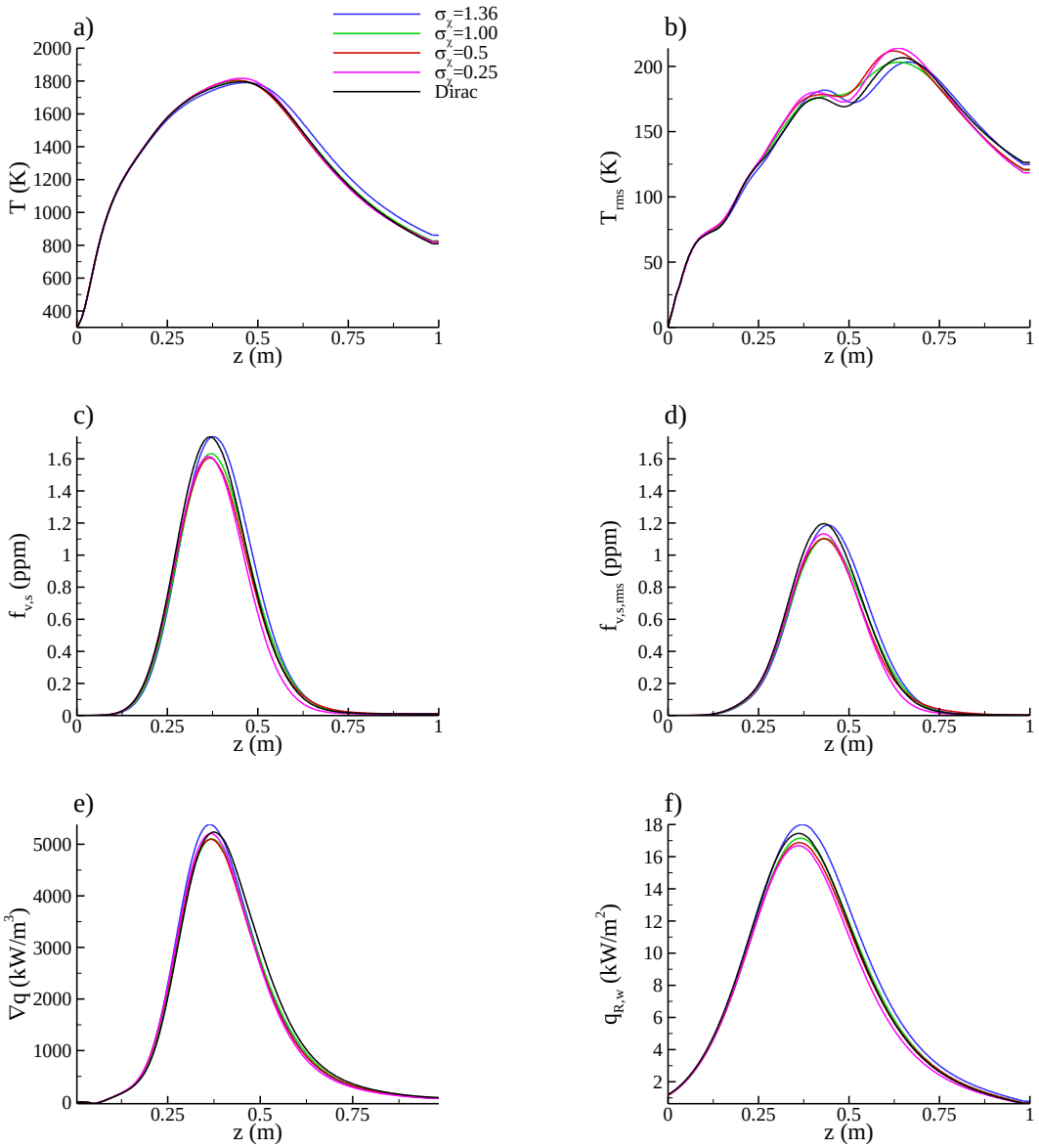


**Figure III-19. Axial profiles of a) mean temperature, b) rms temperature, c) mean soot volume fraction, d) rms soot volume fraction, e) radiative power and f) radiative wall flux for log-normal PDF simulation with $\sigma_\chi$=1.36 and $\sigma_\chi$=1 and Dirac PDF simulations**

# Chapter IV Soot Emission Turbulence-Radiation Interaction

## IV.1 Physical problem

In turbulent sooting flames, radiative transfer is a key process, which must be taken into account to predict accurate flame structure, temperature, soot quantities and radiative heat transfer toward the environment (see Chapter I). Accurate modeling of radiative transfer is a difficult problem for several reasons:

1. A strong dependence of the absorption coefficient of gases on the wavenumber [86];

2. Both gaseous species and soot particles participate to radiation in a non-negligible manner [33];

3. It takes place in a turbulent environment, so that the effect of the interactions between radiation and local fluctuations of the medium radiative properties must be taken into account [10].

These Turbulence-Radiation Interactions (TRIs) emerge when the Radiative Transfer Equation (RTE) is time-averaged:

$$\frac{d\langle I_\eta \rangle}{ds} + \langle \kappa_\eta I_\eta \rangle = \langle \kappa_\eta I_{b\eta} \rangle \quad \text{(IV-1)}$$

The term $\langle \kappa_\eta I_\eta \rangle$ represents the absorption TRI, i.e. the interactions between the local absorption coefficient and the radiative intensity, whereas $\langle \kappa_\eta I_{b\eta} \rangle$ represents emission TRI, i.e. the interactions between the local absorption coefficient and the local blaclbody intensity.

Since it involves non-local quantities, absorption TRI is computationally expensive to take into account in an exact manner, because it requires the knowledge of instantaneous quantities over the entire computational domain. Several numerical studies including the exact computation of this term have been reported, using a particle-based photon Monte Carlo method in both non-sooting [181] and sooting flames [32,33,82]. These studies show that absorption TRI is negligible in moderately sooting turbulent laboratory-scale jet flames. This can be explained by the fact that the instantaneous local intensity of radiation is formed over a path in the entire domain, traversing therefore several turbulent eddies which can be assumed to be weakly correlated to the local radiative properties [122]. It is therefore often simplified by using the Optically Thin Fluctuation Approximation (OTFA) [10,82], which neglects the correlation between the local medium absorption coefficient and incident radiation, and has been shown to be valid for moderately sooting, laboratory-scale flames [82]:

$$\langle \kappa_\eta I_\eta \rangle = \langle \kappa_\eta \rangle \langle I_\eta \rangle + \langle \kappa_\eta{}' I_\eta{}' \rangle \approx \langle \kappa_\eta \rangle \langle I_\eta \rangle \tag{IV-2}$$

On the other hand, emission TRI only involves local properties and can therefore be modeled in an exact manner using the PDF approach:

$$\langle \kappa_\eta I_{b\eta} \rangle = \int_{\boldsymbol{\phi}} \kappa_\eta(\boldsymbol{\psi}) I_{b\eta}(\boldsymbol{\psi}) f_{\boldsymbol{\phi}}(\boldsymbol{\psi}) d\boldsymbol{\psi} \tag{IV-3}$$

where $\boldsymbol{\psi}$ is a vector representative of local quantities.

Emission TRI introduces three separate correlations: the absorption coefficient self-correlation, the Planck-function self-correlation and the correlation between temperature and the absorption coefficient [10]. In the case of gas emission TRI, Habibi *et al.* [119] and Consalvi [121] showed, using a presumed PDF approach, that the complete absorption coefficient-Planck function correlation must be considered to obtain a reliable evaluation. The same conclusions were drawn by Li and Modest [122] by using a transported PDF approach.

However, soot emission TRI and gas emission TRI may differ. To understand the differences the emission TRI is expressed by using a second-order Taylor development of the Planck Function $I_{b\eta}(T)$ around the mean temperature [10]:

$$\langle \kappa_\eta I_{b\eta} \rangle \approx \langle \kappa_\eta \rangle I_{\eta b}(\langle T \rangle) + \langle \kappa_\eta \rangle \frac{\langle T'^2 \rangle}{2} \frac{\partial^2 I_{b\eta}}{\partial T^2} \Big)_{\langle T \rangle} + \langle \kappa_\eta{}' T' \rangle \frac{\partial I_{b\eta}}{\partial T} \Big)_{\langle T \rangle} \quad \text{(IV-4)}$$

Partial derivatives of the Planck function are positive. The second term on the right-hand side of Eq. (IV-4) is therefore positive. However, determination of the sign of the correlation term $\langle \kappa_\eta{}' T' \rangle$ is not straightforward. For gaseous species, this correlation is positive [10,119,122,124]. On the contrary, in the case of soot, the correlation between the soot volume fraction and the temperature, which follows similar trends as the correlation between the soot absorption coefficient and the blackbody intensity, was found experimentally [126,127] and numerically [56] to be highly negative, suggesting that this correlation reduces soot emission.

# IV.2 Soot emission TRI in an oxygen-enhanced propane turbulent jet flame

The correlation between temperature and soot absorption coefficient in an oxygen-enhanced propane turbulent jet flame [55,148] has been studied. The flame was investigated experimentally by Wang *et al.* [164]. Experiments were carried out in a 200-mm i.d. stainless steel chamber. The burner consisted of a 3-mm i.d. fuel tube centered in a 200-mm i.d. laminar oxidizer coflow. Propane was released with a velocity of 21.8 m/s, corresponding to a jet Reynolds number of 15,000. The oxygen index (OI), defined as the volume fraction of oxygen in the oxidizer, was set to 40%. The coflow velocity was 0.6 m/s. Since the soot absorption coefficient is proportional to soot volume fraction, the sign of the term $\langle \kappa_{s\eta}{}' T' \rangle$ appearing in Eq. (IV-4) can be analyzed by studying the correlation coefficient $C(f_{v,s}, T)$ between soot volume fraction and temperature, defined as:

$$C(f_{v,s}, T) = \frac{\langle f_{v,s}{}' T' \rangle}{\sqrt{\langle f_{v,s}{}'^2 \rangle} \sqrt{\langle T' \rangle^2}} \quad \text{(IV-5)}$$

Calculations have been run with and without considering the full correlation between soot volume fraction and Planck function to provide a better physical interpretation of this correlation. The corresponding results will be referred to as Full and No Corr. hereafter. Figure IV-1a shows the evolution of the correlation between the soot volume fraction and the temperature along the flame centerline. The axial profile of soot

volume fraction is also plotted in this figure. The lower part of the flame is the starting point of soot formation (z ≤ 0.15 m). In this region, the correlation between soot volume fraction and temperature is highly positive. As the soot volume fraction increases, the influence of soot on the radiative loss becomes increasing and a rapid decrease of the correlation is observed (0.15 m ≤ z ≤ 0.35 m). In the region where radiative loss becomes dominated by soot radiation (0.25 m ≤ z ≤ 0.5 m), the correlation becomes highly negative. This highly negative character was evidenced experimentally by Sivathanu *et al.* [126,127] and by Murphy *et al.* [128] and numerically by Kollmann *et al.* [56]. As soot is oxidized, soot volume fraction and its contribution to radiative heat transfer decreases (z ≥ 0.5 m) and the correlation remains negative over the entire soot oxidation region. Figure IV-1b displays the radial profile of $C(f_{v,s}, T)$ at a height above the burner of 0.35m corresponding to the axial location where the soot volume fraction reaches a maximum. Soot volume fraction and temperature appears also to be negatively correlated in the part of the flame dominated by soot radiation. The previous discussion shows that the third term of Eq. (IV-4) is negative since the spectral absorption coefficient and temperature are negatively correlated in regions where soot radiation is significant. This term thus contributes to reduce soot emission. The importance of this reduction varies across the flame and should depend on the amount of soot and on the level of turbulence. A complete analysis of the influence of this term on radiative heat transfer will be discussed in the next section.

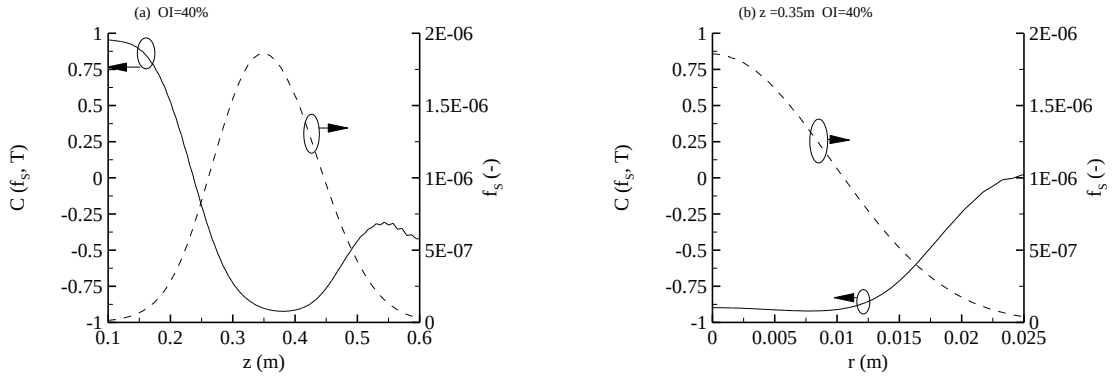


**Figure IV-1. Evolution of the cross correlation between the soot volume fraction and temperature (solid line), and of the soot volume fraction (dashed line) a) along the flame axis, b) as a function of the radius at z=0.35 m**

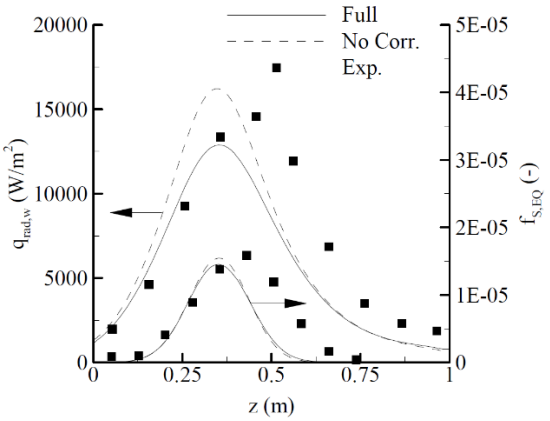


**Figure IV-2. Evolution of the equivalent soot volume fraction and radiative wall flux as a function of the height above the burner for the Full. and No Corr. computations**

Figure IV-2 shows the equivalent soot volume fraction, predicted by using the full model (Full), as a function of the height above the burner. As expected, the equivalent soot volume fraction first increases with the distance from the burner owing to soot growth, reaches a peak, and then decreases as a result of soot oxidation. Numerical predictions are on the whole consistent with the experimental data. The numerical model reproduces well the evolution of the soot equivalent fraction in the soot growth region up to z=0.35 m. However, the peak location is predicted upstream as compared to the experiments and the peak magnitude is underestimated by about 9%. As a consequence of the underestimation of the peak location, the equivalent soot volume fraction in the oxidation zone is under-predicted and soot burnout occurs earlier as compared to the experiments. A careful examination of Figure IV-2 shows that the rate of decrease of the equivalent soot fraction in the soot oxidation region is in good agreement with the measurements. The incident radiative flux along the enclosure wall is also displayed in Figure IV-2. The numerical predictions obtained by using the Full model are in reasonable agreement with the experimental data. The peak value is underestimated by about 12% and the peak location is predicted upstream as compared to the experiments. These discrepancies are consistent with those observed for the equivalent soot volume fraction and can then be attributed to uncertainties on the soot model rather than to the radiation model. It should be pointed out that the level of agreement between model and experiment is found to be at least as good as any that has been published earlier [33].

The radiant fraction has been computed as the ratio between the total radiative loss, determined by integrating the divergence of the radiative flux over the entire

computational domain and the chemical heat release rate. The predicted radiant fraction, computed with the Full model, is of 0.27 in close agreement with the measured value of 0.24.

Calculations have been also run without considering the full correlation between soot volume fraction and Planck function. The corresponding results are referred as No Corr. in Figure IV-2. Neglecting this correlation increases significantly the wall radiative flux, the peak of this quantity being increased by about 26%. In addition, the radiant fraction, that quantifies the total heat loss from the flame, is also substantially enhanced by about 16%.

In order to generalize the previous discussion about $C(f_{v,s}, T)$, other propane flames with the same injection characteristics (same Reynolds number) but with different OI values of 21, 30 and 75% have been considered. These flames are characterized by different level of temperatures and different sooting behavior. The temperature increases monotonically with the OI whereas the sooting propensity exhibits a non-monotonic behavior, increasing first when the OI is increased between 21% and about 40% and then decreasing as the OI is further increased. The behavior of $C(f_{v,s}, T)$ is similar whatever the OI and follows the trends discussed previously for an OI of 40% [148].

# IV.3 Detailed analysis

A set of five turbulent jet flames is considered, using different injection Reynolds numbers and several fuels in order to analyze the effect of fuel sooting propensity. A detailed study of the local and global soot radiation characteristics is presented, including the effect of the three correlations of interest (absorption coefficient self-correlation, temperature self-correlation and absorption coefficient/Planck function correlation).

## IV.3.1 Flames characteristics

Table IV-1 shows the burning characteristics of the turbulent jet flames considered in the present study. These flames were designed from the experimental configuration of Lee *et al*. [161] who investigated experimentally ethylene jet flames burning in air. In their experiments, the fuel nozzle diameter was 2.18 mm and injection velocities were modified to provide injection Reynolds numbers ranging from 4,000 to 23,200. In the present

study, ethylene flames with Reynolds numbers of 8,000, 12,000 and 20,000 are considered. It should be pointed out that the flame with a Reynolds number of 12,000 is part of the set of turbulent jet flames used to validate the numerical method (see Chapter III). In addition, two other flames fueled by propane and methane and with a Reynolds number of 12,000 are considered in order to investigate the effects of the fuel sooting propensity. The propensity of a fuel to produce soot varies inversely with its smoke point height (the minimum height of an over-ventilated laminar axi-symmetric diffusion flame at which soot starts to be released from the flame tip). The smoke point flame heights, $L_{sp}$, reported in Table IV-1, show that the sooting propensity of ethylene is higher than that of propane which is higher than that of methane.

| Name | Fuel | Re | $d_n$ (mm) | $U_{inj}$ ($m.s^{-1}$) | $L_{sp}$ (m) | $\tau$ | $\tau_s$ |
|---|---|---|---|---|---|---|---|
| **$C_2H_4$-8000** | $C_2H_4$ | 8000 | 2.18 | 32.5 | 0.102 | 0.0947 | 0.0618 |
| **$C_2H_4$-12000** | -- | 12000 | -- | 48.7 | -- | 0.102 | 0.064 |
| **$C_2H_4$-20000** | -- | 20000 | -- | 81.2 | -- | 0.0938 | 0.0498 |
| **$C_3H_8$-12000** | $C_3H_8$ | 12000 | -- | 97.1 | 0.162 | 0.0437 | $8.4\times10^{-3}$ |
| **$CH_4$-12000** | $CH_4$ | 12000 | -- | 25.3 | 0.29 | 0.0504 | $1.4\times10^{-3}$ |

**Table IV-1. Characteristics of the flames studied.**

Predicted mean and fluctuations of temperature and soot volume fraction were found to be in reasonable agreement with the experimental data. Figure IV-3 shows the fields of temperature and soot volume fraction for the five flames, while Fig. IV-4 shows the axial evolutions of mean soot volume fraction and the rms values of the soot volume fraction fluctuations.

In the case of ethylene flames, Lee *et al.* [161] reported the effects of increasing the Reynolds number (by increasing the fuel injection velocity) on flame structure. In particular, their axial profiles (see Fig. IV-4) show that the location of the peak of mean soot volume fraction is insensitive to the jet velocity whereas, as the Reynolds number is increased, the initial soot formation takes place downstream and the peaks of mean and rms soot volume fraction are reduced. These features are well reproduced by the model, which also provides good quantitative agreement concerning the axial mean and fluctuations of soot volume fraction (see Fig. IV-4). In addition, Lee *et al*. observed that, at a given height, the flame and the radial profiles of soot volume fraction becomes broader as the Reynolds number is increased. Figure VI-3 shows that the numerical model

captures also well this trend. The comparison of $C_2H_4$-12000, $C_3H_8$-12000, and $CH_4$-12000 flames allows quantifying the effects of the fuel sooting propensity. The peak of soot volume fraction is 2.05 ppm for the ethylene flame and is reduced to 0.35 ppm and 0.04 ppm for the propane and methane flames, respectively.

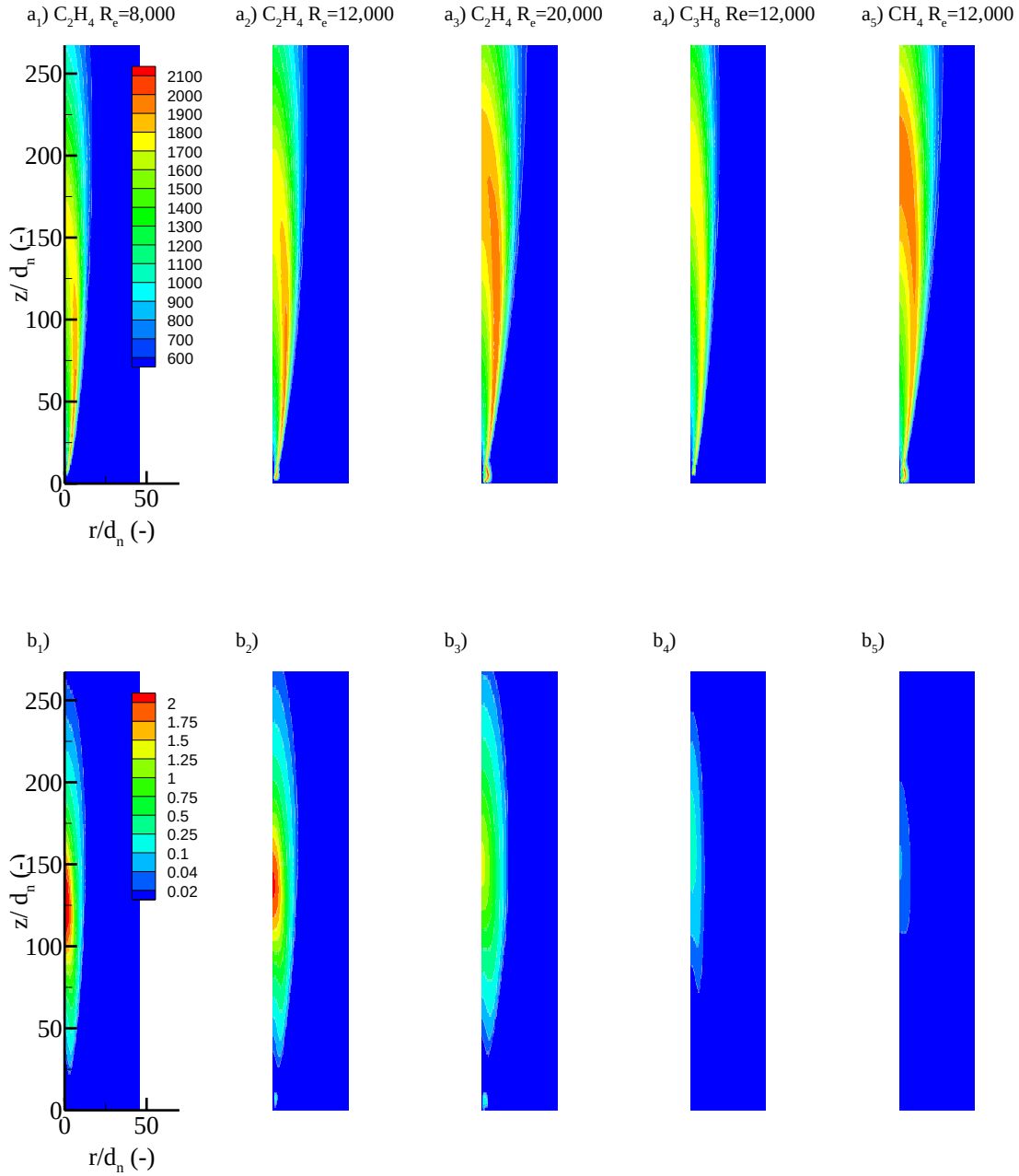


**Figure IV-3. Fields of a) mean temperature (K) and b) mean soot volume fraction (ppm) for all five flames.**

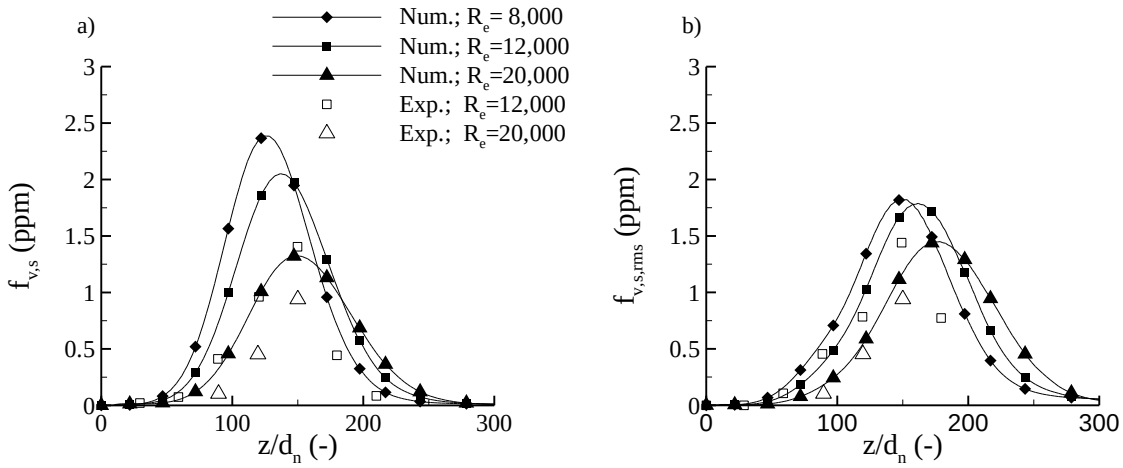


**Figure IV-4. Axial profiles of a) mean soot fraction and b) r.m.s value of soot volume fraction for the ethylene flames.**

# IV.3.2 Results and dicussions

## IV.3.2.1 Background and notations

The local emission term can be written as follows:

$$\langle E \rangle = \langle E_g \rangle + \langle E_s \rangle = 4\pi \int_0^\infty \langle \kappa_{g,\eta} I_{b\eta}(T) \rangle d\eta + 4\pi \int_0^\infty \langle \kappa_{s,\eta}(f_{v,s}) I_{b\eta}(T) \rangle d\eta \qquad \text{(IV-6)}$$

Let us focus on the contribution of soot. This term can be rewritten as:

$$\langle E_s \rangle = 4\pi \langle \int_0^\infty \kappa_{s,\eta}(f_{v,s}) I_{b\eta}(T) d\eta \rangle = 4\pi \langle \kappa_{s,P}(f_{v,s}, T) I_b(T) \rangle \qquad \text{(IV-7)}$$

where $\kappa_{s,P}$ is the Planck mean soot absorption coefficient and $I_b$ is the spectrally-integrated black-body intensity, defined as:

$$\kappa_{s,P}(f_{v,s}, T) = \frac{\int_0^\infty \kappa_{s,\eta}(f_{v,s}) I_{b\eta}(T) d\eta}{I_b(T)} \quad \text{with} \quad I_b(T) = \int_0^\infty I_{b\eta}(T) d\eta = \frac{\sigma T^4}{\pi} \qquad \text{(IV-8)}$$

When TRI is neglected the soot emission term can be evaluated as:

$$\langle E_s \rangle_{NoTRI} \approx 4\pi \kappa_{s,P}(\langle f_{v,s} \rangle, \langle T \rangle) I_b(\langle T \rangle) = 4\pi \kappa_{s,P}(\langle f_{v,s} \rangle, \langle T \rangle) \frac{\sigma \langle T \rangle^4}{\pi} \qquad \text{(IV-9)}$$

This closure will be denoted NoTRI hereafter. When TRI is considered, the soot emission term can be expended as:

$$\begin{aligned}\langle E_s\rangle &= 4\pi\left(\langle\kappa_{s,P}\rangle\langle I_b\rangle + \langle\kappa_{s,P}{}'I_b{}'\rangle\right)\\ &= \underbrace{\underbrace{4\pi\langle\kappa_{s,P}\rangle\frac{\sigma\langle T\rangle^4}{\pi}}_{\mathrm{TRI}_1} + \underbrace{4\pi\langle\kappa_{s,P}\rangle\left[\frac{6\sigma\langle T\rangle^2\langle T'^2\rangle}{\pi} + \frac{4\sigma\langle T\rangle^2\langle T'^3\rangle}{\pi} + \frac{\sigma\langle T'^4\rangle}{\pi}\right]}_{\mathrm{TRI}_2} + 4\pi\langle\kappa_{s,P}{}'I_b{}'\rangle}_{\text{Full TRI}}\end{aligned} \tag{IV-10}$$

$\mathrm{TRI}_1$ extends the NoTRI closure by considering the influence of TRI on the Planck mean soot absorption coefficient. $\mathrm{TRI}_2$ extends the $\mathrm{TRI}_1$ closure by including the effects of the temperature fluctuations but neglects the correlation between Planck-mean soot absorption coefficient and the blackbody intensity. Finally, the full TRI extends the $\mathrm{TRI}_2$ closure by including the effects of the correlation between the Planck-mean soot absorption coefficient and the blackbody intensity. The total emission, the total soot emission and the total contribution of the correlation between the Planck mean soot absorption coefficient and the blackbody intensity are obtained by integrating the corresponding local quantities over the entire computational domain:

$$\langle E\rangle_t = \int_{Vol}\langle E\rangle dV\,; \quad \langle E_s\rangle_t = \int_{Vol}\langle E_s\rangle dV\,; \quad \langle\kappa_{s,P}{}'I_b{}'\rangle_t = \int_{Vol}\langle\kappa_{s,P}{}'I_b{}'\rangle dV \tag{IV-11}$$

## IV.3.2.2 Local and global characteristics of soot emission

Figure IV-5a shows the fields of soot emission for the five flames. Soot emission follows the same trends as observed for the soot volume fractions. The peak of soot emission occurs in the vicinity of the flame axis in the region where the soot volume fraction is the largest. As the Reynolds number is enhanced, the region of significant soot emission becomes broader and the peak value of soot emission decreases owing to a reduction of the soot volume fraction. Comparison between the $C_2H_4$-12000, the $C_3H_8$-12000 and the $CH_4$-12000 flames shows that as expected, the soot emission decreases with the fuel sooting propensity.

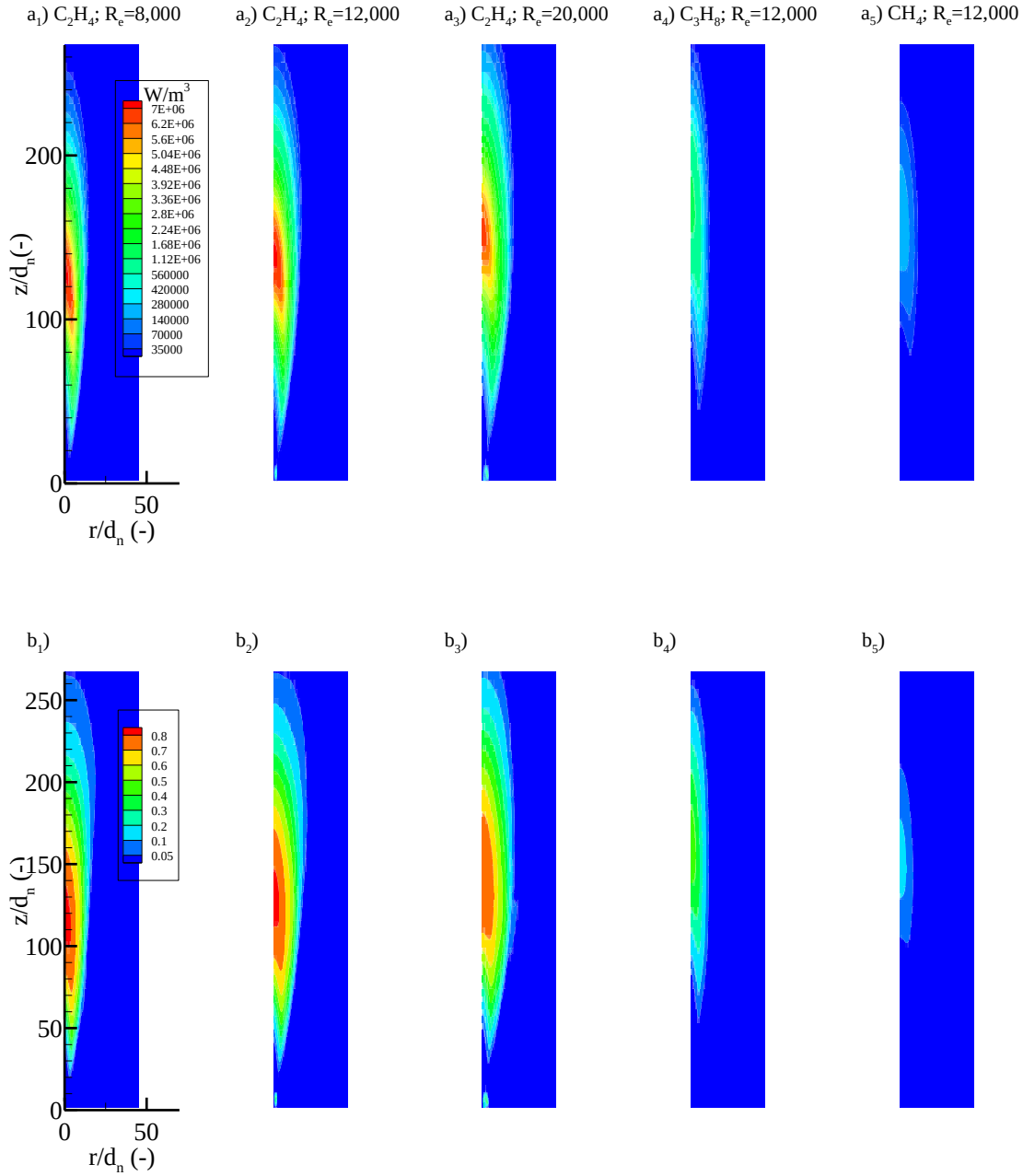


**Figure IV-5. Fields of a) soot emission term, b) fraction of the emission due to soot.**

The second, third and fourth columns in Table IV-2 provide information on the total emission, the total soot emission and the contribution of soot to the total emission, respectively. The total emission represents about 35-40% of the total heat release rate in ethylene flames, 22% in the propane flame and 28% in the methane flame. The contribution of soot emission is the highest for the $C_2H_4$-8000 flame and represents 51%

of the total emission. As the Reynolds increases the part of soot in the total emission is reduced to reach 35% for the $C_2H_4$-20000 flame. The contribution of soot emission decreases also significantly with the fuel sooting propensity, reaching about 10% and 1.5% in the propane and methane flames, respectively. The local fraction of emission due to soot is displayed in Fig. VI-5b. Figures VI-5b$_1$, b$_2$ and b$_3$ show that soot emission in ethylene flames contributes for approximately 80% in regions where soot emits strongly. This maximum value is reduced to about 45% and 11% in the propane and methane flames, respectively. These local contributions show that soot emission cannot be neglected even in weakly sooting hydrocarbons.

| Name | $\langle E\rangle_t/\dot{Q}_C$ | $\langle E_s\rangle_t/\dot{Q}_C$ | $\langle E_s\rangle_t/\langle E\rangle_t$ | $\langle \kappa_{S,P}{}'I'_b\rangle_t/\langle E_s\rangle_t$ | $\langle \kappa_{S,P}{}'I'_b\rangle_t/\langle E\rangle_t$ |
|---|---|---|---|---|---|
| **$C_2H_4$-8000** | 0.380 | 0.194 | 0.51 | -0.138 | -0.0744 |
| **$C_2H_4$-12000** | 0.382 | 0.178 | 0.47 | -0.178 | -0.0828 |
| **$C_2H_4$-20000** | 0.356 | 0.127 | 0.356 | -0.204 | -0.0763 |
| **$C_3H_8$-12000** | 0.216 | 0.022 | 0.103 | -0.190 | -0.0198 |
| **$CH_4$-12000** | 0.284 | 0.004 | 0.014 | -0.188 | -0.0027 |

**Table IV-2. Global radiative characteristics of the flames studied.**

### IV.3.2.3 Correlation between soot volume fraction and temperature

The first expression on the right hand side of Eq. (IV-10) shows that the correlation between the soot volume fraction and the temperature affects soot emission through the time-averaged value of the Planck-mean soot absorption coefficient, $\langle \kappa_{s,P}\rangle$, and the correlation between Planck mean soot absorption coefficient and the blackbody intensity, $\langle \kappa_{s,P}{}'I_b{}'\rangle$. The influence of the time-averaged value of the Planck mean soot absorption coefficient can be better understood, without any loss in generality, by assuming that the index of refraction of soot does not depend on the wavenumber. In this case the Planck-mean soot absorption coefficient can be expressed as $\kappa_{s,P} = \mathrm{C} f_{v,s} T$ where C is a constant. Its time averaged value can be developed as follow:

$$\langle \kappa_{s,P}\rangle = \langle \mathrm{C} f_{v,s} T\rangle = \mathrm{C}\big(\langle f_{v,s}\rangle\langle T\rangle + \langle f_{v,s}{}'T'\rangle\big) = \kappa_{s,P}\big(\langle f_{v,s}\rangle, \langle T\rangle\big) + \mathrm{C}\langle f_{v,s}{}'T'\rangle \qquad \text{(IV-12)}$$

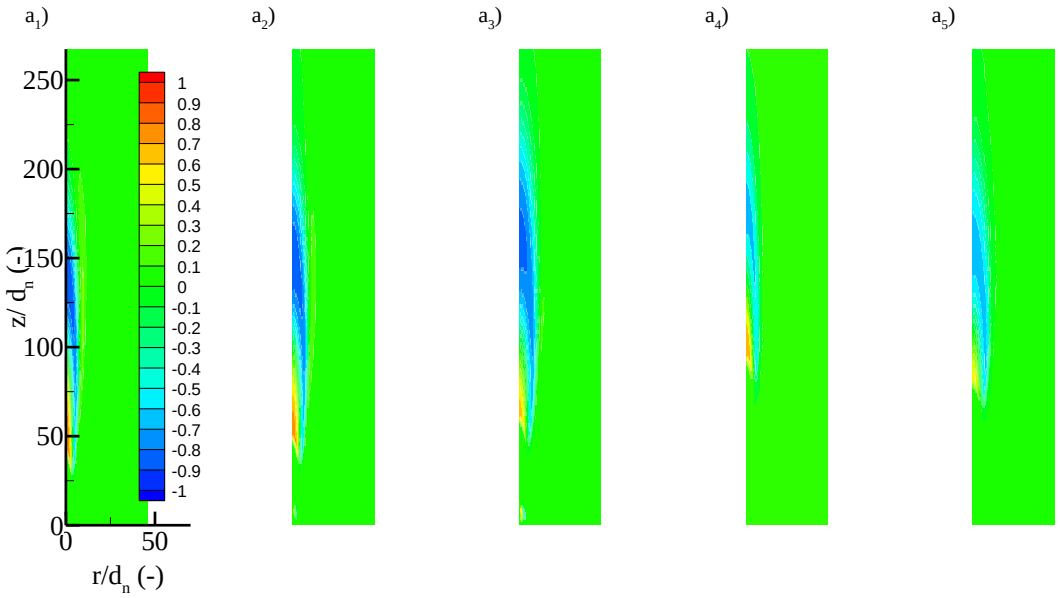


**Figure IV-6. Fields of cross-correlation between soot volume fraction and temperature.**

Figure IV-6 shows the fields of the correlation coefficient of the soot volume fraction and the temperature, defined as Eq. (IV-5). As expected, it shows that the temperature and the soot volume fraction are negatively correlated in the regions where soot emits significantly. They are more negatively correlated in the ethylene flames where the correlation coefficient reaches -0.85 than in propane and methane flames where the correlation coefficient does not get lower than -0.65. As discussed in the introduction of this chapter, this negative correlation between temperature and soot volume fraction was observed in both experimental [126] and numerical [56] studies concerning moderately and strongly sooting turbulent flames. The present results extend this conclusion, showing that it is also valid for weakly sooting flames.

The negative correlation between soot volume fraction and temperature can be explained by two mechanisms. The first mechanism can be understood from Figs. IV-7a and b. They show the axial evolution of the soot emission, the correlation coefficients between mixture fraction and soot volume fraction and between temperature and soot volume fraction, and the soot oxidation rate for the $CH_4$-12000 and the $C_2H_4$-12000

flames, respectively. In both diagrams, the dashed vertical line indicates the location of the mean stoichiometry (i.e. the axial position where the mean mixture fraction reaches its stoichiometric value). In both flames, a significant part of soot emission occurs in a region located on the mean fuel rich side. In addition, a significant part of the soot oxidation occurs also in this region. As expected from the conclusions drawn by Moss and co-workers [52,53], Figs. IV-7a and b show that mixture fraction and soot volume fraction are relatively well correlated in this region with a correlation coefficient of about 0.65. Therefore, a negative fluctuation of the mixture fraction moves the system toward the stoichiometry and then tends to increase temperature and decrease soot volume fraction since soot particles are further oxidized. This explains that the negative correlation between soot volume fraction and temperature in this part of the flame. This mechanism is independent on the soot loading and therefore on soot emission. The second mechanism is related to the radiative emission due to soot and becomes significant in strongly sooting flames. A positive fluctuation of soot volume fraction increases soot emission and the radiative loss and, then, leads to a negative fluctuation of the temperature. This explains why the correlation coefficient between soot volume fraction and temperature is more negative in the $C_2H_4$-12000 flame than in the $CH_4$-12000 flame.

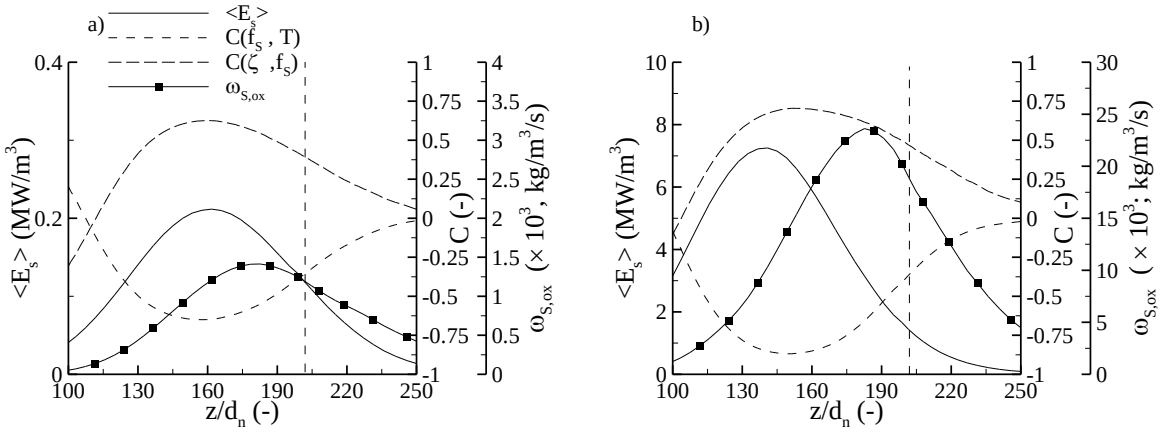


**Figure IV-7. Structure of the flame in the region of significant soot emission along the axis for $CH_4$-12000 flame (a) and $C_2H_4$-12000 flame (b). The vertical dashed line indicates the location of the stoichiometry.**

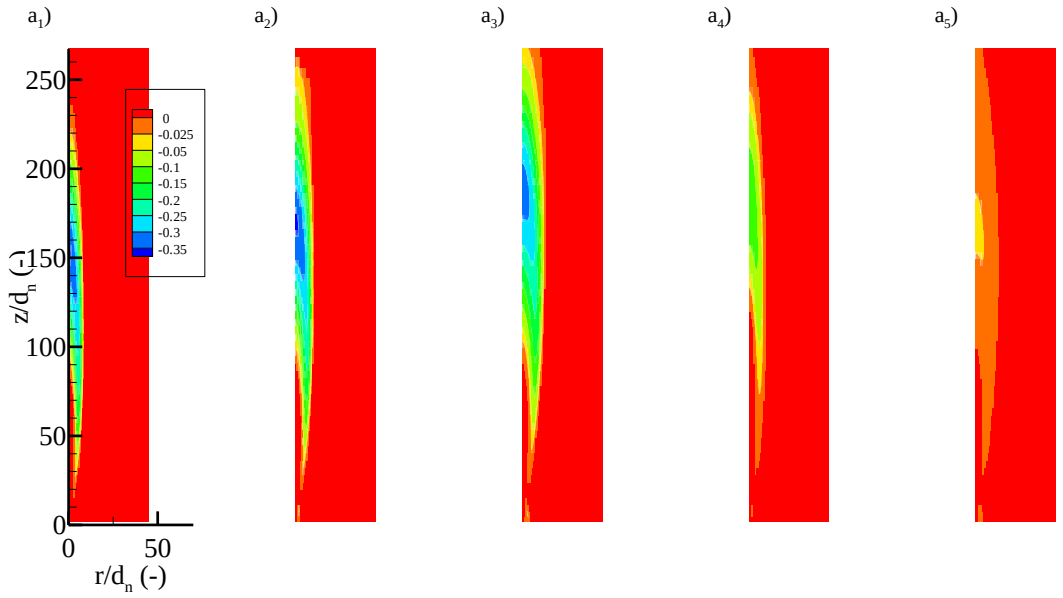


**Figure IV-8. Fields of the fraction of the soot emission due to the correlation between the soot absorption coefficient and the temperature**

Let us discuss the importance of the correlation between the Planck mean soot absorption coefficient and the black body intensity $\langle \kappa_{s,P}{}' I_b{}' \rangle$. This correlation, which evolves in the same manner as the correlation between soot volume fraction and the temperature, is negative and, therefore, tends to reduce soot emission. Figure IV-8 displays the fields of $\langle \kappa_{s,P}{}' I_b{}' \rangle / \langle E_s \rangle$. The results show that $\langle \kappa_{s,P}{}' I_b{}' \rangle$ can represent locally up to 56% of the soot emission as observed in the $C_2H_4$-20000 flame. This maximum increases with the Reynolds number from 49% in the $C_2H_4$-8000 flame to 56% in the $C_2H_4$-20000 flame whereas it decreases with the fuel sooting propensity. It is 52 % in the $C_2H_4$-12000, 38% in the $C_3H_8$-12000 flame and 31% in the $CH_4$-12000 flame. The penultimate column in Table IV-2 provides $\langle \kappa_{s,P}{}' I_b{}' \rangle_t / \langle E_s \rangle_t$ for each flames. The overall contribution of the correlation between the Planck mean soot absorption coefficient and blackbody intensity represents about 15 %, 18% and 20% of the total soot emission in the $C_2H_4$-8000, -12000, and -20000 flames, respectively. This confirms that this contribution increases with the Reynolds number. It is interesting to note that $\langle \kappa_{s,P}{}' I_b{}' \rangle_t / \langle E_s \rangle_t$ does not vary significantly with the fuel sooting propensity.

Figure IV-9a shows the axial evolution of $\langle \kappa_{s,P}' I_b' \rangle / \langle E_s \rangle$ as a function of the height above the burner normalized by the flame length. As discussed previously, the contribution of the correlation between the Planck mean absorption coefficient and the blackbody intensity to the soot emission increases with the Reynolds number. Figure IV-9b shows the axial evolution of $\langle \kappa_{s,P}' I_b' \rangle / \langle E_s \rangle$ normalized by:

$$I_T = \frac{\sqrt{\langle \kappa_{s,P}'^2 \rangle} \sqrt{\langle I_b'^2 \rangle}}{\langle \kappa_{s,P} \rangle \langle I_b \rangle} \tag{IV-13}$$

as a function of the height above the burner normalized by the flame height. $I_T$ can be interpreted as a measure of the turbulent intensity. Results shows that this normalization allows to collapse the data for the three flames on a single curve, suggesting that an increase of $I_T$ with the Reynolds number is responsible for the increase in the contribution of the correlation to the soot emission.

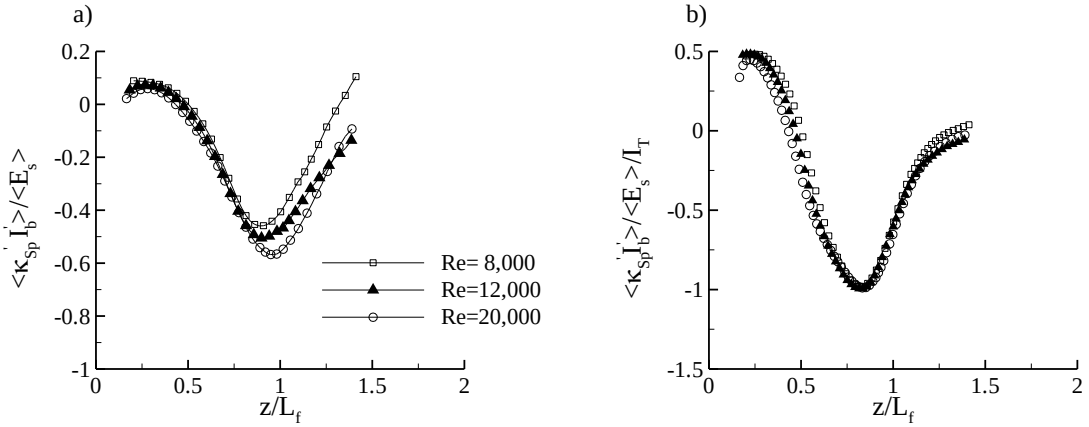


**Figure IV-9. a) Axial evolution of the ratio between the soot absorption coefficient-blackbody intensity correlation and the soot emission term as a function of the height above the burner normalized by the flame length for the three-ethylene flames. b) Same as a) with the ratio between the soot absorption coefficient-blackbody intensity correlation and the soot emission term normalized by the turbulent intensity $I_T$.**

## IV.3.2.4 Effect of different TRI closures on soot emission

The effects of the different TRI closures for the soot emission term, discussed in section IV.3.2.1, are evaluated. Table IV-3 provides the influence of the TRI closure on the

total soot emission term for the different flames whereas Figs. IV-10a to e show the corresponding axial profiles in order to discuss local effects.

Let us start with the global influence of the different closures reported in Table IV-3. Including the influence of TRI on the Planck mean soot absorption coefficient ($TRI_1$ vs. No TRI) tends to reduce the total emission of soot, due to the negative correlation between the soot absorption coefficient and the temperature. As discussed previously, an increase in the Reynolds number enhances the effects of this correlation. This explains the higher reduction in soot emission as the Reynolds number increases. $TRI_2$ extends $TRI_1$ by including the effects of the temperature fluctuations. This term enhances substantially the total soot emission. Table IV-3 shows that the $TRI_2$ closure leads to an enhancement of the total soot emission by more than 30% as compared to the No TRI case. The comparison between full TRI closure and $TRI_2$ quantifies the influence of the correlation between the soot absorption coefficient and the blackbody intensity. As expected from the previous discussion (see section IV.3.2.2), adding this term decreases the total soot emission and this reduction is higher as the Reynolds number is enhanced.

| **Name** | $\langle E_s \rangle_{noTRI,t}$ **(W)** | $\langle E_s \rangle_{TRI_1,t}$ **(W)** | $\langle E_s \rangle_{TRI_2,t}$ **(W)** | $\langle E_s \rangle_t$ **(W)** |
|---|---|---|---|---|
| **$C_2H_4$-8000** | 1125 | 1049 (-6.76%) | 1561 (38.8%) | 1372 (22.0%) |
| **$C_2H_4$-12000** | 1630 | 1490 (-8.59%) | 2123 (30.2%) | 1802 (10.6%) |
| **$C_2H_4$-20000** | 1963 | 1741 (-11.3%) | 2577 (31.3%) | 2140 (9.01%) |
| **$C_3H_8$-12000** | 161 | 151 (-6.21%) | 219 (36.0%) | 184 (14.3%) |
| **$CH_4$-12000** | 50 | 47 (-6.00%) | 57 (14.0%) | 48 (-4%) |

**Table IV-3. Influence of different TRI closure on the soot emission. % indicate the relative effects (in %) defined as $|\langle E_s \rangle_{noTRI,t} - \langle E_s \rangle_{model,t}| / \langle E_s \rangle_{noTRI,t}$**

Table IV-3 shows that the overall effects of TRI tend to enhance the total soot emission (Full TRI vs. No TRI) with the exception for the methane flame where a small reduction is observed. However, soot emission is completely negligible in the CH4-12000 flame and this point will not be discussed further. Table IV-3 shows also that increasing the Reynolds number reduces the enhancement in soot emission due to TRI. The previous discussion suggests that this reduction is primarily due to the effects of the correlation between the soot absorption coefficient and temperature. In order to quantify these effects, the total soot emission term is re-written as follows:

$$\langle E_s \rangle = \langle E_s \rangle_{noTRI} + \underbrace{\left(\langle E_s \rangle_{TRI_1} - \langle E_s \rangle_{noTRI}\right)}_{F_1} + \underbrace{\left(\langle E_s \rangle_{TRI_2} - \langle E_s \rangle_{TRI_1}\right)}_{F_2} + \underbrace{\left(\langle E_s \rangle - \langle E_s \rangle_{TRI_2}\right)}_{F_3} \quad \text{(IV-14)}$$

The different contributions are reported in Table IV-4. The results show clearly that the contributions of the TRI on both the Planck-mean soot absorption coefficient (third column of Table IV-4) and the correlation between the soot absorption coefficient and the blackbody intensity (fifth column of Table IV-4), which contributes to reduce the total soot emission, are enhanced with the Reynolds number. On the other hand, the contribution of the temperature self-correlation, which enhance the total soot emission, is approximately insensitive to the Reynolds number.

| Name | $\langle E_s \rangle_{noTRIs,t}/\langle E_s \rangle$ | $F_{1,t}/\langle E_s \rangle_t$ | $F_{2,t}/\langle E_s \rangle_t$ | $F_{3,t}/\langle E_s \rangle_t$ |
|---|---|---|---|---|
| **$C_2H_4$-8000** | 82.0% | -5.5% | 37.3% | -13.8% |
| **$C_2H_4$-12000** | 90.5% | -7.8% | 35.1% | -17.8% |
| **$C_2H_4$-20000** | 91.7% | -10.4% | 39.1% | -20.4% |
| **$C_3H_8$-12000** | 87.4% | -5.4% | 37.0% | -19.0% |
| **$CH_4$-12000** | 104.2% | -6.3% | 20.8% | -18.8% |

**Table IV-4. Proportion of each contribution of TRI to soot radiative emission**

Let's now focus on the axial evolution of the soot emission term computed by these different closures (Figs. IV-10a to e). For all flames, $\langle f_s' T' \rangle$ is strongly negative in locations where soot emission is important, so that the axial profile of $\langle E_s \rangle_{TRI_1}$ is lower than $\langle E_s \rangle_{NoTRIs}$: the peak value decreases by about 10-15%. Adding the positive contribution of temperature fluctuations causes this peak to increase by about 25-35% compared to $\langle E_s \rangle_{TRI_1}$. However, adding the contribution of the correlation coefficient between Planck soot absorption coefficient and black-body emission seems to fully compensate for the effect of temperature fluctuations: for all flames, axial profiles of $\langle E_s \rangle_{TRI_1}$ and $\langle E_s \rangle$ almost overlap. The peak value of $\langle E_s \rangle$ is lower than that of $\langle E_s \rangle_{TRI_2}$ by about 20-26%. Overall, the decrease of the peak of soot radiative emission between no TRIs and full TRI is about 15-20%, showing that while total radiative loss is enhanced by soot emission TRI, local soot emission is actually inhibited by TRI.

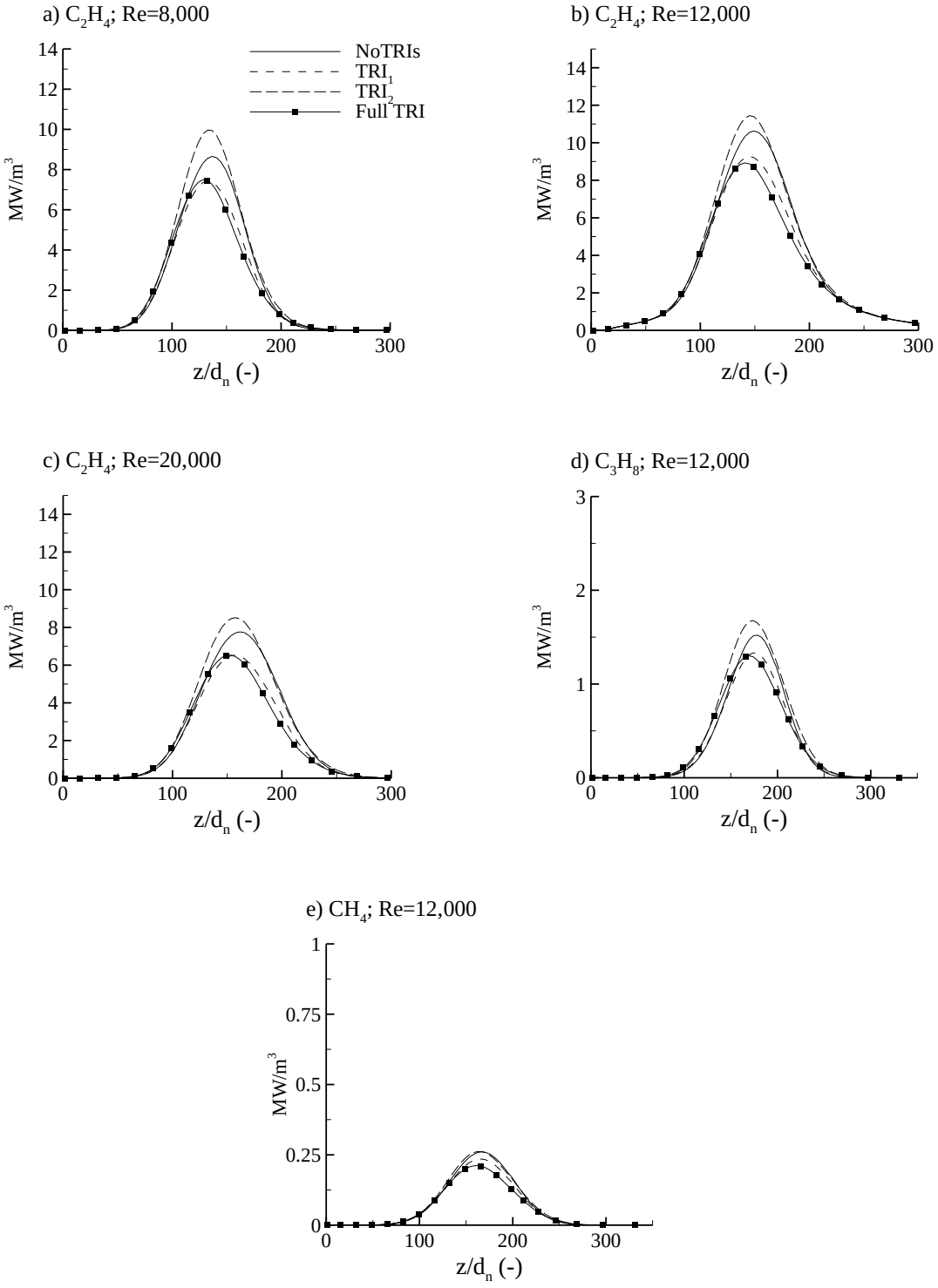


**Figure IV-10. Axial profiles of the emission term computed with the four different closures (no TRIs, $TRI_1$, $TRI_2$ and full TRI) for the five studied flames**

# IV.4 Conclusions

An extensive study of the effects of emission TRI in turbulent, moderately sooting jet flames, has been performed in this chapter, focusing on the soot emission term. A set of five turbulent sooting jet flames has been considered: three ethylene flames for which the Reynolds number was varied between 8,000, 12,000 and 20,000, one propane flame with Re=12,000 and one methane flame with Re=12,00. An analysis of the radiative characteristics of these flames has been presented, followed by a study of the effects of the different quantities contributing to TRI on the soot emission term.

The following conclusions can be drawn:

- The proportion of emission due to soot can be locally non-negligible, even for fuels with low sooting propensity.
- The total soot emission, as well as the contribution of the soot emission, decrease with the fuel sooting propensity and as the Reynolds number increases.
- TRI affects soot emission through three terms, namely, the Planck-mean absorption coefficient-self correlation, the temperature-self correlation and the correlation between the Planck-mean absorption coefficient and the Blackbody intensity. The temperature-self correlation tends to enhance soot emission whereas the two other terms tend to reduce it due to the negative correlation between the soot volume fraction and the temperature.
- TRI tends to enhance the global soot emission but may locally inhibit it. This enhancement was found to be less important when increasing the Reynolds number. This is due to the fact that the effects of the negative correlation between the soot volume fraction and the temperature increases with the Reynolds number.
- The negative correlation between soot volume fraction and temperature results primarily from the structure of the turbulent diffusion flame and, as such, is independent of the fuel. Increasing the radiative heat transfer due to soot enhances this negative behavior.

# Chapter V Effect of the correlation between mixture fraction and enthalpy defect parameter on radiative heat transfer and flame structure

## V.1 Introduction

An accurate modeling of turbulent flames requires, on the one hand, to consider detailed chemical mechanisms that consider the main reaction pathways and, on the other hand, to model the turbulence-chemistry interactions. The size of the chemical mechanisms increases in a non-linear manner with the number of carbon atom that composes the fuel or with application considered. As an example, in the case of sooting flames, the chemical mechanism has to be sufficiently exhaustive to give access to the intermediate species involved in the production of soot. As a consequence, the large number of chemical species and reactions involved in soot formation and oxidation is prohibitive for solving the species and energy equations simultaneously to the equations which describe the flow field when performing numerical simulation of soot formation with CFD codes.

Under the assumption of widely separated time scales for chemical reactions and transport processes, the combustion chemistry attains a quasi-steady state and adjusts with short relaxation times to local flow conditions. As a consequence, the chemical kinetics can be decoupled from the mixing process. This idea is realized in the flamelet concept [3]. Temperature, species mass fractions and the scalars related to these quantities can be represented by the mixture fraction, $\zeta$, the scalar dissipation rate, $\chi$, which accounts for the influence of the flow field on the flamelet structure, and an enthalpy defect parameter, $X_R$, that quantifies the radiative loss [4,7]. To determine the

moments of these scalars a Probability Density Function (PDF) of $(\zeta, \chi, X_R)$ [3,19] is then required. In practice, these parameters are assumed to be statistically independent and the PDFs are modeled as a presumed PDF for $\zeta$ (a $\beta$–PDF is often considered) and as a Dirac function for $X_R$ and $\chi$ [52,119,182–185]. A notable exception in the field of presumed-PDF method is the work of Hartick *et al.* [186], who generated a two-dimensional PDF of mixture fraction and enthalpy defect from the first and the second moments of these two quantities. Nmira *et al.* [148] used a transported PDF method to investigate the evolution of the correlation between mixture fraction and enthalpy defect in an oxygen-enhanced jet turbulent flame. They found that mixture fraction and enthalpy defect are correlated over a large part of the flame, suggesting that the assumption of statistical independence is not valid. The objective of this chapter is to investigate the influence of this correlation on flame structure and radiative heat transfer in an ethylene turbulent jet flame where heat transfer by radiation dominates in the strongly sooting regions of the flame [187]. To the author' best knowledge, such an analysis has not been reported in the literature.

# V.2 Results and discussion

The modeled flame is an ethylene turbulent jet flame at atmospheric pressure investigated experimentally by Kent and Honnery [18]. The fuel is injected at 52.9 m/s by a 3 mm internal diameter injector (Re=15000). This flame belongs to the set of flames used to validate the model [67].

Figure V-1 shows the axial evolution of the cross correlation between the mixture fraction and the enthalpy defect, $C(\zeta, X_R)$, defined as:

$$C(\zeta, X_R) = \frac{\widetilde{X_R''\zeta''}}{\sqrt{\widetilde{X_R''^2}}\sqrt{\widetilde{\zeta''^2}}} \qquad \text{(V-1)}$$

The axial evolutions of the enthalpy defect and soot volume fraction are also plotted in this figure. The axial evolutions are plotted as a function of the mean mixture fraction in Fig V-1a and as a function of the height above the burner in Fig V-1b. It should be pointed out that the enthalpy defect is negative. The vertical continuous line in Fig V-1a represents the location of the mean stoichiometry.

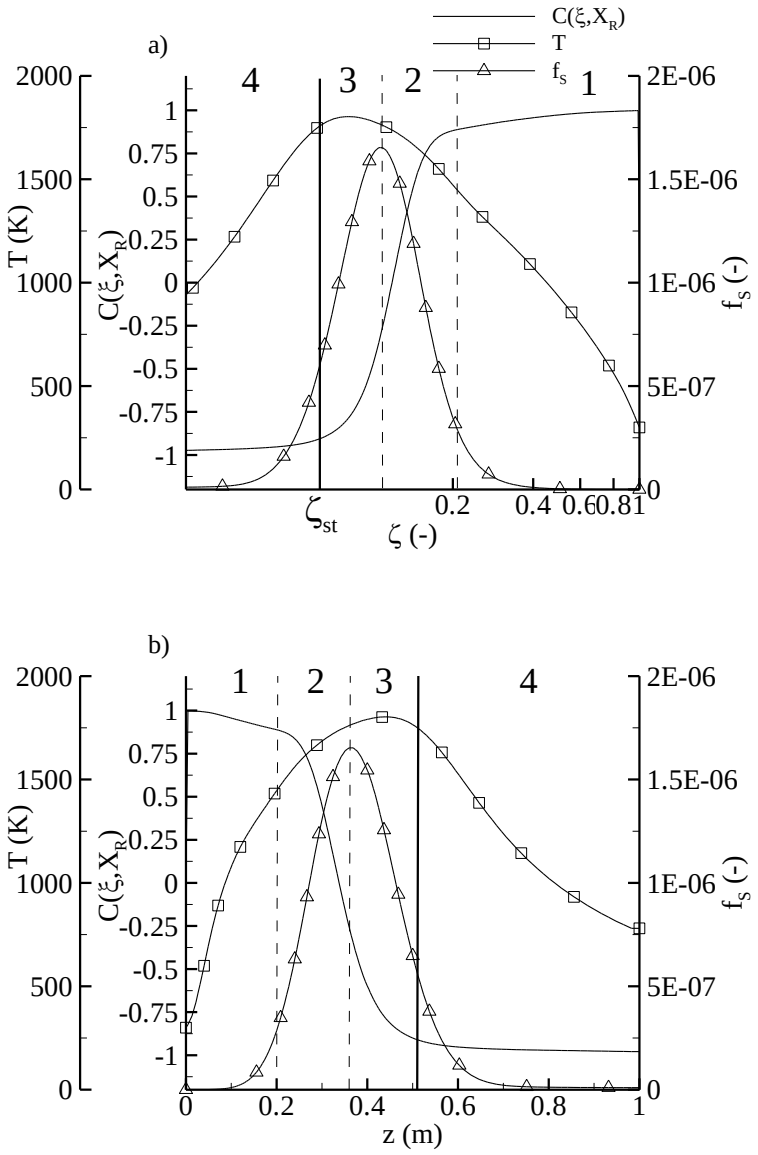


**Figure V-1. Axial evolution of the cross correlation between mixture fraction and enthalpy defect. a) as a function of the mixture fraction, b) as a function of the height above the burner. The evolutions of the mean enthalpy defect and the soot volume fraction are also plotted. The vertical continuous line in Fig. IV-1a represents the location of the mean stoichiometry. The vertical lines delimit the four regions.**

Four regions can be clearly distinguished and are delimited by vertical lines in Figs V-1a and b. The first region corresponds to $0.208 < \zeta < 1$ ($0 < z < 0.2$ m). In this part of the fuel rich region, the soot volume fraction is low and the radiative loss is dominated by gas radiation. $C(\zeta, X_R)$ is close to 1. The positive correlation between mixture fraction and

enthalpy defect can be explained as follows: a negative fluctuation of the mixture fraction moves the mixture fraction toward its stoichiometric value. This induces an increase in temperature and molar concentrations of $CO_2$ and $H_2O$, leading to higher radiative loss and, in turn, to a lower value of the enthalpy defect. In addition, temperature and species molar concentrations are directly related to the mixture fraction which explains that the mixture fraction and the enthalpy defect parameter are perfectly correlated. The second region corresponds to the soot growth region ($0.1091 < \zeta < 0.208$ and $0.2\ \text{m} < z < 0.36\ \text{m}$). The radiative loss becomes progressively dominated by soot and the enthalpy defect parameter becomes strongly dependent of both soot volume fraction and temperature. Soot volume fraction and mixture fraction are expected to be non-correlated in the region of soot formation [53]. As a consequence, $C(\zeta, X_R)$ decreases to reach approximately zero at the peak of soot volume fraction ($\zeta = 0.1091$ and $z = 0.36$ m). The third region correspond to the region located between the peak of soot volume fraction and the stoichiometry wheresoot oxidation prevails ($0.0635 < \zeta < 0.1091$ and $0.36\text{m} < z < 0.51$ m). The soot volume fraction and mixture fraction in the soot oxidation region is expected to be better correlated [53] (see also the results of the previous chapter). As a consequence, a negative fluctuation of mixture fraction induces a decrease in soot volume fraction and then leads to a higher value of the enthalpy defect. This explains that the cross correlation between the mixture fraction and the enthalpy defect parameter becomes negative. The last region corresponds to the fuel lean region ($\zeta > 0.0635$ and $z > 0.51$ m). Soot is fully oxidized and radiative loss results from gas-phase radiation. A positive fluctuation of the mixture fraction moves the mixture fraction toward the stoichiometry, leading to higher temperature and molar concentrations of the radiatively participating species and, in turn, to lower value of the enthalpy defect parameter. Consequently, mixture fraction and enthalpy defect parameter are found to be perfectly negatively correlated.

In summary, the mixture fraction and enthalpy defect are positively correlated in the soot free region located just above the burner ($0 < z < 0.2$ m), becomes statistically-independent in the region of soot growth ($0.2\ \text{m} < z < 0.36$ m) and becomes negatively correlated in the region located downstream the soot peak ($z > 0.36$ m). Figure V-1b shows also that the enthalpy defect appears to be low in the region located below z =0.2

m. This means that, in this part of the flame, the radiative loss does not affect significantly the flame structure.

As mentioned in the introduction, mixture fraction and enthalpy defect are correlated over a large part of the flame. The effects of this correlation on the flame structure and the radiative properties are analyzed in the next section. In order to make this analysis, a simulation was run by considering the mixture fraction and the enthalpy defect as statically independent. As usually done in the literature [52,119,182–185], a Dirac delta function centered on the mean value for $X_R$ was considered. As a consequence, the default set of composition variables is reduced to $\boldsymbol{\phi} = (\zeta, Y_s, N_s)$ and the Favre and Reynolds averaged values for a quantity of interest, $Q(\zeta, \chi, X_R, Y_s, N_s)$, are then computed as:

$$\begin{aligned}\tilde{Q} &= \iint Q(\boldsymbol{\psi}, \chi, X_R)\widetilde{f_\phi}(\boldsymbol{\psi}; \boldsymbol{x}, t)\delta[\chi - \tilde{\chi}(\boldsymbol{x}, t)]\delta\left[X_R - \widetilde{X_R}(\boldsymbol{x}, t)\right]d\boldsymbol{\psi}d\chi dX_R \\ &= \frac{1}{N_F}\sum_{n=1}^{N_F} Q(\boldsymbol{\phi_n}, \tilde{\chi}, \widetilde{X_R})\end{aligned} \tag{V-2}$$

$$\begin{aligned}\tilde{Q} &= \iint \frac{\langle\rho\rangle}{\rho(\boldsymbol{\psi}, \chi)} Q(\boldsymbol{\psi}, \chi, X_R)\widetilde{f_\phi}(\boldsymbol{\psi}; \boldsymbol{x}, t)\delta[\chi - \tilde{\chi}(\boldsymbol{x}, t)]\delta\left[X_R - \widetilde{X_R}(\boldsymbol{x}, t)\right]d\boldsymbol{\psi}d\chi dX_R \\ &= \frac{\langle\rho\rangle}{N_F}\sum_{n=1}^{N_F} Q(\boldsymbol{\phi_n}, \tilde{\chi}, \widetilde{X_R})\end{aligned} \tag{V-3}$$

The Reynolds averaged value of the divergence of the radiative flux becomes:

$$\begin{aligned}\langle\nabla \boldsymbol{q_R}\rangle = 4\pi &\int \frac{\langle\rho\rangle}{N_F}\sum_{n=1}^{N_F} \frac{\kappa_\eta(\boldsymbol{\phi_n}, \tilde{\chi}, \widetilde{X_R})I_{b\eta}(\boldsymbol{\phi_n}, \tilde{\chi}, \widetilde{X_R})}{\rho(\boldsymbol{\phi_n}, \tilde{\chi}, \widetilde{X_R})} d\eta \\ &- \int \frac{\langle\rho\rangle}{N_F}\sum_{n=1}^{N_F} \frac{\kappa_\eta(\boldsymbol{\phi_n}, \tilde{\chi}, \widetilde{X_R})}{\rho(\boldsymbol{\phi_n}, \tilde{\chi}, \widetilde{X_R})}\langle G_\eta\rangle d\eta\end{aligned} \tag{V-4}$$

## V.2.1 Effect of the correlation on flame structure

Figure V-2 shows the axial evolutions of the mean temperature and rms values of temperature, (Fig. V-2a), of the mean soot volume fraction and rms values of soot volume fraction (Fig. V-2b), and of the mean soot surface growth and oxidation rates (Fig. V-2c and d). For each quantity, the profiles obtained with and without considering the correlation between mixture fraction and enthalpy defect are plotted. Mean temperature

and soot volume fractions are compared with the experimental data obtained in [18], showing a satisfactory agreement.

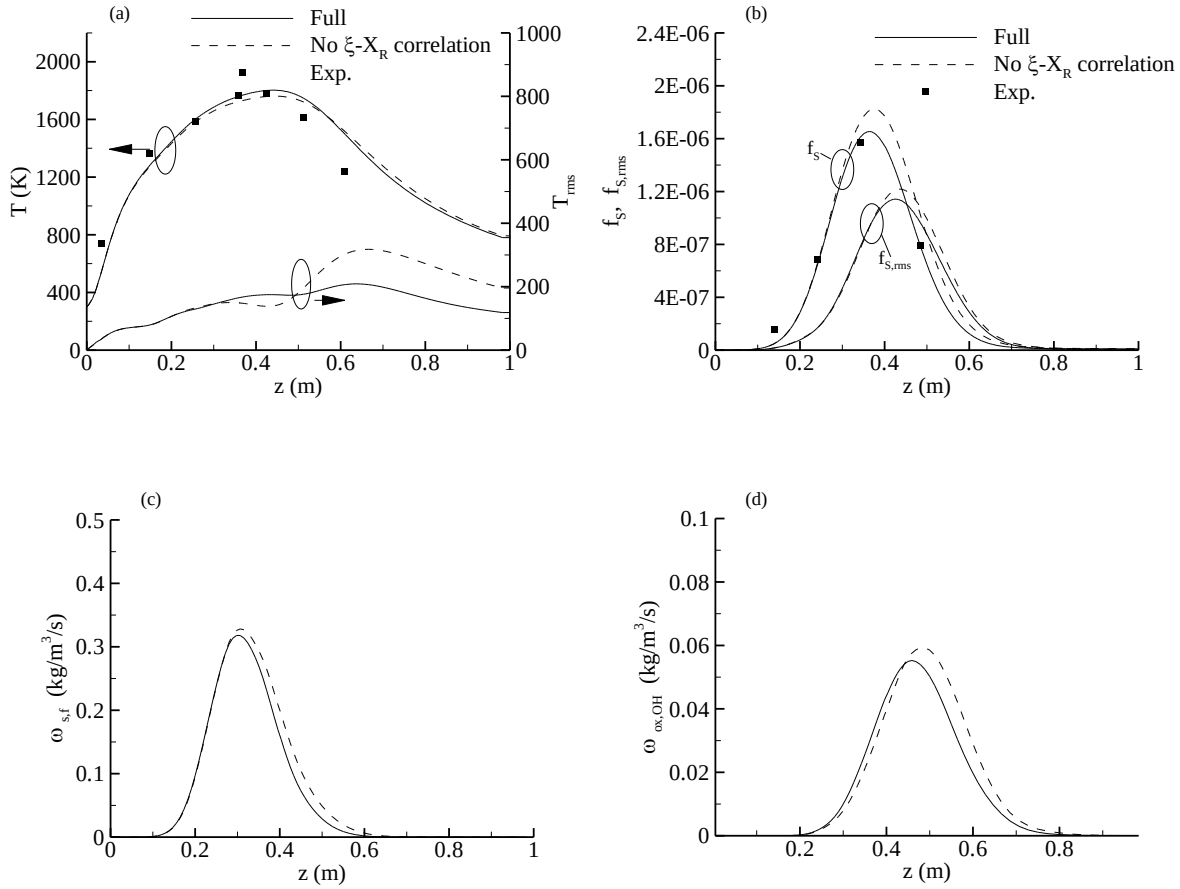


**Figure V-2. Axial evolution of: a) mean temperature and rms values of temperature, b) mean soot volume fraction and rms values of soot volume fraction, c) mean soot formation rate and d) mean soot oxidation rate.**

As discussed in the previous section, enthalpy defect and mixture fraction are strongly positively and negatively correlated in the region located below $z$ = 0.2 m and in the region located above $z$ = 0.36 m, respectively. Consequently, the effects of disregarding the correlation are expected to affect the flame structure in these regions. Figure V-2 shows that the calculations made with and without considering the correlation exhibit differences in the region located above $z$ = 0.36m whereas both simulations are very similar in the region located below $z$ = 0.2 m. The enthalpy defect in this latter part

is relatively low which explains that accounting or not for the correlation does not have a significant impact on the flame structure.

The differences induced by neglecting the mixture fraction/enthalpy defect correlation in the region located above the peak of soot volume fraction ($z$ > 0.36 m) are quantified. Figure V-2a shows that the peak of mean temperature is reduced by about 40 K when the correlation is disregarded. The influence on the temperature fluctuations is more significant. The rms values of temperature at $z$ = 0.65 m are of about 208 K when the correlation is considered and are enhanced to approximately 317 K when the correlation is not taken into account. The peaks of mean soot volume fraction and fluctuations of soot volume fraction are enhanced by 11% and 7% as the correlation is not considered. In addition, non-negligible discrepancies are observed downstream the peaks. Soot production results from a balance between soot formation and soot oxidation. The soot formation rate consists in the sum of the inception and surface growth rates (Fig. V-2c). The soot oxidation rate is computed as the sum of the oxidation rates by $O_2$, OH and O (Fig. V-2d). Figure V-2c shows that a significant part of the soot mass growth occurs in the region (0.2 m < $z$ < 0.36 m) where the mixture fraction and the enthalpy defect are not well correlated. This explains that the peak of soot formation is not significantly affected when the correlation is neglected, with an enhancement of only 3 %. In an opposite way, the most important part of the oxidation takes place for $z$ > 0.36 m. Soot oxidation appears then more affected than the soot formation. The peak is increased by about 8 % when the correlation is not considered (Fig. V-2d).

## V.2.2 Effect of the correlation on radiative outputs

The evolutions of the divergence of the radiative flux along the flame axis and of the radiative heat flux at a distance of 0.1 m from the burner are plotted in Fig. V-3a and b, respectively. As discussed previously, the influence of neglecting the correlation has significant effects for $z$ > 0.36 m. In particular, the peak of radiative heat flux is increased by about 20% when the correlation is disregarded. In addition, in the region located downstream of the peak, the radiative heat flux is also strongly overestimated when the correlation is neglected. The radiant fraction, defined as the ratio between the energy radiated away from the flame to the heat release rate, is 0.21 when the correlation is taken

into account and is increased to 0.259 when the correlation is disregarded, leading to discrepancies of 23 %.

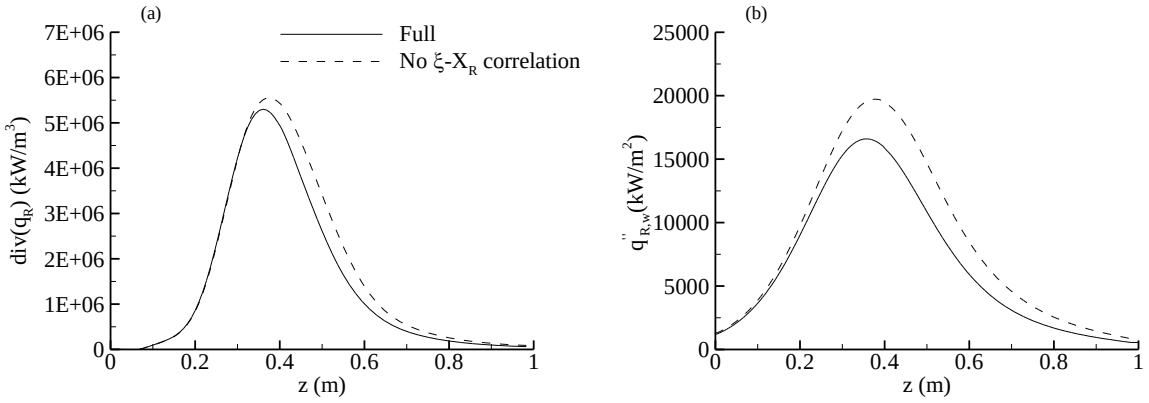


**Figure V-3. a) Evolution of the divergence of net heat flux along the flame axis, b) axial distribution of the incident heat flux at a distance of 0.1 m from the flame axis.**

# V.3 Conclusions

The influence of the correlation between mixture fraction and enthalpy defect on flame structure and radiative heat transfer is investigated by simulating an ethylene turbulent jet flame and by considering or not this correlation. Mixture fraction and enthalpy defect are found to be strongly correlated over a large part of the flame. A strong positive correlation between these quantities is observed in the fuel-rich free-soot part of the flame located just above the burner. However, radiative loss in this part of flame is low and neglecting the correlation does not affect the flame structure. A strong negative correlation is observed in the region of the flame located downstream the peak of soot volume fraction. Disregarding the correlation in this part of flame leads to non-negligible effects on mean and fluctuations of temperature and soot volume fraction. Neglecting this correlation is also found to increase the radiative loss by about 20%.

# Conclusions and perspectives

The numerical simulation of confined fires is a challenging task. It involves fluid dynamics, heat and mass transfer including radiative transfer, multi-phase flow, combustion, soot production, thermal degradation of solid/liquid materials, and turbulence. This Phd thesis focused on gas-phase phenomena. The global objective was to develop, implement and validate a transported Probability Density Function (PDF) method. This method is a flexible numerical tool, providing an effective resolution to the closure problems that arise from averaging or filtering the highly nonlinear chemical source terms, and terms that correspond to other one-point physical processes (e.g., radiative emission) in the instantaneous governing equations. A special attention was paid on the PDF-based modeling of radiative heat transfer and turbulence–radiation interactions and on PDF-based models for soot production since soot radiation is the main mode of heat transfer in industrial fires. The developments were made on a RANS framework and by using a flamelet combustion model. These choice are not related to limitations of the model since transported PDF methods can be also used as subfilter-scale models for large-eddy simulation (filtered density function methods) and are designed to model chemical source terms.

The joint scalar PDF, considered in the present study, is a function of the mixture fraction, enthalpy defect, scalar dissipation rate and representative soot properties. Soot production is modeled by a semi-empirical acetylene/benzene-based soot model. Spectral gas and soot radiation is modeled using a Wide-Band Correlated-k model. Emission turbulent radiation interactions (TRIs) are computed exactly based on the transported PDF method, whereas absorption TRIs are modeled using the Optically-Thin Fluctuation Approximation. The Stochastic Eulerian Field method was chosen to solve the PDF transport equation.

The model was validated by simulating twelve well documented turbulent jet diffusion flames, covering a large range of fuel sooting propensity and flow conditions. Model predictions are found to be in reasonable agreement with experimental data in terms of flame structure, soot quantities and radiative loss. Mean soot volume fractions are predicted within a factor of two of the experiments whereas radiant fractions and peaks of wall radiative fluxes are within 20%. The transported PDF approach was found to improve significantly the predictions of soot production and radiative heat transfer as compared to classical presumed-PDF approaches. These latter methods ignore the coupling between the soot quantities and the scalars that defines the thermochemical state of the gas phase, resulting in a poor description of the soot production and soot emission term of radiation.

The numerical model has been used to evaluate in details the effect of Turbulence-Radiation Interactions (TRIs) on the soot emission term. To the best of the author knowledge, such an evaluation has not been reported in literature in the past. Five turbulent jet flames, characterized by different Reynolds numbers to evaluate the influence of turbulence and by different fuels to evaluate the effects of fuel sooting propensity, were simulated. It was found that total soot emission, as well as the contribution of soot emission to the total emission, decreases with the fuel sooting propensity and as the Reynolds number increases. Furthermore, soot emission can never be neglected, even for low sooting fuels. It was also found that TRIs tend to enhance soot radiative emission, but that this increase is reduced when increasing the Reynolds. TRIs affect the total soot emission term through three terms:

- The temperature self-correlation. It is the source of enhancement of soot emission. This term is globally independent of turbulence intensity and fuel sooting propensity.
- The time-averaged Planck-mean absorption coefficient, which behaves in the same manner as the correlation between soot volume fraction and temperature. This correlation was found to be negative. This term therefore tends to reduce soot emission.
- The correlation between soot absorption coefficient and the Planck function, which has the same behavior as the correlation between the soot volume fraction and the temperature and also tends to reduce soot emission. It is also more strongly negative

as the Reynolds number increases, which explains the inhibition of the increase in soot emission due to TRI as the Reynolds number increases.

In addition, it was shown that the negative behavior of the correlation between soot volume fraction and temperature results from the structure of the turbulent diffusion flame and, as such, is independent of the fuel. In addition, this negative behavior increased as the radiative heat transfer due to soot is enhanced.

The model was also applied to provide a better understanding of the effects of the correlation between mixture fraction and enthalpy defect parameter on the flame structure and radiative loss. The influence of this correlation was studied by simulating an ethylene-air turbulent jet diffusion flame. The analysis of the correlation coefficient between these two parameters shows that mixture fraction and enthalpy defect parameter are strongly correlated over a large part of the flame, positively upstream and negatively downstream the peak of soot volume fraction. The impact of this correlation on flame structure and radiative loss was evaluated by comparing two simulations, one including the correlation, and another neglecting it by assuming that the enthalpy defect is statistically independent of the other scalars. The effect on flame structure and radiative output was more strongly visible in the downstream part of the flame, where radiative transfer is more important. Temperature fluctuations increased by about 50% and overall radiative loss increased by about 20% when the correlation was neglected.

There are a significant number of perspectives to this work. Four of them will be described below.

The purely buoyant fire plume above a pool fire is an important canonical problem in fire science. Early attempts to use RANS models to simulate pool fires revealed that significant discrepancies between model predictions and experiments and a strong dependence on upstream boundary conditions [22–24]. In general, RANS models are less successful in predicting purely buoyant flames than momentum jet flames. This outcome is attributed to the difficulties in modeling buoyancy-driven turbulence, its induced high flame intermittency, as well as the fact that all turbulent scales need to be modeled in RANS. Many recent numerical studies [25–31] of fire plumes are carried out by Large Eddy Simulations (LES), which may alleviate the difficulties inherent in RANS by resolving transient large turbulent eddies. As discussed above, transported PDF methods can be

also used as subfilter-scale models for LES (filtered density function methods) and are then well designed to be applied in LES.

The Steady Laminar Flamelet model is a point function where species mass fraction distributions versus mixture fraction depend on scalar dissipation and enthalpy defect only. As a consequence, it does not contain the transport terms and is unable to predict situations where chemical reactions are frozen and unreactive mixing occurs, as it may be the case in under-ventilated fire scenarios. However, PDF methods can provide an exact closure of chemical source terms when directly coupled to chemical mechanisms and are well designed to address this issue.

The absorption turbulence radiation interactions are not fully understood. They represent the nonlinear coupling between incident radiation and the local absorption coefficient. They are the consequence of property fluctuations across the domain and their modeling requires having a detailed knowledge of the instantaneous fields of temperature and species. Modest, Haworth and co-workers take advantage of the fact that transported PDF method based on the Lagrangian Particles Method provides realizations of the flow. This allows to model these interactions in an exact manner by introducing a particle-based photon Monte Carlo method coupled to the PDF method [20,33]. They found that absorption TRI can be neglected for lab-scale non-luminous and luminous flames by using the Optically Thin Fluctuations Approximation (OTFA), but has to take into account for larger flames. However, the limit of validity of the OTFA has not been established. This question is of importance since the photo Monte Carlo Method appears to be particularly time-consuming which raises the question of the development of simplified approaches in order to include absorption TRIs.

The modeling of the soot production can be improved in two ways. The first is relative to the soot kinetics and the consideration of PAH-based soot production models. One of the difficulties lies in the treatment of the PAH which are governed by relatively slow chemistry and cannot, a priori, be directly included in the flamelet library. The second point is relative to a better description of the morphology of soot particle. Bi-variate number density function of the volume and surface of aggregate particle can be used and a method has to be developed to solve the corresponding population balance equation. Among these methods, moment methods seems to be appropriate [34–42].

# Bibliography


[1] V. Novozhilov, *Computational fluid dynamics modeling of compartment fires*, Progress in Energy and Combustion science 27 (2001), pp. 611–666.

[2] G. Cox, *Fire research in the 21st century*, Fire safety journal 32 (1999), pp. 203–219.

[3] N. Peters, *Laminar diffusion flamelet models in non-premixed turbulent combustion*, Progress in Energy and Combustion Science 10 (1984), pp. 319–339.

[4] D. Carbonell, C. Perezsegarra, P. Coelho and A. Oliva, *Flamelet mathematical models for non-premixed laminar combustion*, Combustion and Flame 156 (2009), pp. 334–347.

[5] K.M. Leung, R.P. Lindstedt and W.P. Jones, *A simplified reaction mechanism for soot formation in nonpremixed flames*, Combustion and flame 87 (1991), pp. 289–305.

[6] P.R. Lindstedt, *Simplified Soot Nucleation and Surface Growth Steps for Non-Premixed Flames*, in *Soot Formation in Combustion*, H. Bockhorn, ed., Springer Berlin Heidelberg, 1994, pp. 417–441.

[7] D. Carbonell, A. Oliva and C.D. Perez-Segarra, *Implementation of two-equation soot flamelet models for laminar diffusion flames*, Combustion and Flame 156 (2009), pp. 621–632.

[8] J. Ströhle, *Wide band correlated-k approaches for non-grey radiation modelling in oxy-fuel combustion with dry recycling*, Fuel 90 (2011), pp. 3007–3013.

[9] H. Chang and T.T. Charalampopoulos, *Determination of the Wavelength Dependence of Refractive Indices of Flame Soot*, Proceedings of the Royal Society of London A: Mathematical, Physical and Engineering Sciences 430 (1990), pp. 577–591.

[10] P.J. Coelho, *Numerical simulation of the interaction between turbulence and radiation in reactive flows*, Progress in Energy and Combustion Science 33 (2007), pp. 311–383.

[11] J.C.-K. Chai, *A Finite-Volume Method for Radiation heat transfer*, PhD Thesis, University of Minnesota, 1994.

[12] S.B. Pope, *PDF methods for turbulent reactive flows*, Progress in Energy and Combustion Science 11 (1985), pp. 119–192.

[13] D.C. Haworth, *Progress in probability density function methods for turbulent reacting flows*, Progress in Energy and Combustion Science 36 (2010), pp. 168–259.

[14] R.O. Fox, *Computational Models for Turbulent Reacting Flows*, Cambridge University Press, 2003.

[15] D.C. Haworth and S.B. Pope, *Transported probability density function methods for Reynolds-averaged and large-eddy simulations*, in *Turbulent Combustion Modeling*, Springer, 2011, pp. 119–142.

[16] L. Valiño, *A Field Monte Carlo Formulation for Calculating the Probability Density Function of a Single Scalar in a Turbulent Flow*, Flow, Turbulence and Combustion 60 (1998), pp. 157–172.

[17] G. Hauke and L. Valiño, *Computing reactive flows with a field Monte Carlo formulation and multi-scale methods*, Computer Methods in Applied Mechanics and Engineering 193 (2004), pp. 1455–1470.

[18] J.H. Kent and D. Honnery, *Soot and Mixture Fraction in Turbulent Diffusion Flames*, Combustion Science and Technology 54 (1987), pp. 383–398.

[19] T. Poinsot and D. Veynante, *Theoretical and Numerical Combustion*, Edwards, 2005.

[20] R.S. Mehta, M.F. Modest and D.C. Haworth, *Radiation characteristics and turbulence–radiation interactions in sooting turbulent jet flames*, Combustion Theory and Modelling 14 (2010), pp. 105–124.

[21] D. Burot, F. Nmira and J.-L. Consalvi, *On the influence of the correlation between enthalpy defect and mixture fraction in sooting turbulent jet flames*, Journal of Quantitative Spectroscopy and Radiative Transfer 184 (2016), pp. 68–75.

[22] F. Tamanini, *Reaction rates, air entrainment and radiation in turbulent fire plumes*, Combustion and Flame 30 (1977), pp. 85–101.

[23] H.Z. You and G.M. Faeth, *Buoyant axisymmetric turbulent diffusion flames in still air*, Combustion and Flame 44 (1982), pp. 261–275.

[24] N.L. Crauford, S.K. Liew and J.B. Moss, *Experimental and numerical simulation of a buoyant fire*, Combustion and flame 61 (1985), pp. 63–77.

[25] H.R. Baum, K.B. McGrattan and R.G. Rehm, *Three dimensional simulations of fire plume dynamics*, Fire Safety Science 5 (1997), pp. 511–522.

[26] Y. Xin, J. Gore, K.B. McGrattan, R.G. Rehm and H.R. Baum, *Large eddy simulation of buoyant turbulent pool fires*, Proceedings of the Combustion Institute 29 (2002), pp. 259–266.

[27] T.G. Ma and J.G. Quintiere, *Numerical simulation of axi-symmetric fire plumes: accuracy and limitations*, Fire Safety Journal 38 (2003), pp. 467–492.

[28] Y. Xin, J.P. Gore, K.B. McGrattan, R.G. Rehm and H.R. Baum, *Fire dynamics simulation of a turbulent buoyant flame using a mixture-fraction-based combustion model*, Combustion and Flame 141 (2005), pp. 329–335.

[29] Y. Xin, S.A. Filatyev, K. Biswas, J.P. Gore, R.G. Rehm and H.R. Baum, *Fire dynamics simulations of a one-meter diameter methane fire*, Combustion and Flame 153 (2008), pp. 499–509.

[30] Y. Kang and J.X. Wen, *Large eddy simulation of a small pool fire*, Combustion science and technology 176 (2004), pp. 2193–2223.

[31] J.X. Wen, K. Kang, T. Donchev and J.M. Karwatzki, *Validation of FDS for the prediction of medium-scale pool fires*, Fire Safety Journal 42 (2007), pp. 127–138.

[32] L. Tessé, F. Dupoirieux and J. Taine, *Monte Carlo modeling of radiative transfer in a turbulent sooty flame*, International Journal of Heat and Mass Transfer 47 (2004), pp. 555–572.

[33] L. Wang, D.C. Haworth, S.R. Turns and M.F. Modest, *Interactions among soot, thermal radiation, and NOx emissions in oxygen-enriched turbulent nonpremixed flames: a computational fluid dynamics modeling study*, Combustion and Flame 141 (2005), pp. 170–179.

[34] G. Blanquart, P. Pepiot-Desjardins and H. Pitsch, *Chemical mechanism for high temperature combustion of engine relevant fuels with emphasis on soot precursors*, Combustion and Flame 156 (2009), pp. 588–607.

[35] D.L. Marchisio and R.O. Fox, *Computational Models for Polydisperse Particulate and Multiphase Systems*, Cambridge University Press, 2013.

[36] M. Balthasar and M. Kraft, *A stochastic approach to calculate the particle size distribution function of soot particles in laminar premixed flames*, Combustion and Flame 133 (2003), pp. 289–298.

[37] M. Balthasar, A. Heyl, F. Mauß, F. Schmitt and H. Bockhorn, Flamelet modeling of soot formation in laminar ethyne/air-diffusion flames, in Symposium (International) on Combustion, 26 (1996), pp. 2369–2377.

[38] X.S. Bai, M. Balthasar, F. Mauss and L. Fuchs, *Detailed soot modeling in turbulent jet diffusion flames*, Symposium (International) on Combustion 27 (1998), pp. 1623–1630.

[39] M. Frenklach and S.J. Harris, *Aerosol dynamics modeling using the method of moments*, Journal of Colloid and Interface Science 118 (1987), pp. 252–261.

[40] A. Zucca, D.L. Marchisio, A.A. Barresi and R.O. Fox, *Implementation of the population balance equation in CFD codes for modelling soot formation in turbulent flames*, Chemical Engineering Science 61 (2006), pp. 87–95.

[41] D.L. Marchisio and A.A. Barresi, *Investigation of soot formation in turbulent flames with a pseudo-bivariate population balance model*, Chemical Engineering Science 64 (2009), pp. 294–303.

[42] M.E. Mueller, G. Blanquart and H. Pitsch, *Hybrid method of moments for modeling soot formation and growth*, Combustion and Flame 156 (2009), pp. 1143–1155.

[43] B. Sapa, *Contribution à l'extension d'un schéma incompressible pour les flammes à bas nombre de Froude-Pré-requis à la modélisation de l'incendie*, PhD Thesis, ISAE-ENSMA Ecole Nationale Supérieure de Mécanique et d'Aérotechique-Poitiers, 2011.

[44] J. De Ris, Fire radiation—a review, in Symposium (International) on Combustion, 17 (1979), pp. 1003–1016.

[45] G. Cox, *Combustion Fundamentals of Fire*, Acad. press London etc, 1995.

[46] R.S. Cant and E. Mastorakos, *An Introduction to Turbulent Reacting Flows*, Imperial College Press, 2008.

[47] T. Echekki and E. Mastorakos, *Turbulent Combustion Modeling*, Vol. 95, Fluid Mechanics and Its ApplicationsSpringer Netherlands, Dordrecht, 2011.

[48] J.-L. Consalvi, R. Demarco, A. Fuentes, S. Melis and J.P. Vantelon, *On the modeling of radiative heat transfer in laboratory-scale pool fires*, Fire Safety Journal 60 (2013), pp. 73–81.

[49] J.-L. Consalvi, R. Demarco and A. Fuentes, *Modelling thermal radiation in buoyant turbulent diffusion flames*, Combustion Theory and Modelling 16 (2012), pp. 817–841.

[50] A.C.Y. Yuen, G.H. Yeoh, V. Timchenko, S.C.P. Cheung and T.J. Barber, *Importance of detailed chemical kinetics on combustion and soot modelling of ventilated and under-ventilated fires in compartment*, International Journal of Heat and Mass Transfer 96 (2016), pp. 171–188.

[51] W. Yao, J. Zhang, A. Nadjai, T. Beji and M.A. Delichatsios, *A global soot model developed for fires: Validation in laminar flames and application in turbulent pool fires*, Fire Safety Journal 46 (2011), pp. 371–387.

[52] S.J. Brookes and J.B. Moss, *Predictions of soot and thermal radiation properties in confined turbulent jet diffusion flames*, Combustion and Flame 116 (1999), pp. 486–503.

[53] I.M. Aksit and J.B. Moss, *A hybrid scalar model for sooting turbulent flames*, Combustion and Flame 145 (2006), pp. 231–244.

[54] J.-L. Consalvi and F. Nmira, Modeling sooting turbulent diffusion flames with an hybrid flamelet/DQMOM-IEM model, in 9th Mediterranean Combustion Symposium, 2015.

[55] J.L. Consalvi and F. Nmira, *Effects of soot absorption coefficient–Planck function correlation on radiative heat transfer in oxygen-enriched propane turbulent diffusion flame*, Journal of Quantitative Spectroscopy and Radiative Transfer (2015), .

[56] W. Kollmann, I.M. Kennedy, M. Metternich and J.-Y. Chen, *Application of a Soot Model to a Turbulent Ethylene Diffusion Flame*, in *Soot Formation in Combustion*, H. Bockhorn, ed., Springer Berlin Heidelberg, 1994, pp. 503–526.

[57] S.B. Pope, *Turbulent Flows*, Cambridge University Press, 2000.

[58] B. Karlsson and J. Quintiere, *Enclosure Fire Dynamics*, CRC press, 1999.

[59] J. Quintiere, *Fundamentals of Fire Phenomena*, Wiley, 2006.

[60] S. Melis and L. Audouin, *Effects of vitiation on the heat release rate in mechanically-ventilated compartment fires*, Fire Safety Science 9 (2008), pp. 931–942.

[61] K.-O. Lee, C.M. Megaridis, S. Zelepouga, A.V. Saveliev, L.A. Kennedy, O. Charon et al., *Soot formation effects of oxygen concentration in the oxidizer stream of laminar coannular nonpremixed methane/air flames*, Combustion and Flame 121 (2000), pp. 323–333.

[62] C.K. Law, *Combustion Physics*, Cambridge university press, 2010.

[63] U. Maas and S.B. Pope, *Simplifying chemical kinetics: intrinsic low-dimensional manifolds in composition space*, Combustion and flame 88 (1992), pp. 239–264.

[64] F. Liu, H. Guo, G.J. Smallwood and Ö.L. Gülder, *Effects of gas and soot radiation on soot formation in a coflow laminar ethylene diffusion flame*, Journal of Quantitative Spectroscopy and Radiative Transfer 73 (2002), pp. 409–421.

[65] R. Demarco, F. Nmira and J.-L. Consalvi, *Influence of thermal radiation on soot production in Laminar axisymmetric diffusion flames*, Journal of Quantitative Spectroscopy and Radiative Transfer 120 (2013), pp. 52–69.

[66] R.S. Mehta, D.C. Haworth and M.F. Modest, *Composition PDF/photon Monte Carlo modeling of moderately sooting turbulent jet flames*, Combustion and Flame 157 (2010), pp. 982–994.

[67] J.-L. Consalvi, F. Nmira and D. Burot, *Simulations of sooting turbulent jet flames using a hybrid flamelet/stochastic Eulerian field method*, Combustion Theory and Modelling 20 (2016), pp. 221–257.

[68] M. Frenklach and H. Wang, *Detailed Mechanism and Modeling of Soot Particle Formation*, in *Soot Formation in Combustion*, H. Bockhorn, ed., Springer Berlin Heidelberg, 1994, pp. 165–192.

[69] M. Frenklach, *Reaction mechanism of soot formation in flames*, Physical Chemistry Chemical Physics 4 (2002), pp. 2028–2037.

[70] A. De Filippo, L.A. Sgro, G. Lanzuolo and A. D'Alessio, *Probe measurements and numerical model predictions of evolving size distributions in premixed flames*, Combustion and Flame 156 (2009), pp. 1744–1754.

[71] L.A. Sgro, A. De Filippo, G. Lanzuolo and A. D'Alessio, *Characterization of nanoparticles of organic carbon (NOC) produced in rich premixed flames by differential mobility analysis*, Proceedings of the Combustion Institute 31 (2007), pp. 631–638.

[72] B. Zhao, Z. Yang, Z. Li, M.V. Johnston and H. Wang, *Particle size distribution function of incipient soot in laminar premixed ethylene flames: effect of flame temperature*, Proceedings of the Combustion Institute 30 (2005), pp. 1441–1448.

[73] M. Frenklach and H. Wang, Detailed modeling of soot particle nucleation and growth, in Symposium (International) on Combustion, 23 (1991), pp. 1559–1566.

[74] H. Wang, D.X. Du, C.J. Sung and C.K. Law, Experiments and numerical simulation on soot formation in opposed-jet ethylene diffusion flames, in Symposium (International) on Combustion, 26 (1996), pp. 2359–2368.

[75] A. D'alessio, A. D'Anna, P. Minutolo, L.A. Sgro and A. Violi, *On the relevance of surface growth in soot formation in premixed flames*, Proceedings of the Combustion Institute 28 (2000), pp. 2547–2554.

[76] J.Y. Hwang and S.H. Chung, *Growth of soot particles in counterflow diffusion flames of ethylene*, Combustion and flame 125 (2001), pp. 752–762.

[77] C. Lautenberger, J.L. de Ris, N.A. Dembsey, J.R. Barnett and H.R. Baum, *A simplified model for soot formation and oxidation in CFD simulation of non-premixed hydrocarbon flames*, Fire Safety Journal 40 (2005), pp. 141–176.

[78] S.A. Zelepouga, A.V. Saveliev, L.A. Kennedy and A.A. Fridman, *Relative effect of acetylene and PAHs addition on soot formation in laminar diffusion flames of methane with oxygen and oxygen-enriched air*, Combustion and flame 122 (2000), pp. 76–89.

[79] M.D. Smooke, C.S. McEnally, L.D. Pfefferle, R.J. Hall and M.B. Colket, *Computational and experimental study of soot formation in a coflow, laminar diffusion flame*, Combustion and Flame 117 (1999), pp. 117–139.

[80] C.A. Echavarria, I.C. Jaramillo, A.F. Sarofim and J.S. Lighty, *Studies of soot oxidation and fragmentation in a two-stage burner under fuel-lean and fuel-rich conditions*, Proceedings of the Combustion Institute 33 (2011), pp. 659–666.

[81] L.-H. Dorey, *Modélisation des phénomènes couplés combustion-formation des suies-transferts radiatifs dans les chambres de combustion de turbine à gaz*, PhD Thesis, Ecole Centrale Paris, 2012.

[82] R.S. Mehta, *Detailed modeling of soot formation and turbulence-radiation interaction in turbulent jet flames*, PhD Thesis, Pennsylvania State University, 2008.

[83] I.M. Kennedy, *Models of soot formation and oxidation*, Progress in Energy and Combustion Science 23 (1997), pp. 95–132.

[84] Q. Zhang, M.J. Thomson, H. Guo, F. Liu and G.J. Smallwood, *A numerical study of soot aggregate formation in a laminar coflow diffusion flame*, Combustion and Flame 156 (2009), pp. 697–705.

[85] F. Gelbard, Y. Tambour and J.H. Seinfeld, *Sectional representations for simulating aerosol dynamics*, Journal of Colloid and Interface Science 76 (1980), pp. 541–556.

[86] M.F. Modest, *Radiative Heat Transfer*, Access Online via Elsevier, 2013.

[87] R. Goody, R. West, L. Chen and D. Crisp, *The correlated-k method for radiation calculations in nonhomogeneous atmospheres*, Journal of Quantitative Spectroscopy and Radiative Transfer 42 (1989), pp. 539–550.

[88] A.A. Lacis and V. Oinas, *A description of the correlated k distribution method for modeling nongray gaseous absorption, thermal emission, and multiple scattering in vertically inhomogeneous atmospheres*, Journal of Geophysical Research: Atmospheres 96 (1991), pp. 9027–9063.

[89] A. Soufiani and J. Taine, *High temperature gas radiative property parameters of statistical narrow-band model for H2O, CO2 and CO, and correlated-K model for H2O and CO2*, International Journal of Heat and Mass Transfer 40 (1997), pp. 987–991.

[90] A. Wang and M.F. Modest, *High-accuracy, compact database of narrow-band k-distributions for water vapor and carbon dioxide*, Journal of Quantitative Spectroscopy and Radiative Transfer 93 (2005), pp. 245–261.

[91] W.A. Fiveland, *Discrete-ordinates solutions of the radiative transport equation for rectangular enclosures*, Journal of Heat Transfer 106 (1984), pp. 699–706.

[92] G.D. Raithby and E.H. Chui, *A finite-volume method for predicting a radiant heat transfer in enclosures with participating media*, Journal of Heat Transfer 112 (1990), pp. 415–423.

[93] S.S. Sazhin, E.M. Sazhina, O. Faltsi-Saravelou and P. Wild, *The P-1 model for thermal radiation transfer: advantages and limitations*, Fuel 75 (1996), pp. 289–294.

[94] F. Liu, ö. L. Gülder, G.J. Smallwood and Y. Ju, *Non-grey gas radiative transfer analyses using the statistical narrow-band model*, International Journal of Heat and Mass Transfer 41 (1998), pp. 2227–2236.

[95] L. Zhang, A. Soufiani and J. Taine, *Spectral correlated and non-correlated radiative transfer in a finite axisymmetric system containing an absorbing and emitting real gasparticle mixture*, International Journal of Heat and Mass Transfer 31 (1988), pp. 2261–2272.

[96] M.E. Kounalakis, J.P. Gore and G.M. Faeth, Turbulence/radiation interactions in nonpremixed hydrogen/air flames, in Symposium (international) on combustion, 22 (1989), pp. 1281–1290.

[97] M.E. Kounalakis, J.P. Gore and G.M. Faeth, *Mean and fluctuating radiation properties of nonpremixed turbulent carbon monoxide/air flames*, Journal of heat transfer 111 (1989), pp. 1021–1030.

[98] Y.R. Sivathanu, J.P. Gore and J. Dolinar, *Transient scalar properties of strongly radiating jet flames*, Combustion science and technology 76 (1991), pp. 45–66.

[99] P.J. Coelho, P. Perez and M. El Hafi, *Benchmark numerical solutions for radiative heat transfer in two-dimensional axisymmetric enclosures with nongray sooting media*, Numerical Heat Transfer: Part B: Fundamentals 43 (2003), pp. 425–444.

[100] V. Goutiere, F. Liu and A. Charette, *An assessment of real-gas modelling in 2D enclosures*, Journal of Quantitative Spectroscopy and Radiative Transfer 64 (2000), pp. 299–326.

[101] F. Liu, *Numerical solutions of three-dimensional non-grey gas radiative transfer using the statistical narrow-band model*, Journal of heat transfer 121 (1999), pp. 200–203.

[102] F. Liu, G.J. Smallwood and Ö.L. Gülder, *Application of the statistical narrow-band correlated-k method to low-resolution spectral intensity and radiative heat transfer calculations—effects of the quadrature scheme*, International Journal of Heat and Mass Transfer 43 (2000), pp. 3119–3135.

[103] F. Liu, G.J. Smallwood and Gulder, O., *Band Lumping Strategy for Radiation Heat Transfer Calculations Using a Narrowband Model*, Journal of Thermophysics and Heat Transfer 14 (2000), pp. 278–281.

[104] F. Liu, G.J. Smallwood and Ö.L. Gülder, *Application of the statistical narrow-band correlated-k method to non-grey gas radiation in CO2–H2O mixtures: approximate treatments of overlapping bands*, Journal of Quantitative Spectroscopy and Radiative Transfer 68 (2001), pp. 401–417.

[105] M.F. Modest and R.J. Riazzi, *Assembly of full-spectrum k-distributions from a narrow-band database; effects of mixing gases, gases and nongray absorbing particles, and*

*mixtures with nongray scatterers in nongray enclosures*, Journal of Quantitative Spectroscopy and Radiative Transfer 90 (2005), pp. 169–189.

[106] V.P. Solovjov and B.W. Webb, *SLW modeling of radiative transfer in multicomponent gas mixtures*, Journal of Quantitative Spectroscopy and Radiative Transfer 65 (2000), pp. 655–672.

[107] H.C. Hottel and A.F. Sarofim, *Radiative transfer*, New York (1967), pp. 20–24.

[108] M.F. Modest, *The Weighted-Sum-of-Gray-Gases Model for Arbitrary Solution Methods in Radiative Transfer*, Journal of Heat Transfer 113 (1991), pp. 650–656.

[109] M.K. Denison and B.W. Webb, *A Spectral Line-Based Weighted-Sum-of-Gray-Gases Model for Arbitrary RTE Solvers*, Journal of Heat Transfer 115 (1993), pp. 1004–1012.

[110] M.K. Denison and B.W. Webb, *The spectral line-based weighted-sum-of-gray-gases model in nonisothermal nonhomogeneous media*, Journal of Heat Transfer 117 (1995), pp. 359–365.

[111] M.F. Modest and H. Zhang, *The Full-Spectrum Correlated-k Distribution for Thermal Radiation From Molecular Gas-Particulate Mixtures*, Journal of Heat Transfer 124 (2002), pp. 30.

[112] V.P. Solovjov and B.W. Webb, *An efficient method for modeling radiative transfer in multicomponent gas mixtures with soot*, Journal of heat transfer 123 (2001), pp. 450–457.

[113] J.L. Consalvi and F. Liu, *Radiative Heat Transfer Through the Fuel-Rich Core of Laboratory-Scale Pool Fires*, Combustion Science and Technology 186 (2014), pp. 475–489.

[114] H. Chu, M. Gu, J.-L. Consalvi, F. Liu and H. Zhou, *Effects of total pressure on non-grey gas radiation transfer in oxy-fuel combustion using the LBL, SNB, SNBCK, WSGG, and FSCK methods*, Journal of Quantitative Spectroscopy and Radiative Transfer 172 (2016), pp. 24–35.

[115] H. Chu, F. Liu and H. Zhou, *Calculations of gas thermal radiation transfer in one-dimensional planar enclosure using LBL and SNB models*, International Journal of Heat and Mass Transfer 54 (2011), pp. 4736–4745.

[116] H. Chu, J.-L. Consalvi, M. Gu and F. Liu, Calculations of radiative heat transfer in an axisymmetric jet diffusion flame at elevated pressure, in 8th International Symposium on Radiative Transfer, RAD-16, 2016.

[117] R. Demarco, J.-L. Consalvi, A. Fuentes and S. Melis, *Assessment of radiative property models in non-gray sooting media*, International Journal of Thermal Sciences 50 (2011), pp. 1672–1684.

[118] J.-L. Consalvi and F. Liu, *Radiative heat transfer in the core of axisymmetric pool fires – I: Evaluation of approximate radiative property models*, International Journal of Thermal Sciences 84 (2014), pp. 104–117.

[119] A. Habibi, B. Merci and D. Roekaerts, *Turbulence radiation interaction in Reynolds-averaged Navier–Stokes simulations of nonpremixed piloted turbulent laboratory-scale flames*, Combustion and Flame 151 (2007), pp. 303–320.

[120] P.J. Coelho, *Detailed numerical simulation of radiative transfer in a nonluminous turbulent jet diffusion flame*, Combustion and Flame 136 (2004), pp. 481–492.

[121] J.L. Consalvi, *Influence of turbulence–radiation interactions in laboratory-scale methane pool fires*, International Journal of Thermal Sciences 60 (2012), pp. 122–130.

[122] G. Li and M.F. Modest, *Application of composition PDF methods in the investigation of turbulence–radiation interactions*, Journal of Quantitative Spectroscopy and Radiative Transfer 73 (2001), pp. 461–472.

[123] G. Li and M.F. Modest, *Importance of turbulence-radiation interactions in turbulent diffusion jet flames*, Journal of heat transfer 125 (2003), pp. 831–838.

[124] A. Wang, M.F. Modest, D.C. Haworth and L. Wang, *Monte Carlo simulation of radiative heat transfer and turbulence interactions in methane/air jet flames*, Journal of Quantitative Spectroscopy and Radiative Transfer 109 (2008), pp. 269–279.

[125] J.P. Gore and G.M. Faeth, *Structure and radiation properties of luminous turbulent acetylene/air diffusion flames*, Journal of heat transfer 110 (1988), pp. 173–181.

[126] Y.R. Sivathanu and G.M. Faeth, *Temperature/soot volume fraction correlations in the fuel-rich region of buoyant turbulent diffusion flames*, Combustion and flame 81 (1990), pp. 150–165.

[127] Y.R. Sivathanu and G.M. Faeth, *Soot volume fractions in the overfire region of turbulent diffusion flames*, Combustion and Flame 81 (1990), pp. 133–149.

[128] J.J. Murphy and C.R. Shaddix, *Soot properties measurements in a two-meter diameter JP-8 pool fire*, Combustion Science and Technology 178 (2006), pp. 865–894.

[129] H. Pitsch, E. Riesmeier and N. Peters, *Unsteady flamelet modeling of soot formation in turbulent diffusion flames*, Combustion science and technology 158 (2000), pp. 389–406.

[130] A. Kronenburg, R.W. Bilger and J.H. Kent, *Modeling soot formation in turbulent methane–air jet diffusion flames*, Combustion and Flame 121 (2000), pp. 24–40.

[131] R.P. Lindstedt and S.A. Louloudi, *Joint-scalar transported PDF modeling of soot formation and oxidation*, Proceedings of the Combustion Institute 30 (2005), pp. 775–783.

[132] F. Mauss, K. Netzell and H. Lehtiniemi, *Aspects of modeling soot formation in turbulent diffusion flames*, Combustion science and technology 178 (2006), pp. 1871–1885.

[133] Y. Yunardi, R.M. Woolley and M. Fairweather, *Conditional moment closure prediction of soot formation in turbulent, nonpremixed ethylene flames*, Combustion and Flame 152 (2008), pp. 360–376.

[134] R.M. Woolley, M. Fairweather and Yunardi, *Conditional moment closure modelling of soot formation in turbulent, non-premixed methane and propane flames*, Fuel 88 (2009), pp. 393–407.

[135] V. Sabel'nikov and O. Soulard, *Rapidly decorrelating velocity-field model as a tool for solving one-point Fokker-Planck equations for probability density functions of turbulent reactive scalars*, Physical Review E 72 (2005), .

[136] A.E. Lutz, R.J. Kee, J.F. Grcar and F.M. Rupley, *OPPDIF: A Fortran program for computing opposed-flow diffusion flames*, Sandia National Labs., Livermore, CA (United States), 1997.

[137] H. Pitsch and N. Peters, *A consistent flamelet formulation for non-premixed combustion considering differential diffusion effects*, Combustion and Flame 114 (1998), pp. 26–40.

[138] Z. Qin, V.V. Lissianski, H. Yang, W.C. Gardiner, S.G. Davis and H. Wang, *Combustion chemistry of propane: a case study of detailed reaction mechanism optimization*, Proceedings of the Combustion Institute 28 (2000), pp. 1663–1669.

[139] H. Guo, F. Liu, G.J. Smallwood and Ö.L. Gülder, *Numerical study on the influence of hydrogen addition on soot formation in a laminar ethylene–air diffusion flame*, Combustion and Flame 145 (2006), pp. 324–338.

[140] F. Nmira, J.-L. Consalvi, R. Demarco and L. Gay, Assessment of semi-empirical soot production models in C_1-C_3 axisymmetric laminar diffusion flames, in 8th Mediterranean Combustion Symposium, 2013.

[141] M. Fairweather, W.P. Jones, H.S. Ledin and R.P. Lindstedt, Predictions of soot formation in turbulent, non-premixed propane flames, in Symposium (International) on Combustion, 24 (1992), pp. 1067–1074.

[142] A. Fuentes, R. Henríquez, F. Nmira, F. Liu and J.-L. Consalvi, *Experimental and numerical study of the effects of the oxygen index on the radiation characteristics of laminar coflow diffusion flames*, Combustion and Flame 160 (2013), pp. 786–795.

[143] R.A. Demarco, *Modelling thermal radiation and soot formation in buoyant diffusion flames*, PhD Thesis, Aix-Marseille Université, 2012.

[144] J. Nagle and R.F. Strickland-Constable, Oxidation of carbon between 1000°C and 2000°C, in Proceedings of the Fifth Conference on Carbon, 1 (1962).

[145] C.P. Fenimore and G.W. Jones, *Oxidation of soot by hydroxyl radicals*, The Journal of Physical Chemistry 71 (1967), pp. 593–597.

[146] K.G. Neoh, J.B. Howard and A.F. Sarofim, *Twentieth Symposium (International) on CombustionEffect of oxidation on the physical structure of soot*, Symposium (International) on Combustion 20 (1985), pp. 951–957.

[147] F. Xu, A.M. El-Leathy, C.H. Kim, G.M. Faeth, Z.-G. Yuan, D.L. Urban et al., *Soot Surface Oxidation in Laminar Hydrocarbon/Air Diffusion Flames at Atmospheric Pressure. Appendix I*, (2003), .

[148] F. Nmira, D. Burot and J.-L. Consalvi, Stochastic Eulerian Field Method for radiative transfer in a propane oxygen-enhanced turbulent diffusion flame, 2015.

[149] S.A. Tashkun, V.I. Perevalov, J.-L. Teffo, A.D. Bykov and N.N. Lavrentieva, *CDSD-1000, the high-temperature carbon dioxide spectroscopic databank*, Journal of Quantitative Spectroscopy and Radiative Transfer 82 (2003), pp. 165–196.

[150] L.S. Rothman, I.E. Gordon, R.J. Barber, H. Dothe, R.R. Gamache, A. Goldman et al., *HITEMP, the high-temperature molecular spectroscopic database*, Journal of Quantitative Spectroscopy and Radiative Transfer 111 (2010), pp. 2139–2150.

[151] F. Liu, H. Guo and G.J. Smallwood, *Effects of radiation model on the modeling of a laminar coflow methane/air diffusion flame*, Combustion and Flame 138 (2004), pp. 136–154.

[152] J. Jaishree and D.C. Haworth, *Comparisons of Lagrangian and Eulerian PDF methods in simulations of non-premixed turbulent jet flames with moderate-to-strong turbulence-chemistry interactions*, Combustion Theory and Modelling 16 (2012), pp. 435–463.

[153] J. Jaishree, *Lagrangian and Eulerian Probability Density Function Methods for Turbulent Reacting Flows*, PhD Thesis, Pennsylvania State University, 2011.

[154] A. Garmory, *Micromixing effects in atmospheric reacting flows*, PhD Thesis, University of Cambridge, 2007.

[155] B.P. Leonard and J.E. Drummond, *Why you should not use "Hybrid","Power-Law"or related exponential schemes for convective modelling—there are much better alternatives*, International Journal for Numerical Methods in Fluids 20 (1995), pp. 421–442.

[156] W.K. Chow, *Selection of differencing schemes on simulating the sprinkler hot-air layer problem*, Numerical Heat Transfer: Part A: Applications 35 (1999), pp. 311–330.

[157] E.H. Chui, G.D. Raithby and P.M.J. Hughes, *Prediction of radiative transfer in cylindrical enclosures with the finite volume method*, Journal of Thermophysics and Heat Transfer 6 (1992), pp. 605–611.

[158] S.J. Brookes and J.B. Moss, *Measurements of soot production and thermal radiation from confined turbulent jet diffusion flames of methane*, Combustion and Flame 116 (1999), pp. 49–61.

[159] A. Coppalle and D. Joyeux, *Temperature and soot volume fraction in turbulent diffusion flames: Measurements of mean and fluctuating values*, Combustion and Flame 96 (1994), pp. 275–285.

[160] K.J. Young, *Soot formation in turbulent vaporised kerosine/air jet flames at elevated pressure*, (1993), .

[161] S.-Y. Lee, S. Turns and R. Santoro, *Measurements of soot, OH, and PAH concentrations in turbulent ethylene/air jet flames*, Combustion and Flame 156 (2009), pp. 2264–2275.

[162] S.M. Mahmoud, G.J. Nathan, P.R. Medwell, B.B. Dally and Z.T. Alwahabi, *Simultaneous planar measurements of temperature and soot volume fraction in a turbulent non-premixed jet flame*, Proceedings of the Combustion Institute 35 (2015), pp. 1931–1938.

[163] O. Nishida and S. Mukōhara, *Characteristics of soot formation and decomposition in turbulent diffusion flames*, Combustion and Flame 47 (1982), pp. 269–279.

[164] L. Wang, N.E. Endrud, S.R. Turns, M.D. D'Agostini and A.G. Slavejkov, *A Study of the Influence of Oxygen Index on Soot, Radiation, and Emission Characteristics of Turbulent Jet Flames*, Combustion Science and Technology 174 (2002), pp. 45–72.

[165] J.L.D. Ris, P.K. Wu and G. Heskestad, *Radiation fire modeling*, Proceedings of the Combustion Institute 28 (2000), pp. 2751–2759.

[166] A. Tewarson, *Prediction of Fire Properties of Materials: Part 1. Aliphatic and Aromatic Hydrocarbons and Related Polymers*, Factory Mutual Research, 1986.

[167] L. Li and P.B. Sunderland, *Smoke points of fuel–fuel and fuel–inert mixtures*, Fire Safety Journal 61 (2013), pp. 226–231.

[168] K.J. Young and J.B. Moss, *Modelling Sooting Turbulent Jet Flames Using an Extended Flamelet Technique*, Combustion Science and Technology 105 (1995), pp. 33–53.

[169] G. Ma, J.Z. Wen, M.F. Lightstone and M.J. Thomson, *Optimization of soot modeling in turbulent nonpremixed ethylene/air jet flames*, Combustion Science and Technology 177 (2005), pp. 1567–1602.

[170] C.P. Leusden and N. Peters, *Experimental and numerical analysis of the influence of oxygen on soot formation in laminar counterflow flames of acetylene*, Proceedings of the Combustion Institute 28 (2000), pp. 2619–2625.

[171] A. Beltrame, P. Porshnev, W. Merchan-Merchan, A. Saveliev, A. Fridman, L.. Kennedy et al., *Soot and NO formation in methane–oxygen enriched diffusion flames*, Combustion and Flame 124 (2001), pp. 295–310.

[172] A. Heyl and H. Bockhorn, *Flamelet modeling of NO formation in laminar and turbulent diffusion flames*, Chemosphere 42 (2001), pp. 449–462.

[173] C.N. Markides and N. Chakraborty, *Statistics of the scalar dissipation rate using direct numerical simulations and planar laser-induced fluorescence data*, Chemical Engineering Science 90 (2013), pp. 221–241.

[174] H. Pitsch, C.M. Cha and S. Fedotov, *Interacting flamelet model for non-premixed turbulent combustion with local extinction and re-ignition*, Annual Research Briefs—2001, Center for Turbulence Research, Stanford University (2001), pp. 65.

[175] R. Knaus, J. Oefelein and C. Pantano, *On the Relationship Between the Statistics of the Resolved and True Rate of Dissipation of Mixture Fraction*, Flow, Turbulence and Combustion 89 (2012), pp. 37–71.

[176] D.C. Haworth, M.C. Drake, S.B. Pope and R.J. Blint, The importance of time-dependent flame structures in stretched laminar flamelet models for turbulent jet diffusion flames, in Symposium (International) on Combustion, 22 (1989), pp. 589–597.

[177] E. Effelsberg and N. Peters, Scalar dissipation rates in turbulent jets and jet diffusion flames, in Symposium (International) on Combustion, 22 (1989), pp. 693–700.

[178] S.K. Liew, K.N.C. Bray and J.B. Moss, *A stretched laminar flamelet model of turbulent nonpremixed combustion*, Combustion and Flame 56 (1984), pp. 199–213.

[179] D.C. Haworth, M.C. Drake and R.J. Blint, *Stretched Laminar Flamelet Modeling of a Turbulent Jet Diffusion Flame*, Combustion Science and Technology 60 (1988), pp. 287–318.

[180] H.-W. Ge and E. Gutheil, *Simulation of a turbulent spray flame using coupled PDF gas phase and spray flamelet modeling*, Combustion and Flame 153 (2008), pp. 173–185.

[181] A. Wang, *Investigation of turbulence-radiation interactions in turbulent flames using a hybrid finite volume/Monte Carlo approach*, PhD Thesis, The Pennsylvania State University, 2007.

[182] B. Marracino and D. Lentini, *Radiation Modelling in Non-Luminous Nonpremixed Turbulent Flames*, Combustion Science and Technology 128 (1997), pp. 23–48.

[183] P.J. Coelho, O.J. Teerling and D. Roekaerts, *Spectral radiative effects and turbulence/radiation interaction in a non-luminous turbulent jet diffusion flame*, Combustion and Flame 133 (2003), pp. 75–91.

[184] M.E. Mueller and H. Pitsch, *LES model for sooting turbulent nonpremixed flames*, Combustion and Flame 159 (2012), pp. 2166–2180.

[185] Y. Xuan and G. Blanquart, *Effects of aromatic chemistry-turbulence interactions on soot formation in a turbulent non-premixed flame*, Proceedings of the Combustion Institute 35 (2015), pp. 1911–1919.

[186] J.W. Hartick, M. Tacke, G. Früchtel, E.P. Hassel and J. Janicka, *Interaction of turbulence and radiation in confined diffusion flames*, Symposium (International) on Combustion 26 (1996), pp. 75–82.

[187] C.R. Kaplan, S.W. Baek, E.S. Oran and J.L. Ellzey, *Dynamics of a strongly radiating unsteady ethylene jet diffusion flame*, Combustion and Flame 96 (1994), pp. 1–21.

[188] J. Akroyd, A.J. Smith, L.R. McGlashan and M. Kraft, *Comparison of the stochastic fields method and DQMoM-IEM as turbulent reaction closures*, Chemical Engineering Science 65 (2010), pp. 5429–5441.

[189] S.B. Pope, *A Monte Carlo Method for the PDF Equations of Turbulent Reactive Flow*, Combustion Science and Technology 25 (1981), pp. 159–174.

# **Appendix A** Derivation of the PDF transport equation

The derivation of the transport equation for the joint composition PDF $f_\phi(\boldsymbol{\psi}; \boldsymbol{x}, t) = f_\phi(\zeta, X_R, Y_s, N_s; \boldsymbol{x}, t)$ can be done in several ways (see Haworth, Appendix A [13]) but is based on the basic conservation equation of each scalar. These equations can all be written as:

$$\rho \frac{D\phi_\alpha}{Dt} = \frac{\partial \rho \phi_\alpha}{\partial t} + \frac{\partial \rho u_i \phi_\alpha}{\partial x_i} = -\Theta_\alpha \tag{A-1}$$

where the source term $\Theta_\alpha$ for each scalar is given by:

$$\begin{aligned}
\Theta_\zeta &= -\frac{\partial}{\partial x_i}\left[\rho D_{th} \frac{\partial \zeta}{\partial x_i}\right] \\
\Theta_{X_R} &= -\frac{\partial}{\partial x_i}\left[\frac{\lambda}{C_P} \frac{\partial X_R}{\partial x_i}\right] - \dot{Q}_{rad} \\
\Theta_{Y_s} &= \frac{\partial}{\partial x_i}\left[\rho V_{T,i} \frac{\partial Y_s}{\partial x_i}\right] + S_{Y_s} \\
\Theta_{N_s} &= \frac{\partial}{\partial x_i}\left[\rho V_{T,i} \frac{\partial N_s}{\partial x_i}\right] + S_{N_s}
\end{aligned} \tag{A-2}$$

Here the presented approach is the test-function derivation. An arbitrary function $Q(\boldsymbol{\psi})$ is introduced, and its convected derivative is expressed in two ways. The first expression is derived from the convected derivative definition:

$$\begin{aligned}
\langle \rho \frac{DQ}{Dt} \rangle &= \langle \frac{\partial \rho Q}{\partial t} + \frac{\partial \rho u_i Q}{\partial x_i} \rangle \\
&= \langle \frac{\partial \rho Q}{\partial t} \rangle + \langle \frac{\partial \rho u_i Q}{\partial x_i} \rangle \\
&= \frac{\partial}{\partial t} \langle \rho Q \rangle + \frac{\partial}{\partial x_i} \langle \rho u_i Q \rangle
\end{aligned} \tag{A-3}$$

By definition of the PDF:

$$\langle \rho Q \rangle = \int_{\boldsymbol{\phi}} \rho(\boldsymbol{\psi}) Q(\boldsymbol{\psi}) f_{\phi}(\boldsymbol{\psi}; \boldsymbol{x}, t) d\boldsymbol{\psi} \tag{A-4}$$

and only the PDF is dependent on time, so that:

$$\frac{\partial}{\partial t}\langle \rho Q \rangle = \int_{\boldsymbol{\phi}} Q(\boldsymbol{\psi}) \frac{\partial}{\partial t}\left[\rho(\boldsymbol{\psi}) f_{\phi}(\boldsymbol{\psi}; \boldsymbol{x}, t)\right] d\boldsymbol{\psi} \tag{A-5}$$

Expressing the averaged value of $\rho u_i Q$ introduces the joint velocity, composition PDF $f_{U,\phi}(\boldsymbol{V}, \boldsymbol{\psi}; \boldsymbol{x}, t)$:

$$\langle \rho u_i Q \rangle = \int_{\boldsymbol{\phi}} \int_{\boldsymbol{V}} \rho(\boldsymbol{\psi}) V_i Q(\boldsymbol{\psi}) f_{U,\phi}(\boldsymbol{V}, \boldsymbol{\psi}; \boldsymbol{x}, t) d\boldsymbol{V}\, d\boldsymbol{\psi} \tag{A-6}$$

This PDF is linked to the joint-composition PDF by:

$$f_{U,\phi}(\boldsymbol{V}, \boldsymbol{\psi}; \boldsymbol{x}, t) = f_{U|\phi}(\boldsymbol{V}|\boldsymbol{\psi}; \boldsymbol{x}, t) f_{\phi}(\boldsymbol{\psi}; \boldsymbol{x}, t) \tag{A-7}$$

where $f_{U|\phi}(\boldsymbol{V}|\boldsymbol{\psi}; \boldsymbol{x}, t)$ is the conditional PDF of $\boldsymbol{V}|\boldsymbol{\psi}$. In this case, Eq. (A-6) becomes:

$$\begin{aligned} \langle \rho u_i Q \rangle &= \int_{\boldsymbol{\phi}} \int_{\boldsymbol{V}} \rho(\boldsymbol{\psi}) V_i Q(\boldsymbol{\psi}) f_{U|\phi}(\boldsymbol{V}|\boldsymbol{\psi}; \boldsymbol{x}, t) f_{\phi}(\boldsymbol{\psi}; \boldsymbol{x}, t) d\boldsymbol{V}\, d\boldsymbol{\psi} \\ &= \int_{\boldsymbol{\phi}} \rho(\boldsymbol{\psi}) Q(\boldsymbol{\psi}) f_{\phi}(\boldsymbol{\psi}; \boldsymbol{x}, t) \int_{\boldsymbol{V}} V_i f_{U|\phi}(\boldsymbol{V}|\boldsymbol{\psi}; \boldsymbol{x}, t) d\boldsymbol{V}\, d\boldsymbol{\psi} \\ &= \int_{\boldsymbol{\phi}} \rho(\boldsymbol{\psi}) Q(\boldsymbol{\psi}) f_{\phi}(\boldsymbol{\psi}; \boldsymbol{x}, t) \langle u_i|\boldsymbol{\psi}\rangle d\boldsymbol{\psi} \end{aligned} \tag{A-8}$$

where $\langle u_i|\boldsymbol{\psi}\rangle$ is the average value of the flow velocity conditioned on the value of $\boldsymbol{\psi}$. Finally, in this expression only the term $f_{\phi}(\boldsymbol{\psi}; \boldsymbol{x}, t)\langle u_i|\boldsymbol{\psi}\rangle$ depends on the spatial position so that:

$$\frac{\partial}{\partial x_i}\langle \rho u_i Q \rangle = \int_{\boldsymbol{\phi}} Q(\boldsymbol{\psi}) \frac{\partial}{\partial x_i}\left[\rho(\boldsymbol{\psi}) f_{\phi}(\boldsymbol{\psi}; \boldsymbol{x}, t)\langle u_i|\boldsymbol{\psi}\rangle\right] d\boldsymbol{\psi} \tag{A-9}$$

and the first expression of $\langle \rho \frac{DQ}{Dt} \rangle$ is:

$$\boxed{\langle \rho \frac{DQ}{Dt} \rangle = \int_{\boldsymbol{\phi}} Q(\boldsymbol{\psi}) \left[\frac{\partial}{\partial t}\left[\rho(\boldsymbol{\psi}) f_{\phi}(\boldsymbol{\psi}; \boldsymbol{x}, t)\right] + \frac{\partial}{\partial x_i}\left[\rho(\boldsymbol{\psi}) f_{\phi}(\boldsymbol{\psi}; \boldsymbol{x}, t)\langle u_i|\boldsymbol{\psi}\rangle\right]\right] d\boldsymbol{\psi}} \tag{A-10}$$

The second expression is derived from the chain rule:

$$\begin{aligned}\langle\rho\frac{DQ}{Dt}\rangle &= -\langle\rho\frac{\partial Q}{\partial\psi_\alpha}\frac{D\phi_\alpha}{Dt}\rangle \\ &= -\langle\Theta_\alpha\frac{\partial Q}{\partial\psi_\alpha}\rangle\end{aligned} \tag{A-11}$$

In general, sources terms $\Theta_\alpha$ depend on other variables than the composition vector. All these variables are grouped in a vector $\boldsymbol{z}$ so that $\Theta_\alpha = \Theta_\alpha(\boldsymbol{\phi}, \boldsymbol{z})$. Introducing the joint composition/Z PDF $f_{Z,\phi}(\boldsymbol{Z}, \boldsymbol{\psi}; \boldsymbol{x}, t)$:

$$\langle\rho\Theta_\alpha\frac{\partial Q}{\partial\psi_\alpha}\rangle = \int_{\boldsymbol{\phi}}\int_{\boldsymbol{Z}}\Theta_\alpha(\boldsymbol{Z},\boldsymbol{\psi})\frac{\partial Q}{\partial\psi_\alpha}(\boldsymbol{\psi})f_{Z,\phi}(\boldsymbol{Z},\boldsymbol{\psi};\boldsymbol{x},t)d\boldsymbol{Z}\,d\boldsymbol{\psi} \tag{A-12}$$

The same considerations used to derive Eq. (A-8) from Eq. (A-6) are invoked to obtain:

$$\langle\rho\Theta_\alpha\frac{\partial Q}{\partial\psi_\alpha}\rangle = \int_{\boldsymbol{\phi}}\langle\Theta_\alpha|\boldsymbol{\psi}\rangle\frac{\partial Q}{\partial\psi_\alpha}(\boldsymbol{\psi})f_\phi(\boldsymbol{\psi};\boldsymbol{x},t)d\boldsymbol{\psi} \tag{A-13}$$

The next step is to use integration by part for each variable of the composition vector:

$$\begin{aligned}\langle\rho\Theta_\alpha\frac{\partial Q}{\partial\psi_\alpha}\rangle = &\left[\int_{\boldsymbol{\phi}}\langle\Theta_\alpha|\boldsymbol{\psi}\rangle Q(\boldsymbol{\psi})f_\phi(\boldsymbol{\psi};\boldsymbol{x},t)d\boldsymbol{\psi}_{\boldsymbol{\beta}\neq\boldsymbol{\alpha}}\right]_{\psi_\alpha=\psi_{\alpha,min}}^{\psi_\alpha=\psi_{\alpha,max}} \\ &-\int_{\boldsymbol{\phi}}Q(\boldsymbol{\psi})\frac{\partial}{\partial\psi_\alpha}\left[\langle\Theta_\alpha|\boldsymbol{\psi}\rangle f_\phi(\boldsymbol{\psi};\boldsymbol{x},t)\right]d\boldsymbol{\psi}\end{aligned} \tag{A-14}$$

The first term on the right-hand side of Eq. (A-14) is related to the probability flux at infinity (or at the scalar bounds). Since the PDF and the function $Q(\boldsymbol{\psi})$ are assumed to be well-behaved, the flux at the bounds must be zero so that this term is also zero. Therefore, the final form for the second expression of the convective derivative is:

$$\langle\rho\frac{DQ}{Dt}\rangle = \int_{\boldsymbol{\phi}}Q(\boldsymbol{\psi})\frac{\partial}{\partial\psi_\alpha}\left[\langle\Theta_\alpha|\boldsymbol{\psi}\rangle f_\phi(\boldsymbol{\psi};\boldsymbol{x},t)\right]d\boldsymbol{\psi} \tag{A-15}$$

Eqs. (A-10) and (A-15) must be equal for any arbitrary function $Q(\boldsymbol{\psi})$, so that the composition PDF transport equation is finally written:

$$\frac{\partial}{\partial t}\left[\rho(\boldsymbol{\psi})f_\phi(\boldsymbol{\psi};\boldsymbol{x},t)\right]+\frac{\partial}{\partial x_i}\left[\rho(\boldsymbol{\psi})f_\phi(\boldsymbol{\psi};\boldsymbol{x},t)\langle u_i|\boldsymbol{\psi}\rangle\right]=\frac{\partial}{\partial \psi_\alpha}\left[\langle\Theta_\alpha|\boldsymbol{\psi}\rangle f_\phi(\boldsymbol{\psi};\boldsymbol{x},t)\right] \tag{A-16}$$

The derivation of the Favre composition PDF transport equation is straightforward from its definition:

$$\langle\rho\rangle\widetilde{f_\phi}=\rho f_\phi \tag{A-17}$$

so that:

$$\frac{\partial}{\partial t}\left[\langle\rho\rangle\widetilde{f_\phi}\right]+\frac{\partial}{\partial x_i}\left[\langle\rho\rangle\widetilde{f_\phi}\langle u_i|\boldsymbol{\psi}\rangle\right]=\frac{\partial}{\partial \psi_\alpha}\left[\langle\rho\rangle\widetilde{f_\phi}\left\langle\frac{\Theta_\alpha}{\rho}\middle|\boldsymbol{\psi}\right\rangle\right] \tag{A-18}$$

The conditional averaged velocity can be written:

$$\langle u_i|\boldsymbol{\psi}\rangle=\langle\widetilde{u_\imath}+{u_i}''|\boldsymbol{\psi}\rangle=\langle\widetilde{u_\imath}|\boldsymbol{\psi}\rangle+\langle{u_i}''|\boldsymbol{\psi}\rangle=\widetilde{u_\imath}+\langle{u_i}''|\boldsymbol{\psi}\rangle \tag{A-19}$$

so that finally Eq. (A-18) becomes:

$$\frac{\partial}{\partial t}\left[\langle\rho\rangle\widetilde{f_\phi}\right]+\frac{\partial}{\partial x_i}\left[\langle\rho\rangle\widetilde{f_\phi}\widetilde{u_\imath}\right]+\frac{\partial}{\partial x_i}\left[\langle\rho\rangle\widetilde{f_\phi}\langle{u_i}''|\boldsymbol{\psi}\rangle\right]=\frac{\partial}{\partial \psi_\alpha}\left[\langle\rho\rangle\widetilde{f_\phi}\left\langle\frac{\Theta_\alpha}{\rho}\middle|\boldsymbol{\psi}\right\rangle\right] \tag{A-20}$$

# **Appendix B** Derivation of the Stochastic Partial Differential Equations for the stochastic fields

The derivation of the Stochastic Partial Differential Equations (SPDE) for the Stochastic Eulerian Fields (SEF) method is presented here in the multi case for the conventional PDF $f_\phi(\boldsymbol{\psi};\boldsymbol{x},t)$. In the multi scalar case, using a gradient hypothesis for closing the mesomixing term, and the Interaction by Exchange with the Mean (IEM) model for micromixing, the conventional PDF transport equation can be written [14,17]:

$$\frac{\partial f_\phi}{\partial t}+\langle u_i\rangle\frac{\partial f_\phi}{\partial x_i}-\frac{\partial}{\partial x_i}\left[\Gamma_T\frac{\partial f_\phi}{\partial x_i}\right]=R(\boldsymbol{\psi};\boldsymbol{x},t) \tag{B-1}$$

where $R(\boldsymbol{\psi};\boldsymbol{x},t)=-\frac{\partial}{\partial\psi_\alpha}\left[\frac{1}{2}C_{\phi,\alpha}\frac{\varepsilon}{k_T}(\langle\phi_\alpha\rangle-\psi_\alpha)f_\phi\right]+\frac{\partial}{\partial\psi_\alpha}\left[f_\phi\Theta_\alpha(\boldsymbol{\psi})\right]$.

In the SEF method, the PDF is written:

$$f_\phi(\boldsymbol{\psi};\boldsymbol{x},t)=\frac{1}{N_F}\sum_{n=1}^{N_F}\prod_{\alpha=1}^{N_\alpha}\delta_{\phi_{\alpha,n}} \tag{B-2}$$

where $N_F$ is the number of fields $\boldsymbol{\phi_n}$, $N_\alpha$ the number of scalars in the composition vector, and $\delta_{\phi_{\alpha,n}}=\delta(\psi_\alpha-\phi_{\alpha,n})$. Introducing Eq. (B-2) in Eq. (B-1):

$$\frac{\partial f_\phi}{\partial t}+\frac{1}{N_F}\sum_{n=1}^{N_F}\left[\langle u_i\rangle\frac{\partial}{\partial x_i}\left(\prod_{\alpha=1}^{N_\alpha}\delta_{\phi_{\alpha,n}}\right)-\frac{\partial}{\partial x_i}\Gamma_T\left(\frac{\partial}{\partial x_i}\left(\prod_{\alpha=1}^{N_\alpha}\delta_{\phi_{\alpha,n}}\right)\right)\right]=R(\boldsymbol{\psi};\boldsymbol{x},t) \tag{B-3}$$

The derivative of the product of delta function gives [14,188]:

$$\frac{\partial}{\partial x_i}\left(\prod_{\alpha=1}^{N_\alpha}\delta_{\phi_{\alpha,n}}\right)=-\sum_{\alpha=1}^{N_\alpha}\frac{\partial\phi_{\alpha,n}}{\partial x_i}\delta^{(1)}_{\phi_{\alpha,n}}\prod_{\substack{\beta=1\\\beta\neq\alpha}}^{N_\alpha}\delta_{\phi_{\beta,n}} \tag{B-4}$$

where the m[th] derivative of the delta function $\delta^{(m)}_{\phi_{\alpha,n}}=\frac{\partial^{(m)}\delta_{\phi_{\alpha,n}}}{\partial\phi^{(m)}_{\alpha,n}}$ is defined as [57]:

$$\int_{-\infty}^{+\infty}\delta^{(m)}_{\phi_{\alpha,n}}\,g(x)dx=(-1)^m g^{(m)}(\phi_{\alpha,n}) \tag{B-5}$$

so that Eq. (B-4) becomes:

$$\frac{\partial}{\partial x_i}\left(\prod_{\alpha=1}^{N_\alpha}\delta_{\phi_{\alpha,n}}\right)=-\sum_{\alpha=1}^{N_\alpha}\frac{\partial}{\partial\phi_\alpha}\left[\frac{\partial\phi_{\alpha,n}}{\partial x_i}\prod_{\beta=1}^{N_\alpha}\delta_{\phi_{\beta,n}}\right] \tag{B-6}$$

In the same spirit, the turbulent mixing term develops as [188]:

$$\begin{aligned}\frac{\partial}{\partial x_i}\Gamma_T&\left(\sum_{\alpha=1}^{N_\alpha}\frac{\partial}{\partial\phi_\alpha}\left[\frac{\partial\phi_{\alpha,n}}{\partial x_i}\prod_{\substack{\beta=1\\\beta\neq\alpha}}^{N_\alpha}\delta_{\phi_{\beta,n}}\right]\right)\\&=-\sum_{\alpha=1}^{N_\alpha}\frac{\partial}{\partial\phi_\alpha}\left(\frac{\partial}{\partial x_i}\left(\Gamma_T\frac{\partial\phi_{\alpha,n}}{\partial x_i}\right)\prod_{\beta=1}^{N_\alpha}\delta_{\phi_{\beta,n}}\right)\\&\quad+\sum_{\alpha=1}^{N_\alpha}\sum_{\beta=1}^{N_\beta}\frac{\partial^2}{\partial\phi_\alpha\partial\phi_\beta}\left(\Gamma_T\frac{\partial\phi_{\alpha,n}}{\partial x_i}\frac{\partial\phi_{\beta,n}}{\partial x_i}\prod_{\gamma=1}^{N_\alpha}\delta_{\phi_{\gamma,n}}\right)\end{aligned} \tag{B-7}$$

Inserting Eq. (B-6) and (B-7) in Eq. (B-3):

$$\begin{aligned}\frac{\partial f_\phi}{\partial t}+\frac{1}{N_F}\sum_{n=1}^{N_F}\Bigg[&-\langle u_i\rangle\sum_{\alpha=1}^{N_\alpha}\frac{\partial}{\partial\phi_\alpha}\left[\frac{\partial\phi_{\alpha,n}}{\partial x_i}\prod_{\beta=1}^{N_\alpha}\delta_{\phi_{\beta,n}}\right]\\&+\sum_{\alpha=1}^{N_\alpha}\frac{\partial}{\partial\phi_\alpha}\left(\frac{\partial}{\partial x_i}\left(\Gamma_T\frac{\partial\phi_{\alpha,n}}{\partial x_i}\right)\prod_{\beta=1}^{N_\alpha}\delta_{\phi_{\beta,n}}\right)\\&-\sum_{\alpha=1}^{N_\alpha}\sum_{\beta=1}^{N_\beta}\frac{\partial^2}{\partial\phi_\alpha\partial\phi_\beta}\left(\Gamma_T\frac{\partial\phi_{\alpha,n}}{\partial x_i}\frac{\partial\phi_{\beta,n}}{\partial x_i}\prod_{\gamma=1}^{N_\alpha}\delta_{\phi_{\gamma,n}}\right)\Bigg]=R(\boldsymbol{\psi};\boldsymbol{x},t)\end{aligned} \tag{B-8}$$

The left-hand side of Eq. (B-8) is a Fokker-Planck equation in time-composition space and has an equivalent SPDE [17] describing the contribution to each field:

$$d\phi_{\alpha,n} = -\langle u_i \rangle \frac{\partial \phi_{\alpha,n}}{\partial x_i} dt + \frac{\partial}{\partial x_i}\left(\Gamma_T \frac{\partial \phi_{\alpha,n}}{\partial x_i}\right) dt + \sqrt{2\Gamma_T} \frac{\partial \phi_{\alpha,n}}{\partial x_i} dW_{i,n} \tag{B-9}$$

In the same way, the right-hand side of Eq. (B-9) induce the following contribution to each field:

$$d\phi_{\alpha,n} = -\frac{1}{2} C_{\phi,\alpha} \frac{\varepsilon}{k_T} (\langle \phi_\alpha \rangle - \psi_\alpha) dt + \Theta_\alpha(\boldsymbol{\psi}) dt \tag{B-10}$$

so that the total contribution to each field is finally:

$$\begin{aligned} d\phi_{\alpha,n} = -\langle u_i \rangle \frac{\partial \phi_{\alpha,n}}{\partial x_i} dt + \frac{\partial}{\partial x_i}\left(\Gamma_T \frac{\partial \phi_{\alpha,n}}{\partial x_i}\right) dt - \frac{1}{2} C_{\phi,\alpha} \frac{\varepsilon}{k_T} (\langle \phi_\alpha \rangle - \psi_\alpha) dt + \Theta_\alpha(\boldsymbol{\psi}) dt \\ + \sqrt{2\Gamma_T} \frac{\partial \phi_{\alpha,n}}{\partial x_i} dW_{i,n} \end{aligned} \tag{B-11}$$

# Appendix C A statistically stationary 1D system with imperfect mixing

In this section, the SEF method is implemented in a simplified one-dimensional, one-scalar case, for which the mean velocity and turbulence frequency are uniform. The aim is to analyze the effect of the number of fields considered on statistical convergence and on the overall efficiency of the method.

## C.1 Case presentation

The test case considered here is the one-dimensional plug-flow reactor with imperfect mixing presented by Pope [189], represented by a domain $[0, L]$ [0,L] with $L = 1$. The mean velocity $U$, the density $\rho$, the turbulent diffusion coefficient $\Gamma_T$ and the turbulent frequency $\omega$ are assumed to be uniform and constant in time. Only one scalar $\phi(x,t)$ is considered, representing the concentration of reactants. The IEM (Interaction with Exchange with the Mean) model is used for the molecular mixing term. The chemical source term is assumed to be linear in composition: $S(\psi) = a(1-\psi)$.

The one-dimensional computational domain grid considered here is uniform with a cell-size denoted by $\Delta x$. The associated boundary conditions are $\widetilde{\phi}(0,t) = 0$, $\partial\widetilde{\phi}/\partial x\,(1,t) = 0$ and the domain is initialized as $\widetilde{\phi}(x,0) = 1$. The problem simulated here is non-dimensional with the following numerical values for the constants:

$$U = 1.0; \quad \Gamma_T = 0.1; \quad \omega = 20.0; \quad C_\phi = 1.0; \quad a = 3.0 \tag{V-5}$$

The resulting PDF transport equation is:

$$\frac{\partial f}{\partial t} + U\frac{\partial f}{\partial x} - \frac{\partial}{\partial x}\left(\Gamma_T \frac{\partial f}{\partial x}\right) = -\frac{\partial}{\partial \psi}\left[f\frac{C_\phi \omega}{2}(\widetilde{\phi} - \psi)\right] - \frac{\partial}{\partial \psi}[fS(\psi)] \tag{V-6}$$

The interest of this case is the fact that analytic expressions can be derived for $\widetilde{\phi}$ and $\widetilde{\phi''^2}$, and the four transport processes (convection, diffusion, chemical reaction and micro-mixing) are equally important.

# C.2 Results

The simulation results obtained for several mesh-size are given in Fig. C-1 and for several number of environments are given on Fig. C-2. The agreement with the analytical solution is very good, even if a small gap is visible on the variance results. A minimum of 20 cells and 20 environments is necessary to obtain a satisfactory agreement, and no clear improvement can be observed when these numerical parameters are increased.

Furthermore, the temporal variation of the mean composition at the center of the domain is given on Fig. C-3a for several numbers of environments. As expected, the fluctuations around the mean value decrease when $N_F$ increases.

Finally, one of the important characteristic of this method is the fact that the stochastic part is constant in space (i.e. only one value for dW is selected per time-step and per field), so that there is no spatial statistical error. As can be seen on Fig C-3b which represents the profile of 4 fields as well as the mean composition, this leads to spatially smooth fields around the mean composition.

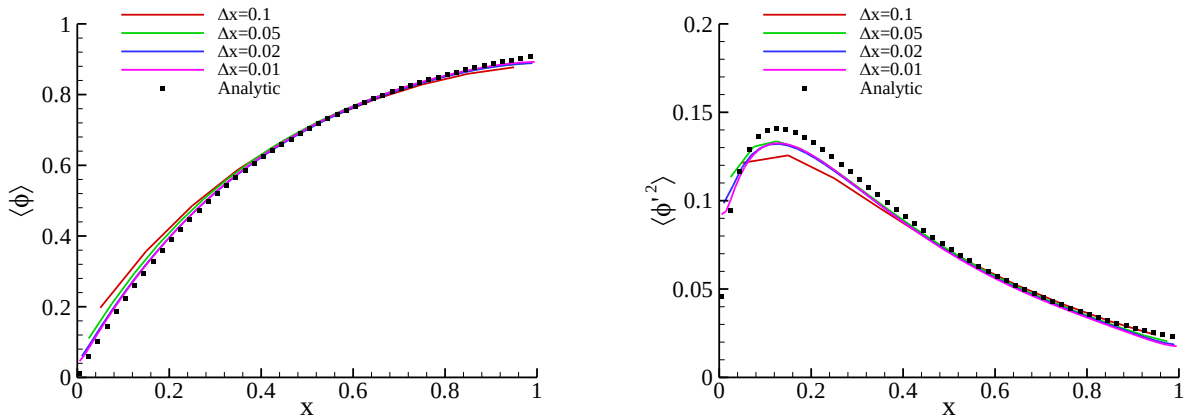


**Figure C-1. a) Mean composition and b) composition variance for various cell-size mesh for $N_F = 60$.**

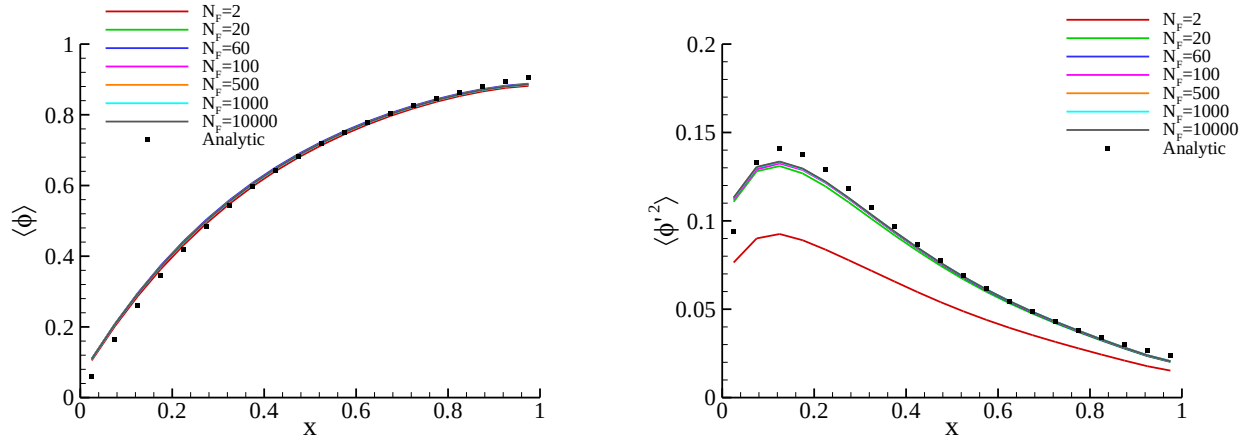


**Figure C-2. a) Mean composition and b) composition variance for various number of fields and $\Delta x = 0.05$.**

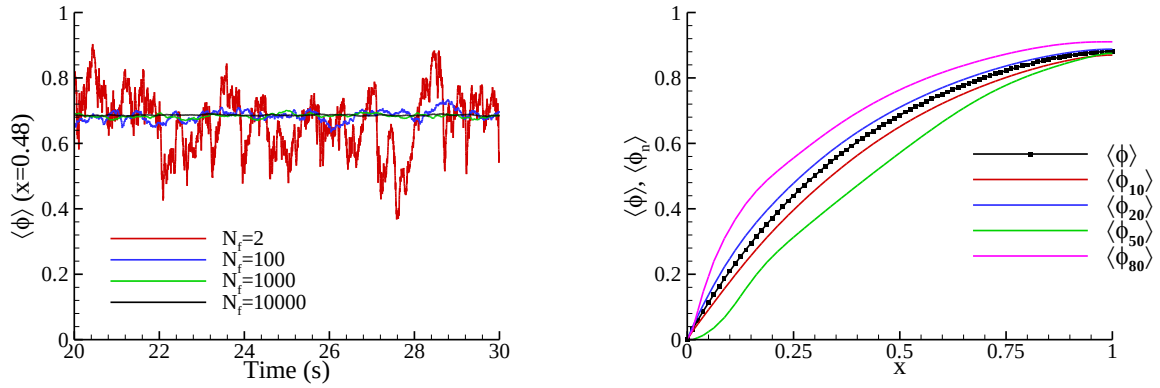


**Figure C-3. a) Temporal variation of the mean composition at x=0.48 for increasing number of environments. b) Mean composition and four stochastic fields.**

**ABSTRACT.** The simulation of fire scenarios in confined environment requires to model critical processes such as the thermal degradation of solid/liquid materials, the heat feedback from the flame toward the environment and the condensed phase, the gas phase combustion, the production of soot, the radiative heat transfer, and local extinction/re-ignition processes that can occur due to the lack of oxygen. An additional difficulty is related to the turbulent nature of the flow which requires to model properly the interactions between turbulence and chemistry, turbulence and soot production, and turbulence and radiation. The main purpose of this thesis is to develop and implement a transported Probability Density Function (PDF) method to model these interactions.

The combustion model is based on the enthalpy defect flamelet model. Soot production is modeled by a semi-empirical acetylene-benzene-based two-equation model. The time-averaged radiative transfer equation is solved by assuming the optically-thin fluctuations approximation for absorption turbulence-radiation interactions (TRIs), using a Wide-Band Correlated-k model for the radiative properties of the radiatively participating gaseous products. Turbulence-chemistry interactions, turbulence-soot production interactions and turbulence-radiation interactions are modeled by a statistical method involving the composition joint-PDF of mixture fraction, scalar dissipation rate, enthalpy defect parameter, soot number density and soot mass fraction. This PDF is obtained by solving its transport equation using the stochastic Eulerian fields method.

First, the model is validated by simulating twelve turbulent jet flames covering a large range of Reynolds numbers and fuel sooting propensity. Model predictions are found to be in reasonable agreement with experimental data in terms of flame structure, soot quantities and radiative loss. Mean soot volume fractions are predicted within a factor of two of the experiments whereas radiant fractions and peaks of wall radiative fluxes are within 20%.

Second, soot emission TRI is studied in details by simulating an oxygen-enhanced propane turbulent diffusion flame. Model results show that the cross correlation between soot volume fraction and temperature is strongly negative in the regions dominated by soot radiation and neglecting this correlation enhances significantly the radiative losses. In addition, soot emission TRI is also studied by simulating five turbulent jet flames of different Reynolds numbers and fuel sooting propensity. TRIs tend to enhance soot emission due to the temperature self-correlation. It is found that the negative correlation between soot absorption coefficient and the Planck function limits the effects of the temperature self-correlation and this limitation increases as the Reynolds number increases.

Finally, the effects of taking into account the correlation between mixture fraction and enthalpy defect on flame structure and radiative characteristics are also studied on an ethylene flame, showing that it has weak effect on the mean flame structure but tends to inhibit both temperature fluctuations (locally by about 50%) and radiative loss (by 20% overall).

**Key-words:** Transported PDF method, stochastic Eulerian field, turbulence-soot production interactions, turbulence-radiation interactions, combustion-radiation interactions.

**RESUME.** La simulation de scénarios d'incendie dans des environnements confinés nécessite de modéliser des processus critiques tels que la dégradation thermique des matériaux solides et liquides, le transfert de chaleur de la flamme et du milieu environnant vers la phase condensée, la combustion en phase gazeuse, la production de suie, les transferts de chaleur, et les processus d'extinction et de ré-inflammation locales provenant du manque d'oxygène. Une difficulté additionnelle provient de la nature turbulente de l'écoulement, ce qui nécessite de modéliser proprement les interactions entre la turbulence et la chimie, entre la turbulence et la production de la suie, et entre la turbulence et le rayonnement. L'objectif principal de cette thèse est de développer et d'implémenter une méthode de transport de la fonction densité de probabilité (PDF) pour modéliser ces interactions.

La combustion est modélisée par un modèle de flammelettes laminaires non-adiabatiques. La production de suie est décrite par un modèle semi-empirique à deux équations basé sur l'acétylène et le benzène. L'équation de transfert radiatif est résolue en faisant l'hypothèse des fluctuations optiquement minces pour le terme d'absorption et un modèle à large bande k-corrélé pour les propriétés radiatives des espèces gazeuses participant aux transferts radiatifs. Les interactions chimie-turbulence, production de suie-turbulence et rayonnement-turbulence sont modélisées par une méthode statistique mettant en jeu la PDF jointe de la fraction de mélange, du taux de dissipation scalaire, du paramètre de non-adiabaticité, du nombre densité de suie et de la fraction massique de suie. Cette PDF est obtenue en résolvant son équation de transport par la méthode des Champs Eulériens Stochastiques.

Dans un premier temps, le modèle est validé par la simulation de douze flammes de diffusion turbulentes de type jet couvrant une large gamme de nombre de Reynolds et de propension à produire de la suie. Les résultats obtenus sont en accord raisonnables avec les données expérimentales en termes de structure de la flamme, des quantités de suie et de perte radiative. Les fractions volumiques de suies moyennes sont prédites dans un facteur deux des données expérimentales, tandis que les fractions rayonnées et les pics de flux radiatifs pariétaux présentent un écart de moins de 20%.

Deuxièmement, les interactions entre la turbulence et l'émission radiative des suies sont étudiées en détails en simulant des flammes de diffusion turbulentes enrichies d'oxygène. Les résultats mettent en évidence que, d'une part, la corrélation entre la fraction volumique de suie et la température est fortement négative dans les régions dominées par le rayonnement des suies et que, d'autre part, le fait de négliger cette corrélation affecte significativement les pertes radiatives. De plus, l'effet de la turbulence sur l'émission radiative des suies est étudié en simulant cinq flammes de diffusion turbulentes de type jet mettant en jeu des combustibles et des nombres de Reynolds différents. Les effets de la turbulence tendent à augmenter l'émission radiative des suies du fait de l'autocorrélation de la température. Cette augmentation est limitée par le caractère négatif de la corrélation entre la fraction volumique de suie et la fonction de Planck et cette limitation augmente avec le nombre de Reynolds.

Finalement, l'influence de la corrélation entre la fraction de mélange et le paramètre de non-adiabaticité est étudiée sur une flamme d'éthylène, montrant qu'elle a peu d'effet sur la structure moyenne de flamme mais tend à limiter les fluctuations de température (de 50% localement) et les pertes radiatives (globalement de 20%)

**Mots-clés** : Méthode de transport de la PDF, champs Eulériens stochastiques, interactions suies/turbulence, rayonnement/turbulence, rayonnement/combustion